

NATIONAL TECHNICAL UNIVERSITY OF ATHENS



SCHOOL OF MECHANICAL ENGINEERING

LABORATORY OF AERODYNAMICS

A THESIS SUBMITTED FOR THE DEGREE OF DOCTOR OF ENGINEERING

Multi-disciplinary design optimization of wind turbine blades including passive load control techniques

Giannis Serafeim

27 September 2023

This page intentionally left blank



NATIONAL TECHNICAL UNIVERSITY OF ATHENS
SCHOOL OF MECHANICAL ENGINEERING
SECTION OF FLUIDS
LABORATORY OF AERODYNAMICS

Multi-disciplinary design optimization of wind turbine blades including passive load control techniques

Ph.D. Thesis

of

Giannis Andreou-Serafeim

Funding by:

The research was supported by the Hellenic Foundation for Research and Innovation (HFRI) under the HFRI PhD Fellowship grant (Fellowship Number: 867).



The implementation of the doctoral thesis was co-financed by Greece and the European Union (European Social Fund-ESF) through the Operational Programme «Human Resources Development, Education and Lifelong Learning» in the context of the Act “Enhancing Human Resources Research Potential by undertaking a Doctoral Research” Sub-action 2: IKY Scholarship Programme for PhD candidates in the Greek Universities (Fellowship Number: 2022-050-0502-52636).



Operational Programme
Human Resources Development,
Education and Lifelong Learning

Co-financed by Greece and the European Union



This page intentionally left blank

Author: Giannis Andreou-Serafeim

Title: Multi-disciplinary design optimization of wind turbine blades including passive load control techniques

Center: NTUA Laboratory of Aerodynamics

Summary: The objective of the current PhD thesis is the optimal design of DTU-10MW RWT wind turbine blades, for minimum Levelized Cost of Electricity (LCoE) by combining different passive load control techniques. Such techniques that have been investigated in this thesis are the material and geometric BTC and FEC. The optimization is based on the multi-disciplinary aero-elastic optimization approach, considering in a common loop the aerodynamics (e.g. chord or/and twist distributions) and the structural (e.g. wall thicknesses) characteristics as well as the load control parameters. In the context of this research, various optimization techniques have been used and compared, like COBYLA, SLSQP and Newton's methods that are more often employed in the existing literature.

Report: National Technical University of Athens

Publication: 27 Sep. 2023

Examination Committee:

1. Dimitrios Saravanos*, professor at Patra's University, Laborator of Applied Mechanics and Vibrations
2. Spyridon Voutsinas*, professor at NTUA, School of Mechanical Engineering
3. Vasilios Riziotis (supervisor)*, associate professor at NTUA, School of Mechanical Engineering
4. Kyriakos Giannakoglou, professor at NTUA, School of Mechanical Engineering
5. Nikolaos Chrysochoides, professor at Patra's University, Department of Mechanical Engineering & Aeronautics
6. Marinos Manolesos, assistant professor at NTUA, School of Mechanical Engineering
7. Manolis Angelou, assistant professor at NTUA, School of Naval Architecture & Marine Engineering

*member of the advisory committee

Pages: 204

Figures: 77

Tables: 38

References: 168

National Technical University of Athens, School of Mechanical Engineering
Heron Polytechniou 9
15780 Zografou – Athens
Greece
seraf@fluid.mech.ntua.gr

This page intentionally left blank

© Copyright 2023

This work is subject to copyright. All rights are reserved by the author, whether the whole or part of the material is concerned, specifically the rights of translation, re-printing, re-use of illustrations, re-citation, broadcasting, re-production on microfilms or in any other physical way and transmission or information storage and retrieval, electronic adaptation, computer software or by similar or dissimilar methodology now known or hereafter developed. Duplication of this thesis or parts thereof is permitted only under the provisions of the Copyright Law of the author's location (Greece) and permission for use must always be obtained from him. Violations are liable to prosecution under the respective Copyright Law. The use of general descriptive names, registered names, trademarks, service marks etc - in this thesis does not imply, even in the absence of a specific statement, that such names are exempt from the relevant protective laws and regulations and therefore there are free for general use. While the advice and information in this thesis are believed to be true and accurate at the date of publication, neither the author nor the NTUA's Aerodynamic Laboratory can accept any legal responsibility for any errors or omissions that may be made. The author makes no warranty, express or implied, with respect to the material contained herein.

This page intentionally left blank

Extended summary

The main pursuit of both the scientific community and the wind energy industry in the last twenty-five years, is the compression of the cost of the energy (Levelized Cost of Electricity – LCoE) produced by wind at comparable or even lower levels than those by the conventional energy sources. The effort to reduce the cost of wind energy during the years of its explosive development was also accompanied by the continuous increase in the size of the wind turbines. Up-scaling their size from 500kW (rotors diameter of about 40m) in the early of 1990s, to 5 – 15MW (rotors diameter > 150m) today, had the consequence of facing various technical challenges, the overcoming of which became possible through the introduction of new innovative manufacturing approaches, the use of modern materials and the application of active and/or passive load control techniques. Today's economic and geopolitical environment makes it imperative to further reduce the cost of wind turbines, entailing the design and development of very large wind turbines (> 15MW) and very large scale wind farms (of hundreds of MWs). The path of the continuous up-scaling of wind turbines has today become a one-way street and the installation of turbines of 10 – 15MW rating is common practice in offshore applications. In order to render their cost comparative to conventional energy sources, manufacturers have employed modern active load control techniques, targeting both to enhancing power production (at the wind farm scale) and reducing loads. However, standard active control techniques alone, usually based on pitch, are not sufficient to suppress cost at desirable levels. This is why recently, the wind energy community has also tackled passive load control methods based on “Aero-elastic Tailoring” (A/T).

A/T is a design technique through which geometric or stiffness properties of a structure are matched with its aero-dynamic characteristics in such a way that overall structural loads are reduced. The subject of A/T and its application to the modern large-scale wind turbines in the context of a holistic blade design framework, is a very hot-field of the today's scientific research. In general, the A/T methods can be distinguished into two categories:

- Bend-Twist-Coupling (BTC): by this term the behavior of a structure that has been designed to undergo torsion deformation under the action of bending loads, is described. The resulting change in sectional angle will affect the aerodynamic loading through a change in the angle of attack. Its materialization can be achieved either through material (by offset ply angle on uni-directional material) or geometrical (so-called sweep) approaches.
- Flap-Edge-Coupling (FEC): is the design concept in which when the blade is excited and undergoes vibrations in one bending direction (e.g. edge-wise) it also vibrates in the other bending direction (flap-wise). As a result, a trading of aerodynamic damping from the highly damped flap-wise motion to the poorly damped edge-wise motion is established and thereby edge-wise vibrations can be reduced. This control method can be materialized either through the shift of the ‘caps’ of the shear box of the blade internal structure (geometric approach) or by non-uniform change of the blades’ walls thickness (material approach).

In the recent years, several EU collaborative projects such as the UpWind and the INNWIND.EU have dealt with the application of BTC control on 5 – 10MW wind turbines, concluding that the use of passive control can reduce the ultimate loads by about 15% in the occurrence of extreme turbulence conditions. In this work, the alleviation of the loads has been utilized, to saving in manufacturing material for the blades, resulting in the design of a rotor with 10% less mass. On the other hand, the FEC has proven to be an effective approach for alleviating severe vibrations observed during the parked or idling state of the

rotors, in storm conditions. In the current thesis it has been shown that a uniform shift of ‘caps’ by 3% (throughout the length of the blade) is sufficient to significantly reduce the vibrations of the blade of a reference 10MW wind turbine.

An optimization framework has been established in the current thesis aiming to design a modified wind turbine rotor based on the Reference Wind Turbine (RWT) DTU-10MW, which can achieve a minimum Levelized Cost of Electricity (LCoE). Alleviation of loads using effective combinations of different passive load control techniques is integrated in the optimization loop. Two pathways for reducing LCOE are addressed in the work a) compressing CAPEX through reduced use of composite material and b) design of rotors with higher S/P (as Specific Power has been defined the ratio of power to area of the rotor disk, so increased S/P rotors implies larger rotor diameters for the same rated power) or increased annual energy production. The numerical tools included in the above framework are listed below:

- Servo-aero-elastic analysis tool: in-house, multibody FEM solver hGAST provides ultimate loads along the span of the blades through non-linear time domain aero-elastic simulations of the full wind turbine system.
- Cross-sectional analysis tool: in-house, cross-sectional analysis tool, based on thin lamination theory provides structural properties, stresses distributions and values of the Tsai-Hill failure criterion over the various cross-sections of the blade.
- Cost model: a cost model has been synthesized with the aim to determine the cost of the full wind turbine. It is based on actual cost data for modern wind turbines and existing in the literature simplified cost formulas.
- Optimization framework: an optimization framework has been established using ready-made functions from the published available scipy library of Python.

Some of the above numerical tools (e.g. hGAST) have been developed, used and validated in the context of several research projects (EU and national), while others were either upgraded (e.g. cross-sectional tool) or developed exclusively (e.g. cost model) in the framework of the present thesis.

The main result of the aforementioned process is a hybrid blade design with 8 – 10% less mass. The ‘caps’ of this blade has been shifted by 3% (FEC 3%) and a moderate offset angle (about 5° – 7.5°) in the uni-directional material has been introduced along the whole blade (starting from 20 – 30% onwards) or in two discrete segments, if the increase in the manufacturing complexity does not incur substantial increase in cost.

At the next level, a multi-disciplinary optimization procedure, has been adopted with the aim of LCoE minimization. In the above environment, in addition to the necessary materials mass and the parameters of the passive control, the distributions of chord and twist as well as the length of the blade have been considered as optimization parameters. The above approach results in a modified blade that is 1% heavier, and 3.7% longer. In the same context, a gradually developing hybrid configuration, which includes material BTC, material and geometric FEC and re-twist design, has been proposed. The result is a modified rotor with 19.5% and 1.36% less mass and LCoE respectively, evaluating it through full-time domain aero-elastic simulations of extreme turbulence (DLC-1.3) and parked or idling case (DLC-6.x).

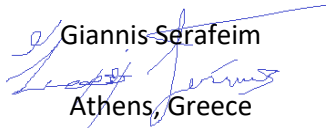
Preface

This thesis is submitted as a result of the fulfillment of the required conditions for obtaining the PhD degree at the National Technical University of Athens. The PhD project was carried out at the Laboratory of Aerodynamics during five and a half years, for full time. The project was funded for 29 months by the Hellenic Foundation for Research and Innovation (HFRI), while in the last 16 months, it was supported by the State Scholarships Foundation of Greece (SSFG). In the uncovered time period, the financing was carried out by the private renewable energy research company of iWind. Their financial support is greatly appreciated!

My motivation for pursuing a PhD in the field of optimal design and development of green solutions stems from my passion for mathematics and the physical sciences, my personal interest in modern optimization techniques and the collective dream of a sustainable and ecological shift. So, I am most grateful for the opportunity that I had, and the privilege of working with many smart, kind, and creative people. Such a person is my supervisor Associate Professor Vasilis Riziotis, who about six years ago gave me an amazing opportunity to deal with such an interesting topic in the context of the preparation of the current thesis. He was always by my side along the way, supporting me and inspiring me, while with his knowledge and experience around the subjects of aerodynamics and renewable sources, he always gave the guidelines to tackle any problem. Unfortunately, my admiration for his personality, his knowledge and his mentality cannot be expressed in a few words... Of course, it would be remiss of me if I did not thank the other two members of the advisory committee, Professors Spyros Voutsinas and Dimitris Saravanos, for their useful comments that helped in shaping my thesis. Our discussions both on the progress of the thesis and on other matters were endless. Their advice was so helpful and their interest is really focused on the progress and improvement of all their students. By the way, I would like to express my gratitude to the all members of the examination committee for reading the thesis and making constructive comments on the this work.

My special thanks go to Dimitris Manolas both for introducing me in the field of wind energy and for his unconditional and relentless support despite the busy schedules in his daily work. I know how hard it can be to squeeze in the extra work next to your project responsibilities and therefore appreciate very much the swift and good support you provided in the review processes in every single case! Furthermore, a special thanks to my friend Theologos Andronikos, with whom I shared an office at the greater part of my PhD studies. Last but not least, I want to express my thanks to all of my present and former colleagues on the laboratory: Kostas Diakakis, Panagiotis Schinas, Nikos Spyropoulos, Dimitris Ntouras and Dimitris Vlastos as well as colleagues and MSc students for the very friendly environment. The working environment is fantastic and I am grateful for the nice discussions and good company, both on scientific and personal level.

Finally, I would like to thank my family. My sister and especially my parents, who support me in any situation. It help me a lot and it would be much harder to go through the thesis without it. It is very important to know that you are never more than a phone call or 1.5hr flight away. I am sorry that you had to endure me during the holidays when I was very busy finishing this thesis.


Giannis Serafeim
Athens, Greece
27 September 2023

This page intentionally left blank

Abstract: The objective of this thesis is the optimal design of wind turbine blades. Various design concepts have been tested, with special emphasis on the techniques involving passive control. Among them, the possibility of reducing both the ultimate and fatigue loads, by applying Bend Twist Coupling or/and Flap Edge Coupling, have been evaluated. The investigation has shown that, for the DTU-10MW RWT a 3 – 5% reduction in the ultimate loads as well as 5 – 10% in fatigue loads is feasible by applying such techniques. The above alleviation, creates the conditions for the capital cost compression, through the reduction of the necessary materials mass. Nevertheless, these techniques are often in competition with each other, while they also have a negative effect on the material strength. This problem is solve through the application of optimization framework. This optimization framework includes various numerical tools (some of them already existed, while most of them have been developed to satisfy the present work), has been established. The main result from the aforementioned process is a hybrid blade design with 8 – 10% less mass, which has shifted the ‘caps’ by 3% (FEC 3%) and has introduced in one or better in two parts (starting from 20 – 30% onwards) a moderate offset angle (about 5° – 7.5°) in the uni-directional material. At the next level, a multi-disciplinary optimization procedure, has been adopted with the aim of LCoE minimization. In the above environment, in addition to the necessary materials mass and the parameters of the passive control, the distributions of chord and twist as well as the length of the blade have been considered as optimization parameters. Approach results in a modified blade that is 1% heavier, and 3.7% longer. In an alternative MDAO approach, the combined application of material BTC, material and geometric FEC and re-twist design has been evaluated, proposing a lightweight rotor by 19.5%.

This page intentionally left blank

Acronyms

AEP	A nnual E nergy P roduction
A/T	A ero-elastic T ailoring
AVATAR	A d V anced A erodynamic T ool for I Arge R otors
BECAS	B Eam C ross-section A nalysis S oftware
BEMT	B lade E lement M oment T heory
BFGS	B royden F letcher G oldfarb S hanno
BLD	B lade L ocal D isk
BoP	B alance of P lant (=281\$/KW)
BTC	B end T wist C oupling
CAPEX	C A P ital E Xpenditure
CFD	C omputational F luid D ynamics
COBYLA	C onstrained O ptimization B Y L inear A pproximation
C/P	C ontrol P oints
DEL	D amage E quivalent L oads
DFP	D avidon F letcher P owell
DLC	D esign L oads C ases
DTU	D enmark's T echnical U niversity
EASY	E volutionary A lgorithms S ystem
EERA	E uropean E nergy R esearch A lliance
ETC	E xtension T wist C oupling
ETM	E xtrême T urbulence M odel
EU	E uropean U nion
EWM	E xtrême W ind M odel

FEC Flap Edge Coupling

FEM Finite Element Method

FLS Fatigue Limits State

HBFGS Hybrid Broyden Fletcher Goldfarb Shanno

HFRI Hellenic Foundation for Research and Innovation

H/P High Pressure

ICC Initial Capital Cost

IEA International Energy Agency

IEC International Electro-technical Commission

IFC Individual Flap Control

INNWIND INNovative WIND

IPC Individual Pitch Control

KKT Karush Kuhn Tucker

KP Key Point

LCoE Levelized Cost of Electricity

L/E Leading Edge

L/P Low Pressure

LQG Linear Quadratic Gaussian

L/R Lightweight Rotor

L/T Lamination Theory

LWST Low Wind Speed Technology

MDAO Multi-Disciplinary Aero-elastic Optimization

NTM Normal Turbulence Model

NASA National Aeronautics and Space Administration

NREL National Renewable Energy Laboratory

NTUA	N ational T echnical U niversity of A thens
OEM	O riginal E quipment M anufacture
O&M	O perational and M aintenance
OPEX	O Perating E Xpenses (usually is equal to 5% of ICC)
OpenMDAO	O pen-source M ulti-disciplinary D esign, A nalysis and O ptimization
PMI	P oly M ethacryl I mide
PVC	P oly V inyl C hloride
PVI	P oly V inyl I sobutyl ether
QP	Q uadratic P rogram
R&D	R esearch and D evelopment
RD	R otor D isk
R/W	R enewable
RWT	R eference W ind T urbine
S/F	S caling F actor
SLSQP	S equential L east S quares P rogramming
S/P	S pecific P ower
SQP	S equential Q uadratic P rogramming
SRO	S ymmetric R ank O ne
SSFG	S tate S cholarships F oundation of G reece
STAR	S weep T wist A daptive R otor
T/E	T railing E dge
ULS	U ltimate L imits S tate
UPS	U ninterrupted P ower S upply
VABS	V ariational A syptotic B eam S ection
VARTM	V acuum A ssisted R esin T ransfer M odelling

WISDEM Wind plant Integrated System Design and Engineering Model

W/T Wind Turbine

Symbols

a	angle of attack	[deg]
a_{BTC}	material BTC coefficient	[-]
γ_L	load safety factor	[-]
$\gamma_{L\&O}$	exponent of Labor & Others expression, $\gamma_{L\&O} = 2.5225$, (vary between 2 to 3)	[-]
γ_m	material safety factor	[-]
γ_{s-u}	exponent of scale-up expression, $\gamma_{s-u} = 2.1557$, (vary between 2 to 3)	[-]
θ_{FEC}	structural twist	[deg]
θ_p	local pitch angle	[deg]
θ_t	local twist angle	[deg]
ρ	density	[kg/m ³]
Ψ	out-of-plane warping function	[-]
Ω	rotational speed	[rad/s]
a	axial induction factor	[-]
a'	circumferential induction factor	[-]
c	local chord	m
C_D	aerodynamic drag coefficient	[-]
C_L	aerodynamic lift coefficient	[-]
C_M	aerodynamic moment coefficient	[-]
C_T	thrust coefficient	[-]
E	Young's modulus	[N/m ²]
F_{FV}	volume fraction	[-]
F_{Pra}	tip loss coefficient factor	[-]
$f_{T/H}$	Tsai-Hill criterion	[-]

G	shear modulus	$[Nm/m^2]$
k_x	flap-wise Timoshenko shear factor	$[-]$
k_z	edge-wise Timoshenko shear factor	$[-]$
N_{ble}	number of blade	$[-]$
N_{cell}	number of cells	$[-]$
N_{el}	number of elements	$[-]$
N_{layer}	number of layers	$[-]$
P	rated power of the wind turbine	$[MW]$
r	radius position on blade	$[m]$
R_{tip}	radius of blade tip	$[m]$
ν	Poisson ratio	$[-]$

Contents

Extended summary	v
Preface	vii
Abstract	ix
Acronyms	xi
Symbols	xv
Contents	xvii
List of figures	xxiii
List of tables	xxix
1. Introduction	1
1.1. History and background of wind energy technology development	1
1.1.1. Wind energy in Europe and Worldwide; Global policies	2
1.1.2. State-of-art in W/T technology development and flagship research projects	4
1.1.3. Load control of wind turbines	7
1.2. Objectives and innovations of this thesis	11
1.3. Thesis outline	13
2. Numerical tools and validation	15
2.1. Aero-elastic solver hGAST	15
2.1.1. State-of-art in aero-elastic solvers and hGAST	16
2.1.2. Aerodynamic module	17
2.1.2.1. Implementation of BEMT in hGAST	19
2.1.2.2. Tip loss	21

2.1.2.3. Correction of the thrust coefficient C_T for highly loaded rotors	21
2.1.2.4. Dynamic inflow modeling	21
2.1.2.5. Shed vorticity effects and dynamic stall	22
2.1.2.6. Correction for skewed wake (yaw and tilt)	22
2.1.2.7. Solution procedure	23
2.1.2.8. Loads calculation	23
2.1.3. Structural dynamics module	23
2.1.3.1. Multi-body dynamics model	23
2.1.3.2. Multi-body kinematics model	24
2.1.3.3. Timoshenko beam model	26
2.1.3.4. FEM analysis	29
2.1.3.5. Multi-body constraint equations	32
2.1.3.6. Aero-elastic coupling	34
2.2. Cross-sectional analysis tool	36
2.2.1. Lamination theory	37
2.2.2. Timoshenko shear factor prediction method	40
2.2.3. Evaluation of the shear factor prediction method	40
2.2.4. Cross-sectional stress analysis and equivalent stress criteria	41
2.2.5. Thin lamination model application examples – DTU-10MW RWT blade analysis	41
2.3 Overall wind turbine cost model	46
2.3.1. Cost model of modern wind turbine	47
2.3.1.1. Cost of tower, gearbox and generator	47
2.3.1.2. Cost of labor, hub, pitch mechanism and spinner	48
2.3.1.3. Cost of blade manufacturing	49
2.3.2. Estimation of LCoE	52

2.3.3. Verification of the cost model	53
2.4. Optimization methods	55
2.4.1. COBYLA method	56
2.4.2. SLSQP method	57
2.4.3. Newton’s and quasi-Newton methods	58
2.5. Optimization framework	60
2.6. Summary	62
3. Design of lightweight rotor of a 10MW-scale wind turbine	63
3.1. Active and passive control techniques – state-of-art	64
3.2. Assessment of load control techniques that alleviate blade loads	66
3.2.1. Active aero-elastic control	67
3.2.2. Passive aero-elastic control	71
3.2.2.1. Re-twisting of the blades in the application of BTC	71
3.2.2.2. Material BTC	72
3.2.2.3. Geometric BTC	75
3.2.2.4. Geometric FEC	76
3.3. Blade mass reduction methodology – application of structurally focused multi-disciplinary optimization	79
3.4. Application examples	81
3.4.1. Lightweight rotor using sweep	81
3.4.1.1. Manual tailoring of sweep and optimization studies	81
3.4.1.2. Verification of sweep- <i>6m</i> and sweep-opt	83
3.4.2. Lightweight rotor using BTC technique	84
3.4.2.1. Manual search and optimization	84

3.4.2.2. Verification of the $N = 2$ and $N = 3$ designs	87
3.4.3. Lightweight rotor using combination of BTC and FEC control	90
3.4.3.1. Rotor mass minimization through various optimization methods	91
3.4.3.2. Verification of the BTC 5°, FEC 3% and “ <i>modified</i> ” designs	92
3.5. Summary	97
4. Multi-disciplinary aero-elastic optimization of DTU-10MW RWT	101
4.1. Alternatives to FEC control of loads – combined application of passive control methods	102
4.2. Application examples	104
4.2.1. LCoE minimization through MDAO, using BTC techniques	104
4.2.1.1. Description of the optimization procedure and results	105
4.2.1.2. Assessment of “ <i>modified</i> ” design	107
4.2.2. LCoE minimization through MDAO, focusing on storm conditions	109
4.2.2.1. Description of the design cases	109
4.2.2.2. Material and geometric FEC (CASE A and B)	111
4.2.2.3. Combined application of passive control methods (CASE C, D and E)	113
4.2.2.4. Verification of optimum designs	118
4.3. Summary	120
5. Conclusions	123
5.1. General concluding remarks	123
5.1.1. Summary of thesis	123
5.1.2. Application examples and main conclusions	125
5.2. Future research topics	128
5.3. Dissemination of results	129

5.3.1. Published papers	129
5.3.2. Participation in seminars and conferences	130
5.4. Acknowledgements	130
A. Description of RWT	133
A.1. Overall	133
A.2. Airfoils and geometric parameters of the blade	135
A.3. Structural design of blade	136
A.4. Control	139
A.5. Power curve analysis	139
A.6. RWT loads analysis	140
A.6.1. Eigen-value analysis	140
A.6.2. Fatigue analysis	141
A.6.3. ONERA Vs Beddoes-Leishman dynamic stall model	141
A.6.4. Ultimate loads and stresses analysis	143
B. Cross-sectional analysis	145
B.1. Layer stiffness analysis	145
B.1.1. Layer stiffness without offset ply angle	146
B.1.2. Layer stiffness with offset ply angle	146
B.2. Laminate stiffness analysis	147
B.3. Section configuration of cross-section	148
B.3.1. Theory for torsion	148
B.3.2. Geometry of cross-section and shear factors	149
B.3.2.1. Theory of Timoshenko shear factors	149

B.3.2.2. Procedure for Timoshenko shear factors calculation	152
B.3.2.3. Application of Timoshenko shear factors	152
B.3.3. Cross-sectional stiffness analysis	153
B.3.4. Shear center	155
B.3.5. Cross-sectional stresses analysis	157
B.4. Thin lamination model application example – static cantilever	158
References	161

List of figures

Figure 1.1	Evolution of various energy sources intended for electricity generation in the 2000-2020 period, at World level	3
Figure 1.2	The mixture on the European Union of various energy sources intended for electricity generation, at 2020	3
Figure 1.3	Sketches of active and passive loads control: (a) trail-flap application and (b) geometry BTC through sweep	7
Figure 1.4	The basic fiberglass layers used to construction the modern wind turbine blades: (a) "UNIAX" $[0^\circ]$, (b) "BIAX" $[+45^\circ/-45^\circ]$ and (c) "TRIAx" $[+45^\circ/0^\circ/-45^\circ]$	8
Figure 1.5	Stresses over a layer form composite material	9
Figure 1.6	Coupling mechanisms in composite beams: (a) extension-twist-coupling through "helical" lay-up and (b) bend-twist-coupling through "mirror" lay-up	9
Figure 1.7	Ply angle of fiber orientation for BTC blades	11
Figure 1.8	The directions (flap-wise and edge-wise) of blades	11
Figure 2.1	Definition of co-ordinate systems	18
Figure 2.2	Local velocity triangle definition	19
Figure 2.3	Simple model of a wind turbine. Examples of local body co-ordinate systems. The local co-ordinate system of the blade the tower and the drive train are indicated	25
Figure 2.4	Application of multibody kinematics at the body level (connected sub-bodies). Connection of sub-bodies $k - 1$ and k in body m	25
Figure 2.5	Example of constraint equations applied at the end nodes of connected bodies/sub-bodies	32
Figure 2.6	Definition of unit bases e_i^r and e_i^m of two connected sub-bodies	32
Figure 2.7	Free or elastic constraint equations	33
Figure 2.8	Definition of aero-dynamic and structural grids. Un-reformed state	35
Figure 2.9	Definition of aero-dynamic and structural grids. Deformed state	35
Figure 2.10	Interpolation of aero-dynamic loads to the structural grid	36

Figure 2.11	Typical material layers layout of a composite thin-walled laminate of wind turbine blade's shell	38
Figure 2.12	Definition of the cross-section regions of the DTU-10MW RWT blade	38
Figure 2.13	Span-wise distribution of the stiffness matrix elements mostly affected by the Timoshenko shear factors (T.S.F.); comparison between present work (L/T) and BECAS for the DTU-10MW RWT blade	41
Figure 2.14	Span-wise distribution of basic sectional characteristics of the DTU-10MW RWT blade provided by present work (L/T) and BECAS: a) shear center, b) torsional stiffness, c) flap-wise bending stiffness, d) edge-wise bending stiffness, e) bending-torsion stiffness coupling and f) structural twist	42
Figure 2.15	Effect of ply offset angle on the natural frequencies in [Hz] of the DTU-10MW RWT blade: (a) 1 st flap-wise, (b) 1 st edge-wise, (c) 2 nd flap-wise and (d) 2 nd edge-wise. Comparison between present work (L/T) and BECAS. Percentage relative differences with respect to BECAS are shown above the bars	43
Figure 2.16	Stress analysis results; distribution of maximum and contemporary Tsai-Hill criterion values on the a) TRIAX and b) UNIAX material layers at the cross-section at $r/R_{tip} = 40\%$ and c) span-wise distribution of the maximum and averaged along the cross-section circumferential distribution Tsai-Hill criterion values. Cross-sectional loads are taken from Table 2.1	45
Figure 2.17	The industrial construction of the modern wind turbine blades is based on VARTM modeling and involves placing fiberglass with a resin mixture and glue on molds	49
Figure 2.18	Mapping the cost of wind turbine blades, relative to their length	55
Figure 2.19	Comparison of the basic parameters of two land-based wind turbine of 10MW	55
Figure 2.20	Overview of the optimization process	61
Figure 3.1	Ply angle of fiber orientation of BTC blades	65
Figure 3.2	Geometrically based FEC (right). Upper right figure shows the reference cross-section, while lower right figure introduction of FEC by the appropriate displacement of the spar cap nodes	65
Figure 3.3	Block diagram of the IPC and/or IFC controller. The out-of-plane bending moment signals at the blade root are transformed into yaw and tilt moments. Then these moments are filtered and return as pitch and flap angles of the individual blades	67
Figure 3.4	Flow-chart of re-twisting process. The necessary adjustment of the twist is sought, so as under the action of the aerodynamic loads at the reference speed the deformed blade obtains the optimum twist distribution	72

Figure 3.5	Dependence on ply rotation angle of a) BTC coefficient at $r/R_{tip} = 50\%$, b) maximum combined moment at the root of the blade, c) blade maximum value of Tsai-Hill criterion and d) blade maximum value of averaged along the cross-section circumferential direction Tsai-Hill criterion. Percentage relative differences with respect to the reference configuration (ply 0°) are shown above the bars	73
Figure 3.6	Span-wise distribution of the maximum value of Tsai-Hill criterion for various BTC configurations	74
Figure 3.7	Snapshot of equivalent stresses distribution on the cross-section at $r/R_{tip} = 40\%$ where maximum Tsai-Hill value (on the caps) is depicted, for the reference (top) and BTC 5° (bottom) designs	74
Figure 3.8	(a) Distribution of flap-edge coupling term K_{13}^D along the blade and (b) average (along the blade span) structural twist angle for various caps displacements, expressed as percentages of the chord length. Percentage relative differences with respect to the reference configuration (FEC 0%) are shown above the bars	77
Figure 3.9	(a) Maximum combined moment at the blade root for various yaw angles for the reference and the FEC 3% cases and (b) standard derivation of the edge-wise moment at the blade root for various caps displacements for DLC-6.x at 30° yaw. Percentage relative differences with respect to the reference configuration (FEC 0%) are shown above the bars	78
Figure 3.10	Flow-chart presenting the procedure for estimating the optimal BTC distribution in terms of maximum blade mass reduction while maintaining the same maximum Tsai-Hill values with the reference blade, The dashed red box contains the steps of inner loop	80
Figure 3.11	Sweep configuration of: (i) reference blade, (ii) sweep- $6m$ and (iii) sweep-opt	83
Figure 3.12	Combine moment at the blade root, for various wind speed. The study includes the configurations of: (i) reference, (ii) sweep- $6m$ and (iii) sweep-opt	84
Figure 3.13	Torsional moment at the blade root for various wind speed. The study includes the configurations of : (i) reference, (ii) sweep- $6m$ and (iii) sweep-opt	84
Figure 3.14	Mass reduction of BTC blades as a function of the ply angle (i.e. 5° , 7.5° and 10°) and ply angle offset starting positions (points on the curves correspond to different values of starting position) – <i>left plot</i> . Convergence of the inner optimization loop for ply angle starting position=0.3 – <i>right plot</i> . Mass reduction is estimated for given BTC blade parameters (ply angle & starting position) to maintain the Tsai-Hill value of the reference blade	85
Figure 3.15	Optimum (in terms of mass reduction) ply angle span-wise distribution – <i>left plot</i> and maximum blade mass reduction – <i>right plot</i> of the BTC configurations considered	86

Figure 3.16	Layout of the optimized BTC blade in case $N = 2$. The plot provides the ply angle span-wise distribution of the UD material of the spar cap	87
Figure 3.17	Optimum span-wise distribution of the wall thickness multiplier which specifies the reduction of the BTC blades mass, while maintaining the Tsai-Hill value of the reference configuration	87
Figure 3.18	Convergence of the design variables (<i>upper plot</i>) and of the cost function (<i>bottom plot</i>) of the outer optimization loop for the case $N = 2$	87
Figure 3.19	Ultimate load assessment of the DTU-10MW RWT and BTC configurations with $N = 2$ and $N = 3$ considering the DLC-1.3. (a) Blade maximum Tsai-Hill values, (b) maximum combined bending moment at the blade root and (c) maximum combined bending moment at the tower	89
Figure 3.20	Fatigue load assessment of the reference DTU-10MW RWT and the BTC configurations with $N = 2$ and $N = 3$ considering the DLC-1.2. (a) DELs span-wise distribution of the spar mean normal stress and (b) of the blade moments	89
Figure 3.21	Span-wise distribution of the thickness coefficient (inner optimization loop) and offset ply angle of the uni-directional material (outer optimization loop), as a result of the mass minimization process	92
Figure 3.22	DLC-1.3 ultimate loads vs wind speed of different configurations (with safety factors) (a) Blade maximum value of Tsai-Hill failure criterion, (b) maximum combined bending moment at blade root and (c) maximum combined bending moment at tower base. Percentage relative differences with respect to the reference configuration are shown above the bars	96
Figure 3.23	DLC-6.x ultimate loads vs wind yaw of different configuration (with safety factors) (a) standard deviation (std) of edge-wise bending moment at blade root, (b) maximum combined bending moment at blade root and (c) maximum combined bending moment at tower base. Percentage relative differences with respect to the reference configuration are shown above the bars	96
Figure 4.1	Definition of blade cross-section, demonstrating the material (left) and geometrically (right) based FEC through appropriate asymmetric thickness increase or displacement of the spar caps	103
Figure 4.2	Comparison of the design variables between the reference and the “ <i>modified</i> ” blade design with $R_{tip} = 92.49m$, (a) Chord distribution, (b) twist distribution, (c) distribution of thickness coefficient and offset ply angle and (d) power curve comparisons	106

Figure 4.3	Ultimate loads analysis resulting from aero-elastic simulations of DLC-1.3 for various wind speeds: (a) maximum value of Tsai-Hill criterion ($f_{T/H}^{max}$) along the blade span and (b) maximum value of the combined bending moment at the tower base. Percentage relative differences with respect to the reference configuration are shown above the bars	108
Figure 4.4	Material FEC (CASE A): coefficients of change in thickness of the materials “TRIAX” and “UNIAX”, for the regions H/P “trailing” and L/P “leading” and global coefficient of the cross-section thickness (with green color). Cyan and orange symbols depict control points, connected with straight lines	111
Figure 4.5	Geometric FEC (CASE B): span-wise distributions of percentage shift in the caps relative to the chord and global coefficient for the cross-section thickness (with green color). Cyan and orange symbols depict control points, connected with straight lines	111
Figure 4.6	(a) Blade mass, (b) annual energy production and (c) Levelized Cost of Energy, of the material FEC (CASE A) and the geometric FEC (CASE B) designs and relative percentage differences with respect to the reference configuration	112
Figure 4.7	Structural twist distribution of the design configurations: on the left plot shows the full distribution and on the right the range 0.2 – 1.0 (zoom)	113
Figure 4.8	Distribution of the material FEC coefficient for the (a) leading and (b) trailing region of the cases: A, C, D and E	114
Figure 4.9	Distribution of the geometric FEC coefficient for the (a) high-pressure and (b) low-pressure cap of the cases: B, C, D and E	114
Figure 4.10	Twist distribution of the cases: reference (A-C), D and E	115
Figure 4.11	CASE E: distribution of (a) FEC material approach, (b) FEC geometrical approach, (c) twist and (d) offset ply angle of ‘UNIAX’ material and coefficient of wall thickness	116
Figure 4.12	(a) Blade mass, (b) annual energy production and (c) levelized cost of energy of the different designs and relative percentage differences with respect to the reference configuration	116
Figure 4.13	DLC-1.3 ultimate loads vs. wind speed of examined configurations (including safety factors) maximum combined bending moment (a) at the blade root and (b) at the tower base	119
Figure 4.14	DLC-6.x ultimate loads vs. yaw angle of examined configurations (including safety factors) maximum combined bending moment (a) at the blade root and (b) at the tower base	119
Figure A.1	A sketch of DTU-10MW RWT	134

Figure A.2	Relative thickness distribution, with airfoils positions along the blade	136
Figure A.3	Cross-section of the wind turbine blade with three webs and qualitative description of the different regions	136
Figure A.4	Maximum combined bending moment at the blade root, using ONERA and Beddoes-Leishman aerodynamic model, for: (a) DLC-1.3 and (b) DLC-6.x, for various wind speeds and wind yaw angles respectively	142
Figure A.5	Maximum combined bending moment at the blade root (red color) and tower base (blue color), for the cases: (a) DLC-1.3 for various wind speeds and (b) DLC-6.x yaw angles	143
Figure B.1	Material $[Ox_my_mz_m]$ and local $[Oxyz]$ coordinate system and example of layer with off-set ply angle	146
Figure B.2	Cross-section regions and focus on a point (layers structure of fiberglass)	148
Figure B.3	Prismatic cantilever beam	150
Figure B.4	Sketch of simple geometric shapes (ellipse and hollow circle), used for determining the Timoshenko shear factors	152
Figure B.5	Assumed section with coordinate system and notations used in appendix B	155
Figure B.6	Sketch of the tubular composite cantilever of 1m long. The cross-section of beam has elliptical shape, with ratio 1: 2 and it consists by different lay-up configuration between 'caps' and skin region	158
Figure B.7	Distribution of the coupling factor α_{BTC} , of the tubular cross-section, relative to the offset ply angle of the UNIAX material. The comparison is performed using BECAS and L/T tools	158

List of tables

Table 2.1	Comparison between the present work (L/T) and BECAS of the ultimate loads distribution (forces are shown in $[kN]$ and moments in $[kNm]$) along the blade half span in case of extreme turbulence wind at $13m/s$ wind speed (safety factors γ_L applied)	44
Table 2.2	Basic parameters of $1.5MW$ RWT described in [108] and the costing of its main components	48
Table 2.3	List of mathematical expressions that describe blade consumables, proportional to R_{tip}	50
Table 2.4	List of mathematical expressions that describe blade consumables, proportional to A_{molds}	51
Table 2.5	List of mathematical expressions that describe blade consumables, proportional to A_{out}	52
Table 2.6	Cost analysis of the DTU-10MW RWT blade [$10^3\$$]	53
Table 2.7	Cost and APE breakdown of the $1.5MW$ RWT (which is described in Table 2.2) and DTU-10MW RWTs [$10^3\$$]	54
Table 3.1	T/E flap layout applied on the DTU-10MW RWT	68
Table 3.2	Controller gains for the IPC and combined IPC&IFEC loops	68
Table 3.3	Lifetime DELs comparison of DTU-10MW RWT between reference (absolute values $[kNm]$) and active load control designs (relative differences [%]) based on DLC-1.2, calculated for twenty years lifetime with Weibull parameters $C = 11 m/s$ and $k = 2$, Wöhler coefficient $m = 10$ for the blades and $m = 4$ for the tower and $N_{ref} = 10^8$ cycles	69
Table 3.4	Ultimate loads comparison of the DTU-10MW RWT between reference (absolute values $[kNm]$) and active load control design (relative differences [%]) based on DLC-1.3 (safety factors $\gamma_L = 1.35$, have been applied)	70
Table 3.5	Ultimate loads comparison of the DTU-10MW RWT between reference (absolute values $[kNm]$) and various sweep deflection at the tip (S_{tip}) designs (relative difference [%]) based on DLC-1.3 – safety factors have been applied	75

Table 3.6	Ultimate and lifetime DELs loads comparison of the DTU-10MW RWT between reference (absolute values [kNm]) and BTC load control (relative differences [%]) based on DLC-1.3 (ultimate) and DLC-1.2 (fatigue). Fatigue calculate for 20 years lifetime with Weibull parameters $C = 11 m/s$ and $k = 2$. Wöhler coefficient $m = 10$ and $N_{ref} = 10^8$ cycles	76
Table 3.7	Effect of sweep on blade mass and loads	82
Table 3.8	Standstill natural frequencies comparison between the DTU-10MW RWT and $N = 2$ and $N = 3$ configurations. Absolute frequencies (in Hz) are provided for the reference turbine and relative percentage differences with respect to the reference configuration are provided for the modified designs	88
Table 3.9	DELs of the tower base moments of the reference DTU-10MW RWT and relative percentage difference of the BTC configurations, with $N = 2$ and $N = 3$ considering the DLC-1.2	90
Table 3.10	Number of objective function calls for the tested optimization algorithms	92
Table 3.11	List of DTU-10MW RWT designs studied with passive control techniques (Weibull parameters $C = 11 m/s$ and $k = 2$ considered for the mean annual power calculation)	93
Table 3.12	Standstill natural frequencies comparison between the DTU-10MW RWT and the variants with passive load control techniques. Absolute frequencies (in Hz) are provided for the reference turbine and relative percentage differences with respect to the reference configuration are provided for the modified designs	94
Table 3.13	DLC-1.2 fatigue loads comparison between the DTU-10MW RWT and its variants with passive load control techniques. DELs calculated for twenty years lifetime with Wöhler coefficient $m = 10$ for the blades and $m = 4$ for the tower and $N_{ref} = 10^7$ cycles and Weibull parameters $C = 11 m/s$ and $k = 2$. Absolute load (in kNm) are provided for the reference turbine and relative percentage difference with respect to the reference configuration are provided for the modified designs	97
Table 4.1	Comparison between the DTU-10MW RWT, the Lightweight Rotor – L/R from section 3.4.2. and the “ <i>modified</i> ” design with the optimized rotor for reduced LCoE	106
Table 4.2	Standstill natural frequencies of the DTU-10MW RWT, the up-scaled $S/F = 1.037$ and the “ <i>modified</i> ” design	108
Table 4.3	DTU-10MW RWT passive control designs aimed at minimizing the LCoE	109
Table 4.4	Results for the design variables of the considered configurations. Numbers in red correspond to design variable values that remain fixed in the simulation	117

Table 4.5	Standstill natural frequencies of the reference DTU-10MW RWT and FEC designs. Relative percentage differences with respect to the reference configuration are also provided	118
Table 5.1.	DTU-10MW RWT passive control designs parametrization aimed at minimizing the LCoE	127
Table A.1	Key parameters of the DTU-10MW RWT compared to a direct up-scale of the NREL-5MW RWT	134
Table A.2	Geometric characteristics of the wind turbine blade of DTU-10MW RWT. The non-dimensional distance of KP are counting from L/E	135
Table A.3	RWT blade material cost and structural properties	136
Table A.4	Thickness of material distribution in $[mm]$, per region of blade cross-section	137
Table A.5	Integrated of pitch angle, probability and power produced, as function of wind speed	140
Table A.6	DLCs definition for loads assessment	140
Table A.7	Standstill natural frequencies of DTU-10MW RWT, in $[Hz]$	140
Table A.8	Lifetime DELs of the DTU-10MW RWT cross-sections (absolute values $[kNm]$), based on DLC-1.2, calculated for twenty years lifetime with Weibull parameters $C = 11 m/s$ and $k = 2$, Wöhler coefficient $m = 10$ for the blades and $m = 4$ for the tower and $N_{ref.} = 10^7$ cycles	141
Table A.9	Dynamic stall model that has been adopted in each application of the thesis	142
Table A.10	Operational ultimate loads distribution along the blade and tower, for DTU-10MW RWT	144
Table B.1	Timoshenko shear factors for a) full elliptical cross-section ($\nu = 0.333$), for various semi-axis ratios r_2/r_1 and b) hollow circle with ratio of inner over outer radius of 0.9, for various Poisson's ratios. Comparison between present work (L/T) and results in [168] and [99]	153
Table B.2	Diagonal stiffness characteristics and maximum stress of the ellipse section, provided by BECAS, L/T and Analytic approach	159

This page intentionally left blank

Chapter 1

1. Introduction

Wind Energy progressed over the years by constantly increasing the size of wind turbines (W/T) in view of compressing the Levelized Cost of Electricity (LCoE). This trend came along with several design challenges invoked by the increase in loading that demand technology breakthroughs and innovations. New and advanced materials, hybrid manufacturing methods, new inner-structure designs different from the standard spar concept, new high performance thick airfoils and active or/and passive aero-elastic control techniques. Among the above, passive control methods have been proven very promising in alleviating loads and they have been employed in the current thesis as a mean for compressing LCoE through their optimal combination. Towards this end, a novel multi-disciplinary servo-aero-elastic optimization framework is synthesized, based on existing and newly developed models that simulate the servo-aero-elastic response of the full wind turbine system, over the full spectrum of external and operational conditions the machines encounter during their lifetime combined with cost modeling. Two passive load control techniques are addressed. The Bend-Twist-Coupling technique (BTC), as a means to alleviate operational loads, is considered first separately and then in an optimal combination the Flap-Edge-Coupling (FEC) as a means to mitigate extreme loads under survival wind conditions, in which the wind turbine is parked or idling.

1.1. History and background of wind energy technology development

The first experimental wind turbine designed for electricity generation, was constructed in July of 1887, by professor James Blyth from the Anderson's Collage of Glasgow [1]. However, the first large scale installation of wind turbines took place in the 1940s, and was motivated by the increased energy needs due to the 2nd World War. Early wind turbines have had much more in common with traditional wind-mills than with modern turbines [2]. During the 2nd World War, the energy needs were so big that small

wind generators were used on German U-boats to re-charge submarine batteries as a fuel-saving measure [3]. In the years that followed, the interest in wind energy dropped and its use was limited to agricultural applications [4], until the oil-crisis in the 1970s. Huge wind farms were installed in the United States, however the experience of that time was disappointing. Without sound knowledge, the industry ignored some important aspects such as wind farm effects, high vibrations due to turbulence and stall. It took quite a while until wind turbine scientists and engineers realized that the accumulated knowledge from aviation is not directly applicable to wind turbines, and that know-how specifically for wind turbines should be built. Airplanes operate in most of their lifetime in “smooth” conditions well away from the ground where atmospheric turbulence is high, while in aerodynamic terms stall should never be approached. Most wind turbines of that time were stall regulated, and the passage to pitch regulated ones became dominant some decades later.

Of course, a lot of the knowledge developed in aviation was extremely valuable and has fueled the fast evolution of wind turbines which have reached the size of several *MW* in less than 50 years [5]. In our days wind turbines have been massively deployed in plains, hills, mountains and seas and they have rotors with twice the diameter of the Airbus A-380 wing span. This development is understandable since wind energy has become economically competitive to conventional sources of energy and at the same time is renewable (R/W), which means that may contribute to the protection of the environment and the reduction of CO_2 emissions.

1.1.1. Wind energy in Europe and Worldwide; Global policies

Although there has been much discussion on the need to reduce pollution emissions, according to available data [6], the global community still relies on fossil fuels! In Fig. 1.1, the evolution of the contribution of each source of energy in the global energy mix for electricity generation from 2000 to 2020 is presented. Based on this chart, the total energy demand is increasing. In response, the share of every source except for nuclear, increased in the same way without a clear sign of behavior change in favor for the renewables (wind, solar, other-R/W). As can be seen in Fig. 1.1, the penetration of wind energy has become significant in the recent years, with very promising prospects. In the two “landmark” years 2008 and 2016, wind energy rose from 7th to 6th and from 6th to 5th place respectively. Then in geographical terms, the 27-member European Union (Fig. 1.2) shows a greater participation of “green” sources in their energy mix, proving in practice EU’s environmental concerns. The production of nuclear power is mainly due to France and Germany, while the contribution of wind seems to occupy the first place among all renewables. Although small, the contribution of solar energy, which is mainly coming from the southern member-countries, is significant, while the gas imported mainly from Russia (at least until recently) remains the protagonist, occupying 1/5 of the pie.

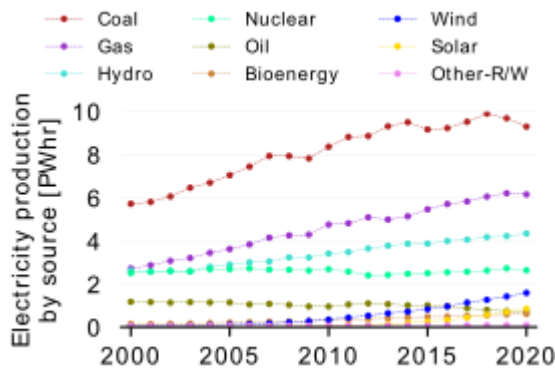


Figure 1.1: Evolution of various energy sources intended for electricity generation in the 2000-2020 period, at World level.

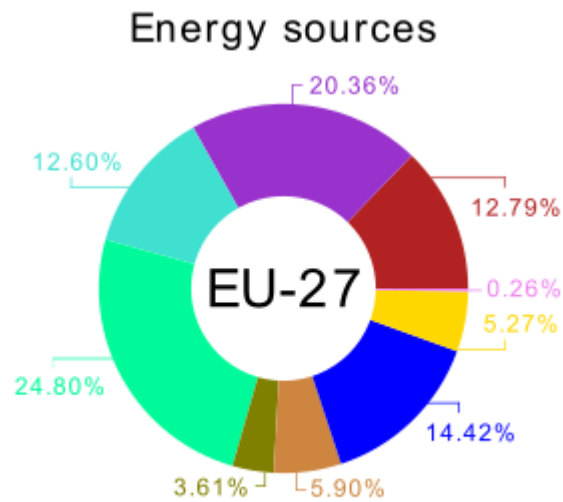


Figure 1.2: The mixture on the European Union of various energy sources intended for electricity generation, at 2020.

Despite the steps taken towards further using renewable energy sources, the implications of our past behavior to climate change are becoming apparent today without obvious relent. Therefore, the search for alternative solutions and massive adoption of more environmentally friendly energy sources is imperative. Various policies have been implemented in this direction, and targets have been set by governments to reduce the use of fossil fuels. For example, by year 2030, at least 20% of the United States energy is expected to be supplied by onshore and offshore wind farms [7]. At the same time, on the other side of the Atlantic ocean - the European Union, recognized the severity of the challenge, and introduced the Renewable Energy Directive 2018/2001/EU [8], that establishes a new binding EU target by 2030 demanding that at least 32% to electricity production should come from renewable sources, with a possibility of an up-wards revision. The recent geopolitical developments and the military conflicts taking place in our neighborhood, led the Commission to publish the REPowerEU plan [9], which aims at rapidly reducing EU's dependence on fossil fuels. Based on this plan, the Commission proposed to increase the target in the directive to 45% by 2030. This transition can only be made by granting generous incentives (and in some cases dis-incentives) to both private individuals and industry, to switch to renewable. Allies to that are, the newly developed efficient energy storage capabilities [10] either based on Li batteries [11] or hydrogen [12] – the so-called “fuels of the future”, along with the advances of other “green” technologies, the geothermal, solar and of course wind energy. According to Eurostat, the contribution of the non-fossil sources (wind and hydropower are their main representatives) to energy accounted for over two-thirds of the total electricity generated from renewable sources in the EU, at the year of 2021 [13].

From a technology stand point, vast deployment of wind energy, both onshore and offshore, will be needed in order to fulfill the above targets. In fact it is recognized that a vast deployment can be accomplished only with very large wind turbines, exceeding the rating of today's commercial turbines (the maximum rating of the single wind turbine unit today is 15MW). Wind turbines of > 20MW rating, must be thoroughly optimized in order to be cost efficient. Thorough optimization should not independently optimize the subcomponents, but instead optimizing the wind turbine as whole system, by combining all underlying physics (aerodynamics, hydrodynamics, structural dynamics and control system) in one simulation and optimization package. Furthermore, in order to beat the well-known up-scaling cubic law [14] and further suppress costs, smart load reduction techniques will be necessitated.

1.1.2. State-of-art in W/T technology development and flagship research projects

In order to support its political targets and initiatives, EU has systematically funded large collaborative research projects addressing the various aspects that could lead to more efficient and more cost effective wind turbines. In these projects, research institutes, academia and the wind industry came together in a cost and knowledge sharing context. Their aim was to achieve major advancement in technologies and concepts and to generate new knowledge that was meant to fuel the wind energy industry. There are five flagship research projects in which new improved numerical tools have been developed and major advancements were accomplished in the areas of aero-elastic tailoring and wind turbine cost analysis; they are listed and briefly described below. These five research projects, to a great extent formed the basis for the developments presented in the present thesis:

- DAMPBLADE [15] (2001-2004): The program lasted for four-years and it was financed by the 5th Framework Programme. The main goal was to develop wind turbine blades with high damping, using mechanisms/techniques such as: (i) tailoring of laminate damping anisotropy, (ii) damping layers and (iii) damped polymer matrices. Due to the above research, various composite materials were evaluated and characterized, based on their damping properties. In addition, new technologies were evaluated for the design and fabrication of damped prototype blades and their full-scale laboratory testing, while the modeling of the composite structure were clarified in such a way that its aero-elastic stability and fatigue life can be predicted. The result of the afore-mentioned research, was the design, manufacturing and testing of a 19m long composite wind turbine blade, made of glass/polyester. This blade was tested in the Greek Centre for Renewable Energy Sources. The analysis of the tests, showed an ~80% increase in the damping ratio of both the first flap and lag modes compared with the earlier standard design practice.
- STABCON [16] (2002-2006): The main objective of this project was to develop reliable design tools and techniques, for the aero-elastic stability characterization of large wind turbines. The overall budget has exceeded three-million euros, with EU contribution approaching 60% of the total expenditure. In this way, the European wind turbine industry as well as the research community, aspired to reinforce their position at the world map of the wind energy. This project had two parts: (i) In Part-1, new stability tools were developed and used in predicting the stability limits of an

existing 2.5MW turbine. These tools were evaluated against full scale stability measurements. The main outcome of this part, was the thorough understanding of wind turbine instabilities (stall, blade flap/lead-lag and low damped tower vibrations) and the compilation of design guidelines for passive (built-in) suppression of these instabilities. (ii) Part-2 concerned the morphological study of possible wind turbine control algorithms that enhance aero-elastic damping and mitigate loads. Specifically, the project focused on three objectives: the instability suppression, turbulence and gust loads alleviation and power enhancement, using active load control. The milestones of this project were:

- mapping of the aero-elastic stability of 2.5MW wind turbine
 - establishment of a firm basis to evaluate and further develop different concepts
 - integrated design of aero-elastic control based on site, grid and turbine specific conditions
 - aero-elastic control system for gust alleviation, instability suppression and power enhancement
 - knowledge of non-linearities for large wind turbines
 - validated aero-elastic stability tools
- UpWind [17] (2006-2011): This project had 40 partners from the industry (OEMs and others), service providers, academia (universities and research institutes), R&D establishments and professional organizations. This project has been identified as “Europe’s largest R&D wind energy research project”! During the five-years of its life, the project delivered improved models and design tools of the primary wind turbine components, that were validated. The above models are indispensable for the industry, for the design and manufacturing of the modern multi-megawatt wind turbines. Understanding the future potential and prospects in the sector of the renewable sources, the project was aimed towards large-scale applications, e.g. offshore wind farms of several hundred-MW. Such applications can only be realized using very large wind turbines with a power of 8 – 10MW and a rotor diameter of over 120m. At the time, traditional design approaches, conventional materials and standard manufacturing techniques, were not considered adequate for this up-scaling. Thus, in the context of the project and in order to achieve the necessary up-scaling before the end of the 2010s, full understanding of external design conditions, innovative materials with a sufficient strength to mass ratio and advanced control and measuring systems were addressed. Various critical areas have been the subject of study and benefited by the above project, such as:
 - metrology
 - foundations and support structures
 - transmission and conversion
 - control systems
 - smart rotor blades and rotor control
 - aerodynamics and aero-elastics
 - INNWIND.EU [18] (2012-2017): Foreseeing the strong expansion of wind energy in the sea, the EU co-financed a big project of 19-million euros, with 14 million. The project aimed at ‘INNNovative WIND conversion systems (10 – 20MW) for offshore applications’ and was essentially the ambitious successor of the UpWind project. The project lasted five-years, it was coordinated by DTU and consisted a partnership of 27 European partners representing large wind turbine manufactures,

certification bodies, consulting companies, research institutions and leading universities. Apart from the collaboration between the wind energy researchers and the industry, INNWIND.EU developed several innovative rotor designs in view and in reference to the anticipated very large rotors of the future, drivetrain components, bottom fixed and floating sub-structures that greatly reduce the LCoE for 10 – 20MW offshore wind turbines by 20% and 25%, respectively – as compared to the existing 5MW offshore turbine. In summary, the most important innovations proposed by the above project, were:

- low Induction Rotor, which constrains the extreme loads at the blade root
 - pseudo-Magnetic Direct drives that also significantly increase transmission efficiency
 - optimized aerodynamic and structural platforms of blades for reduced blade root and tower base fatigue
 - advanced optimal jacket designs to support wind turbines at 10MW and 20MW capacities
 - active control with focus on blade trailing edge flaps and blade trailing edge section morphing for load alleviation
 - guyed articulated sub-structure, that avoids resonant excitation for 2-bladed and 3-bladed rotors
 - high temperature super-conducting generators to increase efficiency
 - novel triple-spar semi-submersible floating wind turbine for 10MW wind turbines
- AVATAR [19] (2013-2017): One year after the beginning of INNWIND.EU, the AdVanced Aerodynamic Tool for lArge Rotors was announced, which was concluded four-years later. The overall budget of this project exceeded nine-million euros, with 2/3 of it being covered by EU. In order to quickly achieve the aim of designing and implementing 10 – 20MW very large wind turbines, radical innovations and reliable numerical tools are required. This has been the main motivation of the current project. Specifically, aerodynamic and aero-elastic tools have been evaluated, validated and improved, thus ensuring their applicability to high-scale turbines. The ability of such models to produce valid load predictions at all levels of modeling complexity was deemed imperative for a smooth transition to tomorrow's wind turbines. In the AVATAR work-plan, aerodynamic models are developed and calibrated for all aspects which play a role in the design of large wind turbines. Thereto the entire chain of aerodynamic modelling is mobilized ranging from computational efficient engineering tools to very advanced high fidelity but high cost-computationally tools. The philosophy behind the development of new comprehensive models is based on the concept of calibrating the lower complexity tools with the results produced by the high fidelity tools. Additional measurements on wind tunnel or/and field are used to validate and improve the models. A large-scale rotor with and without flow control devices has been used to demonstrate the capabilities of the resulting tools. The project was carried out by a world class consortium since it consisted of a selected group of participants from the sub-program aerodynamics EERA Joint Program Wind (European Energy Research Alliance), in which all leading institutes in the field of aerodynamics participated, complemented with two leading industrial partners.

The starting point of the afore-mentioned projects, is the need to increase the size of the wind turbine rotors and their transition to offshore applications, which ensures the compression of LCoE. This challenge calls for the development of new numerical tools and modern control strategies (e.g. passive or/and active loads control). For example, in the context of AVATAR, MaPFlow [20] tool has been finalized, the free wake vortex code GenUVP was coupled with the aero-elastic solver hGAST [21] and the modeling of the ambient turbulence in a vortex particle context was performed. Furthermore, all the above modeling options were validated against full scale measurements and wind tunnel tests. Additionally, during INNWIND.EU, the thesis entitled “Hydro-aero-elastic analysis of offshore wind turbine” [22] has been concluded. In this work, the aero-elastic modeling of very-large wind turbines is revised and improved by introducing new models that expand the applicability of existing tools to offshore applications. This work is of great relevance to the present thesis, because it developed integrated and validated numerical tools that form the core of the multi-disciplinary optimization tool developed by the present thesis.

1.1.3. Load control of wind turbines

In many cases, the up-scaling of the size of wind turbines is hindered by the high manufacturing, labor, transfer and installation cost. This is a result of the cubic law [14] that dictates the increase in mass of up-scaled components, which also drives gravitational loads. New materials and in general technology innovations such as active/passive load control, may help circumventing this law. For example Bossanyi [23], studied the individual blade pitch control for load reduction, based on a Linear-Quadratic-Gaussian (LQG) controller. An alternative load control concept concerns trailing edge flaps proposed by Matthew Lackner and Gijs Kuik in 2009 [24] and more recently by Mralleekrishnan and Fernando Ponta [25] in 2022. Inspired by aviation applications, a control system based on flaps (see Fig. 1.3a), has been established on a 5MW wind turbine with the aim to alleviate fatigue loads. This was combined with cyclic control of the pitch.

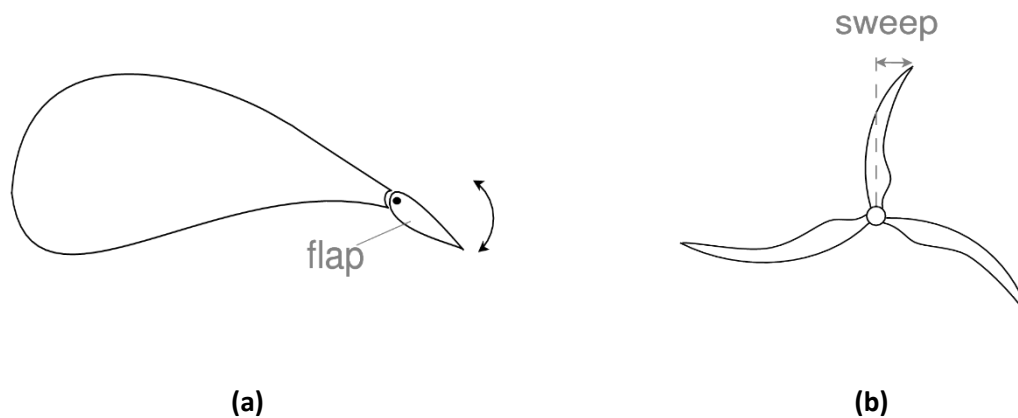


Figure 1.3: Sketches of active and passive loads control: (a) trail-flap application and (b) geometry BTC through sweep.

With regards to passive load control, they were first implemented through geometric Bend-Twist-Coupling (BTC) based on blade sweep. Among the first who studied this technique, was the Wind Energy Department of Sandia National Laboratories [26] and [27] – for more detail see Fig. 1.3b. The final design concerned the STAR-27.1m, which was also fabricated and then tested in the laboratory and in the field. The resulting static and fatigue loading, allowed re-dimensioning the rotor and gaining 10 – 12% extra energy, under the same level of critical loads. In 2014, a similar approach was adopted by Scott Larwood et al. [28], for wind turbines in the range of 750kW to 3MW, resulting in an average increase of 5% in energy production. In conclusion, this technique is applicable to small to medium size wind turbines, either exclusively or complemented by other control mechanisms. The main drawback of blade sweep, is that more material is needed in the fabrication of the blade as well as new curved molds which generally entail additional manufacturing costs as compared to the traditional process.

The blades of modern multi-megawatt wind turbines are long, slender and flexible structures, fabricated from composite materials. Such materials may mainly contain glass fibers and to a lesser extent carbon fibers and various plastics (i.e. PolyVinyl Chloride – PVC, PolyVinylsobutyl ether – PVI and PolyMethacryllimide – PMI). An extensive review of the above materials has been performed in 2005 by Brøndsted et al. in [29].

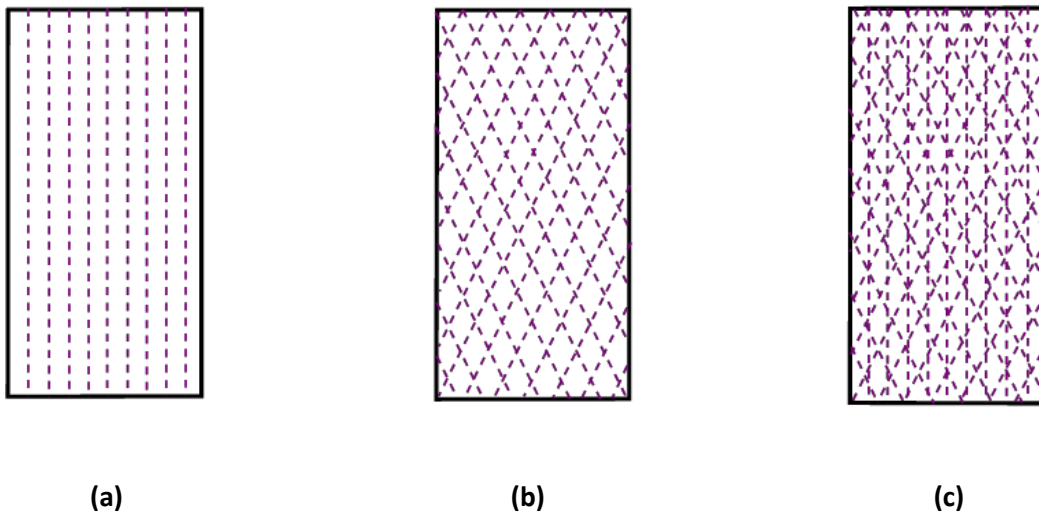
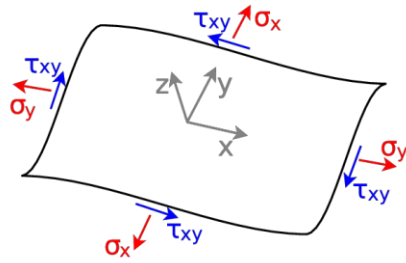


Figure 1.4: The basic fiberglass layers used to construction the modern wind turbine blades: (a) “UNIAX” $[0^\circ]$, (b) “BIAX” $[+45^\circ/-45^\circ]$ and (c) “TRIAX” $[+45^\circ/0^\circ/-45^\circ]$.

Typically, industry uses the composite materials in the form of fabrics (i.e. TRIAX, BIAX and UNIAX – see illustrations in Fig. 1.4) by placing them in successive layers on either side of a core of Balsa. Using resin and a chemical exothermic process, the fabrics harden to form a stiff structure, fairly light, with predictable mechanical properties. This procedure is known by the acronym VARTM (Vacuum Assisted Resin Transfer Modelling). So, the glass or carbon fiber layers can be considered as the building material of the wind turbine blades, determining the mechanical properties and so their structural behavior.



$$\begin{Bmatrix} \sigma_x \\ \sigma_y \\ \tau_{xy} \end{Bmatrix} = \begin{bmatrix} K_{11} & K_{12} & K_{13} \\ K_{12} & K_{22} & K_{23} \\ K_{13} & K_{23} & K_{33} \end{bmatrix} \begin{Bmatrix} \varepsilon_x \\ \varepsilon_y \\ \gamma_{xy} \end{Bmatrix} \quad (1.1)$$

Figure 1.5: Stresses over a layer form composite material.

In general, a separate layer of fiber reinforced composite material (see Fig. 1.5), can be approximated (with good accuracy) as an orthotropic material due to the symmetry of its mechanical properties with respect to several directions. In the special case that all the fibers are directed along the same axis (so-called uni-directional material), the layer can be well treated as transversely isotropic material. The classical Laminate Theory (L/T) as derived in-depth by Hyer W. in 1982 [30] and applied to wind turbine blades, three decades later by Chortis [31], is able to capture the mechanical properties of the layer. In case that fibers are parallel to one principal axis (x -axis or y -axis), the off-diagonal elements of the stiffness matrix (see Eq. 1.1) become zero. The above indicates the case that shear stresses and strains are fully uncoupled from the two other principal stresses/strains in the layer. In any other case, where there is an offset angle between the fibers and the main axes, additional coupling terms arise (off-diagonal elements in Eq. 1.1 are activated).

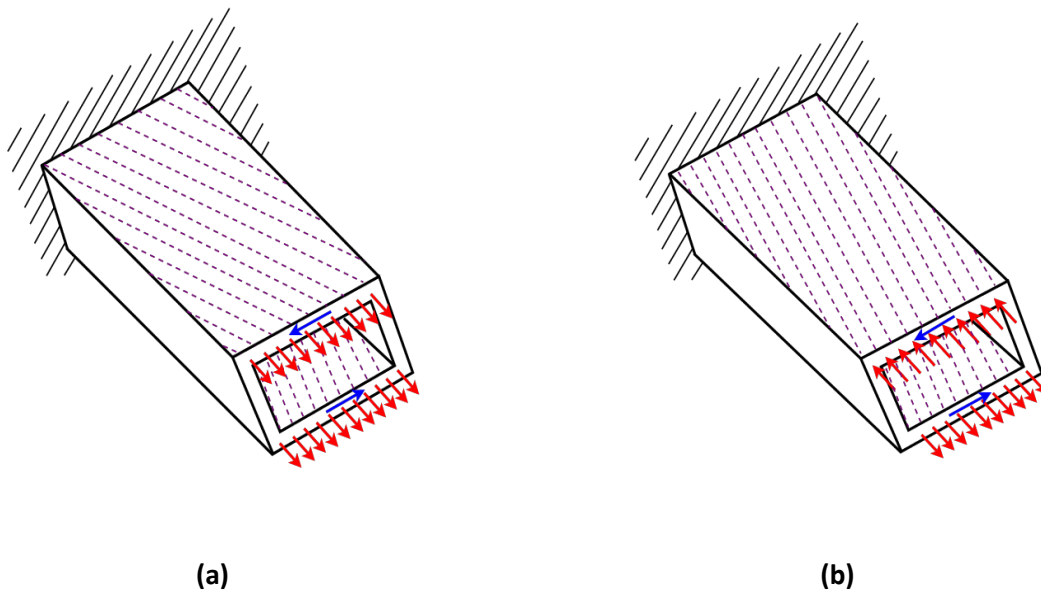


Figure 1.6: Coupling mechanisms in composite beams: (a) extension-twist-coupling through “helical” lay-up and (b) bend-twist-coupling through “mirror” lay-up.

Smart tailoring of the coupling effects within the structure of a composite structure can offer new possibilities for the passive control of loads. In materials science, two well-known tailoring methods are considered:

- The Extension-Twist-Coupling: This effect was first observed by Campbell in 1919 [32] and Peeling in 1913 [33], and it is referred to as “bifilar effect”. This effect can be easily realized in a beam of rectangular cross-section, having the fibers over the two flanges laid in an anti-symmetric configuration – as shown in the Fig. 1.6a. The normal stresses (red arrows) that develop in response to the extension force, simultaneously cause shear stresses (blue arrows) that twist the beam.
- The Bend-Twist-Coupling: This option has been studied in several developments [34],[35] and [31], and can be realized by placing the fibers over the flanges (the horizontal walls) laid in a symmetric configurations – as shown in the Fig. 1.6b. The mechanism of this coupling is similar to that of the Extension-Twist-Coupling, except that it activated by bending and not extension.

The Extension-Twist-Coupling (ETC) has been studied over many years, and concerned cases with significant extension stresses, as for example the stresses due to high centrifugal forces, which is often seen in aviation and rotorcraft applications. Ozbay in 2006, in his PhD thesis [36], investigated the possibility of applying ETC technique to the composite blades of the XV-15 tiltrotor aircraft. The aim was to achieve suitable twisting deformations, so that efficiency attains its maximum. A few years later, an optimization methodology to study ETC capability of composite rotor blades was proposed by the Rensselaer Polytechnic Institute of Troy [37]. From this optimization study, an ETC rotor has been proposed rotating at 20% lower rotor speed, thereby reducing the noise. Such intervention could improve a wide range of rotor performance metrics, including power, hub vibrations and rotor bending loads.

In cases that bending dominates the loading, Bend-Twist-Coupling (BTC) is mainly employed. Although the concept of material BTC, originates from helicopter applications (see for example [38] and [39]), in the literature it is often referred to as a passive means of load control on wind turbine rotors (see [40], [41] and [42]). According to Lobitz in 1996 [43], a 10 – 15% increase in the rotor diameter is possible (therefore also of the annual energy production) by applying a moderate offset ply angle on the uni-directional material over the regions occupied by the caps (see Fig. 1.7). It is noted that through the above intervention there will be no change in the rated power of the turbine nor any increase in the mean loading of the rotor. So far, several research publications within the wind energy community dealt with BTC, either by focusing on testing composite beams or actual blades. Among them, of outstanding importance is the research work by Fedorov from DTU [44], in which the applicability of material BTC to a blade segment of a commercial wind turbine was evaluated. In his work Fedorov verified the theoretical models through comparisons against experimental studies and explored the range along the blade length that such a technique may be applied in order to effectively reduce vibrations. Additionally, Stäblein [45] also from DTU, numerically assessed fatigue load reduction levels on BTC blades. Stäblein reported an annual reduction on blade root flap-wise moment of about 15% but also a small penalty in the energy output (close to 1%). More recently, Roeleven [46] has investigated the optimal design of 10MW wind turbine blades including BTC effects. In this work, an optimization framework was

established including a cross-section analysis software, finite element beam approximations and aero-elastic coupling. The question set was to estimate the fibers angle distribution along the blade, under specific structural constraints.

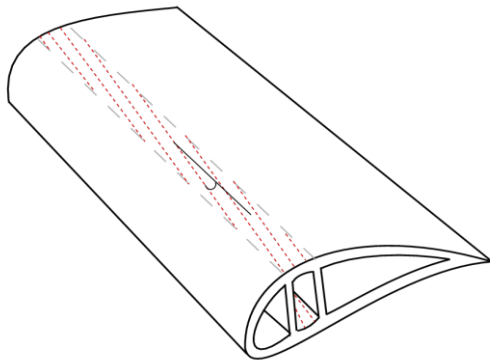


Figure 1.7: Ply angle of fiber orientation for BTC blades.

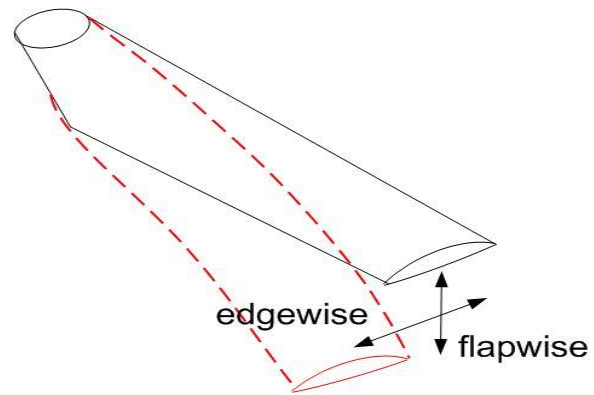


Figure 1.8: The directions (flap-wise and edge-wise) of blades.

Furthermore, a common problem observed during installation of wind turbines or in idling operation mode, is the management of high angles of attack that trigger stall-induced vibrations. Wang at al. in 2016 published a paper [47], in which the rotor stability in slow idling operation is assessed on the basis of non-linear time domain and linear eigenvalue analyses. The study focused on DTU-10MW RWT and the stability characteristics were assessed using an eigenvalue stability tool, while the results were also assessed through time domain aero-elastic predictions of loads for the idling turbine. Finally, the analysis has shown that at the yaw misalignment of $+30^\circ$ the asymmetric out-of-plane horizontal/tilt mode is negatively damped over the entire range of azimuth angles. Practical solutions to this problem, are thoroughly addressed in chapters 3 and 4 of the current thesis, through the FEC technique (see Fig. 1.8).

1.2. Objectives and innovations of this thesis

The current thesis aims at developing new optimized rotor designs of $10MW$ wind turbines, of minimum LCoE. The alleviation of loads, attained through application of passive load control techniques, is part of the above optimal rotor design strategy, allowing either the reduction of CAPital EXpenditure (CAPEX), and/or the increase of the Annual Energy Production (AEP), by increasing the rotor diameter within the margin offered by the load reduction. So, various numerical tools have been employed in their original form, others have been suitably modified and others have been developed from scratch (which constitute novel contribution of the present work work), in order to finalize a consistent optimization environment, appropriate for the reduction of LCoE. The main objectives of this thesis are summarized below:

- In the first phase, the numerical tools employed are evaluated and validated through a number of application examples and comparisons of their results against other similar existing in the literature

tools. Ultimate load distributions along the span of the blades are obtained through non-linear time domain aero-elastic simulations of the coupled turbine system using the in-house, multi-body, FEM (Finite Element Method), servo-aero-elastic tool hGAST. In order to fill in hGAST, the 6×6 full stiffness and mass matrices of the blades cross-sections is required. The necessary beam structural data are provided by a cross sectional analysis tool. The corresponding software was formulated by University of Patras and based on thin lamination theory [31]. In the present thesis, the software has been up-graded to include three webs and the geometrical shape of each section. A-priori, it provides beam equivalent structural properties, while once the simulations are concluded, it provides stress distributions and the value of the Tsai-Hill failure criterion along the blades.

- To develop a cost model that has been also synthesized with the aim to determine the cost of the full wind turbine (plus additional Balance of Plant - BoP and Operational and Maintenance – O&M costs). This model includes the estimation of the blades material and labor costs. The cost of all other components of the wind turbine (e.g. tower, gearbox, generation and other) have been estimated through existing in the literature empirical formulas. Finally, various optimization methods have been evaluated. The most common methods, are available through scipy library of Python, as the free-gradient method of COBYLA or the gradient-based method of SLSQP.
- Initially the various passive load control techniques are parameterized and evaluated by investigating the range of their applicability. Specifically, the operational loads are controlled through the ply offset angle of the fibers on the uni-directional material of the spar caps – *material BTC*. The results of the material BTC technique are compared to those of the geometric BTC (blade sweep). Then strong vibrations during parked or idling operation are reduced through the non-symmetric change of wall thicknesses – *material FEC* or by shifting the spar caps in opposite directions – *geometric FEC*. Finally, parametric evaluation of CAPEX compression (blade mass minimization) for various offset ply angles and the standard deviation of the edge-wise bending moment at the blade root for different shifts of the caps, have been tested respectively.
- An integrated framework that couples the above numerical tools has been established, with the aim to minimize LCoE. The above framework has been designed so that it can estimate, in addition to the parameters related to the passive control techniques (e.g. the offset ply angle of uni-directional material or the internal structure of the blade), the design parameters of the blade geometry e.g. the chord and twist distributions. The values of the above design parameters, constitute the design variables of the problem and are manipulated by the optimizer, which sets as objective function of the optimization, minimum values of LCoE. Optimization is performed in a Multi-Disciplinary servo-Aero-elastic Optimization (MDAO) context where all underlying disciplines, i.e. the aerodynamics, the structural mechanics and dynamics, the control system and most importantly their interactions are treated within the same simulation package.
- The final step of the present work is to test the MDAO procedure of rotor optimization in an holistic manner (concurrent consideration of structural and aerodynamic design variables within the same loop) and to assess the newly developed cost model. This is the main innovation of the present thesis in comparison to most of the existing MDAO developments [48] of the last years, which usually employ simplified, cost-based, objective functions but not an actual cost model which can

provide realistic estimates of the LCoE. Another important innovation of the thesis, is the quantification of the potential of reducing rotor's specific power (S/P) as a result of combined application of passive control techniques (BTC & FEC).

1.3. Thesis outline

The current thesis is divided into five chapters and includes two appendices:

- Chapter 2: It contains the description of the different numerical tools that are employed in the MDAO framework, followed by their validation in case they were revised either within the thesis or in parallel outside of it. More specifically, the bundle of tools considered include: (i) the in-house aero-servo-elastic solver hGAST [21], (ii) the 2D cross-sectional analysis tool based on lamination theory [49], (iii) the overall wind turbine cost model [50] and (iv) the gradient based or/and gradient-free optimization methods used in this thesis [51].
- Chapter 3: This chapter refers to the use of passive control techniques employing BTC and FEC. Both technologies are assessed on the reference turbine DTU-10MW RWT [52]. Also, the chapter evaluates the potential of reducing the mass of the blade, because of the relief in loads attained through passive control of loads.
- Chapter 4: This chapter presents the formulation of an iterative multi-disciplinary optimization process for minimizing LCoE. The set up has the passive control parameters (e.g. offset ply angle of uni-directional material) as well as wind turbine geometric parameters (e.g. chord and twist distributions), as design/optimization variables. At the end of this chapter, a set of optimized blade designs is proposed.
- Chapter 5: It contains the conclusions drawn from the current work along with recommendations for future research.
- Appendix A: An extensive description in terms of dimensions and physical properties of the reference wind turbine of the thesis, the DTU-10MW RWT is provided. This Appendix also includes the results of the aero-elastic analyses of the reference turbine, both in terms of ultimate and fatigue loading.
- Appendix B: A detailed description of the thin lamination theory employed in this thesis is provided. Also, the procedures for estimating the beam-equivalent properties and a posteriori stresses distributions over thin-walled structures as well as the method for calculating Timoshenko shear factors.

This page intentionally left blank

Chapter 2

2. Numerical tools and validation

In the present chapter, the numerical models used in this work are presented. They are a set of independent modules that are effectively synthesized into a multi-disciplinary optimization framework. The first module is the servo-aero-elastic solver hGAST [21], which is used for the calculation of the wind turbine design loads based on the provisions of the IEC 61400-1 standard [53]. It has been developed in previous PhD projects [54],[22] and its results have been compared against measurements and predictions of other similar aero-elastic design tools in as the context of the EU research projects outlined in section 1.1.2. The other two modules are either extended or exclusively developed in the context of the present thesis. These are: 1) a sectional thin lamination model which has been extended to i) also consider cross sections with three shear webs instead of two in its original form ii) account for the shear shape factors in deriving the shear rigidities and iii) provide stress results over the laminates of the composite material as well as equivalent stress results on the basis of Tsai-Hill criterion, and 2) a cost model for the evaluation of CAPital EXPenditures (CAPEX) of the candidate designs which is developed by the present thesis. The presentation of the models includes the description of the underlying theory and the demonstration of their prediction capabilities (with the exception of hGAST, which has been sufficiently validated in previous works). The evaluation is carried out by comparing the predictions of the herein models, against those from other similar tools such as the BECAS [55] in the case of the thin lamination model and the WISDEM [56] in the case of the blade cost model analysis.

2.1. Aero-elastic solver hGAST

Technological breakthroughs in material science, manufacturing methods and load control strategies have led to an ever increasing size of modern wind turbines. The increase in size is mainly dictated by the need for further increasing penetration of wind energy in the European and the global energy

systems. The excessive increase in size entails the design of highly flexible, long and slender blades, with low mass – relative to their size – which in normal operation conditions undergo large bending deflections (in some cases they can even exceed 10% of the radius of the blade) and high torsion angles which can affect their performance and stability. Every new wind turbine design (as with any new product), must be certified for safety and reliability. Therefore, an important requirement for a safe design is the accurate determination of the design loads of a wind turbine. The more accurate is the estimation of the design loads, the more safety factors can decrease and so does the cost. So, the current section begins, with the presentation of the in-house high-fidelity servo-aero-elastic solver hGAST which is used in this thesis for determining wind turbine's lifetime loads.

2.1.1. State-of-art in aero-elastic solvers and hGAST

Since the 1980s and mainly from the middle 1990s, several aero-elastic solvers for wind turbines have been developed, adopting simple linear beam theory [57], with some corrections for non-linear effects, as for example the effect of centrifugal stiffening due to the rotation of the blades. Many of the existing tools are based on the application of the Finite Element Method (FEM) to the full system of the dynamic equations [58],[59] and others, with the aim to compress computational cost, have adopted simpler and reduced order models like Craig-Bampton modal method [60]. The need for substantially reducing computational cost in conjunction with the requirement by the standards of performing several design simulations within the certification loop, led some codes to even neglect torsion deformation degree of freedom [61], assuming that blades are rather stiff in torsion. Although such an assumption would be convenient due to the large amount of simulations required by IEC standard, it is not valid in modern multi-megawatt wind turbines.

In the new generation of aero-elastic tools, higher order non-linear beam models have been adopted, either based on truncation methodologies which allow reducing non-linear contributions to the most important and relevant ones [62], or on generalized geometrically exact Timoshenko methodologies [63]. The above beam models are combined with multi-body dynamic formulations [64] that account for complex kinematic and dynamic constraint conditions and rigid body motions. Beam equations are derived through the application of an extended form of Hamilton's principle. The models belonging to the second category (geometrically exact formulations) are usually based on intrinsic formulations of the beam theory [65] (they consider deflection velocity and angular velocity as primary dofs instead of displacements and rotations). On the other hand, some methods are based on first order linear beam models but they divide each flexible component into a number of interconnected sub-bodies that each one follows the deflected body state. The sub-bodies are either considered as flexible beams or as rigid bodies. In this way, condition of the geometrically exact beam is satisfied at the level of the discrete sub-bodies and not at every single position along the beam.

hGAST is a servo-aero-elastic simulation toolbox, that has been entirely developed at NTUA and it is based on the latter approach [21]. The core of this solver, consists of a non-linear aero-elastic solver for the full wind turbine system in the time domain, in which there is provision to also include the control

equations and the dynamics of the floater. Essentially, hGAST is an upgraded version of the GAST solver [66], in which dynamic equations are derived under the assumption of the homogenous isotropic material. In hGAST the full stiffness matrix [67] of the composite lay-up (e.g. the detailed inner structure of the composite materials), is considered. This is a necessary modeling feature for simulating blades with aero-elastic tailoring and passive load control capabilities [67],[68]. Major contributions were made by Manolas in his PhD [22] where more details can be found regarding the capabilities of hGAST. In particular, it was based on the PhD thesis by Riziotis [54], while the control equations were added and the toolbox was extended to offshore concepts both bottom fixed and floating. In that form hGAST supported the AVATAR [19] and INNWIND.EU [18] research projects (see section 1.1.2.). In [21] and [69], extensive cross comparisons of hGAST results against HAWC2 code [70], on NREL-5MW RWT [71] can be found.

The hGAST simulation toolbox consists of:

- an aerodynamics module for the analysis of rotor aerodynamics.
- a structural dynamics module that applies FEM beam modeling of all flexible components.
- a multi-body dynamic module that also considers the floater motion.
- a hydrodynamic module for incorporating current and wave loading on offshore sub-structures.

All the above modules (except for the hydrodynamic since the present thesis deals only with onshore turbines) are briefly described in the following sections.

2.1.2. Aerodynamic module

The aerodynamic module of hGAST consists of several modeling options of varying fidelity. Available in hGAST are:

- a low fidelity Blade Element Momentum Theory (BEMT) module [72].
- a medium fidelity free wake vortex model [73].
- a high fidelity Computational Fluid Dynamics (CFD) model [74].

The last two options have been used in aero-elastic analyses mainly for predicting challenging conditions that exceed the limits of BEMT validity [75]. They have also been used for tuning engineering correction models in BEMT which allow them predicting the above challenging conditions. However, because of their excessive computational cost, they are not suitable for multi-disciplinary (multi-point) optimization simulations. The BEMT model on the other hand, is well suited for that kind of optimizations and so it is the only aerodynamic model adopted in the current thesis.

As mentioned above, the BEMT method includes empirical add-ons and corrections in order to account for the following effects which originally are not supported by the theory, but are crucial for the accurate estimation of the aerodynamic loads:

- actual blade geometry (cone, pitch, pre-bend and pre-sweep blade angles).

- consideration of the deformation velocities in case of aero-elastic coupling.
- correction of the thrust coefficient C_T for highly loaded rotors.
- reduction of energy extraction due to tip losses.
- dynamic inflow.
- shed vorticity effects and dynamic stall.
- correction for skewed wake (yaw and tilt).

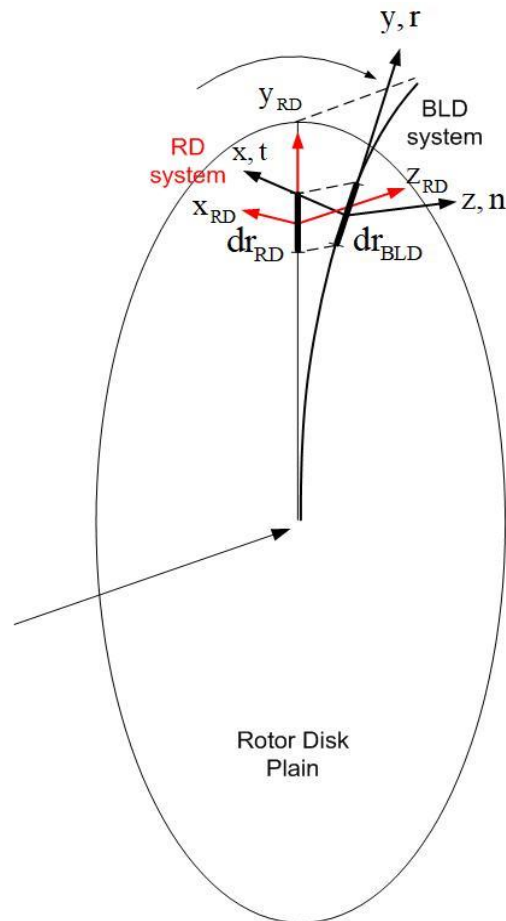


Figure 2.1: Definition of co-ordinate systems.

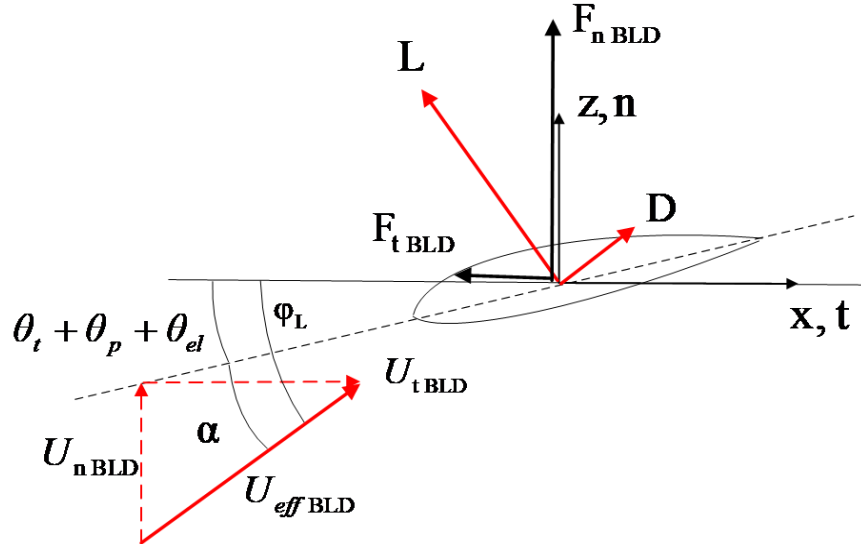


Figure 2.2: Local velocity triangle definition.

2.1.2.1. Implementation of BEMT in hGAST

Two coordinate systems (c.s.) are defined for every strip of the blade:

- i) the rotor disk (RD) c.s. (see Fig. 2.1) which has the z -axis normal to the rotor disk, pointing towards the wind direction, the y -axis along the radial direction pointing from the blade root to the tip and the x -axis normal to the other two, lying over the rotor disk plain and pointing opposite to the direction of rotation.
- ii) the local to the blade section c.s. (BLD) (see Fig. 2.1).

The first is attached to the rotor disk plain following the tilt and the yaw rotations of the nacelle, the azimuthal angle of each blade (including the initial azimuthal angle) and the rotational deformations of the tower and the shaft. The BLD local coordinate system includes in addition to RD the rotations for the coning angle, the pitch angle of the blades and the build in curvature (x -axis: pre-bend, z -axis: pre-sweep) angles.

Let \mathbf{A}_{strip} denote the transformation matrix from the RD c.s. to the BLD c.s.:

$$\mathbf{A}_{strip} = \mathbf{A}_{cone} \cdot \mathbf{A}_{pitch} \cdot \mathbf{A}_{curve} \quad (2.1)$$

where \mathbf{A}_{cone} , \mathbf{A}_{pitch} and \mathbf{A}_{curve} denote the elementary rotational matrices for cone, pitch, pre-bend and pre-sweep angles. It is noted that the twist and the torsion angle of the blade are not included in \mathbf{A}_{strip} .

The total velocity vector, defined with respect to the RD c.s. is,

$$\begin{aligned} \mathbf{U}_{RD} &= [(U_W - U_B)_{xRD}(1 + a'), (U_W - U_B)_{yRD}, (U_W - U_B)_{zRD}(1 - a)]^T \\ &= [U_{tRD}(1 + a'), U_{rRD}, U_{nRD}(1 - a)]^T \end{aligned} \quad (2.2)$$

where $U_{Wx,y,z RD}$ are the three components of the wind velocity including shear, yaw, inclination and turbulence, and $U_{Bx,yz RD}$ are the three components of the body velocity including rigid body motions (i.e. the rotation) and elastic deformation velocities both defined with respect to the rotor disk system, while a and a' are the axial and circumferential induction factors.

The total velocity with respect to the local BLD c.s. is defined as,

$$\mathbf{U}_{BLD} = \mathbf{A}_{strip} \cdot \mathbf{U}_{RD} = (U_{t BLD}, U_{r BLD}, U_{n BLD})^T \quad (2.3)$$

where n, t, r refer to normal, tangential and blade-wise directions of the BLD system (corresponding to z, x, y). The local effective velocity, the local flow angle and the angle of attack are defined as,

$$U_{eff BLD} = \sqrt{U_{n BLD}^2 + U_{t BLD}^2} \quad (2.4)$$

$$\varphi_L = \tan^{-1} \left[\frac{U_{n BLD}}{U_{t BLD}} \right] \quad (2.5)$$

$$a = \varphi_L - \vartheta_t - \vartheta_p - \vartheta_{el} \quad (2.6)$$

where the radial component has been neglected in Eq. 2.4 as $U_{eff BLD}$ corresponds to the 2D sectional effective velocity. The angles ϑ_t , ϑ_p and ϑ_{el} denote the twist, pitch and the torsion deformation defined with respect to the BLD c.s.

In case of a rotor with cone and pre-curvature and also accounting for the hub and the tip losses, the BEMT equations are written as,

$$N_{blade} \frac{\rho}{2} U_{eff BLD}^2 C_{n BD} c dr_{BLD} = 4\pi \rho U_{n RD}^2 r_{RD} dr_{RD} \underbrace{a(1-a)F_{loss}}_{\hat{C}_T} \quad (2.7)$$

$$N_{blade} \frac{\rho}{2} U_{eff BLD}^2 C_{t RD} c r_{RD} dr_{BLD} = 4\pi \rho U_{t RD} U_{n RD} a'(1-a)r_{RD}^2 dr_{RD} F_{loss} \quad (2.8)$$

where N_{blade} is the number of blades, ρ is the density of air, c is the airfoil chord, C_n and C_t are the normal and tangential force coefficients respectively, F_{loss} is the tip loss factor, dr_{BLD} denotes the actual width of the annular tube and dr_{RD} is the projected width on the rotor disk plane (see Fig. 2.1).

Considering λ the local tip speed ratio and σ the local solidity given by:

$$\lambda = \frac{U_{t RD}}{U_{n RD}} \quad (2.9.a)$$

$$\sigma = \frac{N_{blade} c}{2\pi r_{RD}} \frac{dr_{BLD}}{dr_{RD}} \quad (2.9.b)$$

Eq. 2.7 and Eq. 2.8 are cast in the form:

$$C_T - \sigma C_{n RD} \frac{C_{eff BLD}^2}{C_{n RD}^2} = 0 \quad (2.10)$$

$$4a'(1-a)\lambda F_{loss} - \sigma C_{t RD} \frac{U_{eff BLD}^2}{U_{n RD}^2} = 0 \quad (2.11)$$

The local C_t and C_n coefficients are defined as,

$$\begin{aligned} C_t &= C_L \sin \varphi_L - C_D \cos \varphi_L \\ C_n &= C_L \cos \varphi_L + C_D \sin \varphi_L \end{aligned} \quad (2.12)$$

where C_L and C_D are the lift and drag coefficients respectively. When transformed to the RD c.s, local C_t and C_n are defined as,

$$\begin{aligned} C_{t\ RD} &= \mathbf{A}_{strip}(1,1)C_t - \mathbf{A}_{strip}(1,3)C_n \\ C_{n\ RD} &= \mathbf{A}_{strip}(3,3)C_n - \mathbf{A}_{strip}(3,1)C_t \end{aligned} \quad (2.13)$$

Note that the positive direction for C_t is opposite the x direction by convention.

2.1.2.2. Tip loss

In Eq. 2.7 and Eq. 2.8 F_{loss} denotes the tip loss factor originally proposed by Prandtl [76] and defined as,

$$F_{loss}(r) = \frac{2}{\pi} \cos^{-1} \left(e^{-\frac{N_{blade}}{2} \frac{R_{RD} - r_{RD}}{r_{RD} \sin \varphi_L}} \right) \quad (2.14)$$

where R_{RD} denotes the projected radius of the tip of the rotor blade.

2.1.2.3. Correction of the thrust coefficient C_T for highly loaded rotors

The thrust coefficient C_T in Eq. 2.7, including the correction for high values of the induction factor a (exceeding the value of 1) [77] is defined as,

$$C_T = \begin{cases} 4a(1-a)F_{loss} & , a < 0.33 \\ (0.425 + 1.39a)F_{loss} & , a > 0.33 \end{cases} \quad (2.15)$$

2.1.2.4. Dynamic inflow modeling

In case of dynamic inflow modeling, Eq. 2.10 becomes,

$$4 \frac{R_{RD}}{U_W} f_a \left(\frac{r_{RD}}{R_{RD}} \right) \dot{a} + C_T - \sigma C_{n\ RD} \frac{U_{eff\ BLD}^2}{U_{n\ RD}^2} = 0 \quad (2.16)$$

f_a term originates from the integration of the unsteady momentum equation and accounts for the inertia of the wake [78] defined as,

$$f_a \left(\frac{r_{RD}}{R_{RD}} \right) = 2\pi \left[\int_0^{2\pi} \frac{\left(1 - \frac{r_{RD}}{R_{RD}} \cos \psi\right) d\psi}{\left[1 + \left(\frac{r_{RD}}{R_{RD}}\right)^2 - 2 \frac{r_{RD}}{R_{RD}} \cos \psi\right]^{3/2}} \right]^{-1} \quad (2.17)$$

where ψ is the azimuth angle.

2.1.2.5. Shed vorticity effects and dynamic stall

In order to capture the effect of the unsteady flow due to the shed vorticity emanating from the blade, as well as dynamic stall effects on the aerodynamic coefficients C_L , C_D and C_M , a dynamic stall model is applied. The coefficients do not retain their steady values based on the angle of attack α but instead they are defined by solving the ONERA [79] or the Beddoes – Leishman [80] dynamic stall model equations. Details can be found in [54].

2.1.2.6. Correction for skewed wake (yaw and tilt)

A simple cylindrical skewed wake model is considered. Based on the expression originally proposed by Glauert [81] the axial induction factor a in Eq. 2.7 and Eq. 2.8 is modified as,

$$a_{skewed} = a \left[1 + K(\chi) F_e \left(\frac{r_{RD}}{R_{RD}} \right) \sin \psi \right] \quad (2.18)$$

where K is a function expressed in terms of the wake skew angle χ and F_e the flow expansion function. Eq. 2.18 introduces a radial (due to F_e) and an azimuthal (due to $\sin \psi$) variation of the induction factor and in turn of the induced velocity.

In the current implementation two possibilities are available. The first adopts the K function by Coleman [82],[83],

$$K(\chi) = \tan \left(\frac{\chi}{2} \right) \quad (2.19.a)$$

and the flow expansion function by Øye [84],

$$F_e \left(\frac{r_{RD}}{R_{RD}} \right) = \frac{r_{RD}}{R_{RD}} + 0.4 \left(\frac{r_{RD}}{R_{RD}} \right)^3 + 0.4 \left(\frac{r_{RD}}{R_{RD}} \right)^5 \quad (2.20.a)$$

while the second adopts the K function by Drees [85]

$$K(\chi) = \frac{4}{3} \left[1 - 1.8 \left(\frac{\sin \gamma}{\lambda} \right)^2 \right] \tan \left(\frac{\chi}{2} \right) \quad (2.19.b)$$

and the linear flow expansion function by Glauert,

$$F_e \left(\frac{r_{RD}}{R_{RD}} \right) = \frac{r_{RD}}{R_{RD}} \quad (2.20.b)$$

The wake skew angle χ is defined as,

$$\chi = \tan^{-1} \left[\frac{U_W \sin \gamma}{U_W \cos \gamma (1 - a)} \right] \quad (2.21)$$

where γ denotes the skew angle, defined as the angle between the vector normal to the rotor plane and the mean wind velocity due to yaw and tilt.

2.1.2.7. Solution procedure

The system of the two non-linear equations Eq. 2.10 and Eq. 2.11 is solved with a Newton Raphson method, providing for each individual strip the induction factors a and a' . It is noted that all the aforementioned corrections and add-ons (dynamic inflow, shed vorticity and dynamic stall model) are coupled to the BEMT solution and are considered during the iterations loop.

2.1.2.8. Loads calculation

Once the iterative process has converged the normal and the tangential force and the pitching moment with respect to the BLD c.s. along the blade span-wise direction are calculated as,

$$\begin{aligned}
 F_{n\ BLD} &= \frac{\rho}{2} C_{n\ BLD} U_{eff\ BLD}^2 c\ dr_{BLD} \\
 F_{t\ BLD} &= -\frac{\rho}{2} C_{t\ BLD} U_{eff\ BLD}^2 c\ dr_{BLD} \\
 M_{BLD} &= \frac{\rho}{2} C_{M\ BLD} U_{eff\ BLD}^2 c^2\ dr_{BLD}
 \end{aligned} \tag{2.22}$$

2.1.3. Structural dynamics module

The full wind turbine is a multi-component dynamic system having as components the blades, the drive train and the tower, all approximated as Timoshenko beam structures. The assembly of the above components into the full system is carried out in the framework of the so-call “multi-body approach”. It consists of considering each component separately from the others, but subjected to specific free-body kinematic and loading conditions, imposed at the connection points of the components. The multi-body formulation may be also extended to the component level. Highly flexible components, such as the blades can be divided into a number of interconnected “sub-bodies”, considered as an assembly of linear beam elements. Large deflections and rotations gradually build up, whereas non-linear dynamics are introduced by imposing to each sub-body the deflections and rotations of preceding sub-bodies as rigid body-non-linear-motions. This approach allows capturing the geometrical non-linear effects due to large deflections and rotations using linear beam theory at the element level, but considering non-linear effects at the sub-body level.

2.1.3.1. Multi-body dynamics model

Multi-body dynamics is adopted in the modelling of all the structural components/elements of the wind turbine assembly. In the present multibody dynamics analysis, all flexible components are represented as 1D flexible (beam) structures, whereas numerical discretization employs non-linear FEM. Multi-body dynamics can concurrently accommodate rigid body motions and structural flexibility, together with the non-linear inertial and structural effects and geometric couplings that large deflections of highly flexible

components may cause (e.g. blades). Rigid motions are imposed by either the control system (e.g. blades' pitch motion, drive train rotational speed) or by external excitations (effect of inflow/environmental conditions to wind turbine kinematics).

2.1.3.2. Multi-body kinematics model

The main structural components of a wind turbine assembly are the blades, the drive train system and the tower. All the above flexible components, which are usually sufficiently elongated, are approximated as a collection of linear Timoshenko beam structures. In multi-body dynamics, assembly of the components into the full system is carried out by imposing appropriate kinematic and loading conditions at the connection points. In brief, at any connection point one of the connected components specifies the position (displacements) and orientation (rotations) while all others contribute their reaction loads [69].

A local coordinate system $[Oxyz]$ (see Fig. 2.3) is assigned to every component (body) with respect to which local elastic displacements are defined. The y -axis of the local body system is chosen to coincide with the body elastic axis. The local frame of each body (e.g. blades) is subjected to (a) rigid body and (b) elastic motions. For the k^{th} body, let $\mathbf{q}^k = \{\mathbf{q}_t^k, \mathbf{q}_r^k\}^T$ (index "t" stands for translations and "r" for rotations) denote a set of time invariant and/or time variant displacements and rotations that define the origin and orientation of the local system of the k^{th} body in the undeflected state. The \mathbf{q}^k vector contains, i) all constant translations and rotations that in the still/undeflected state define the local coordinate system of the body with respect to the inertial frame, ii) time variant body self-motions (e.g. pitch angle of the blades), iii) global rigid body kinematic d.o.fs that apply to a collection of bodies including the k -th body (eg. rotor rotational speed, yaw motion undergone by all blades of the rotor) and iv) translations and rotations induced by other bodies, in particular elastic motions induced by other bodies connected to the k^{th} body (see Fig. 2.4).

The (global) position vector \mathbf{r}_G^k of any arbitrary point P over the deflected k^{th} body with respect to the global inertia frame $[O_G x_G y_G z_G]$ (see Fig. 2.3) is expressed through the (local) position vector of P in the un-deflected state $\mathbf{r}_l^k = (x_l^k, y_l^k, z_l^k)^T$ and the vector of the local elastic deflections (displacements and rotations) $\mathbf{u}^k = (u^k, v^k, w^k, \theta^k, \theta^k, \theta^k)^T$ (both defined in body local co-ordinates - see Fig. 2.4), and the motions \mathbf{q}^k as follows:

$$\mathbf{r}_G^k = \mathbf{R}^k(\mathbf{q}^k; t) + \mathbf{T}^k(\mathbf{q}_r^k; t)[\mathbf{r}_l^k + \mathbf{S} \cdot \mathbf{u}^k(t)] \quad (2.23)$$

where, \mathbf{R}^k is the position vector of the origin of the local coordinate system of the k -th body with respect to the global system, \mathbf{T}^k is the rotation matrix from the local system of the k -th body to the global co-ordinate system and \mathbf{S} matrix is given by:

$$\mathbf{S} = \begin{bmatrix} 1 & 0 & 0 & 0 & z_l^k & 0 \\ 0 & 1 & 0 & -z_l^k & 0 & x_l^k \\ 0 & 0 & 1 & 0 & -x_l^k & 0 \end{bmatrix} \quad (2.24)$$

Where the right 3×3 part of \mathbf{S} is related to displacement induce as the result of the elastic rotation. It is noted that both \mathbf{T}^k is expressed as a sequence of consecutive elementary rotations each about a single axis:

$$\mathbf{T} = T_1(q_r^1) \cdot T_2(q_r^2) \cdots T_{m-1}(q_r^{m-1}) \cdot T_m(q_r^m) \quad (2.25)$$

Moreover, \mathbf{R}^k is expressed as a sum of elementary rotations (around one axis) multiplied with elementary translations:

$$\mathbf{R} = R_1(q_t^1) + T_1(q_r^1) \{ R_2(q_t^2) + T_2(q_r^2) \cdots [R_{m-1}(q_t^{m-1}) + T_{m-1}(q_r^{m-1}) \cdot R_m(q_t^m)] \cdots \} \quad (2.26)$$

Of particular importance is that the above multi-body formulation is extended to the body level. Highly flexible bodies, such as the blades, are divided into a number of interconnected sub-bodies, each considered as a single or as an assembly of linear beam elements. Large deflections and rotations gradually build up and non-linear dynamics are introduced by imposing to each sub-body, the deflections and rotations of preceding sub-bodies as rigid body motions. Dynamic coupling of the sub-bodies is again introduced by communicating the reaction loads (three forces and three moments) at the first node of every sub-body to the free node of the previous sub-body as external load. Illustration of the extension of the multi-body framework at the level of a body is illustrated in (Fig. 2.4). Fig. 2.4 shows how a body (local co-ordinate system $[O_m x_m y_m z_m]$ of the m -th body) can be discretized into a number of interconnected sub-bodies (local co-ordinate system $[Oxyz]$) and eventually every sub-body into a number of linear Timoshenko beam FEM elements.

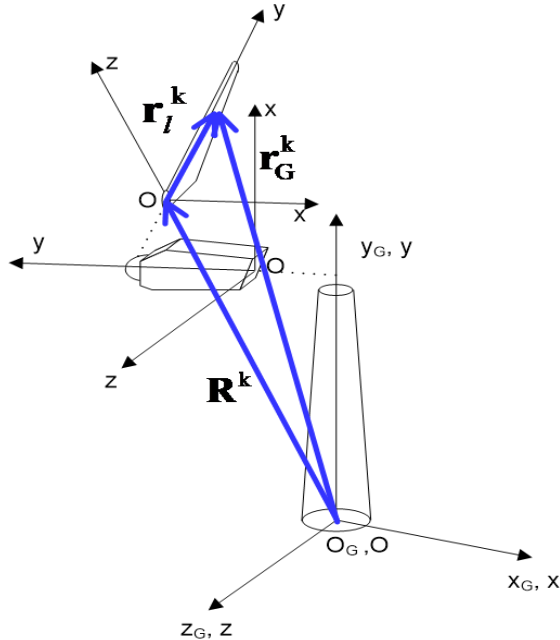


Figure 2.3: Simple model of a wind turbine. Examples of local body co-ordinate systems. The local co-ordinate system of the blade the tower and the drive train are indicated.

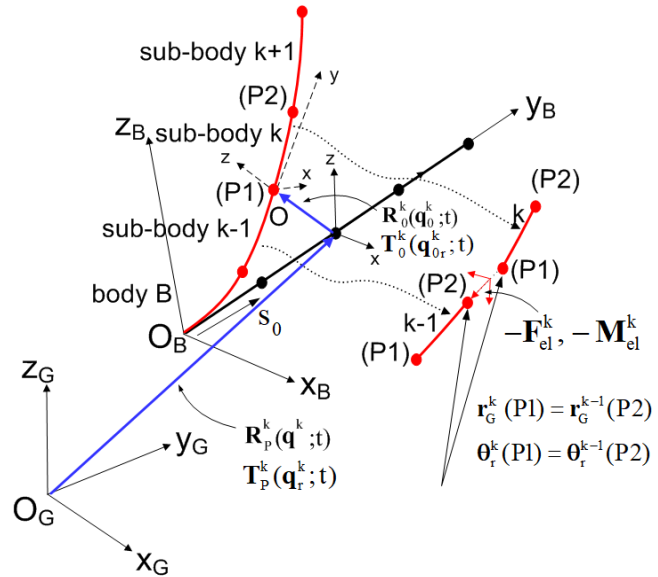


Figure 2.4: Application of multibody kinematics at the body level (connected sub-bodies). Connection of sub-bodies $k - 1$ and k in body m .

2.1.3.3. Timoshenko beam model

Linear Timoshenko beam modeling is applied in order to account for the local deflections vector \mathbf{u}^k of every flexible body/sub-body. The coordinate system $[O'\xi\eta\zeta]$ shown in Fig. 2.4 is the cross section local system. Around the axes of this system, local bending and torsion rotations take place. The set of dynamic equilibrium equations per unit length of beam (the first express the 3 force equation and the last the 3 moment equations) of the k -th body takes the form:

$$\int_A \rho dA \mathbf{S}^T \cdot \mathbf{T}^{kT} \cdot \ddot{\mathbf{r}}_G^k = \begin{bmatrix} F'_x \\ F'_y \\ F'_z \\ M'_x + F_z - F_y w'^k \\ M'_y \\ M'_z + F_x - F_y u'^k \end{bmatrix}^k + \begin{array}{l} \text{external loads including} \\ \text{reaction loads communicated} \\ \text{by connected bodies} \end{array} \quad (2.27)$$

where $(\)' = \partial/\partial y$ denotes derivatives with respect to the beam-wise local y direction. The terms $F_y w'^k$ and $F_y u'^k$ in the moment x and z equations are the only non-linear terms considered in the analysis. This is because they are expected to contribute significantly, especially in the case of rotating beams in which axial force increases due to the centrifugal effect. The two terms give rise to virtual stiffening of the beam as rotational speed increases.

It is noted that equilibrium equations Eq. 2.27 are written with respect to the local body or sub-body co-ordinate system. The acceleration of an arbitrary point P of the k -th body is expressed as:

$$\mathbf{T}^{kT} \cdot \ddot{\mathbf{r}}_G^k = \underbrace{\mathbf{T}^{kT} \cdot \ddot{\mathbf{R}}^k}_{\text{acceleration of origin}} + \underbrace{\mathbf{T}^{kT} \cdot \dot{\mathbf{T}}^k [\mathbf{r}_l^k + \mathbf{S} \cdot \mathbf{u}^k(t)]}_{\text{centrifugal}} + \underbrace{2\mathbf{T}^{kT} \cdot \dot{\mathbf{T}}^k \cdot \mathbf{S} \cdot \dot{\mathbf{u}}^k(t)}_{\text{Coriolis}} + \underbrace{\mathbf{S} \cdot \ddot{\mathbf{u}}^k(t)}_{\text{local}} \quad (2.28)$$

As indicated under every term of Eq. 2.28, besides local acceleration due to local deflection of the body/sub-body, the acceleration of the origin of the local body/sub-body co-ordinate system and the centrifugal and Coriolis terms due to the rotation of the local body/sub-body co-ordinate system are taken into account in the analysis. It is noted that the first, second and third term of Eq. 2.28 depend non-linearly on vectors $\mathbf{q}^k = [\mathbf{q}_t^k, \mathbf{q}_r^k]^T$ (time dependent translations and rotations).

The constitutive relation between the generalized structural loads over a cross section of a beam and the strains-curvatures is given by:

$$\mathbf{F}^k = \mathbf{K}^k \cdot \boldsymbol{\varepsilon}^k \quad (2.29)$$

where,

$$\mathbf{F}^k = [F_x^k \quad F_y^k \quad F_z^k \quad M_x^k \quad M_y^k \quad M_z^k]^T$$

$$\boldsymbol{\varepsilon}^k = [\gamma_x^k \quad \varepsilon_y^k \quad \gamma_z^k \quad k_x^k \quad k_y^k \quad k_z^k]^T$$

$$\mathbf{K}^k = \begin{bmatrix} K_{11}^A & K_{12}^A & K_{13}^A & K_{11}^B & K_{12}^B & K_{13}^B \\ & K_{22}^A & K_{23}^A & K_{21}^B & K_{22}^B & K_{23}^B \\ & & K_{33}^A & K_{31}^B & K_{32}^B & K_{33}^B \\ & \text{sym.} & & K_{11}^D & K_{12}^D & K_{13}^D \\ & & & & K_{22}^D & K_{23}^D \\ & & & & & K_{33}^D \end{bmatrix}^k$$

and,

$$\varepsilon_y = v', \gamma_x = u' + \theta_z, \gamma_z = w' - \theta_x, k_x = \theta'_x, k_y = \theta'_y, k_z = \theta'_z \quad \text{for the } k\text{-th body} \quad (2.30)$$

In Eq. 2.29 \mathbf{K}^k is the sectional Timoshenko full stiffness matrix. With respect to a standard Timoshenko beam approach the elements K_{11}^A and K_{33}^A represent transverse shear rigidity, K_{22}^A axial stiffness, K_{11}^D and K_{33}^D flexural stiffness in flap-wise and edge-wise directions respectively and K_{22}^D torsional stiffness. The off-diagonal elements K_{12}^D and K_{13}^D are responsible for the activation of bend-twist coupling. By introducing Eq. 2.30 into Eq. 2.29, \mathbf{K}^k can be split as follows:

$$\mathbf{F}^k = \mathbf{K}^k \cdot \boldsymbol{\varepsilon}^k = \mathbf{K}_1^k \mathbf{u}^k + \mathbf{K}_2^k \mathbf{u}^k \quad (2.31)$$

where,

$$\mathbf{K}_1^k = \mathbf{K}^k$$

and,

$$\mathbf{K}_2^k = \begin{bmatrix} 0 & 0 & 0 & -K_{13}^A & 0 & K_{11}^A \\ 0 & 0 & 0 & -K_{23}^A & 0 & K_{12}^A \\ 0 & 0 & 0 & -K_{33}^A & 0 & K_{13}^A \\ 0 & 0 & 0 & -K_{31}^B & 0 & K_{11}^B \\ 0 & 0 & 0 & -K_{23}^B & 0 & K_{12}^B \\ 0 & 0 & 0 & -K_{33}^B & 0 & K_{13}^B \end{bmatrix}^k$$

By substituting Eq. 2.31 into Eq. 2.27 the dynamic equations are expressed with respect to the local deflections dofs in the form:

$$\int_A \rho dA \mathbf{S}^T \cdot \mathbf{T}^{kT} \cdot \ddot{\mathbf{r}}_G^k = (\mathbf{K}_1^k \mathbf{u}^k)' + (\mathbf{K}_2^k \mathbf{u}^k)' + (\mathbf{K}_3^k \mathbf{u}^k) + (\mathbf{K}_4^k \mathbf{u}^k) + \begin{matrix} \text{external loads/} \\ \text{reactions} \end{matrix} \quad (2.32)$$

where,

$$\mathbf{K}_3^k = \begin{bmatrix} 0 & 0 & 0 & 0 & 0 & 0 \\ 0 & 0 & 0 & 0 & 0 & 0 \\ 0 & 0 & 0 & 0 & 0 & 0 \\ K_{13}^A & K_{23}^A & K_{33}^A - F_y & K_{31}^B & K_{32}^B & K_{33}^B \\ 0 & 0 & 0 & 0 & 0 & 0 \\ -K_{11}^A + F_y & -K_{12}^A & -K_{13}^A & -K_{11}^B & -K_{12}^B & -K_{13}^B \end{bmatrix}^k$$

$$\mathbf{K}_4^k = \begin{bmatrix} 0 & 0 & 0 & 0 & 0 & 0 \\ 0 & 0 & 0 & 0 & 0 & 0 \\ 0 & 0 & 0 & 0 & 0 & 0 \\ 0 & 0 & 0 & -K_{33}^A & 0 & K_{13}^A \\ 0 & 0 & 0 & 0 & 0 & 0 \\ 0 & 0 & 0 & K_{13}^A & 0 & -K_{11}^A \end{bmatrix}^k$$

In the case of a uniform/isotropic material beam the matrices \mathbf{K}_1^k , \mathbf{K}_2^k , \mathbf{K}_3^k , \mathbf{K}_4^k take the form:

$$\mathbf{K}_1^k = \begin{bmatrix} G_x A & 0 & 0 & 0 & G_x A_x & 0 \\ 0 & EA & 0 & -EA_x & 0 & EA_z \\ 0 & 0 & G_z A & 0 & -G_z A_z & 0 \\ 0 & -EA_x & 0 & EI_{xx} & 0 & -EI_{xz} \\ G_x A_x & 0 & -G_z A_z & 0 & GJ & 0 \\ 0 & EA_z & 0 & -EI_{xz} & 0 & EI_{zz} \end{bmatrix}^k \quad (2.33.a)$$

$$\mathbf{K}_2^k = \begin{bmatrix} 0 & 0 & 0 & 0 & 0 & G_x A \\ 0 & 0 & 0 & 0 & 0 & 0 \\ 0 & 0 & 0 & -G_z A & 0 & 0 \\ 0 & 0 & 0 & 0 & 0 & 0 \\ 0 & 0 & 0 & G_z A_z & 0 & G_x A_x \\ 0 & 0 & 0 & 0 & 0 & 0 \end{bmatrix}^k \quad (2.33.b)$$

$$\mathbf{K}_3^k = \begin{bmatrix} 0 & 0 & 0 & 0 & 0 & 0 \\ 0 & 0 & 0 & 0 & 0 & 0 \\ 0 & 0 & 0 & 0 & 0 & 0 \\ 0 & 0 & G_z A - F_y & 0 & -G_z A_z & 0 \\ 0 & 0 & 0 & 0 & 0 & 0 \\ -G_x A + F_y & 0 & 0 & 0 & -G_x A_x & 0 \end{bmatrix}^k \quad (2.33.c)$$

$$\mathbf{K}_4^k = \begin{bmatrix} 0 & 0 & 0 & 0 & 0 & 0 \\ 0 & 0 & 0 & 0 & 0 & 0 \\ 0 & 0 & 0 & 0 & 0 & 0 \\ 0 & 0 & 0 & -G_z A & 0 & 0 \\ 0 & 0 & 0 & 0 & 0 & 0 \\ 0 & 0 & 0 & 0 & 0 & -G_x A \end{bmatrix}^k \quad (2.33.d)$$

where,

$$\begin{aligned}
 EA &= \int_A E dA & EA_x &= \int_A Ez dA \\
 EI_{zz} &= \int_A Ex^2 dA & EA_z &= \int_A Ex dA \\
 EI_{xx} &= \int_A Ez^2 dA & EI_{xz} &= \int_A Exz dA \\
 G_x A &= \int_A G_x dA & G_z A &= \int_A G_z dA \\
 G_x A_x &= \int_A G_x z dA & G_z A_z &= \int_A G_z x dA
 \end{aligned}$$

In order to apply FEM, the above set Eq. 2.33 is written in weak form by applying the principle of virtual work:

$$\begin{aligned}
 \int_L \delta \mathbf{u}^{kT} \left[\int_A \varrho dA \mathbf{S}^T \cdot \mathbf{T}^{kT} \cdot \dot{\mathbf{r}}_G^k \right] dy &= \int_L \delta \mathbf{u}'^{kT} (\mathbf{K}_1^k \mathbf{u}'^k) dy + \int_L \delta \mathbf{u}'^{kT} (\mathbf{K}_2^k \mathbf{u}^k) dy \\
 + \int_A \delta \mathbf{u}^{kT} (\mathbf{K}_3^k \mathbf{u}'^k) dy &+ \int_L \delta \mathbf{u}^{kT} (\mathbf{K}_4^k \mathbf{u}^k) dy + \\
 &+ \text{work of external loads} + \text{boundary terms}
 \end{aligned} \tag{2.34}$$

2.1.3.4. FEM analysis

The approximation of the local deflections along every element (of length L_e) of the beam is expressed through nodal dofs $\hat{\mathbf{u}}$:

$$\mathbf{u}(y, t) = \mathbf{N}(y) \cdot \hat{\mathbf{u}}(t) \tag{2.35}$$

where \mathbf{N} is the shape function matrix of the beam. 1st order shape functions for extension and torsion, and modified C^1 Hermitian functions for the two bending displacements that prevent shear locking [86] are used (by satisfying static equilibrium compatibility relations).

In Eq. 2.35,

$$\hat{\mathbf{u}}(t) = [u^1, v^1, w^1, \theta_x^1, \theta_y^1, \theta_z^1, u^2, v^2, w^2, \theta_x^2, \theta_y^2, \theta_z^2]^T \tag{2.36}$$

and

$$N(y) = \begin{bmatrix} N_{1u}^1 & 0 & 0 & 0 & 0 & N_{2u}^1 & N_{1u}^2 & 0 & 0 & 0 & 0 & N_{2u}^2 \\ 0 & N_v^1 & 0 & 0 & 0 & 0 & 0 & N_v^2 & 0 & 0 & 0 & 0 \\ 0 & 0 & N_{1w}^1 & N_{2w}^1 & 0 & 0 & 0 & 0 & N_{1w}^2 & N_{2w}^2 & 0 & 0 \\ 0 & 0 & N_{1\theta_x}^1 & N_{2\theta_x}^1 & 0 & 0 & 0 & 0 & N_{1\theta_x}^2 & N_{2\theta_x}^2 & 0 & 0 \\ 0 & 0 & 0 & 0 & N_{\theta_y}^1 & 0 & 0 & 0 & 0 & 0 & N_{\theta_y}^2 & 0 \\ N_{1\theta_z}^1 & 0 & 0 & 0 & 0 & N_{2\theta_z}^1 & N_{1\theta_z}^2 & 0 & 0 & 0 & 0 & N_{2\theta_z}^2 \end{bmatrix} \quad (2.37)$$

where, with $\xi = y/L_e$

$$\begin{aligned} N_v^1(\xi) &= N_{\theta_y}^1(\xi) = 1 - \xi & N_v^2(\xi) &= N_{\theta_y}^2(\xi) = \xi \\ N_{1u,w}^1(\xi) &= 1 - \xi\Phi_{x,z1} - 3\xi^2\Phi_{x,z2} + 2\xi^3\Phi_{x,z2} & N_{1u,w}^2(\xi) &= 1 - N_{1u,w}^1(\xi) \\ N_{2u,w}^1(\xi) &= (-\xi + 0.5\xi\Phi_{x,z1} + 0.5\xi^2\Phi_{x,z1} + 2\xi^2\Phi_{x,z2} - \xi^3\Phi_{x,z2})L_e \\ N_{2u,w}^2(\xi) &= (0.5\xi\Phi_{x,z1} - 0.5\xi^2\Phi_{x,z1} + \xi^2\Phi_{x,z2} - \xi^3\Phi_{x,z2})L_e \\ N_{1\theta_x,\theta_z}^1(\xi) &= 6\xi(1 - \xi)\frac{\Phi_{x,z1}}{L_e} & N_{1\theta_x,\theta_z}^2(\xi) &= -N_{1\theta_x,\theta_z}^1(\xi) \\ N_{2\theta_x,\theta_z}^1(\xi) &= 1 - \xi\Phi_{x,z1} + \xi(3\xi - 4)\Phi_{x,z1} & N_{2\theta_x,\theta_z}^2 &= -\xi\Phi_{x,z1} + \xi(3\xi - 2)\Phi_{x,z1} \\ \Phi_{x,z1} &= \frac{\varphi_{x,z}}{1 + \varphi_{x,z}} & \Phi_{x,z2} &= \frac{1}{1 + \varphi_{x,z}} & \varphi_{x,z} &= \frac{12\overline{EI}_{xx,zz}}{G_{x,z}\overline{AI}_e^2} \end{aligned}$$

In the above, $\overline{EI}_{xx,zz}$, $\overline{G_{x,z}A}$ are the average bending stiffness and shear rigidity over the element.

Non-linear equations Eq. 2.34 are linearized and written in perturbed form with respect to a reference (steady or periodic) state denoted by the index (0). It is thereby assumed that:

$$\begin{aligned} \mathbf{q}^k &= \mathbf{q}^{k0} + \delta\mathbf{q}^k, \dot{\mathbf{q}}^k = \dot{\mathbf{q}}^{k0} + \delta\dot{\mathbf{q}}^k \text{ and } \ddot{\mathbf{q}}^k = \ddot{\mathbf{q}}^{k0} + \delta\ddot{\mathbf{q}}^k \\ \mathbf{u}^k &= \mathbf{u}^{k0} + \delta\mathbf{u}^k, \dot{\mathbf{u}}^k = \dot{\mathbf{u}}^{k0} + \delta\dot{\mathbf{u}}^k, \ddot{\mathbf{u}}^k = \ddot{\mathbf{u}}^{k0} + \delta\ddot{\mathbf{u}}^k \end{aligned}$$

Thereby, the different non-linear terms in Eq. 2.28 can be written in the following form with respect to the reference state:

$$\begin{aligned} \mathbf{T}^{kT} \cdot \ddot{\mathbf{R}}^k &= (\mathbf{T}^{kT} \cdot \ddot{\mathbf{R}}^k)^0 + \partial_q(\mathbf{T}^{kT} \cdot \ddot{\mathbf{R}}^k)^0 \cdot \delta\mathbf{q}^k + \partial_{\dot{q}}(\mathbf{T}^{kT} \cdot \ddot{\mathbf{R}}^k)^0 \cdot \delta\dot{\mathbf{q}}^k + \partial_{\ddot{q}}(\mathbf{T}^{kT} \cdot \ddot{\mathbf{R}}^k)^0 \cdot \delta\ddot{\mathbf{q}}^k \\ \mathbf{T}^{kT} \cdot \dot{\mathbf{T}}^k &= (\mathbf{T}^{kT} \cdot \dot{\mathbf{T}}^k)^0 + \partial_q(\mathbf{T}^{kT} \cdot \dot{\mathbf{T}}^k)^0 \cdot \delta\mathbf{q}^k + \partial_{\dot{q}}(\mathbf{T}^{kT} \cdot \dot{\mathbf{T}}^k) \cdot \delta\dot{\mathbf{q}}^k \\ \mathbf{T}^{kT} \cdot \ddot{\mathbf{T}}^k &= (\mathbf{T}^{kT} \cdot \ddot{\mathbf{T}}^k)^0 + \partial_q(\mathbf{T}^{kT} \cdot \ddot{\mathbf{T}}^k)^0 \cdot \delta\mathbf{q}^k + \partial_{\dot{q}}(\mathbf{T}^{kT} \cdot \ddot{\mathbf{T}}^k) \cdot \delta\dot{\mathbf{q}}^k + \partial_{\ddot{q}}(\mathbf{T}^{kT} \cdot \ddot{\mathbf{T}}^k) \cdot \delta\ddot{\mathbf{q}}^k \end{aligned} \quad (2.38)$$

Using Eq. 2.34, Eq. 2.35 and Eq. 2.38 the local linearized mass, damping and stiffness matrices of every FEM element along the beam are written:

$$\mathbf{M}_e = \int_{L_e} \left[\int_A (\rho dA) \mathbf{N}^T \cdot \mathbf{S}^T \cdot \mathbf{S} \cdot \mathbf{N} \right] dy \quad (2.39.a)$$

$$\mathbf{C}_e^a = \int_{L_e} \left[\int_A (\rho dA) \mathbf{N}^T \cdot \mathbf{S}^T \cdot \mathbf{2} \cdot (\mathbf{T}^{kT} \cdot \dot{\mathbf{T}}^k)^0 \cdot \mathbf{S} \cdot \mathbf{N} \right] dy \quad (2.39.b)$$

$$\mathbf{K}_e = \int_{L_e} \mathbf{N}'^T \cdot \mathbf{K}_1 \cdot \mathbf{N}' dy - \int_{L_e} \mathbf{N}'^T \cdot \mathbf{K}_2 \cdot \mathbf{N} dy + \int_{L_e} \mathbf{N}^T \cdot \mathbf{K}_3 \cdot \mathbf{N}' dy - \int_{L_e} \mathbf{N}^T \cdot \mathbf{K}_{21} \cdot \mathbf{N} dy \quad (2.39.c)$$

$$\mathbf{K}_e^a = \int_{L_e} \left[\int_A (\varrho dA) \mathbf{N}^T \cdot \mathbf{S}^T \cdot (\mathbf{T}^{kT} \cdot \dot{\mathbf{T}}^k)^0 \cdot \mathbf{S} \cdot \mathbf{N}_e \right] dy \quad (2.39.d)$$

$$\mathbf{M}_e^q = \int_{L_e} \left[\int_A (\varrho dA) \mathbf{N}^T \cdot \mathbf{S}^T \cdot \partial_{\ddot{q}} (\mathbf{T}^{kT} \cdot \ddot{\mathbf{R}}^k)^0 \right] dy \quad (2.39.e)$$

$$+ \int_{L_e} \left[\int_A (\varrho dA) \mathbf{N}^T \cdot \mathbf{S}^T \cdot \partial_{\dot{q}} (\mathbf{T}^{kT} \cdot \dot{\mathbf{T}}^k)^0 \cdot (\mathbf{r}_l^k + \mathbf{S} \cdot \mathbf{u}^{k0}) \right] dy$$

$$\mathbf{C}_e^q = \int_{L_e} \left[\int_A (\varrho dA) \mathbf{N}^T \cdot \mathbf{S}^T \cdot \partial_{\dot{q}} (\mathbf{T}^{kT} \cdot \dot{\mathbf{R}}^k)^0 \right] dy \quad (2.39.f)$$

$$+ \int_{L_e} \left[\int_A (\varrho dA) \mathbf{N}^T \cdot \mathbf{S}^T \cdot \partial_{\dot{q}} (\mathbf{T}^{kT} \cdot \dot{\mathbf{T}}^k)^0 \cdot (\mathbf{r}_0 + \mathbf{S} \cdot \mathbf{u}^{k0}) \right] dy$$

$$+ \int_{L_e} \left[\int_A (\varrho dA) \mathbf{N}^T \cdot \mathbf{S}^T \cdot 2 \cdot \partial_{\dot{q}} (\mathbf{T}^{kT} \cdot \dot{\mathbf{T}}^k)^0 \cdot \mathbf{S} \cdot \dot{\mathbf{u}}^{k0} \right] dy$$

$$\mathbf{K}_e^q = \int_{L_e} \left[\int_A (\varrho dA) \mathbf{N}^T \cdot \mathbf{S}^T \cdot \partial_q (\mathbf{T}^{kT} \cdot \ddot{\mathbf{R}}^k)^0 \right] dy \quad (2.39.g)$$

$$+ \int_{L_e} \left[\int_A (\varrho dA) \mathbf{N}^T \cdot \mathbf{S}^T \cdot \partial_q (\mathbf{T}^{kT} \cdot \dot{\mathbf{T}}^k)^0 \cdot (\mathbf{r}_l^k + \mathbf{S}^0 \cdot \mathbf{u}^{k0}) \right] dy$$

$$+ \int_{L_e} \left[\int_A (\varrho dA) \mathbf{N}^T \cdot \mathbf{S}^T \cdot 2 \cdot \partial_q (\mathbf{T}^{kT} \cdot \dot{\mathbf{T}}^k)^0 \cdot \mathbf{S}^0 \cdot \dot{\mathbf{u}}^{k0} \right] dy$$

$$\mathbf{Q}_e = - \int_{L_e} \left[\int_A (\varrho dA) \mathbf{N}^T \cdot \mathbf{S}^T \cdot (\mathbf{T}^{kT} \cdot \ddot{\mathbf{R}}^k)^0 \right] dy \quad (2.39.h)$$

$$- \int_{L_e} \left[\int_A (\varrho dA) \mathbf{N}^T \cdot \mathbf{S}^T \cdot (\mathbf{T}^{kT} \cdot \dot{\mathbf{T}}^k)^0 \cdot (\mathbf{r}_l^k + \mathbf{S} \cdot \mathbf{u}^{k0}) \right] dy$$

$$- \int_{L_e} \left[\int_A (\varrho dA) \mathbf{N}^T \cdot \mathbf{S}^T \cdot 2 \cdot (\mathbf{T}^{kT} \cdot \dot{\mathbf{T}}^k)^0 \cdot \mathbf{S} \cdot \dot{\mathbf{u}}^{k0} \right] dy$$

$$- \int_{L_e} \int_A (\varrho dA) \mathbf{N}^T \cdot \mathbf{S}^T \cdot \mathbf{S} \cdot \dot{\mathbf{u}}^{k0} dy - \mathbf{K}_e \cdot \hat{\mathbf{u}}^{k0} + \int_{L_e} \mathbf{N}^T \cdot \mathbf{Q} dy$$

2.1.3.5. Multi-body constraint equations

Kinematic constraints are applied to the end nodes of connected bodies/sub-bodies, as shown in Fig. 2.5, where $P2$ end nodes of the sub-bodies (sb) 1 and 3, are connected to $P1$ node of sub-body 2. If two sub-bodies are rigidly connected to each other, one sub-body (node) defines the kinematics (in the example sub-body 1) and the other provides reaction loads. These reactions loads (3 forces and 3 moments) are applied as external point forces/moments to the node which defines the kinematics.

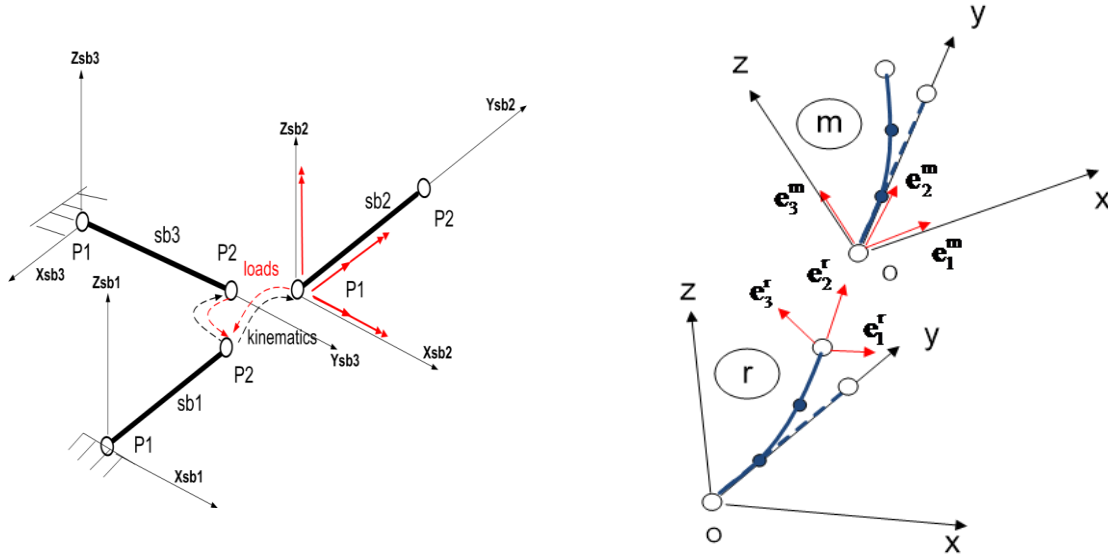


Figure 2.5: Example of constraint equations applied at the end nodes of connected two connected sub-bodies. **Figure 2.6:** Definition of unit bases e_i^r and e_i^m of two connected sub-bodies.

For two rigidly connected bodies/sub-bodies sbr and sbm, 3 translation and 3 rotation non-linear constraint equations are defined:

$$\mathbf{r}_G^r(P1 \text{ or } P2) = \mathbf{r}_G^m(P1 \text{ or } P2) \quad (2.40)$$

$$\boldsymbol{\theta}_r^{r,m} = \text{const.}, \text{ relative angle between } P1 \text{ or } P2 \text{ of sbr and } P1 \text{ or } P2 \text{ of sbm}$$

where \mathbf{r}_G in Eq. 2.40 is given by Eq. 2.23, while $\boldsymbol{\theta}_r^{r,m} = (\theta_{r1}^{r,m}, \theta_{r2}^{r,m}, \theta_{r3}^{r,m})^T$ is a column matrix containing relative rotation angles between connected nodes with respect to the 3 local axes of sbr. The above combination of connections covers all possible assemblies of connected sub-bodies realizing multiple load path configurations.

The relative angles $\theta_{ri}^{r,m}$ are given by [87]:

$$\begin{aligned} \cos \theta_{r1}^{r,m} (\mathbf{e}_2^r \cdot \mathbf{e}_3^m) - \sin \theta_{r1}^{r,m} (\mathbf{e}_3^r \cdot \mathbf{e}_2^m) &= 0 \\ \cos \theta_{r2}^{r,m} (\mathbf{e}_3^r \cdot \mathbf{e}_1^m) - \sin \theta_{r2}^{r,m} (\mathbf{e}_1^r \cdot \mathbf{e}_3^m) &= 0 \\ \cos \theta_{r3}^{r,m} (\mathbf{e}_1^r \cdot \mathbf{e}_2^m) - \sin \theta_{r3}^{r,m} (\mathbf{e}_2^r \cdot \mathbf{e}_1^m) &= 0 \end{aligned} \quad (2.41)$$

where e_i^r and e_i^m are two unit vector bases defining the local co-ordinate systems of the connected nodes of the sub-bodies r and m respectively (see Fig. 2.6).

It is noted that vectors e_i appear as columns in the rotation matrix T , when referring to $P1$ or as columns in $T \cdot T_l$ where:

$$T_l = \begin{bmatrix} 1 & -\theta_z(P2) & \theta_y(P2) \\ \theta_z(P2) & 1 & -\theta_x(P2) \\ -\theta_y(P2) & \theta_x(P2) & 1 \end{bmatrix}$$

When referring to $P2$, the definition of T_l implies that local deflection angles at the end node $P2$ are small.

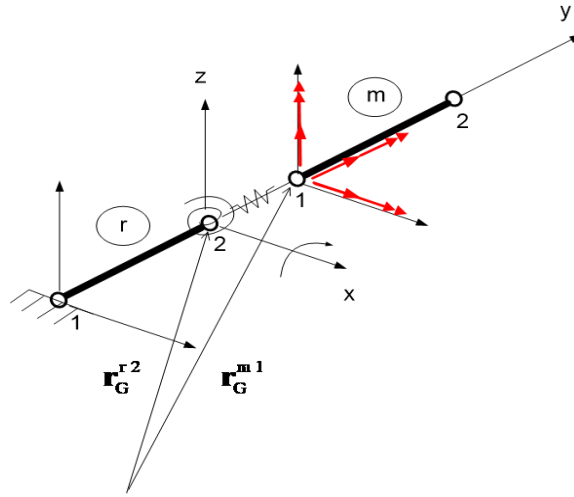


Figure 2.7: Free or elastic constraint equations.

For the simulation of a free or elastic constraint equation between two sub-bodies r and m (as shown in Fig. 2.7), the following conditions are satisfied:

$$\begin{aligned} & k_{x,y,z}^t [(T^r)^T \cdot r_G^r(P2) - (T^r)^T \cdot r_G^m(P1 \text{ or } P2)]_{x,y,z} + \\ & d_{x,y,z}^t [(T^r)^T \cdot \dot{r}_G^r(P2) - (T^r)^T \cdot \dot{r}_G^m(P1 \text{ or } P2)]_{x,y,z} = F_{x,y,z}^R \end{aligned} \quad (2.42)$$

$$k_{x,y,z}^r [\theta_r^{r,m} - \theta_{r0}^{r,m}]_{x,y,z} + d_{x,y,z}^r [\dot{\theta}_r^{r,m}]_{x,y,z} = M_{x,y,z}^R$$

where, $k_{x,y,z}^t$ and $d_{x,y,z}^t$ are the linear and $k_{x,y,z}^r$ and $d_{x,y,z}^r$ are the angular stiffness and damping properties of the elastic connection, $F_{x,y,z}^R$ and $M_{x,y,z}^R$ are the reaction loads at the connection point and $\theta_{r0}^{r,m}$ is the initial relative angle of the connected sub-bodies.

Along with the relative rotation angles between sub-bodies, the global angular velocities of the sub-body r , expressed with respect to its local co-ordinate system can be calculated through:

$$\mathbf{T}^{rT} \cdot \dot{\mathbf{T}}^r = \begin{bmatrix} 0 & -\dot{\theta}_{l3}^r & \dot{\theta}_{l2}^r \\ \dot{\theta}_{l3}^r & 0 & -\dot{\theta}_{l1}^r \\ -\dot{\theta}_{l2}^r & \dot{\theta}_{l1}^r & 0 \end{bmatrix} \quad (2.43)$$

where $\dot{\boldsymbol{\theta}}_l^r = (\dot{\theta}_{l1}^r, \dot{\theta}_{l2}^r, \dot{\theta}_{l3}^r)^T$ is the vector of global angular velocity of sbr expressed with respect to the local co-ordinate system of the sub-body.

It is noted that reaction loads $\mathbf{Q}^R = (\mathbf{F}^R, \mathbf{M}^R)^T$ where $\mathbf{F}^R = (F_x^R \ F_y^R \ F_z^R)^T$ and $\mathbf{M}^R = (M_x^R \ M_y^R \ M_z^R)^T$ are the vectors of the reaction force and reaction moments at the connection points, can be expressed as linear functions of the local deflection dofs $\hat{\mathbf{u}}$ and the global = \mathbf{q} dofs respectively of the sub-body m and its element (e) on which reaction loads are calculated using linearized matrices of Eq. 2.39.

$$\begin{bmatrix} \mathbf{Q}^R(1) \\ \mathbf{Q}^R(2) \end{bmatrix}^{m(e)} = \mathbf{M}_e \delta \ddot{\mathbf{u}}^{m(e)} + \mathbf{C}_e^a \delta \dot{\mathbf{u}}^{m(e)} + (\mathbf{K}_e + \mathbf{K}_e^a) \delta \hat{\mathbf{u}}^{m(e)} \\ + \mathbf{M}_e^q \delta \ddot{\mathbf{q}}^m + \mathbf{C}_e^q \delta \dot{\mathbf{q}}^m + \mathbf{K}_e^q \delta \mathbf{q}^m - \mathbf{Q}_e \quad (2.44)$$

where $\mathbf{Q}^R(1)$ and $\mathbf{Q}^R(2)$ are the reaction loads on node 1 and 2 of any (e) FEM element (matrix 12×1) of sub-body m .

2.1.3.6. Aero-elastic coupling

Aero-elastic coupling consists of the interaction between the aerodynamic and elasto-dynamic modules within every time step of the numerical process. In order to materialize such an interaction, there are two different options of similar fidelity. The first one (full coupling) is to combine the two systems and solve them as one; alongside with their off-diagonal coupling terms. There is a formulation issue when combining everything in one system, that one should mention. The flow equations are 1st order in time and therefore the structural equations must be recast (the size however doubles) in first order state-space form. An advantage is that the system may reveal coupled aero-elastic modes and their corresponding damping. Alternatively, the two systems can be solved separately. Internal iterations are required in both formulations. In the first one, until the unified non-linear aero-elastic system converges. In the second approach until convergence is achieved for both systems. It is also noted that in the second approach, within every internal iteration, compatibility information will be exchanged between the systems (strong coupling). In this way, it is easy to interchange between various aerodynamic or structural models of varying fidelity. Even though / in any case, every pair of models will need an interface protocol of its own.

In the strong coupling context, the aerodynamic code will have to feed the elasto-dynamic module with loads, whereas the structural model will communicate kinematics to the aerodynamic one. More precisely, the distribution of the aerodynamic loads calculated by the aerodynamic model over the strips along the body reference aerodynamic line is fed to the structural dynamic module. In turn, the deformed coordinates of the reference line and the deflection velocities of the blade, calculated by the

structural analysis, are communicated to the aerodynamic module. This procedure is repeated within every time step until convergence of both the aerodynamic and elastic solution is attained.

The reference line of the aerodynamic loading is commonly chosen to be at the quarter-chord, $c/4$ line of the blade. The structural reference line is considered to be the one with respect to which structural properties of the blade are defined. In general, the two lines can be offset with respect to each other. Due to the above offset an extra twisting moment should be communicated when transferring loads from the aerodynamic line to the elastic line. The above offset must also be taken into account when transferring deflections and velocities from the elastic line to the aerodynamic line, as rotations around the structural axis induce translations at the $c/4$ points.

In general, the 1D discretization of the aerodynamic and structural reference lines is different. In the aerodynamic model, the reference line is divided into a number of aerodynamic strips over which aerodynamic loads are calculated and considered uniformly distributed. With regard to the structural model and in the multi-body context, the elastic line of a single blade can be shared among several connected sub-bodies, which in turn are discretized into a number of linear FEM elements. The above definitions for the aerodynamic strips, the structural elements and the corresponding grids are shown in Fig. 2.8. The correspondence of the aerodynamic and structural grids is defined based on the material co-ordinate s_0 in the un-deformed state (see Fig. 2.7). The material co-ordinate s_0 represents the arc-length that positions the point along the deformed reference it belongs and has a unitary numbering along the blade, no matter how many sub-bodies have been used to describe it. If the blade is straight, s_0 coincides with the radial y co-ordinate of the blade local system. If the blade is curved, s_0 is the arc length along the curved reference line (see Fig. 2.8). The need for introducing the material co-ordinate s_0 stems from the fact that when the blade is deformed the structural nodes are displaced in all directions and, depending on the deformation field, the length of the deformed blade changes (increases in case of pure tension, decreases in case of bending deflection).

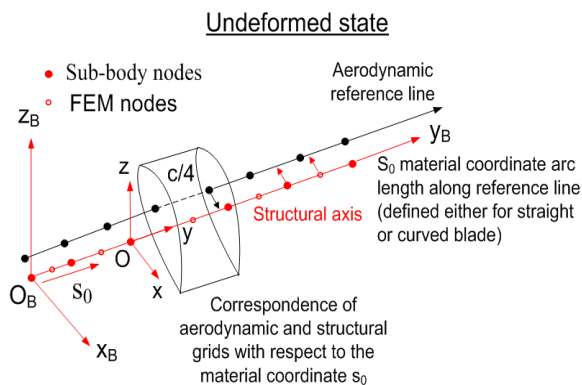


Figure 2.8: Definition of aero-dynamic and structural grids. Un-reformed state.

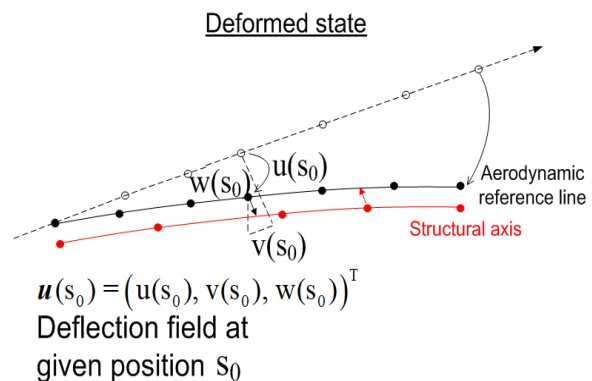


Figure 2.9: Definition of aero-dynamic and structural grids. Deformed state.

It is noted that appropriate interpolation procedure shall be defined in order to deal with the different grids and more particularly with the transfer of loads, deflections and deflection velocities from one grid

to the other. The transfer of loads from the aerodynamic grid to the structural grid is schematically illustrated in Fig. 2.10. Aerodynamic loads are integrated over all strips lying within one FEM of the structural grid. Partial integration is performed over the elements that are not entirely lying within the same FEM (see Fig. 2.10). The overall load is renormalized based on the length of the section and gets redistributed as piecewise constant load over it. The loads communicated to every section of the structural grid consists of span-wise (radial) distributions of a normal and tangential force components and the twisting moment contributed by the aerodynamic pressures. When a direct integration does not apply and look up tables are used, the twisting moment includes the quarter chord pitching moment plus the moment due to the offset between $c/4$ and the structural reference point.

The interpolation method presented here satisfies conservation of the total thrust force; however, it does not ensure full conservation of flap-wise moments. Nevertheless, the accuracy of the approach is reasonably good for the standard grid resolutions considered both in the aerodynamic and structural analysis.

Deflections and deflection velocities are calculated on the aerodynamic control points based on the degrees of freedom (dofs) of the neighboring elastic grid nodes and on the FEM interpolation functions (cubic for bending and linear for extension and torsion). As in the case of the loads, the offset between the two axes will generate additional displacement and linear velocity components induced by the rotational degrees of freedom.

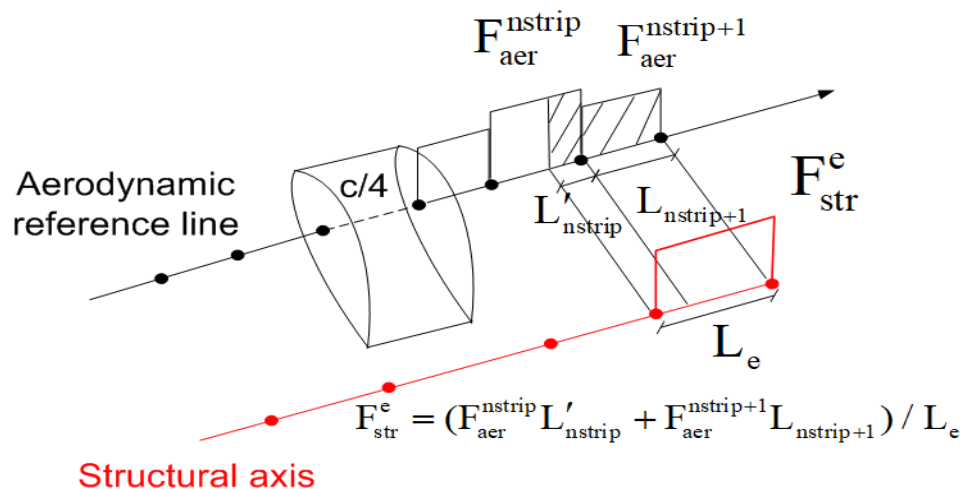


Figure 2.10: Interpolation of aero-dynamic loads to the structural grid.

2.2. Cross-sectional analysis tool

While in the early years of wind energy, i.e. before and immediately after World War II, wind turbine blades were manufactured from aluminum and wood, the blades of a modern multi-megawatt wind turbine are thin-walled multi-cell structures, made of fiberglass (TRIAX, BIAx and UNIAX) layers (see [52] and [88]). The use of composite materials offers many advantages, among which the low cost of

material and the low ratio of mass over strength. The extensive use of composite materials in aeronautical and wind energy applications, led to the establishment of composite mechanics theories while many numerical methods have been developed to support them. Among them, the most computationally intensive are based on 3D FEM [89],[90], while other more cost effective methods have been developed and presented in [91],[92],[93].

Many components in aeronautics as well as in wind energy (i.e. blades, shaft and tower), can be considered as one-dimensional beams, thereby making it possible to split the 3D problem into two lower order problems: i) the 1D problem which provides the internal resultant loads (internal forces and moments) along the beam, and ii) 2D cross-sectional analysis which has the dual purpose of deriving the equivalent properties that feed the 1D beam problem and on the other hand, of providing the stresses field over the section resulting from the application of corresponding load resultants. The above approach has been adopted by many of the well-known analysis packages (e.g. VABS [94] and BECAS [55]). The above models are based on asymptotic analysis, producing for each cross-section a full mass and stiffness matrix, which among other, describes every possible coupling arising between different deformation directions. In the above models, a 2D mesh is generated over every cross-section along the span of the beam, which accounts for the geometric and composite material lay-up details of the section. Equations of elasticity are solved on this mesh using FEM discretization and either stresses field for given input resultant loads or cross-sectional beam like properties are provided as output, feeding any aero-elastic solver, for example the hGAST code, which has been described in-depth in the previous section. 2D FEM models are able to handle a large range of cross-section geometries and determine the coupling effects due to the in-homogeneous and anisotropic nature of the material distributed along the blade span. Different regions over the section can be defined, having different lamination sequences (wall thickness, orientation of the fibers and material type of each layer) and different mechanical properties per anisotropic composite layer. The main advantage of the approach is that it substantially suppresses the computational cost of the 3D analysis to some seconds/minutes, while the output results remain sensitive to the computational mesh (both density and quality).

Another alternative is to use analytical thin-walled (thin-lamination) theory [95], referred to as L/T. Computation of equivalent beam properties in these methods is based on the consistent integration of the structural properties over the walls and laminates (in case of composite structures as the blades) of the cross-section. This approach, is an ideal choice for optimization purposes, because although less accurate than the FEM approach (since it is based on many approximations such as the anisotropy of material or the multi-cell theory), is faster and insensitive to meshing parameters and therefore more robust. In the present multi-disciplinary optimization framework the latter approach has been adopted mainly due to its robustness, which is an indispensable when large numbers of evaluations are required.

2.2.1. Lamination theory

Thin Lamination Theory, is adopted in the calculation of the structural cross sectional properties along the blade span. It is based on previous works by University of Patras [96],[97] and it has been further

upgraded to include an additional shear web (three in total) and to account for the effect of the shape of the cross-sectional geometry on shear rigidity properties. The developed tool provides fully populated stiffness matrices, taking into account all material driven coupling effects and it can be used for the modelling of blades with rotated material plies by angle θ (see Fig. 2.11) with respect to their axis (i.e. material BTC) or blades with shifted spar caps (i.e. geometry FEC). In addition, this tool provides the stresses distribution and the Tsai-Hill failure criterion [98] over the plies of the cross-section, based on the resultant sectional loads provided at a reference position (i.e. ultimate loads calculated through aero-elastic simulations of the turbine).

Wind turbine blades are constructed by composite laminates that form a thin-walled shell structure (i.e. the cross-section). Each laminate is consisted of various material layers (i.e. TRIAX, BIAX, UNIAX and BALSA) as shown in Fig. 2.11. Furthermore, every cross-section consists of a number of cells, depending on the number of webs (see Fig. 2.12). Specifically, for the cross-section shown in the last figure (see Fig. 2.12) in which three webs are considered, four cells (closed loops) are defined in total. Each cell is formed by a sequence of segmented elements over the skin and the webs of the cross-section. In the present section, i, j and k denote the index of a cell, laminate element and material layer, whereas N_{cell} , N_{el} and N_{layer} denote the total number of cells, elements and material layers respectively. Three coordinate systems (c.s.) are define, i) the material layer c.s. $x_L y_L z_L$ (x_L represents the fiber direction), ii) the laminate c.s. xyz and iii) the cross-section c.s. XYZ , as shown in Fig. 2.12.

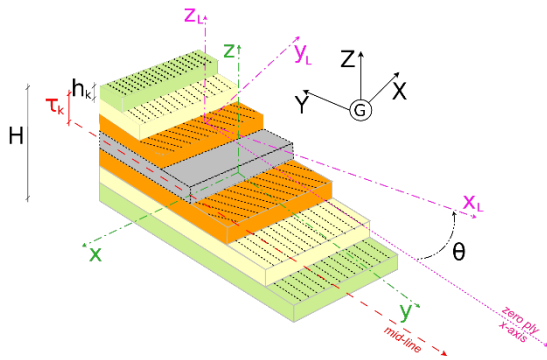


Figure 2.11: Typical material layers layout of a composite thin-walled laminate of wind turbine blade's shell.

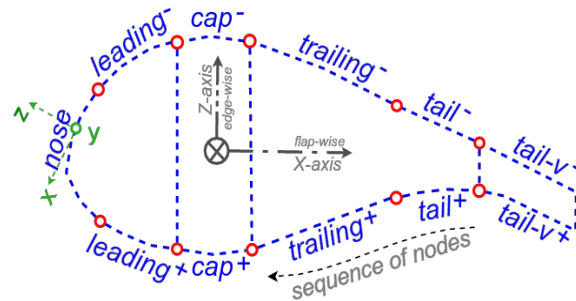


Figure 2.12: Definition of the cross-section regions of the DTU-10MW RWT blade.

For every material layer Hooke's law is written with respect to the material layer coordinate system $x_L y_L z_L$ (shown in figure 2.11) in the form:

$$\boldsymbol{\sigma} = \mathbf{q}_L \cdot \boldsymbol{\varepsilon} = \begin{bmatrix} E_{11} & 0 & 0 \\ 0 & G_{13} & 0 \\ 0 & 0 & G_{12} \end{bmatrix} \cdot \boldsymbol{\varepsilon} \quad (2.45)$$

In above equation, \mathbf{q}_L is the local stiffness matrix, $\boldsymbol{\varepsilon}$ is the strains tensor, $\boldsymbol{\sigma}$ the stresses tensor, E_{11} is the modulus of elasticity along the fiber longitudinal direction, while G_{13} and G_{12} are the out-of-plane-longitudinal and in-plane shear moduli respectively.

In order to determine stiffness properties with respect to the local skin coordinate system xyz , the rotated by θ stiffness matrix \mathbf{q}_c is calculated (for more information, see [97]). Then, by integrating the stiffness properties along the thickness of the skins and webs (under the assumption of a sufficiently thin shell) the following 3×3 stiffness matrices associated with \mathbf{A}^j , bending \mathbf{D}^j and their coupling \mathbf{B}^j of the j^{th} element of a laminate are obtained:

$$\mathbf{A}^j = \sum_{k=1}^{N_{layer}} \mathbf{q}_{ek} h_k \quad \mathbf{B}^j = \sum_{k=1}^{N_{layer}} \mathbf{q}_{ck} h_k \bar{\tau}_k \quad \mathbf{D}^j = \sum_{k=1}^{N_{layer}} \mathbf{q}_{ck} h_k \left(\frac{h_k^2}{12} + \bar{\tau}_k^2 \right) \quad (2.46)$$

In Eq. 2.46, h_k is the thickness of the k^{th} layer and is the distance of the mid-line of the k^{th} layer from the mid-line of the skin (see Fig. 2.11) given by:

$$\bar{\tau}_k = \begin{cases} \frac{h_k - H}{2} & , for k = 1 \\ \bar{\tau}_{k-1} + \frac{h_{k-1} + h_k}{2} & , for k = 2, 3, \dots, N_{layer} \end{cases} \quad (2.47)$$

where H denotes the total thickness of the laminate.

By integrating laminate stiffness properties of Eq. 2.46 along the skins and the webs of the cross-section, the stiffness matrix \mathbf{K} , relating resultant section forces and moments \mathbf{F} , \mathbf{M} with global section strain and curvature characteristics $\boldsymbol{\varepsilon}$, $\boldsymbol{\kappa}$, is obtained with respect to the cross-section coordinate system XYZ :

$$\begin{Bmatrix} \mathbf{F} \\ \mathbf{M} \end{Bmatrix} = \mathbf{K} \begin{Bmatrix} \boldsymbol{\varepsilon} \\ \boldsymbol{\kappa} \end{Bmatrix} \Rightarrow \begin{Bmatrix} F_x \\ F_y \\ F_z \\ M_x \\ M_y \\ M_z \end{Bmatrix} = \begin{bmatrix} K_{11}^A & K_{12}^A & K_{13}^A & K_{11}^B & K_{12}^B & K_{13}^B \\ & K_{22}^A & K_{23}^A & K_{21}^B & K_{22}^B & K_{23}^B \\ & & K_{33}^A & K_{31}^B & K_{32}^B & K_{33}^B \\ & & & K_{11}^D & K_{12}^D & K_{13}^D \\ & & & & K_{22}^D & K_{23}^D \\ & & & & & K_{33}^D \end{bmatrix} \begin{Bmatrix} \varepsilon_x \\ \varepsilon_y \\ \varepsilon_z \\ \kappa_x \\ \kappa_y \\ \kappa_z \end{Bmatrix} \quad (2.48)$$

Indicative expressions for the bending and torsional stiffness elements of the \mathbf{K} matrix of Eq. 2.48 are given below:

$$\begin{aligned} K_{11}^D &= EI_{xx} = \sum_{j=1}^{N_{el}} \ell_j (A_{11}^j Z_j^2 - 2B_{11}^j Z_j \cos \theta_j + D_{11}^j X_j^2) \\ K_{12}^D &= EI_{xy} = x_{sc} K_{14} - z_{sc} K_{34} + \sum_{j=1}^{N_{el}} \ell_j (-A_{13}^j A h^j Z_j + B_{13}^j (A h^j \cos \theta_j - 2Z_j) + 2D_{13}^j \cos \theta_j) \\ K_{13}^D &= EI_{xz} = \sum_{j=1}^{N_{el}} \ell_j (A_{11}^j X_j Z_j + B_{11}^j (Z_j \sin \theta_j - X_j \cos \theta_j) - D_{11}^j \sin \theta_j \cos \theta_j) \\ K_{22}^D &= GJ = z_{sc} G_x A_x + x_{sc} G_z A_z + \sum_{j=1}^{N_{el}} \ell_j (A_{33}^j (A h^j)^2 + 4B_{33}^j A h^j + 4D_{33}^j) \end{aligned} \quad (2.49)$$

where x_{sc} and z_{sc} denote the position of the shear center with respect to the cross-section c.s. The reader can find more details concerning the derivation of the equations of L/T method in appendix B.

2.2.2. Timoshenko shear factor prediction method

The original form of L/T, as presented in section 2.2.1. and detailed in appendix B, does not account for the shear factors related to the shape of the cross section geometries. The effect of the shear factors can be introduced using the Saint-Venant's semi-inverse method, which provides two distinct shear factors k_x and k_z with respect to x and z shear directions respectively, for an arbitrary cross-section shape made of isotropic material (the reader is cited to [99] for details). The two shear factors directly affect the diagonal terms of the stiffness matrix that represent transverse shear rigidity, $K_{11}^A = G_x A$ and $K_{33}^A = G_z A$, while they indirectly affect all shear related stiffness elements – all this terms are indicated in the Eq. 2.48 with red color. The estimated shear factors are applied within the cross-sectional analysis tool, so that shear center and coupled stiffness terms, as well as the stresses field, are consistently calculated by taking into account the corrected for the shape of the geometry shear properties. Apart from the isotropic material assumption, in this analysis the webs are not taken into consideration. However their effect on shear factors is minor as demonstrated in the following paragraph for the case of a wind turbine blade. Details on the implementation of the method can be found in appendix B.

2.2.3. Evaluation of the shear factor prediction method

In the following, predictions of the beam stiffness properties (integrated over different cross sections) for the blade of the reference wind turbine of the present thesis, DTU-10MW RWT, are compared against predictions by running BECAS tool. In connection with the previous discussion on shear factor calculations, in Fig. 2.13 the model predictions of the span-wise distribution of the flap-wise (along z -axis) shear rigidity term K_{33}^A (i.e. direct effect of k_z) and of the shear force-torsion coupling term K_{32}^B (i.e. indirect effect of k_z) of the DTU-10MW RWT blade are shown, with and without taking into account the application of the locally calculated shear factor. It is noted that in the present example the results pertain to cross-sections of varying geometry along the blade span, having non-uniform composite material. Application of the shear factor bridges the gap between the baseline L/T model and BECAS in the prediction of both stiffness properties. In line with the good agreement of the two models in the prediction of the shear-torsion stiffness term is also the agreement in the prediction of the shear center (both x - and z - co-ordinates) shown in Fig. 2.14 of section 2.2.5.

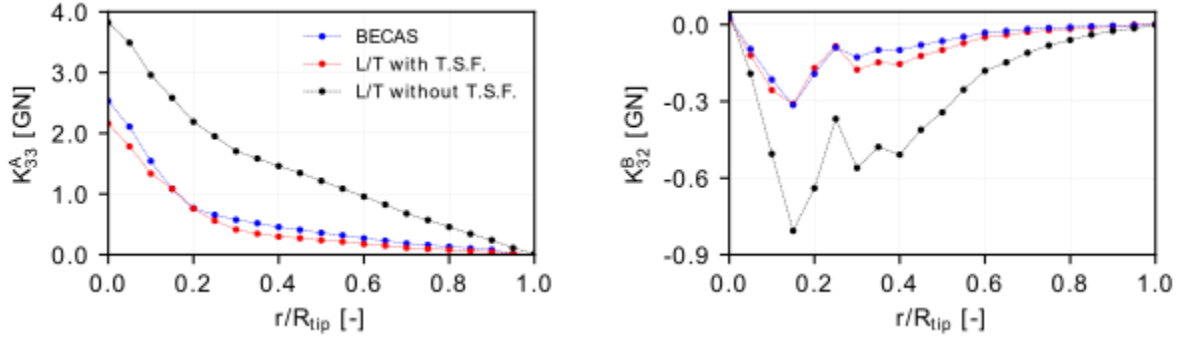


Figure 2.13: Span-wise distribution of the stiffness matrix elements mostly affected by the Timoshenko shear factors (T.S.F.); comparison between present work (L/T) and BECAS for the DTU-10MW RWT blade.

2.2.4. Cross-sectional stress analysis and equivalent stress criteria

Finally, the cross-sectional analysis tool can estimate the developing stresses, produced for a given set of internal loads $\{\mathbf{F} \ \mathbf{M}\}^T$, through inversion of Eq. 2.48 and calculation of the generalized strains $\{\boldsymbol{\varepsilon} \ \boldsymbol{\kappa}\}^T$. Then, the distribution of normal (σ_n) and shear (σ_s) stresses are calculated over the material laminates through application of Hook's law. The above two stresses are consolidated and related with the material strength (S_1 -longitudinal strength and S_2 -shear strength) through the Tsai-Hill failure criterion, by considering a material safety factor of $\gamma_m = 1.2$. Failure occurs for criterion values exceeding 1, whereas the criterion is given by:

$$f_{T/H} = \frac{\sigma_n^2}{S_1^2} - \frac{|\sigma_n \sigma_s|}{S_1^2} + \frac{\sigma_s^2}{S_2^2} \quad (2.50)$$

2.2.5. Thin lamination model application examples – DTU-10MW RWT blade analysis

The purpose of the current section is to verify the present tool (L/T) against BECAS, through comparisons of predicted beam properties, eigen-frequencies, loads and stresses considering as application example the DTU-10W RWT (for more information, see appendix A). This comparison indicates that, besides being cost effective, it is also a reliable tool which can be trusted for optimization analyses. During the verification of the tool, emphasis is put on the prediction of the shear rigidity parameters which are linked to the improvements performed in the original model and the cross-stiffness parameters (off-diagonal elements of the 6×6 stiffness matrix) which are responsible for the activation of the BTC and FEC cross-directional couplings. Both the methodology followed and the results described above, are part of the published work [49].

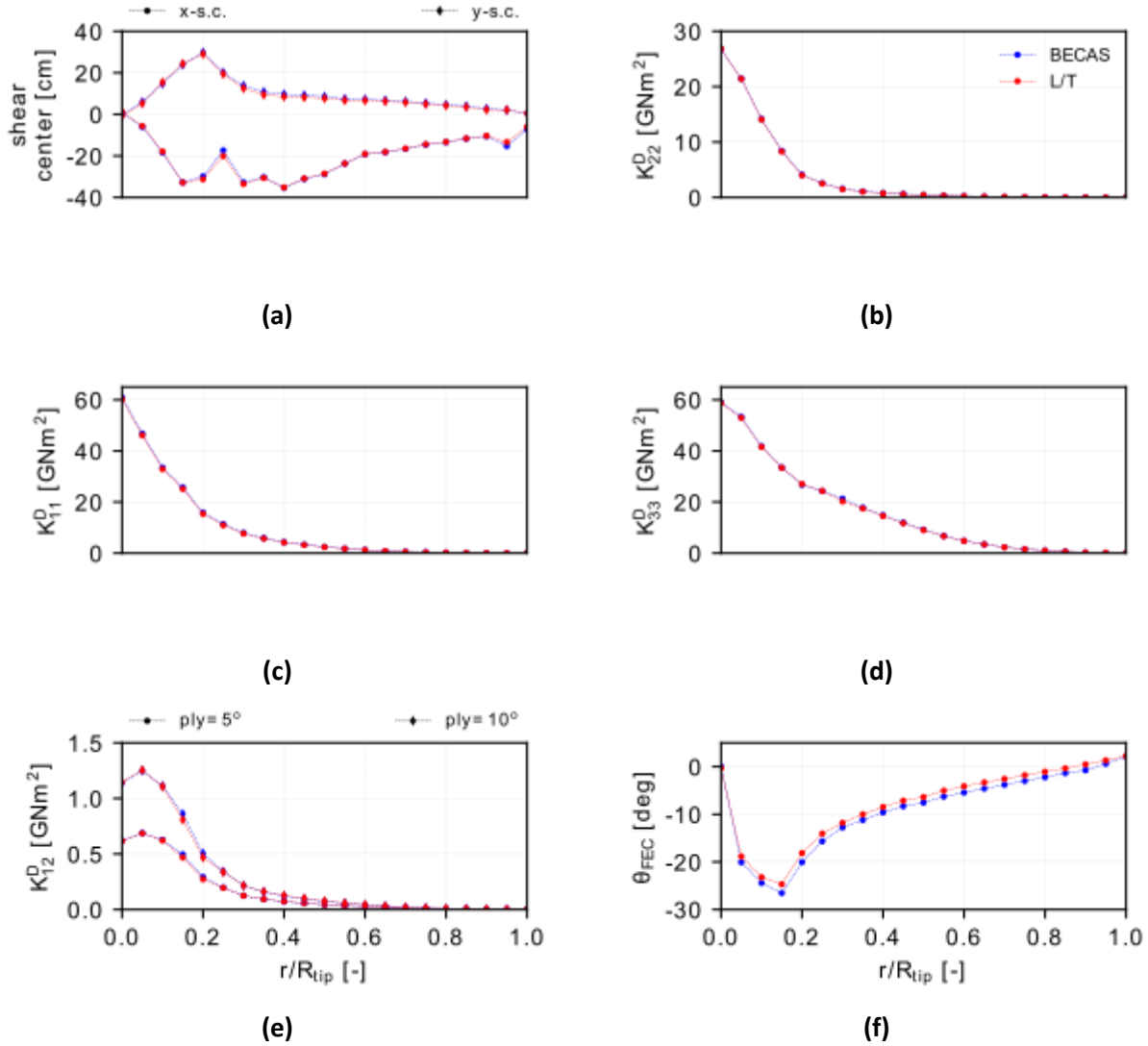


Figure 2.14: Span-wise distribution of basic sectional characteristics of the DTU-10MW RWT blade provided by present work (L/T) and BECAS: a) shear center, b) torsional stiffness, c) flap-wise bending stiffness, d) edge-wise bending stiffness, e) bending-torsion stiffness coupling and f) structural twist.

In Fig. 2.14, predictions by the two models of the span-wise distribution of the two bending stiffnesses K_{11}^D (flap-wise) and K_{33}^D (edge-wise), the torsion stiffness K_{22}^D and the two cross stiffness K_{12}^D and K_{13}^D are compared. The latter is represented by the so called “structural twist” angle given by the Eq. 2.51.

$$\theta_{FEC} = \frac{1}{2} \tan^{-1} \left[\frac{2K_{13}^D}{K_{11}^D - K_{33}^D} \right] \quad (2.51)$$

An almost excellent agreement is noted in the prediction of the diagonal elements of the stiffness matrix (K_{11}^D , K_{33}^D and K_{22}^D). What is more important though, is the good agreement obtained in the results of the cross stiffness terms. This is directly linked with the objective of the present work to assess aero-

elastic tailoring techniques dictated by material driven coupling. These terms are responsible for the activation of the couplings between flap-wise bending and torsion (K_{12}^D) and between flap-wise and edge-wise bending (K_{13}^D) and they determine the tailoring capacity of the structure (passive control authority). It is noted that K_{12}^D term in Fig. 2.14 is plotted for two different ply offset angles (5° and 10°) of the UNIAX material over the upper and lower caps of the spar-box. As expected, the increase in the ply offset angle from 5° to 10° leads to increased values of K_{12}^D all along the blade span. Small deviations of the order of $\sim 1^\circ$ are seen in the prediction of the structural twist angle θ_{FEC} . It is noted that the present comparison of θ_{FEC} predictions concerns the baseline blade with zero angle of the plies.

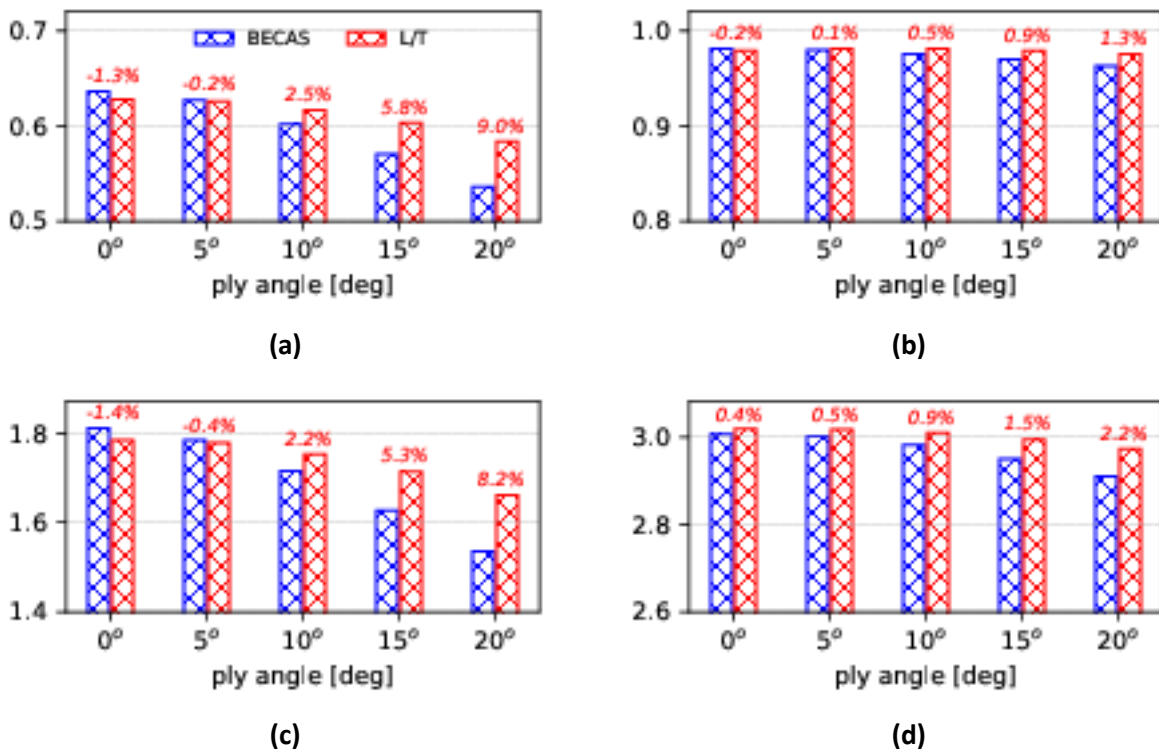


Figure 2.15: Effect of ply offset angle on the natural frequencies in [Hz] of the DTU-10MW RWT blade: (a) 1st flap-wise, (b) 1st edge-wise, (c) 2nd flap-wise and (d) 2nd edge-wise. Comparison between present work (L/T) and BECAS. Percentage relative differences with respect to BECAS are shown above the bars.

The comparison of the blade's lowest natural frequencies (of the 1st and 2nd flap-wise and edge-wise modes), using the above compared sets of beam data (generated by the present model and BECAS) is shown in Fig. 2.15 with parameter the ply offset angle of the UNIAX material over the caps. A very good agreement in all frequencies is obtained up to the ply angle of 10° . The maximum recorded difference is 2.5%, obtained in the first flapwise mode. Beyond 10° ply angle, deviations begin to grow, in particular in the prediction of the frequencies of the flap-wise modes. At the ply angle of 20° , the difference in the

two flap-wise frequencies is 9% in the first and 8.2% in the second, while the maximum difference in the two edge-wise frequencies is 2.2%. Apparently, the offset of the plies deteriorates the stiffness capacity of the blade in the flap-wise direction. The present model predicts a reduction in the flap-wise stiffness as the ply angle increases (seen through the reduction in the frequency of the flap-wise modes), however it underestimates the effect as ply angles increase, compared to BECAS. As will be made explicit in the sequel, ply offset angles greater than 10° are impractical for the reason that reduction in the flap-wise stiffness diminishes blades' ability to carry flap-wise loads. Therefore, the limitation of the present method to correctly predict K_{12}^D at high ply offset angles is not expected to have any important implications in the capability of the established procedure to predict bend-twist coupling effect on actual blade designs.

Table 2.1: Comparison between the present work (L/T) and BECAS of the ultimate loads distribution (forces are shown in $[kN]$ and moments in $[kNm]$) along the blade half span in case of extreme turbulence wind at $13m/s$ wind speed (safety factors γ_L applied).

r/R_{tip}	Edge-wise shear force			Extensional force			Flap-wise shear force		
	BECAS	L/T	diff.	BECAS	L/T	diff.	BECAS	L/T	diff.
0.0	-247	-245	-0.8%	1148	1145	-0.3%	1271	1268	-0.2%
0.1	-212	-211	-0.7%	1178	1175	-0.2%	1259	1259	+0.0%
0.2	-179	-178	-0.4%	1112	1110	-0.2%	1232	1234	+0.1%
0.3	-147	-147	-0.4%	990	988	-0.2%	1176	1177	+0.1%
0.4	-128	-128	-0.8%	841	842	+0.1%	1057	1056	-0.1%
0.5	-122	-122	+0.1%	661	659	-0.3%	907	910	+0.3%
r/R_{tip}	Flap-wise moment			Torsion moment			Edge-wise moment		
	BECAS	L/T	diff.	BECAS	L/T	diff.	BECAS	L/T	diff.
0.0	66997	66898	-0.1%	547	494	-9.6%	8160	8093	-0.8%
0.1	56049	55969	-0.1%	538	487	-9.6%	6182	6131	-0.8%
0.2	45352	45268	-0.2%	526	476	-9.5%	4511	4468	-1.0%
0.3	35161	35067	-0.3%	510	464	-9.1%	3121	3079	-1.4%
0.4	25740	25685	-0.2%	430	387	-9.8%	2604	2565	-1.5%
0.5	17652	17641	-0.1%	306	268	-12.4%	2043	1986	-2.8%

Next, ultimate loads (forces and moments) of the blade are predicted using again both sets of structural data (generated by L/T model and BECAS). They are compared in Table 2.1. Ultimate loads are derived through aero-elastic simulations of DLC-1.3 of the IEC-61400-1 standard at the wind speed of 13m/s , using hGAST tool. These conditions have been found to stress the RWT more, see appendix A. The above mentioned load case corresponds to normal operation of the turbine (power production mode) under extreme turbulence conditions. This load case, in particular at the wind velocity of 13m/s (close to rated wind velocity), has been identified in previous studies [100] as the most critical power production case that drives maximum loads on the blade. In Table 2.1 maximum instantaneous forces and moments along the blade span (up to mid-span) are compared for the two sets of beam data (safety factor $\gamma_L = 1.35$ has been applied to all loads in accordance with the provision of the IEC-61400-1 standard). The highest differences are noted in the torsion moment M_y (order of 10%). They are attributed to the combined effect of a small offset in the prediction of the mass center position and small deviations in the predicted mass distribution. Small differences up to a maximum of 2.8% are also noted in the edge-wise force F_x and the edgewise moment M_z . They are again due to deviations in the predicted mass. The agreement in the predicted flap-wise force F_x and moment M_x is almost perfect. The predicted maximum loads of Table 2.1 are fed back to both tools and equivalent stresses distributions are determined.

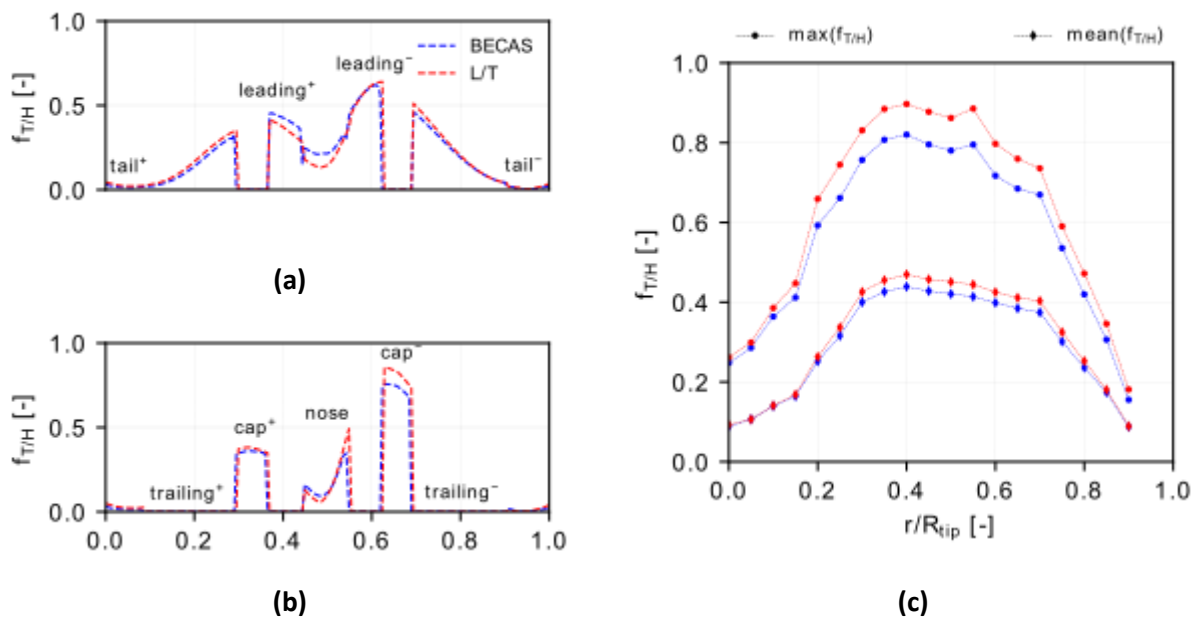


Figure 2.16: Stress analysis results; distribution of maximum and contemporary Tsai-Hill criterion values on the a) TRIAX and b) UNIAX material layers at the cross-section at $r/R_{tip} = 40\%$ and c) span-wise distribution of the maximum and averaged along the cross-section circumferential distribution Tsai-Hill criterion values. Cross-sectional loads are taken from Table 2.1.

Equivalent stresses distributions (cross-section-wise and span-wise) in terms of Tsai-Hill criterion of Eq. 2.50, are provided in Fig. 2.16a and b. This figures compare “cross-section-wise” (i.e. along the cross-

section perimeter) predictions by the two models (L/T and BECAS) of the maximum Tsai-Hill values on the “TRIAX” and “UNIAX” materials at the radial position $r/R_{tip} = 40\%$. It is noted that the differences between the two models is due to the way that BECAS handles the transition adjacent between regions. BECAS can not handle the step change in the thickness or the material and applies a ramp type transition adding this material that in reality does not exist. Fig. 2.16c compares span-wise distributions of the mean and maximum Tsai-Hill values over different cross-sections along the blade span. It is noted that higher stresses (Tsai-Hill exceeding 0.8) are obtained over the span-wise range of 30% – 60%. Both models predict that the absolute maximum Tsai-Hill value is obtained at the 40% cross-section. As seen in Fig. 2.16 this occurs on “UNIAX” material of the cap on the suction side of the blade. Comparing cross-sectional equivalent stresses distribution, it is seen that a fair agreement between the two models is obtained over the trailing edge area and the pressure side cap, while some bigger deviations ($\sim 15\%$) are noted at the L/E-nose region and the suction side cap. The L/T model predicts about 10% higher equivalent stress on the cap of the suction side. Given that the maximum stress occurs on the cap of the suction side, this 10% difference is also transferred to the overall maximum equivalent stress predicted by the two models.

2.3. Overall wind turbine cost model

A prerequisite for the feasibility study and assessment of innovative wind turbine concepts and new technologies (material, control etc.) is the existence of models that estimate the cost of the wind turbine sub-components and eventually of the wind turbine as a whole. Such models have been proposed in the literature in numerous scientific papers [101], books [102] and technical reports [103]. In recent years cost models are becoming more and more detailed, including information about the cost of the different material used in the manufacturing of the sub-components, information about labor cost etc. The purpose of the newly developed cost models is to replace existing over-simplified global sub-component cost functions used in the past (e.g. based on quantities such as the blade or turbine total mass or rotor diameter) [49],[100]. Apart from the wind turbine industry, which focuses on developing as accurate as possible cost models for obvious reasons, interest in the above models is also shown by the research community, as it is an ingredient of utmost importance for multi-disciplinary optimization tools. Most existing wind turbine design optimization frameworks (see for example [42] and [104]), include cost models of the various components, usually based on simple semi-empirical mathematical formulae (e.g. for the generator, the gearbox, and the tower) or even on more elaborate calculation processes (e.g. for the blades) due to the inherent complexity of their design and manufacturing. The aim of integrating cost models within multi-disciplinary optimization processes is to set objective functions which are directly related to cost metrics such as: compressing CAPEX like in [105], or minimizing the LCoE like in [106], which also stresses out other than the manufacturing costs, such as: the Balance of Plant (BoP) cost, the maintenance and Operation EXpenses cost (OPEX) and eventually weights all these costs by the Annual Energy Produced (AEP).

Next, a complete cost model is described, including the step-by-step detailed costing, in 2019 USA dollars, of multi-megawatt wind turbine blades as well as simpler formulae for other individual components, with the aim to determine Levelized Cost of Electricity (LCoE).

2.3.1. Cost model of modern wind turbine

In the last decade, three interesting wind turbine costing models have been proposed in the literature. The simplest model, has been proposed in the Wind Energy Handbook [107] uses simple mathematical up-scaling expressions based on a reference wind turbine. This model has been adopted by the current thesis to determine the cost of the most heavy and bulky components of the wind turbine; the tower, the gearbox and the generator. The second model, developed by NREL [108] in 2006 (henceforth referred as NREL-2006), describes the mass or cost of the various components of the wind turbine through semi-empirical exponential expression which relate them with the radius of the rotor. In this work, the above model is used to estimate the cost of the complementary components of the rotor (hub, pitch mechanism and spinner) as well as the labor cost of the manufacturing of the blade. Finally, due to the complexity of the blade construction, a variant of the costing procedure described by NREL [109] in 2019 (hereafter NREL-2019) has been incorporated into the present study.

2.3.1.1. Cost of tower, gearbox and generator

In 2011, a cost model of the various components of a wind turbine has been proposed in [107]. This model, is based on a known already costed reference wind turbine (which is denoted by '*ref*') and various empirical scaling relations for the various sub-components. Briefly, for the rotor and tower a mathematical expression considering a fixed cost part plus another cost component scaling with rotor diameter, following the "3rd power" rule is proposed. This approach has been used in previous research projects [18] and it is based on the partial correlation of cost (and mass) with the size of the rotor. At the same time, for the gearbox and generator, formulae involving the ratios of power and rotational speed, while the cost of the remaining components (i.e. referred as other parts like the foundation and electrical systems) is considered equal to 80% of the total cost of the rotor, gearbox and generator (this approach has been adopted in [18]).

The present thesis adopts as reference wind turbine the onshore 1.5MW developed and costed in the technical report of [108] and presented in Table 2.2. Also, this thesis, used the relations that have been proposed by the Wind Energy Handbook, for the tower, gearbox and generator, with minor modifications on the value of the exponent ($\gamma_{s-u} = 2.16$).

$$Tower = Tower^{ref} \left[0.90 \times \left(\frac{R_{tip}}{R_{tip}^{ref}} \right)^{\gamma_{s-u}} + 0.10 \right] \quad (2.52)$$

$$Gearbox = Gearbox^{ref} \frac{P\Omega^{ref}}{P^{ref}\Omega} \quad (2.53)$$

$$Generator = Generator^{ref} \frac{P\Omega^{ref}}{P^{ref}\Omega} \quad (2.54)$$

where, P and Ω denote the nominal power and rotation speed respectively.

Table 2.2: Basic parameters of 1.5MW RWT described in [108] and the costing of its main components.

<i>Parameters</i>	
Rated power	1.5MW
Rated omega	20.5rpm
Radius	35m
Hub height	65m
<i>Cost of components [in 2019 USA \$]</i>	
Rotor	336540
Tower	208740
Gearbox	217260
Generator	139160

2.3.1.2. Cost of labor, hub, pitch mechanism and spinner

An alternative approach is proposed by NREL-2006, in which the cost of the blade is estimated as a function of its length raised to the third power. In this report (NREL-2006), the labor cost is approximated by the expression to Eq. 2.55, with the exponent close to $\gamma_{L\&O} = 2.52$.

$$Labor \ \& \ Others = 3.898 \times R_{tip}^{\gamma_{L\&O}} \quad (2.55)$$

The above model, in addition to the cost of the blade and construction labor, is able to provide estimates, through simple mathematical relationships, for the other components of the rotor: hub, pitch mechanism and spinner.

$$hub = 5.757 \times Blade \ Mass + 34280.61 \quad (2.56)$$

$$pitch \ mechanism = 4.303 \times R_{tip}^{2.658} \quad (2.57)$$

$$spinner = 292.65 \times R_{tip} - 4116.84 \quad (2.58)$$

2.3.1.3. Cost of blade manufacturing

The complex structure of modern wind turbine blades raised the need for more elaborate cost models. The National Renewable Energy Laboratory (NREL), developed such a complex model, in 2019 and is presented in the technical report NREL-2019 [109]. This report describes in-detail the manufacturing process of the blade and it can provide accurate estimates of the billing of the materials, the cost of consumables, the number of labour hours and the cycle time based on industry data. The above tool is coded in Python and it is freely available in the repository of the Wind Plant Integrated System Design and Engineering Model (WISDEM) framework [56]. The current work has adopted a variation of the procedure for determining the cost of blade manufacturing and consumables, relative to that described in NREL-2019. This variant includes the grouping of various consumables into three categories (proportional to blade radius, surface area of molds and the outer surface of the blade), as well as simplifying the estimations, as for example the distinction of adhesives suitable for the skin (trailing and leading edge) or the webs.

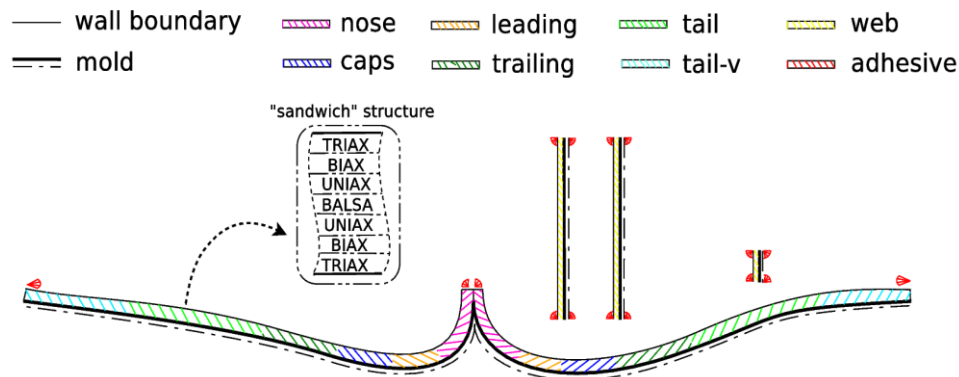


Figure 2.17: The industrial construction of the modern wind turbine blades is based on VARTM modeling and involves placing fiberglass with a resin mixture and glue on molds.

The blades of the multi-megawatt wind turbines consist of thin-walled cross-sections of two or three cells and are usually fabricated using fiberglass and infusion of resin, the shape of which is determined by a mold (see Fig. 2.17). The skins of the blades form a “sandwich” structure with the TRIAX, BIAx and UNIAX materials placed in symmetrical positions on either side of the Balsa core. So, estimating the mass/costing of the materials used to build the blades is an easy task, when the layout of the blade inner structure is known (thickness of material layers). This is done considering the properties and costs of the primary raw materials presented in Table A.3 of the appendix A. However, the conventional manufacturing approach also includes the building of a matrix from epoxy, made of resin and hardener. Both resin and hardener are in liquid form, but when mixed in a given mass ratio, they initiate an

exothermic chemical reaction that brings them to a solid state. In this model, the volume of the matrix that will be needed is considered as the sum of the volumes of the primary materials (TRIAX, BIAx and UNIAX) multiplied by one minus the volume fraction of each material:

$$V_{matrix} = V_{fiberglass} \times (1 - F_{FV}) \quad (2.59)$$

In the sketch of the blade cross-section in Fig. 2.17 (two open halves of the mold), the locations where adhesive is applied are shown in red shade. So, by defining an “adhesive area” over the 2D plane of $70mm \times 7mm$, one can get an estimate of the adhesive cost per meter blade length by multiplying with the adhesive density and the unit cost ($\$/m^3$) of the adhesive.

Table 2.3: List of mathematical expressions that describe blade consumables, proportional to R_{tip} .

Consumable	Formula	Standard values of parameters
Nonsand tape	$\frac{9 * Roll\ Width * R_{tip} * Unit\ Cost}{1 - waste}$	$Roll\ Width = 0.127m$ $Unit\ Cost = 1.67 \$/m^2$ $waste = 10\%$
Chopped strand	$\frac{R_{tip} * Mass/Unit\ Length * Unit\ Cost}{1 - waste}$	$Mass/Unit\ Length = 0.037\ kg/m$ $Unit\ Cost = 2.16 \$/kg$ $waste = 5\%$
Tubing	$\frac{Length/Blade\ Length * R_{tip} * Unit\ Cost}{1 - waste}$	$Length/Blade\ Length = 5\ m/m$ $Unit\ Cost = 0.23 \$/m$ $waste = 5\%$
Tacky tape	$\frac{10 * R_{tip} * Roll\ Cost}{Roll\ Length * (1 - waste)}$	$Roll\ Cost = 21.22 \$/roll$ $Roll\ Length = 3.5m$ $waste = 5\%$
Masking tape	$\frac{R_{tip} * Roll/Length * Roll\ Cost}{1 - waste}$	$Roll/Length = 0.328m$ $Roll\ Cost = 5.50 \$/roll$ $waste = 10\%$

Besides composite materials, modern blades also contain certain metallic parts as the root bolts connecting the blades to the hub and the lightning protection system. The lightning protection system is compulsory and it consists of a metal button, often named puck or interceptor, located at the blade tip and connected to the ground via a metallic cable. The present model assumes a unit cost of $40 \$/m$ based on a $61.5m$ -long blade, following the approach of [109]. However, the greatest amount of metal

is concentrated at the blade root. This model, assumes that the connection of the blade with the hub of the rotor is materialized by using T-bolts and barrel nuts (with total cost of 37\$ per each pair), equally spaced (every $\sim 15\text{cm}$) over the circumference of the blade root. Of course, during the manufacturing of the blades, a number of consumables are required. The current cost model groups the various consumables into three categories according to: the length of the blade (R_{tip}), the mold's area (A_{molds}) and the blade's outer area (A_{out}). A summary of the mathematical expressions, indicative values of unit costs and estimation of waste for all the consumables required during the building of a modern wind turbine blade, is presented in Tables 2.3-2.5.

Table 2.4: List of mathematical expressions that describe blade consumables, proportional to A_{molds} .

Consumable	Formula	Standard values of parameters
Peel ply	$\frac{A_{molds} * Unit\ Cost}{1 - waste}$	$Unit\ Cost = 1.94\ \$/m^2$ $waste = 15\%$
Tackifier adhesive	$\frac{V.\ Bulk/Area * A_{molds} * Unit\ Cost}{1 - waste}$	$V.\ Bulk/Area = 3.1 \times 10^{-5}\ m^3/m^2$ $Unit\ Cost = 6762.8\ \$/m^3$ $waste = 5\%$
Release agent	$\frac{Vol./Area * A_{molds} * Unit\ Cost}{1 - waste}$	$Vol./Area = 2.57 \times 10^{-5}\ m^3/m^2$ $Unit\ Cost = 15691.82\ \$/m^3$ $waste = 5\%$
Flow medium	$\frac{0.70 * A_{molds} * Unit\ Cost}{1 - waste}$	$Unit\ Cost = 0.646\ \$/m^2$ $waste = 15\%$

The application at the end of this section, confirms the high fidelity of the cost model. However, neither the exact model by NREL-2019, nor the simplified model adopted in the current work, can estimate additional costs related to the application of passive control loads techniques. For example, an estimate of the additional material and labour-hours required to insert an offset ply angle on the uni-directional material over the 'caps' (application of Bend-Twist-Coupling) or the economic burden for the construction of a mold with built-in curvature aiming at load control through blade sweeping is missing in the existing literature. Perhaps a future research developing cost models of passive systems would be of interest.

Table 2.5: List of mathematical expressions that describe blade consumables, proportional to A_{out} .

Consumable	Formula	Standard values of parameters
Chop fibers	$\frac{Mass/Area * A_{out} * Unit Cost}{1 - waste}$	$Mass/Area = 0.00976 \text{ kg/m}^2$ $Unit Cost = 6.19 \text{ \$/kg}$ $waste = 10\%$
White lightning	$\frac{Vol./Area * A_{out} * Unit Cost}{1 - waste}$	$Vol./Area = 2.04 \times 10^{-5} \text{ m}^3/\text{m}^2$ $Unit Cost = 3006.28 \text{ \$/m}^3$ $waste = 10\%$
Hardener	$\frac{Tubes/Area * A_{out} * Unit Cost}{1 - waste}$	$Tubes/Area = 0.012 \text{ \#/m}^2$ $Unit Cost = 1.65 \text{ \$/tube}$ $waste = 10\%$
Putty	$\frac{Mass/Area * A_{out} * Unit Cost}{1 - waste}$	$Mass/Area = 0.0244 \text{ kg/m}^2$ $Unit Cost = 6.00 \text{ \$/kg}$ $waste = 10\%$
Putty catalyst	$\frac{Mass/Area * A_{out} * Unit Cost}{1 - waste}$	$Mass/Area = 0.00488 \text{ kg/m}^2$ $Unit Cost = 7.89 \text{ \$/kg}$ $waste = 10\%$

2.3.2. Estimation of LCoE

According to [110] LCoE can be estimated by the following expression:

$$LCoE = \frac{\frac{CAPEX}{(ICC + BoP)} \frac{i}{1 - (1 + i)^{-N}} + OPEX}{AEP} \quad (2.60)$$

where ICC denotes the Initial Capital Cost based on the model that has been described in detail above, BoP in this thesis has been taken equal to 281\$/kW, OPEX is usually taken equal to 5% of the initial capital cost and finally AEP, estimated by means of aero-elastic simulations. Modern wind turbines are designed for a life-time of $N = 20$ years and a typical fixed charge rate of $i = 6\%$ is considered.

As an extension to the cross-sectional analysis tool described in the previous section (see section 2.2.), an in-house tool which computes the geometric details of a blade such as: the area of the blade outer surface, the area of the molds and the thickness of the fiberglass materials has been developed. This tool takes as input the unit cost of the consumables, the lightning system, the T-bolts and Nuts as well as the building materials. Based on the method described in the present section, estimation of the capital

expenditure associated with the rotor itself can be made. The remaining components of the ICC, are estimated using formulas Eq. 2.52 to Eq. 2.58.

The power curve of the wind turbine is obtained through time domain simulations using hGAST, for different wind speed bins (2 m/s) within the operational range of $5 - 25\text{ m/s}$. Then the AEP is calculated for a Weibull distribution with $C = 11\text{ m/s}$ and $k = 2$.

2.3.3. Verification of the cost model

In the present section the cost analysis of the DTU-10MW RWT is performed. The reader can find a complete description of the reference wind turbine with its necessary details, in appendix A. In addition to the blade construction details this appendix provides the costs of the materials gathered over the literature (see Table A.3).

Table 2.6: Cost analysis of the DTU-10MW RWT blade [$10^3\text{\$}$].

	WISDEM	Present work	diff. [%]
UNIAX	16.4	16.3	-0.2%
BIAX	9.4	9.6	1.7%
TRIAX	12.0	12.2	1.2%
BALSA	36.4	36.9	1.4%
Resin & Hardener	23.1	23.1	0.0%
Adhesive	6.6	6.5	-1.0%
T-bolts & Nuts	4.1	4.1	0.0%
Lightning	3.7	3.6	-2.6%
Painting	4.5	4.4	-0.7%
Other consumables	14.7	14.4	-1.6%
Labour & Others	323.5	323.8	0.1%
Total cost	454.3	455.0	0.1%

Table 2.6 provides the cost of the materials and the labour cost of the DTU-10MW RWT blade, based on the approach described above. The estimations of the present cost model are compared against those of the original cost analysis tool WISDEM. The differences of the two models are i) the simplifications

made in WISDEM in connection to the 2D area of the adhesive points, ii) the grouping of consumables and iii) the structural grid built in the present model in order to accurately estimate the outer surface area of the blade and the volume occupied by the materials. The overall agreement is found to be satisfactory (0.1% total difference), while the maximum relative difference of the individual cost components does not exceed 2.6%. Table 2.7, presents the cost breakdown of the complete 1.5MW reference turbine based on data which described in Table 2.2. So, in the following table, the up-scaled cost values for the DTU-10MW RWT are also provided. It is seen that the total cost of the 10MW turbine is 14.67×10^6 \$, being almost 10 times higher than that of the 1.5MW RWT. It is also found that the up-scaled turbine produces 11 times more energy while its LCoE is 12.7% reduced with respect to the reference.

$$\text{Cost of Blade} = 0.571 \times R_{tip}^{\gamma_{s-u}} - 1356.44 + 3.39 \times R_{tip}^{2.52} \quad (2.61)$$

Table 2.7: Cost and APE breakdown of the 1.5MW RWT (which is described in Table 2.2) and DTU-10MW RWTs [10^3 \$].

	1.5MW RWT	DTU-10MW RWT
Wind turbine cost	1456	14665
• Rotor	337	2308
– 3×blades	216	1365
– pitch	54	656
– spinner	6	22
– hub	61	265
• Gearbox	217	3075
• Generator	139	1970
• Tower	209	1431
• Other parts	554	5882
AEP [MWh]	4312	47182
LCoE [\$/MWh]	54.84	47.83

In the last part of this application example, a mapping of the blades' cost as well as the comparison of the individual costs of two wind turbines of 10MW, is established. Specifically, in Fig. 2.18, two curves define the cost estimation range of the blade (for $\gamma_{s-u} = 2 - 3$), in relation to its length, as proposed by NREL-2006 (is expressed by the equation Eq. 2.61). The cost of DTU-10MW RWT has been estimated

using the cost model that has been described above, while the blade cost of the rest of the turbines have been calculated using the WISDEM tool. It follows that an exponent value slightly below 2.5 in the semi-empirical equation of Eq. 2.61, is able to give a very good first approximation of the blade cost, as long as its length is known. Since the necessary data and tools are available, a full comparison between two similar land-based wind turbines is possible. In Fig. 2.19, the comparison of the basic parameters of the IEA-10MW RWT and DTU-10MW RWT are presented. The first turbine has 19.7m larger rotor diameter, which gives 9.0% higher annual energy while the total cost of the machine is 6.1% higher. This results in a 3.2% compression of the LCoE in comparison to the DTU-10MW RWT.

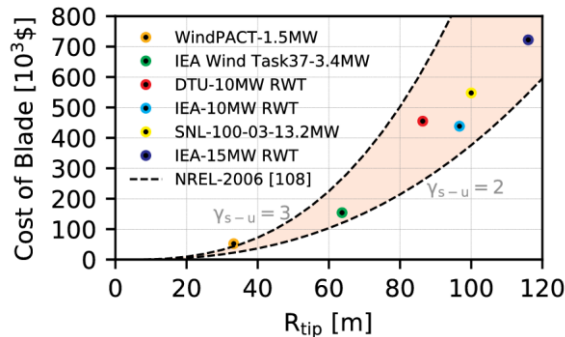


Figure 2.18: Mapping the cost of wind turbine blades, relative to their length.

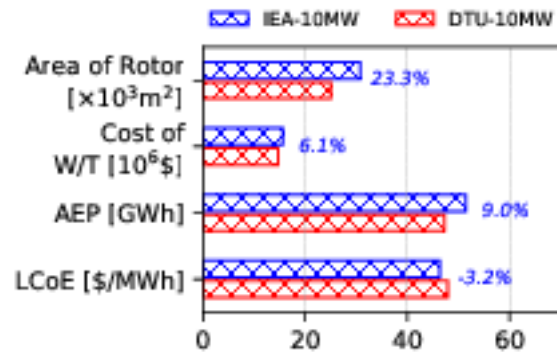


Figure 2.19: Comparison of the basic parameters of two land-based wind turbine of 10MW.

2.4. Optimization methods

Empirical wind turbine design has been out of date for many years. The size of modern wind turbines has imposed limits on the optimization of individual parameters. So, the modern trend is the concurrent optimization of various parameters, which affect both the structural and aerodynamic behavior of the turbine, in the context of a multi-disciplinary optimization process (MDO). The formulation of an optimization problem runs in two levels: (i) in the appropriate definition of the optimization problem (objective function, design variables, constraints) and (ii) the selection of the most appropriate optimization methodology. Over the years, numerous ready to use optimization packages have been developed. These are usually publicly available and free to use (open source or open executable). Among them, the following can be distinguished: (a) EASY [111] which uses genetic algorithms or evolutionary strategies. It offers the freedom to the advanced user to specify and control all parameters of the optimization procedure while it offers “presets” for the beginners and (b) OpenMDO [112], which is an open-source tool that has been developed by NASA. OpenMDO in contrast to EASY is available and aimed at providing the framework for easy and fast implementation of optimization problems and solutions. In this section, the utilization of the most popular ready made optimization packages are discussed: (i) COBYLA, (ii) SLSQP and (iii) traditional Newton’s method (as well as the most popular quasi-Newton of BFGS) is described. The first two methods are freely available in SciPy library of Python [51], while the last one needs to be programmed.

2.4.1. COBYLA method

The need for easy-to-use, understandable and simple optimization techniques made the gradient-free methods particularly attractive. The most widespread technique of the above family (until the end of the 90s), and one of the first gradient free methods was proposed by Nelder and Mead in 1965 [113]. The aim of the method was to calculate the smallest value of a function $F_{aim}(\vec{b})$, $\vec{b} \in R^n$, when there are no constraints on the variables. Since then, various more effective techniques that include the possibility of introducing constraints have been proposed, the most famous of which is the Constrained Optimization BY Linear Approximation (COBYLA) [114],[115]. In this method, only inequality constraints are allowed, while the idea of generating the next vector of variables from function values at the vertices $\{\vec{b}^j: j = 0, 1, \dots, n\}$ of a non-degenerate simplex in R^n , is maintained. The non-linearity of the objective and the constraint functions is treated through the construction of linear polynomial approximations, by interpolation at the vertices of simplices (a simplex in n being the number of variables). Therefore, COBYLA has addressed constrained optimization problems that are expressed in the form:

$$\begin{aligned} \min_{\vec{b} \in R^n} F_{aim}(\vec{b}) \\ s. t.: \quad C_i(\vec{b}) \geq 0, i = 1, 2, \dots, m \end{aligned} \quad (2.62)$$

Every optimization algorithm is based on an iterative process, while the determination of the value of the initial variables vector is necessary. A neighborhood value of this vector, in terms of the optimal solution, ensures its stability and faster approach and for this reason, a manual mapping of the space of possible solutions usually precedes the initiation of the optimization process. In every iteration, a new vector of variables is calculated, which may replace one of the current vertices, either to improve the shape of the simplex or because it is the best vector that has been found so far, according to a merit function that gives attention to the greatest constraint violation. The mathematical expression of this function is given by:

$$\Phi(\vec{b}) = F(\vec{b}) + \mu \max\{-C_i(\vec{b}): i = 1, 2, \dots, m\}^+, \vec{b} \in R^n \quad (2.63)$$

where μ is a parameter adjusted automatically, and the superscript “+” means that the expression in brackets is replaced by zero if and only if its value is negative. Therefore, vector $\vec{b}_1 \in R^n$ is considered a “better” solution than $\vec{b}_2 \in R^n$ if and only if $\Phi(\vec{b}_1) < \Phi(\vec{b}_2)$ holds. Furthermore, in each iteration, a trust-region radius ρ is reduced when the approximations of a well-conditioned simplex fail to yield an improvement to the variables. The process is stopped when ρ reaches a pre-determined value. In the literature, the COBYLA method is a very widespread optimization method, in a wide range of scientific and industrial applications e.g. aerodynamics [116] and structural dynamics [117], providing very good results for a single-digit number of variables, because for more variables the linear approximations can be highly inefficient.

2.4.2. SLSQP method

The relatively large number of optimization variables and the need for compressing computational cost, in the field of mechanical engineering design, make gradient-based methods in many cases indispensable. Such methods have been proven in practice to ensure stability and often lead to the optimal solution in a shorter time. This is the reason why the above methods are preferred by the scientific community for solving optimization problems in the sector of aerodynamics and design engineering (see [118],[119] and [120]). The related python library, provides an extremely popular and directly applicable optimization approach, which wraps in Sequential Least Squares Programming (SLSQP) optimization subroutine originally implemented by Dieter Kraft [121] in 1963. This method minimizes a function of several variables with any combination of bounds, equality and inequality constraints. So, the non-linear optimization problem has the general form:

$$\begin{aligned} \min_{\vec{b} \in \mathbb{R}^n} F_{aim}(\vec{b}) & \quad (2.64) \\ \text{s. t.}: G_j(\vec{b}) = 0, j = 1, 2, \dots, k & \\ G_j(\vec{b}) \geq 0, j = k + 1, \dots, m & \\ \vec{b}_i^{lower} \leq \vec{b}_i \leq \vec{b}_i^{upper}, i = 1, 2, \dots, n & \end{aligned}$$

where \vec{b} is the vector (with size n) of optimization variables, m represents the number of equality and inequality constraints and k is the number of equality constraints. The last inequality equation, expresses the upper and lower bounds for each design variables.

Generally, in a Sequential Quadratic Programming (SQP) algorithm each next step is determined by solving a quadratic sub-problem. So, in every iteration the initial optimization problem Eq. 2.64, is approximated by a Quadratic Program (QP), as an optimization problem with quadratic cost function and linear constraints. Therefore, the quadratic programming is the core unit of the SQP algorithm. An equality constrained QP program has the form:

$$\begin{aligned} \min_{\vec{b} \in \mathbb{R}^n} \frac{1}{2} \vec{b}^T H \vec{b} + h^T \vec{b} & \quad (2.65) \\ \text{s. t.}: A^T \vec{b} = B & \end{aligned}$$

Under Karush-Kuhn-Tucker (KKT) optimal conditions, the solution (b^*, λ^*) can be found by solving the linear system (see [122]):

$$\begin{bmatrix} H & A \\ A^T & 0 \end{bmatrix} \begin{Bmatrix} b \\ \lambda \end{Bmatrix} = \begin{Bmatrix} -h^T \\ B \end{Bmatrix} \quad (2.66)$$

Assuming that A^T has full row rank and the Hessian matrix H is definite positive, the above system has a unique solution that corresponds to the global optimum (b^*, λ^*) . By solving the linear system the solution of an equality constrained QP is provided. To deal with inequalities, an active set method is used. This method is an iterative process: (i) at every step an equality QP is solved using as constraints

only the equality constraints and some of the in-equality ones, (ii) once a step is generated by the solution of the equality QP, it is checked whether a new inequality must enter or leave the active set:

- If the step violates an in-equality that was not active, it is shortened to remain feasible and the blocking constraint becomes active in the next iteration.
- If an inequality that already belongs to the active set is preventing further minimization of the objective function it becomes in-active.

Often SQP methods use a merit function to decide the length of the step for generating the next iteration. The merit function is a weighted sum of the objective function values and the constraint violation. The value of the step, can affect the convergence speed as well as the stability of the minimization process.

The SLSQP is the algorithm implemented in the optimization module, which is available from Python library SciPy and it is a minor variation of the original SQP. Specifically, in the SLSQP, the quadratic sub-problem is replaced by a linear least squares one (which in its general form takes the mathematical expression that described in the relation of Eq. 2.67), so that a dedicated solver for least squares optimization can be used.

$$\min_{\vec{b} \in \mathbb{R}^n} \frac{1}{2} \|E\vec{b} - F_{aim}\|^2 \quad (2.67)$$

$$s. t.: \quad A^T \vec{b} \geq B \text{ and } C^T \vec{b} = D$$

This problem has been extensively treated by Lawson and Hanson [123]. In the context of SQP methods, square matrices E with dimension n and with special structure are considered. The matrices A^T and C^T are of dimension $(m - k) \times n$ and $k \times n$ respectively.

2.4.3. Newton's and quasi-Newton methods

Except from finding solutions to a function (which is approached through Newton-Raphson method), one of the first problems to which Sir Isaac Newton was called to treat, was that of finding the maximum or minimum of a function. He noted that the extremum (i.e. the local maximum, the local minimum or the saddle point) of a function is characterized by its gradient being equal to zero. The idea of the Newton optimization algorithm, is based on the approximation of a function with a quadric function of the form:

$$F_{aim}(\vec{b}) = \frac{1}{2} \vec{b}^T A \vec{b} + B^T \vec{b} + a \quad (2.68)$$

So, if it is assumed that the function $F_{aim}(\vec{b})$ is twice differentiable and continuous, its approximation through a Taylor expansion is described by the mathematical expression:

$$F_{aim}(\vec{b}) \cong F_{aim}(\vec{b}_*) + \nabla F_{aim}(\vec{b}_*)(\vec{b} - \vec{b}_*) + \frac{1}{2} (\vec{b} - \vec{b}_*)^T \nabla^2 F_{aim}(\vec{b}_*)(\vec{b} - \vec{b}_*) + \dots \quad (2.69)$$

where the index “*” denotes the reference point where the value of the function is calculated and without any index, a neighboring point is indicated. Then, focusing on the gradient of the function instead of the value itself and omitting any terms of 2nd order and higher, it is obtained:

$$\nabla F_{aim}(\vec{b}) \cong \nabla F_{aim}(\vec{b}_*) + \nabla^2 F_{aim}(\vec{b}_*)(\vec{b} - \vec{b}_*) \Rightarrow \vec{b} = \vec{b}_* - [\nabla^2 F_{aim}(\vec{b}_*)]^{-1} \nabla F_{aim}(\vec{b}_*) \quad (2.70)$$

If the function is quadratic, the transition to the extremum point can be performed by a single step (without iterations required). Otherwise, if the function is not quadratic, the solution is sought through the following iterative relation, that is obtained by appropriate modification of the Eq. 2.70:

$$\vec{b}_k = \vec{b}_k - \eta_k \frac{[\nabla^2 F_{aim}(\vec{b}_k)]^{-1} \nabla F_{aim}(\vec{b}_k)}{\vec{p}} \quad (2.71)$$

The subscript “ k ” defines the number of iteration and the quantity \vec{p} is called the “direction”. This is a vector describing a segment of a path from the starting point to the solution were the inverse of the second Frechet derivate (Hessian matrix $\nabla^2 F_{aim}(\vec{b}_k)$) determines the “angle” of the direction and the gradient ($\nabla F_{aim}(\vec{b}_k)$) determines its “size”. The coefficient η_k is called “step length” and is a scalar factor, which affects the convergence process. Often, the value of the above coefficient is chosen to have a constant value (regardless of the iteration), while a more correct approach is carried out by solving in each iteration the single-parameter minimization problem $\min_{\eta_k > 0} F_{aim}(\vec{b}_k + \eta_k \vec{p}_k)$ (see [124]).

The main goal in constructing such algorithms is to preserve the balance between convergence and rate of convergence, so in practice, the last prompt is avoided because it significantly delays the convocation. Instead, in each iteration a small number of η_k is selected by choosing the one that gives the smallest value of the objective function, without necessarily meaning that it is the value that gives its minimum value.

In general, Newton’s algorithm belongs to the unconstrained optimization methods and is seen as a traditional approach rarely applied nowadays, due to the difficulty (in terms of CPU-time and availability of computer cores) of calculating the Hessian matrix in each iteration. The literature proposes a number of approximate expressions of the Hessian matrix, which in this thesis will be symbolized by \hat{H} . The first attempt to obtain an estimate of the Hessian matrix was made by Davidon in 1959 [125] and later was made popular by Fletcher and Powell in 1963 [126] and led to the Davidon-Fletcher-Powell (*DFP*) method. Since then, other variants were proposed, the most widespread being the Symmetric Rank One (*SRO*) in 1968 [127] and the Broyden-Fletcher-Goldfarb-Shanno (*BFGS*) in 1970 [128-131], but also more recent modified approaches, like hybrid-BFGS (*HBFGS*) in 2014 [132], aimed at faster convergence of the optimization process. The original BFGS algorithm is based on the formulation of a recursive relationship, where the matrix (\hat{H}_{k+1}) will be calculated based on the (\hat{H}_k) in some other adjacent point. As a result of Taylor expansion, the secant method gives the following mathematical relationship:

$$\frac{\nabla^2 F_{aim}(\vec{b}_{k+1})}{B_{k+1}} \frac{(\vec{b}_{k+1} - \vec{b}_k)}{\vec{s}_k} \cong \frac{\nabla F_{aim}(\vec{b}_{k+1}) - \nabla f(\vec{b}_k)}{\vec{y}_k} \quad (2.72)$$

and according to BFGS method, the recursive relation is given by:

$$\hat{H}_{k+1} = \hat{H}_k - \frac{\hat{H}_k \vec{s}_k \vec{s}_k^T \hat{H}_k}{\vec{s}_k^T \hat{H}_k \vec{s}_k} + \frac{\vec{y}_k \vec{y}_k^T}{\vec{y}_k^T \vec{s}_k} \quad (2.73)$$

$$s. t.: \quad \vec{s}_k^T \vec{y}_k > 0$$

where the last constraint is called ‘‘curvature condition’’ and this ensures that the BFGS updating matrix (\hat{H}_{k+1}) is positive definite. The above recursive relation, needs an estimate of the hessian matrix ($\hat{H}_{k=0}$) as a starting. Where possible, it is preferred to compute the exact Hessian matrix only during the first step of the iteration, otherwise any positive definite matrix (often the identity matrix) is considered as first approximation. In general, the choice of starting matrix is left to the operator and expected to affect the course of the process.

2.5. Optimization framework

The definition of the general optimization problem is given as follows:

Minimization of the objective function $f(\{\nu_S, \nu_A\}, \{c_S, c_A\})$ with design variables ν_S, ν_A and fixed parameters c_S, c_A , subject to the following geometric constraints:

$$g_A(\nu_A) \leq 0, g_S(\nu_S) \leq 0, g_{W/T}(\nu_A, \nu_S) \leq 0 \quad (2.74)$$

and to the following loading constraints:

$$l_S(\nu_A, \nu_S) \leq 0, l_{W/T}(\nu_A, \nu_S) \leq 0 \quad (2.75)$$

where index A is used to denote aerodynamic parameters, S structural parameters and W/T global wind turbine parameters. The scalar objective function f can be either the total mass of the wind turbine or the LCoE of the entire turbine that requires as input the material distribution and mass of the turbine components as well as the AEP. The objective function depends on a number of structural design variables, ν_S (e.g. thickness of skin and webs, position and angle of the shear webs, fiber angle etc.) and aerodynamic design variables, ν_A , (e.g. chord, twist, relative thickness and sweep distributions), a set of fixed structural parameters c_S (e.g. lay-up sequence on different regions on the section) and aerodynamic parameters c_A (e.g. airfoil shapes and lift-drag polars selected from database).

During the optimization loop, the following types of constraints are satisfied, as illustrated in Fig. 2.20:

- geometric constraints that concern (i) the outer geometry of the blade and directly affect the aerodynamics g_A (e.g. maximum chord of the blade or maximum /minimum relative thickness), (ii) the inner-blade structure g_S (e.g. maximum plausible displacement of the spar caps or the offset ply angle of the UD material over the spar caps) and finally, (ii) the overall turbine characteristics, $g_{W/T}$ (e.g. maximum deflection of the blade tip or maximum shift of the blade natural frequencies).
- loading constraints that are (i) maximum stress l_S along the blade and (ii) overall turbine loads $l_{W/T}$ as for example maximum rotor thrust or maximum blade root bending moment.

Communication interfaces are established between the different modules in the optimization loop. An inner-structure geometry parameterization routine is integrated into the cross-sectional analysis tool. This routine is responsible for defining the inner shape of the blade through the global set of design and fixed variables v_S and c_S . A global, span-wise parameterization of the geometry is defined on the basis of Bezier curves for inner-structure parameters, such as the thickness of the skin walls or the position/orientation of the shear webs. A similar parameterization approach is defined for the representation of the external blade shape on the basis of v_A and c_A using Bezier curves.

In the present thesis, the aim of the optimization framework is to minimize the objective function (mass of W/T or LCoE) of the reference wind turbine, through the optimal design of the rotor (including various passive control techniques) – details will be found in the next two chapters (chapter 3 and 4). Apart from the rotor, the remaining wind turbine components remain unchanged, while only loading constraints concerning the maximum stresses along the blades are considered.

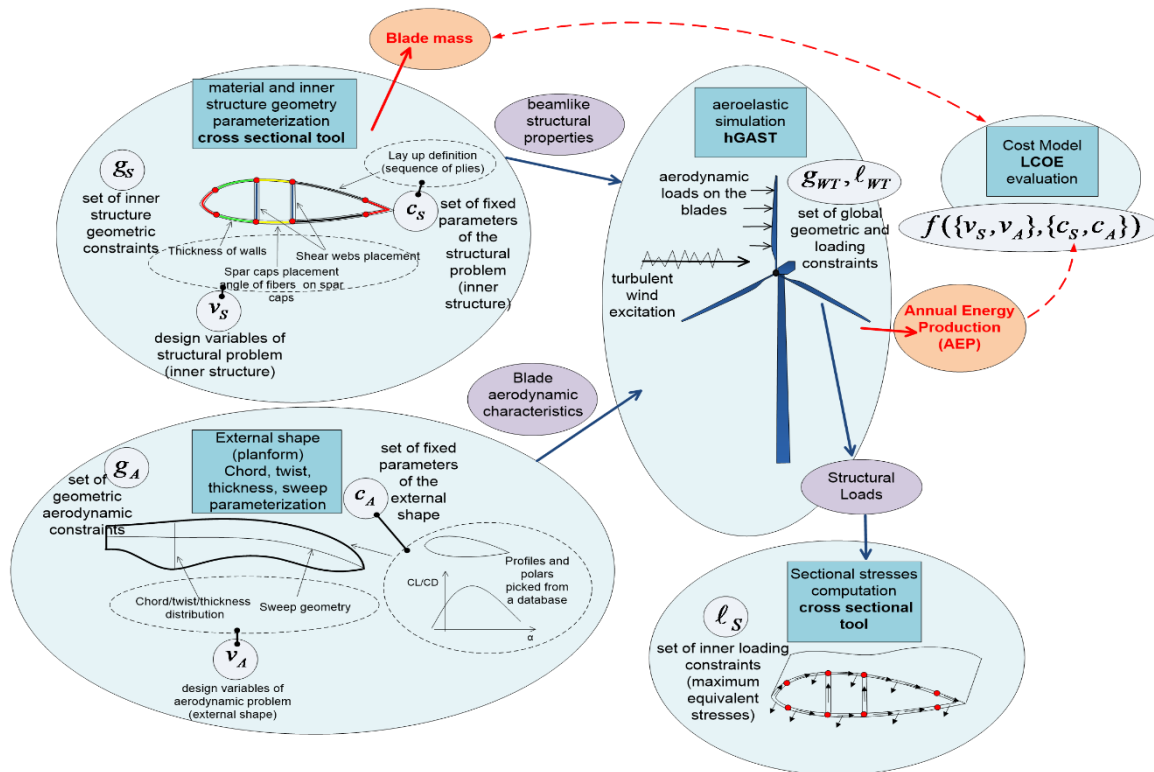


Figure 2.20: Overview of the optimization process.

The AEP is calculated through a series of time domain aero-elastic simulations with hGAST (see subsection 2.1.) over the whole range of the operating wind velocities (from the cut-in to the cut-out). Additional time domain simulations of selected load-driving DLCs of the IEC standard, including both normal operation and parked-idling operation cases, provide ultimate design loads for the candidate optimum solutions. The ultimate loads are then transformed into stresses and Tsai-Hill criterion values

(equivalent stresses) by the thin lamination tool (see section 2.2.) over the blades cross-sections. The imposed constraints to the optimization process demand that the Tsai-Hill criterion values do not exceed the corresponding values of the reference blade. In this way, the thickness of the component walls and the design parameters (e.g. passive load control methods) tested by the optimizer (see section 2.4.) are determined. Knowing the dimensions and the material distribution in the load carrying elements of the components the overall CAPEX of the candidate solution can be estimated using the cost model (see section 2.3.).

2.6. Summary

The current chapter described the individual numerical tools and models being used in the following as ingredients of the multi-disciplinary optimization algorithm, namely the:

- Servo-aero-elastic analysis tool: an in-house, multi-body FEM solver hGAST that provides ultimate loads along the various components of the wind turbine through non-linear time domain aero-elastic simulations of the full wind turbine system in realistic operational and non-operational conditions.
- Cross-sectional analysis tool: an in-house, cross-sectional analysis tool, based on thin L/T theory that provides structural properties, stresses distributions and values of the Tsai-Hill failure criterion over the various cross-sections along the components of the wind turbine.
- Cost model: a cost model aiming at determining the cost of the full wind turbine. It is based on actual cost data for modern wind turbines and existing in the literature formulas.
- Optimization methods: various optimization approaches that are used in the optimization framework, some of them are gradient based, while others are gradient-free. Most of the methods are publicly available through the scipy library of Python.

The numerical tools that have been devised or upgraded in the framework of the present thesis are validated through comparisons with other well established tools in at least one example. More specifically predictions of the thin L/T model are compared against BECAS code results while predictions of the new cost model are compared against WISDEM. Finally, an integrated wind turbine blade design and optimization framework has been described. In this framework, the aforementioned tools are synthesized into a unified tool, in view of performing optimization studies aiming at either compressing blade's mass or the LCoE.

Chapter 3

3. Design of lightweight rotor of a 10MW-scale wind turbine

The goals of up-scaling modern turbines towards the vision of a $20MW$ machine (or greater) and to compress Levelized Cost of Electricity (LCoE) of wind energy to levels far below those of conventional power generation means, can only be achieved through technological breakthroughs and new innovative turbine concepts that render wind turbines lighter and cheaper. Over the last years the target of reducing wind turbines loads and therefore their cost, has been predominantly and effectively supported through breakthroughs in control. There are two distinct categories of load control methods, namely the passive and the active. The objective of the current chapter is to present these methods, placing though special emphasis on the first category – which in the last decade seems to have attracted the interest of both the scientific community and the industry. Through various developments, it has been demonstrated that application of passive load control techniques can significantly reduce the ultimate loads of the blades of a wind turbine during normal operation. So, the cost reduction (by compressing the CAPital EXpenditure - CAPEX), can be achieved through the reduction of the mass of the materials required to build the blades, as a result of the alleviation of their loads. This aspect has been addressed in [100] and [49] and it is also stressed out in the application examples of this chapter. In these examples it is shown that besides alleviating operational loads, passive control methods can also compress loads in parked or idling operation.

3.1. Active and passive control techniques – state-of-art

The most commonly applied load control method is the active one. This is usually realized through Individual Pitching Control (IPC) of the blades or by controlling the torque of the generator, based on different types of sensors (i.e. load sensor, accelerometers, lidars or spinner anemometers) [133]. Active aero-elastic control of loads based on pitch and torque actuators is considered proven technology (especially when combined with standard load or acceleration sensors), which has already been implemented in commercial turbines. Other, innovative actuators such as deployable flaps have also been given a lot of attention by the wind community, mainly at the level of proving the concept through simulations. Individual Flap Control (IFC) but also combined IPC&IFC methods have been numerically tested by several researchers in the past years [24],[134]. Recently some experimental tests, aiming at verifying flap actuators capabilities to reduce wind turbine loads, have also been performed [135].

On the other hand, the passive methods for controlling loads have been described by the wind scientific community through the term “Aero-elastic Tailoring” (A/T). A/T is a design technique through which geometric or stiffness properties of a structure are matched with its aerodynamic characteristics in such a way that the structural loads are reduced, overall. In wind turbines engineering A/T appears as a passive control design option either based on Bend-Twist-Coupling (BTC), or Flap-Edge-Coupling (FEC) [136],[42]. The term BTC describes the behavior of a structure that has been designed to undergo torsion deformation under the action of bending loads. The resulting change in sectional angle will affect the aerodynamic loading through a change in the angle of attack. Modern approach to BTC is to twist the blade sections towards decreasing the angle of attack, which corresponds to the so-called twist-to-feather concept. Apart from ultimate load alleviation, this method has demonstrated significant fatigue reduction potential. On the other hand, FEC is a design concept in which when blade vibrations are excited by the wind in one bending direction (e.g. edge-wise) the blade also vibrates in the other bending direction (flap-wise). As a result, a trading of aerodynamic damping from the highly damped flap-wise motion to the poorly damped edge-wise motion is established and thereby edge-wise vibrations are reduced.

There are two alternative ways for designing the so-called “aero-elastically tailored blade” with BTC or FEC:

- **Material Based:** by exploiting the anisotropic mechanical properties of the composite material. Composite-blade elastic anisotropy can be varied along the span through appropriate selection of the uni-directional “UNIAX” material ply angle (see Fig. 3.1), thickness, and span-wise lay-up.
- **Geometry Based:** the blade outer shape or the inner structure geometry can also be tailored to attain performance, load reduction and stability benefits. BTC coupling can be achieved by sweeping the elastic axis of the blade with respect to the pitch axis. BTC and FEC can be also accomplished by displacing the spar box (see Fig. 3.2).

Passive control methods have been investigated both numerically [42],[45],[137],[138], and experimentally [26],[44], and they have proved their ability to reduce blade loads.

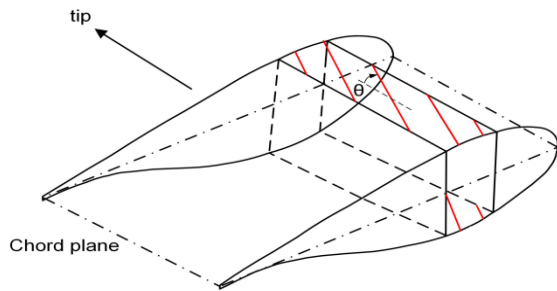


Figure 3.1: Ply angle of fiber orientation of BTC blades.

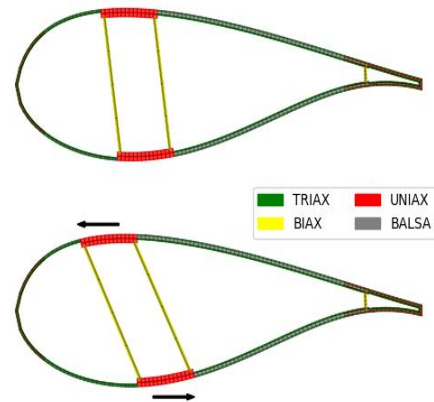


Figure 3.2: Geometrically based FEC (right). Upper right figure shows the reference cross-section, while lower right figure introduction of FEC by the appropriate displacement of the spar cap nodes.

Extreme wind conditions frequently dictate design loads of wind turbine blades. Such extreme wind conditions are specified by the IEC-61400-1 standard [53] through a set of Design Loads Cases (DLC). The most common source of ultimate loading of an operating wind turbine is extreme turbulence (which in IEC standard is addressed through DLC-1.3 – see in appendix A the effect of DLC 1.3 on the loads of the DTU-10MW RWT). According to the existing literature [67],[68], aero-elastic tailoring techniques based on BTC have proven adequate for alleviating the loads due to DLC 1.3 . However, there are cases where the ultimate loads are produced by extreme (survival) winds when the turbine is parked or idling (these conditions are addressed by the IEC standard through the DLC6.x load cases). Such extreme wind conditions, can be either combined (DLC-6.2) or not (DLC-6.1), with some failure of the grid or malfunctioning of the control system. A typical fault for wind turbines is the loss of the grid connection, combined with a failure in the Uninterrupted Power Supply (UPS) system. In this circumstance, the rotor fails to track the wind and therefore, high yaw misalignment angles and high angles of attack in deep stall may occur. A similar condition can be encountered during the installation of the turbine before its electrification.

Aero-elastic simulations of idling rotors indicate that maximum blade loads (combined bending moments) appear at yaw angles in the ranges $[-40^\circ, -15^\circ]$ or $[+15^\circ, +40^\circ]$ [47]. Yaw misalignment angles of $\pm 15^\circ$ are likely to occur even in normal idling operation (DLC-6.1), while higher yaw angles can only be encountered as a result of some fault in the wind-tracking system (DLC-6.2). Aerodynamic loads in such conditions (i.e. in deep stall) can be accurately estimated using engineering tools that rely on tabulated airfoil data (i.e. the so-called polars), only if a valid dynamic stall model is employed. Nevertheless, the uncertainty in the prediction of the aerodynamic loads in dynamic stall is a widely

recognized concern within the wind energy sector [139],[140],[141] and it is the main cause of the subsequent uncertainty in the prediction of the stall-induced edge-wise vibrations. Different state-of-the-art dynamic stall models (e.g. Beddoes-Leishman [80] and ONERA [79]) can give significantly different load results in the onset of dynamic stall due to the quite different aerodynamic damping predicted by the stall models. Therefore, extreme loads of an idling rotor might substantially deviate, especially when the overall aerodynamic damping of certain modes of the system is very low or even negative. This explains why a blade that has been designed using a specific dynamic stall model may appear not to be able to withstand the loads of DLCs-6.x when a different dynamic stall model is considered. However, it is not easy to identify which model is the most appropriate for idling rotor analyses or which model provides the most conservative predictions. Dynamic stall measurements at very high angles of attack that could be used as a means to calibrate engineering state-of-the-art dynamic stall models are scarce.

One possible remedy for mitigating the above-discussed uncertainty in load prediction is to tailor the blade design in such a way that the damping of the poorly damped edge-wise modes is enhanced. The results of the different dynamic stall models tend to converge when the damping of the rotor modes is well above the onset of the instability. An effective way to enhance the damping of the poorly damped edge-wise modes is by means of FEC. Previous studies [142] have shown that, under certain conditions, the coupling of the edge-wise and flap-wise motion, in the low-damped edge-wise modes, increases their aerodynamic damping. The most effective way to enhance FEC is to increase the structural twist angle of the blade, which is achieved by enhancing the cross-bending stiffness along the blade span.

In the present chapter, the capabilities of active and passive control methods are assessed and cross-compared. Moreover, parametric studies aiming at exploring the design space of the passive load control methods, before proceeding to systematic optimization analyses, are performed. At the end of the chapter, three structurally focused multi-disciplinary optimization studies are presented, based on passive load control techniques and aiming at minimizing the mass of the blades. The above signifies that although all disciplines, aerodynamics, structural dynamics, controls, are taken into account in the simulation chain, the design variables only include structural parameters (inner structure thicknesses and passive load control parameters). The chord distribution of the blades is not considered as a design variable while twist is only re-adjusted to moderate power losses and it is not optimized.

3.2. Assessment of load control techniques that alleviate blade loads

In the present section, combined application of different A/T and active load control techniques is performed with the aim to assess maximum load reduction potential. A comparative analysis of different combinations of load control methods is conducted for the DTU-10MW RWT. Both geometric (through blade sweeping) and material (through spar cap “UNIAX” material ply angle offset) BTC are considered, applied separately or in combination. Furthermore, geometric FEC is also considered through displacement of the spar-caps in opposite directions (see Fig. 3.2).

Active load control is based on standard IPC, as well as on combined use of IPC and IFC. Both IPC and IFC are based on the decomposition of the blade root out-of-plane moments of the three blades (measured in the rotating reference frame) into the yaw and tilt moments in the hub fixed system (expressed in the non-rotating frame) by means of Coleman's transformation (Fig. 3.3).

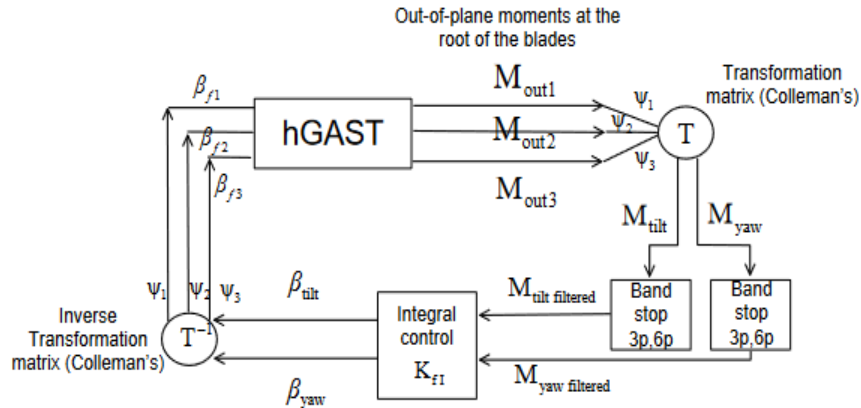


Figure 3.3: Block diagram of the IPC and/or IFC controller. The out-of-plane bending moment signals at the blade root are transformed into yaw and tilt moments. Then these moments are filtered and return as pitch and flap angles of the individual blades.

The reason behind combining different passive control methods lies in the fact that usually geometrical design limitations, associated with the manufacturing process, pose constraints that narrow the limits within which key defining parameters of the above methods can vary. For example, sweeping of the blades cannot exceed certain limits because the manufacturing cost of the curved mold would then become excessive and/or smooth lay-up of the fiber sheet rolls could be hampered. Not to mention transportation constraints. Also, very high material offset angles, besides leading to substantially reduced stiffness characteristics they can also result in increased material wastage. In this respect a combined application of various concepts could sum up to the same amount of overall load reduction, without necessarily exceeding functional and cost effective ranges of the design variables.

Fatigue as well as ultimate load reduction potential is assessed through time domain aero-elastic simulations of the DTU-10MW RWT for a representative subset of IEC DLCs consisting of DLC-1.2 and DLC-1.3. Simulations are performed using NTUA's in-house multi-body, FEM, servo-aero-elastic tool hGAST (see section 2.1.) that is capable of simulating both material and geometric BTC [67], as well as active Trailing Edge (T/E) flaps [143].

3.2.1. Active aero-elastic control

Active load control is based on standard IPC and on combined use of IPC and IFC [143],[144] that are superimposed on the standard power speed controller of the DTU-10MW RWT. The out-of-plane

bending moment signals at the blade root are transformed into yaw and tilt moments M_{yaw} and M_{tilt} by applying the Coleman transformation. $3p$ and $6p$ band-stop filters are applied to M_{yaw} and M_{tilt} . The filtered moments are then passed through the integral control element (I) and the cyclic β_{yaw} and β_{tilt} angles are obtained. These angles are then back transformed into pitch (β_p) and flap angles (β_f) of the individual blades via an inverse Coleman transformation. The block diagram of the controller is illustrated in Fig. 3.3. Since both controls are based on the same working principle, IPC and IFC use the same loop; however integral gains K_{pI} and K_{fI} are tuned separately for every control combination (IPC or IPC&IFC) [143]. In the combined IPC&IFC, the aim of flap control is to assist pitch control and therefore reduce pitch duty cycle (a key objective for very large blades). As shown in Table 3.1, the isolated IPC and the combined IPC&IFC are first applied on the reference model of the DTU-10MW RWT in order to assess their load reduction capabilities.

Table 3.1: T/E flap layout applied on the DTU-10MW RWT.

chord-wise extent	30%
deflection angle limits	$\pm 10^\circ$
deflection speed limit	$20^\circ/sec$
span-wise length	20m (~22.5% of blade radius)
span-wise location	60m – 80m (from hub center)
Airfoil	FFA-W3-241

T/E flaps are placed in the outer part of the blade of the DTU-10MW RWT. The blade of the reference turbine comprises FFA-W-xxx series airfoils. The relative thickness of the outer 35% of the blade is constant and equal to $t/c = 0.24$. The T/E flap extends to 30% of the section chord length and 22.5% of the blade radius (see details in Table 3.1).

Table 3.2: Controller gains for the IPC and combined IPC&IFEC loops.

IPC	$K_{pI} = 1.0 \times 10^{-9} \text{ deg/sec/Nm}$
IPC&IFC	$K_{pI} = 0.6 \times 10^{-9} \text{ deg/sec/Nm}$
	$K_{fI} = 7.0 \times 10^{-9} \text{ deg/sec/Nm}$

In the present analysis constant controller gains have been used both for IFC and IPC. They have been selected on the basis of a sensitivity analysis performed over the wind speeds range of 5 – 25 m/s. Controller gains used in the different control loops are summarized in Table 3.2. Flap motion is bounded in the range $[-10^\circ, +10^\circ]$. In addition, saturation limits have been imposed on the velocity of the flap motion to 20°/sec. In all configurations a delay of 0.1sec has been imposed on the flap motion in order to account for the dynamics of the flap actuator (through a first order filter in flap response).

Fatigue loads are assessed based on the Damage Equivalent Loads (DELs) calculated assuming the following Weibull parameters: $C = 11 \text{ m/s}$ and $k = 2$. In Table 3.3, the lifetime DELs of the reference DTU-10MW RWT are presented together with the percentage relative differences of the considered designs (IPC and IPC&IFC), with respect to the reference configuration.

Table 3.3: Lifetime DELs comparison of DTU-10MW RWT between reference (absolute values [kNm]) and active load control designs (relative differences [%]) based on DLC-1.2, calculated for twenty years lifetime with Weibull parameters $C = 11 \text{ m/s}$ and $k = 2$, Wöhler coefficient $m = 10$ for the blades and $m = 4$ for the tower and $N_{ref} = 10^8$ cycles.

designs	Blade Root			Tower Base		
	Flap	Edge	Torsion	Fore-aft	Side-side	Yaw
reference	31051	24219	382	84986	49299	20218
IPC	-25.5%	-2.6%	-11.6%	1.8%	5.4%	-1.5%
IPC&IFC	-27.6%	-2.5%	52.7%	2.4%	6.6%	-1.7%

IPC configuration significantly reduces flap-wise DELs by 25.5%, while the combined application of IPC&IFC provides a further decrease by 2%. Overall blade root edge-wise DELs are not significantly affected. Specifically, both active control configurations can only reduce the edge-wise DELs by 2.5%. This is because these DELs are mainly driven by gravity loads which are not affected by either the use of pitch or flaps. However, a large decrease in torsion moment DEL by 11.6% is noted when IPC is solely applied. On the other hand, combined application of IPC and IFC, significantly increases torsion moment by 52.7%. This is a known shortcoming of flap based control as the T/E-flap motion locally increases twisting moment of the blade sections that are equipped with flaps. However, it is important to note that the torsion moment is not expected to significantly contribute to the overall cross-sectional stresses, as compared to the two bending moments, in particular the flap-wise one. Therefore, the above reported increase in torsion moment is not expected to give rise to significant design implications at least as far as blades are concerned. It will only affect the design or selection of the pitch bearing which has to withstand increased fatigue loading. It is noted that the present analysis is restricted to

resultant internal load computations, and does not analyze the stresses that develop over the blade sections which is done in the following sections.

With regards to the tower, a slight increase by $\sim 2\%$ is observed in the DEL of the fore-aft bending moment. The reason is that active control loop has been only designed to reduce blade loads, so no control logic exists in the control loop that could effectively be used for the alleviation of the tower loads. If additional logic is implemented, adding also flap motion at $2p$ frequency, tower loads would also decrease. A small increase is also observed in side-side DEL by about 5 – 6%. while the tower yawing moment DEL appears to be slightly reduced by $\sim 1.5\%$.

Table 3.4: Ultimate loads comparison of the DTU-10MW RWT between reference (absolute values [kNm]) and active load control design (relative differences [%]) based on DLC-1.3 (safety factors $\gamma_L = 1.35$, have been applied).

design	Blade Root				Tower Base			
	Flap	Edge	Torsion	Combine	Fore	Side	Yaw	Combine
reference	65708	29537	652	67919	341248	130961	66528	342157
IPC	-4.5%	-8.8%	-0.6%	-4.3%	-0.3%	-0.6%	-19.1%	-0.4%
IPC&IFC	-7.4%	-9.1%	38.8%	-5.5%	8.2%	-1.8%	-18.8%	8.1%

In Table 3.4, the ultimate loads of the DTU-10MW RWT are presented along with the percentage relative differences with respect to the reference. In the application of IPC, ultimate flap-wise bending moment decreases by 4.5%, while a 2.9% further reduction occurs if IFC is additionally applied. Edge-wise moment decreases by 9% while a significant increase by 39% is noted in the torsion moment through the combined application of IPC&IFC. The latter is again attributed to the increase in the twisting moment that yields as a result of the T/E-flap deployment. Sole application of IPC results is a slight decrease in torsion moment by 0.6%. Overall, the ultimate combined blade root moment decreases, following the same trend as the flap-wise moment. Pure IPC reduces ultimate tower fore-aft and combined bending moments by 0.3 – 0.4%, while combined IPC&IFC increases both moments by about 8%. Ultimate side-side bending moments are slightly reduced by IPC and IPC&IFC (0.6 – 1.8%), affected by the blade edge-wise moments. It is noted that the side-side ultimate moment is about 1/3 of the corresponding fore-aft and therefore it does not significantly contribute to the overall combined ultimate loading of the tower. Ultimate tower yawing moment is significantly reduced by about 19% through both IPC and IPC&IFC.

3.2.2. Passive aero-elastic control

In this section, ultimate and fatigue loads alleviation capabilities of passive control methods are assessed. Application of two passive load control methods on the reference turbine DTU-10MW RWT, is performed. The first is the so-called material BTC method [67,68], in which one can achieve a structural coupling between the flap-wise bending and torsion directions by applying an offset angle to the plies of UD material over the spar-box caps of the blade (see Fig. 3.1). The second method, mentioned as FEC, is based on the enhancement of the coupling between the two bending directions of the blades. In the present work, FEC is attained by shifting the upper and lower caps of the spar-box in opposite directions, as shown in Fig. 3.2. Previous developments by the wind energy team of NTUA [47] have indicated that enhanced FEC can substantially improve the aerodynamic damping of the poorly damped rotor edge-wise modes due to the damping trading from the highly damped flap-wise direction towards the poorly damped edge-wise direction. This is especially true in stall conditions. Modern turbines are pitch regulated and therefore high angles of attack within the post stall region are not foreseen in normal operation conditions. However, when the wind turbine is parked or in idling mode the blades may experience very high angles of attack (positive and negative) within stall regime. Since parked or idling operation is combined with extreme winds, in many occasions the corresponding load case drives design loads. Thus, combined application of the above techniques can potentially (i.e. if properly designed) reduce ultimate and fatigue loads of the turbine during both normal and parked/idling operation (see section 3.2.2.1.).

3.2.2.1. Re-twisting of the blades in the application of BTC

As the blade undergoes BTC induced torsion, the deformed shape no longer maintains its aerodynamic optimum twist. Therefore, the twist of the blade needs to be re-adjusted so that the blade shape is optimum at the deformed state. Stäblein [145], has proposed two methods for “correcting” the twist distribution of a wind turbine blades when using passive control techniques:

- In the first approach, the optimal aerodynamic twist distribution is first determined. This is done for the optimum tip speed ratio, while a reference wind speed is selected (often in the range 8 – 10 m/s). Then, the necessary adjustment of the twist is sought, so as under the action of the aerodynamic loads at the reference speed, the deformed blade obtains the optimum twist distribution. This procedure does not ensure maximum efficiency of the rotor at wind speeds far from the reference wind speed – however, the ease of its application renders this option first choice for the designers. The above approach has been followed by Bagherpour et al. in [67], while it is the option adopted in the present chapter in the structural focused multi-disciplinary optimization analyses. The above approach is schematically demonstrated in Fig. 3.4.
- The second approach is more straightforward but also more complex in its implementation. Additional design variables are introduced for determining the optimal twist distribution of the blade, thus ensuring maximum attainable efficiency of the rotor at all wind speeds below the rated

wind speed. This approach is well suited when, besides structural design variables, also aerodynamic design variables are considered in the analysis. Such variables could be, in addition to the twist distribution, the chord distribution and the blade length, while the aim is to determine their optimal combination. This approach has been adopted in the application examples of the next chapter, in the context of full multi-disciplinary aero-elastic optimization analysis.

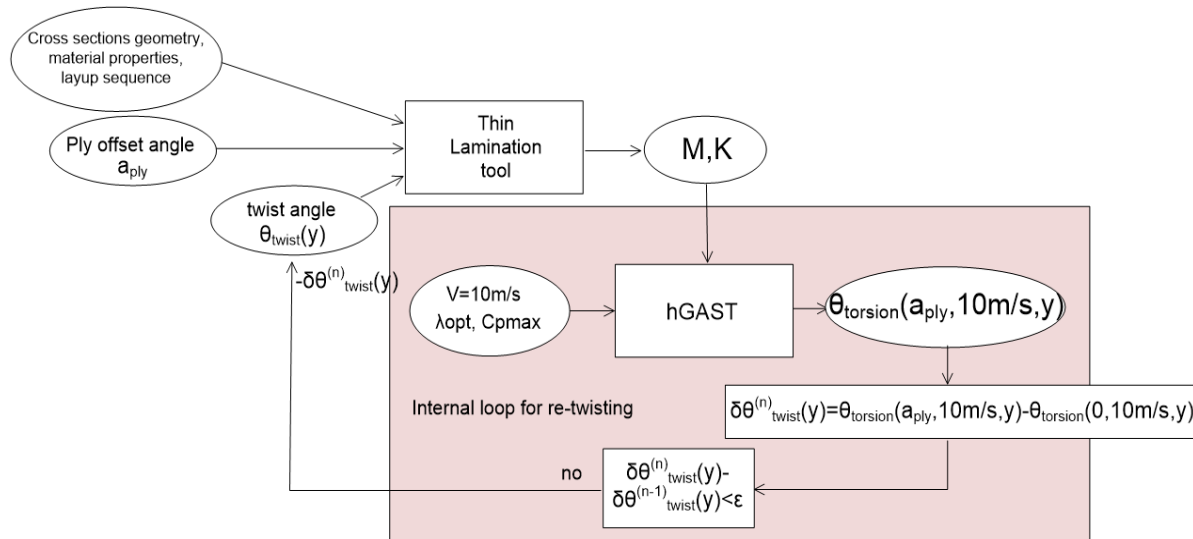


Figure 3.4: Flow-chart of re-twisting process. The necessary adjustment of the twist is sought, so as under the action of the aerodynamic loads at the reference speed the deformed blade obtains the optimum twist distribution.

3.2.2.2. Material BTC

In the present section, the potential to reduce blade extreme and fatigue loads through material BTC is explored. A uniform, along the span, offset angle is applied to “UNIAX” plies on the caps, which begins at the span-wise position of $r/R_{tip} = 20\%$ and extends up to the blade tip. Configurations with ply offset angle ranging in $[0^\circ, +45^\circ]$ are assessed. The present study aims at scanning the design space of the ply offset angle variable and at determining the boundaries within which optimum solutions can be sought.

The assessment of blade load reduction potential is based on aero-elastic simulations of the full wind turbine configuration using hGAST tool. Simulations of the extreme loads driving case DLC-1.3 are performed at the wind speed of 13 m/s . Three different 10 min realizations (seeds) of turbulent wind, with extreme turbulence (ETM of IEC standard) are simulated and maximum loads along the span are extracted (a safety factor of $\gamma_L = 1.35$ is applied to all loads). It is noted that depending on the applied ply offset angle (which determines the magnitude of the blade twisting for a given flap-wise deflection) the twist of the candidate blade variants is adjusted (blade re-twist) with the aim to counterbalance losses of power production due to non-optimum aerodynamic twist distribution following the first method described in section 3.2.2.1. The re-twisting is based on the mean torsion deformation along the

span of the blade at the wind velocity of 10 m/s. For more details on re-twisting procedure the reader may refer to [67] and to section 3.2.2.1.

The BTC capacity of a blade's cross-section, i.e. a quantification of the bend-twist-coupling that describes the section, can be expressed through the coupling coefficient a_{BTC} , initially defined by Lobitz and Laino in [146] by:

$$a_{BTC} = \frac{K_{12}^D}{\sqrt{K_{11}^D \times K_{22}^D}} \quad (3.1)$$

Fig. 3.5a illustrates the magnitude of the coupling coefficient a_{BTC} as function of the ply offset angle. As seen in the figure, maximum a_{BTC} is obtained for ply angles within the range $20^\circ - 25^\circ$.

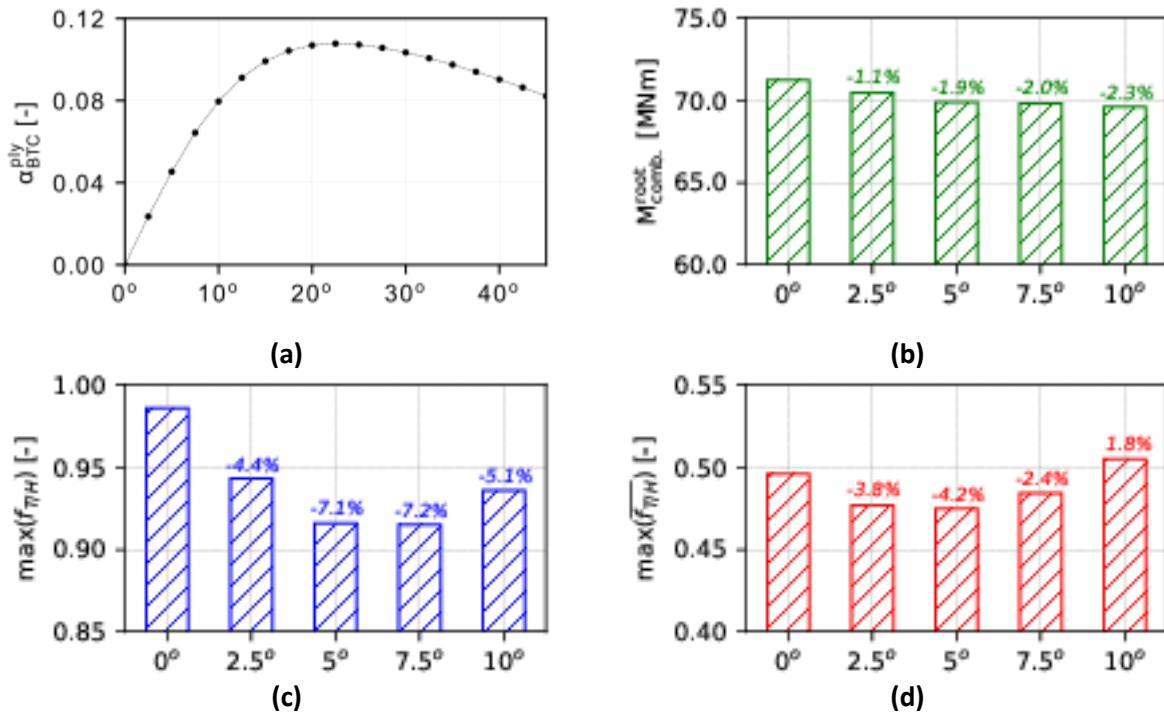


Figure 3.5: Dependence on ply rotation angle of a) BTC coefficient at $r/R_{tip} = 50\%$, b) maximum combined moment at the root of the blade, c) blade maximum value of Tsai-Hill criterion and d) blade maximum value of averaged along the cross-section circumferential direction Tsai-Hill criterion. Percentage relative differences with respect to the reference configuration (ply 0°) are shown above the bars.

As also indicated in previous studies [67], BTC capacity is not always proportional to ply angle. For the specific blade and for ply angles higher than 25° , the capability of the blade to deform in torsion, for a given flap-wise deflection, is deteriorated. A detailed recording of the blade loads (resultant loads and

equivalent stresses) is presented in Fig. 3.5b, c and d for ply angles ranging between 0° and 10° , with a step of 2.5° . As seen in Fig. 3.5b, the ultimate combined bending moment at the root of the blade decreases as the ply angle increases. Up to the angle of 10° , the variation of the resultant loads follows the same pattern as the coupling coefficient. There is an almost proportional variation of the moment versus ply angle. Furthermore, a maximum 2.3% reduction in the combined moment is noted for the ply angle of 10° . Looking into Fig. 3.5c and d one can see that the pattern of the variation of the maximum equivalent stresses is different than the one of the resultant loads. Minimization of the maximum Tsai-Hill value over all blade cross-sections is noted for moderate ply angles 5° and 7.5° (much earlier than the maximum value of the coupling coefficient is reached), while the averaged over the cross-sections Tsai-Hill value is minimized for ply angle 5° . This is because as ply offset angle increases, not only the bending moments decrease but also the capability of the caps to carry bending moments (strength of the material is weakened as a result of the rotation of the fibers). In conclusion, a ply offset angle of 5° reduces the maximum Tsai-Hill value by 7.1% and the average Tsai-Hill value by 4.2%.

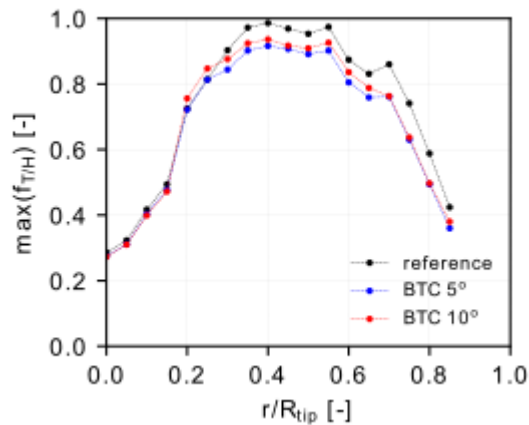


Figure 3.6: Span-wise distribution of the maximum value of Tsai-Hill criterion for various BTC configurations.

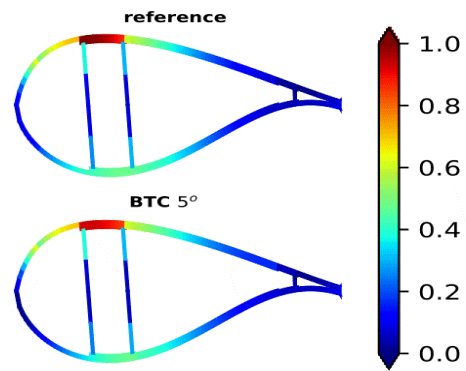


Figure 3.7: Snapshot of equivalent stresses distribution on the cross-section at $r/R_{tip} = 40\%$ where maximum Tsai-Hill value (on the caps) is depicted, for the reference (top) and BTC 5° (bottom) designs.

In Fig. 3.6, the maximum equivalent stresses distribution along the blade span are provided for ply offset angles of 0° , 5° and 10° . It is seen that maximum stress relief is obtained for ply angle equal to 5° . It is the 7.1% reduction reported earlier and it is noted at the cross-section at $r/R_{tip} = 40\%$. Furthermore, it is worth noting that not only the maximum stress is reduced; reduction of stresses is observed in all cross-sections of the blade, all along the span, even at those below radial position $r/R_{tip} = 20\%$ where plies rotation is not applied. Fig. 3.7 illustrates the distribution of equivalent stress over the cross-section at $r/R_{tip} = 40\%$. It is seen that maximum stresses occur on the cap of the suction side. The color pattern indicates the relief in the maximum stress due to the application of 5° angle on the “UNIAX” plies of the caps.

3.2.2.3. Geometric BTC

Geometrical BTC through sweeping of the blades has been also investigated numerically and experimentally by SANDIA laboratories in the framework of Low Wind Speed Technology (LWST) project [147]. Knight & Carver [27] developed a Sweep Twist-Adaptive Rotor (STAR) blade, which was tested on a Zond 750 turbine and demonstrated reduced operating loads. As a result of the lower loads, stretching of the blade and increase in Annual Energy Production (AEP) were made possible. Field testing demonstrated that the sweep twist adaptive rotor exceeded the project goals for improving annual energy capture by producing 10 – 12% more energy compared to the conventional rotor with straight blades. Parallel to the above developments, blades' sweeping has been also investigated as a passive mean to reduce fatigue loads in the framework of the EU funded project UpWind (see section 1.1.2.) by Verelst and Larsen [148], and Riziotis et al [149]. Verelst and Larsen assessed fatigue load reduction levels for different swept blade geometries, while Riziotis et al compared predictions of different aerodynamic and structural models of varying complexity that can be used in simulations of curved blade geometries.

$$sweep = S_{tip} \left(\frac{r}{R_{tip}} \right)^2 \quad (3.2)$$

Table 3.5: Ultimate loads comparison of the DTU-10MW RWT between reference (absolute values [kNm]) and various sweep deflection at the tip (S_{tip}) designs (relative difference [%]) based on DLC-1.3 – safety factors have been applied.

designs	Mass of blade [kg]	Blade Root			Tower Base	
		Flap	Edge	Torsion	Combine	Yaw
0	40017	69248	23219	384	335479	26236
2	+0.016%	-0.74%	-1.06%	+139.49%	-1.69%	-1.40%
4	+0.065%	-1.87%	-1.56%	+410.30%	-3.01%	-2.16%
6	+0.145%	-3.46%	-0.01%	+666.06%	-5.14%	-2.54%
8	+0.258%	-4.87%	+2.28%	+928.73%	-7.50%	-2.92%

Table 3.5 shows the results of the ultimate loads at the blade root as well as at the tower base, for the reference wind turbine, adopting blade sweep curvature, according to Eq. 3.2. It is seen that, the use of sweep leads to slightly increased blade mass due to the increased blade length for the same tip radius. The beneficial effect on the blade root flap-wise moment is proportional to the increase in the sweep deflection of the tip (S_{tip}). Application of this passive control technique provides limited edge-wise moment relief for mild sweeping – while in general it causes very large torsion moment loads. Alleviation of rotor loads, entails a positive effect also on tower base loads (combined bending and yaw moments) as well.

The onset of high torsional loads caused by the off-axis placement of the blade sections due to sweeping, led (see also [68]) to the investigation of the possibility of the combined application of geometric together with material BTC. The results of the combined application are summarized in Table 3.6. In this case, in addition to the extra mass due to blade sweep, material has been added to compensate for the reduction in the stiffness caused by the application of the material BTC. As shown in Table 3.6, the combined use of geometric and material BTC, reduces ultimate flap-wise moment to the same levels as the maximum ply offset angle of 10° . However, the extra mass causes an increase in the loads of the edge-wise moment, while the combined application can lead to a fairly significant increase in the torsion moment. Similar results are obtained for the fatigue loads.

Table 3.6: Ultimate and lifetime DELs loads comparison of the DTU-10MW RWT between reference (absolute values [kNm]) and BTC load control (relative differences [%]) based on DLC-1.3 (ultimate) and DLC-1.2 (fatigue). Fatigue calculate for 20 years lifetime with Weibull parameters $C = 11 m/s$ and $k = 2$. Wöhler coefficient $m = 10$ and $N_{ref} = 10^8$ cycles.

designs	ULTIMATE			FATIGUE		
	Flap	Edge	Torsion	Flap	Edge	Torsion
reference	31051	24219	382	65708	29537	652
BTC 10°	-7.0%	1.3%	-3.7%	-4.7%	2.1%	7.0%
BTC $5^\circ + S_{tip} = 3m$	-6.7%	-0.1%	48.7%	-3.6%	2.3%	93.1%

3.2.2.4. Geometric FEC

Enhanced FEC is intended for increasing the damping of the marginally damped edge-wise modes of the blade. The total (structural plus aerodynamic) aero-elastic damping of those coupled wind turbine

modes usually becomes negative when the rotor operates in the stall regime (due to stall induced vibrations). In modern pitch regulated wind turbines, blades get into stall conditions when the rotor is parked or is idling. In the present study tailoring of FEC is attained through the relative displacement of the caps (suction side cap shifted forward towards the leading edge and pressure side cap shifted backwards towards the trailing edge) as schematically illustrated in Fig. 3.2. The caps are assumed to move along the airfoil periphery and thus the outer airfoil geometry and the aerodynamic design of the rotor remain unchanged; so do the airfoil polars. Furthermore, the elastic deflections of the blades in which FEC tailoring has been applied, do not imply variations of the section shapes (significant distortion/warping effects). A uniform displacement (as percentage of the local chord) is applied all along the blade span. The assessed range is 0 – 4% of the chord relative displacement.

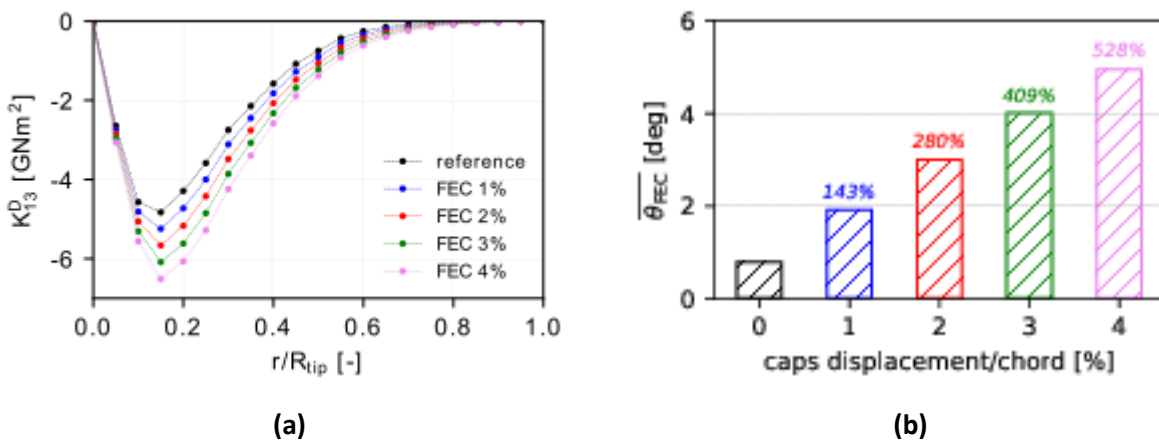


Figure 3.8: (a) Distribution of flap-edge coupling term K_{13}^D along the blade and (b) average (along the blade span) structural twist angle for various caps displacements, expressed as percentages of the chord length. Percentage relative differences with respect to the reference configuration (FEC 0%) are shown above the bars.

In Fig. 3.8a, the effect of different percentages of the caps displacement on the cross stiffness K_{13}^D (see section 2.2.) is shown. The results indicate that shifting of the caps proves to be a very effective method for tailoring FEC. A moderate 4% displacement of the caps can increase the maximum K_{13}^D by 35%. Moreover, as indicated in Fig. 3.8b, this corresponds to about 4^o increase in the average along the blade span structural pitch angle. The effect of FEC on the loads of the turbine when the rotor operates in deep stall is assessed again through aero-elastic simulations of the DTU-10MW RWT using hGAST. Simulations of the IEC DLC-6.2 are performed for turbulent wind conditions (EWM of IEC standard). DLC-6.2 corresponds to operation of the turbine under extreme wind conditions (wind velocity of 50 m/s corresponding to fifty years recurrence period). The turbine is assumed to be in idling mode (blades pitched to feather – generator disengaged) while a simultaneous malfunction of the yaw system occurs.

The malfunction of the yaw system could result in extreme yaw misalignment angles of the rotor with respect to the incoming wind. In many occasions the above DLC proves to be design driving for strength. Moreover, previous studies [47] have shown that maximum stall induced vibrations and loads occur when the yaw angle lies in the range $[+15^\circ, +45^\circ]$. It should be mentioned that for given structural damping values, stall induced vibrations are affected on one hand by the aerodynamics (blade geometry and polars), the wind excitation and the modelling (e.g. dynamic stall implementation) and on the other hand by the structural modelling. However, as mentioned, all the aerodynamic parameters remain fixed (only the inner blade structure is changing) and thus the effect of the geometric FEC on stall induced vibrations is exclusively assessed. The value of applying FEC is that it can improve the aero-elastic response of an already existing blade without needing to re-design the overall external shape of the blade which could have implications on power output.

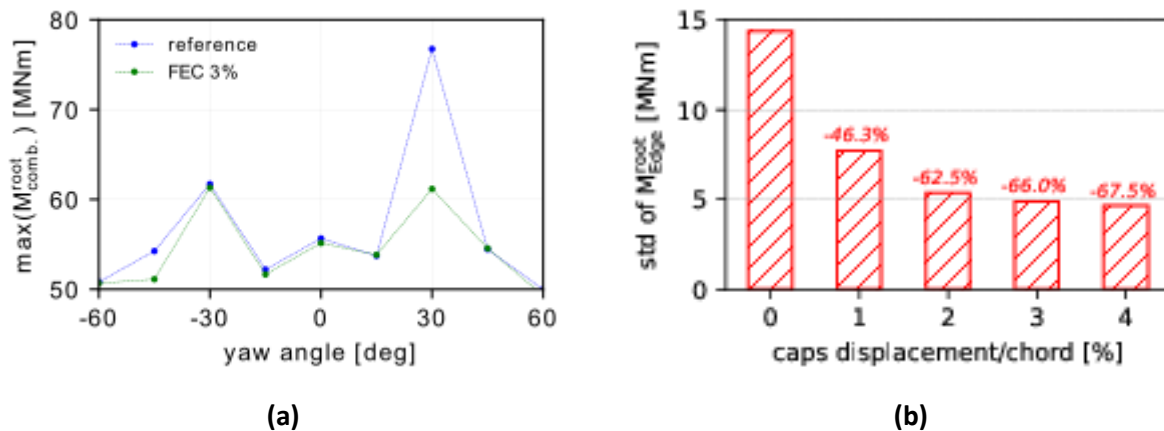


Figure 3.9: (a) Maximum combined moment at the blade root for various yaw angles for the reference and the FEC 3% cases and (b) standard derivation of the edge-wise moment at the blade root for various caps displacements for DLC-6.x at 30° yaw. Percentage relative differences with respect to the reference configuration (FEC 0%) are shown above the bars.

In Fig. 3.9a, the maximum combined bending moment at the root of the blade is shown as function of the yaw misalignment angle, for a representative range of yaw angles from $[-60^\circ, +60^\circ]$, in which maximum stall induced vibrations is expected to occur. The Beddoes-Leishman unsteady aerodynamics and dynamic stall model considered in this special analysis is not valid in deep stall conditions (e.g. for yaw angles $> 30^\circ - 40^\circ$) and is gradually switched off (beyond $\pm 30^\circ$ steady-state C_L and C_D are employed). Further, modelling of vortex shedding which is prompt at $\pm 60^\circ$ yaw is not accounted for. However, this is not expected to affect the effectiveness of FEC in mitigating loads. It is seen that at the yaw angle of $+30^\circ$ the increase in the maximum moment of the reference blade is substantial. A 20% reduction is achieved by introducing a 3% shift in the caps positions. Furthermore, Fig. 3.9b illustrates

the effect of the caps shifting on the standard derivation of the blade root edge-wise moment (caps shifting in the range 0 – 4%). Already a 2% displacement leads to 62.5% reduction in the standard derivation. Further displacement of the caps by 3% and 4% has a minor incremental effect on standard deviation reduction which becomes 66% and 67.5% respectively.

3.3. Blade mass reduction methodology – application of structurally focused multi-disciplinary optimization

The procedure for obtaining maximum mass reduction is divided into two loops. This is done in order to reduce the number of optimization variables and the computational cost which would be excessive if all design variables were handled within the same loop:

- The outer loop which is exclusively handled by the optimizer specifies the values of the primary design variables and evaluates the cost function. In the present application examples, the primary design variables of the optimization problem are the geometric parameters of the BTC (i.e. ply angle distribution along the span), while the cost function of the optimization problem is chosen to be the percentage reduction of the blade mass with respect to the reference blade mass.
- The inner loop within which an iterative procedure is established that determines the secondary design variables of the optimization problem. Secondary design variables is the laminate thickness along the blade span. The inner loop seeks for the minimum thickness values for which the maximum values of the Tsai-Hill failure criterion are at the same level as those of the reference blade. A uniform thickness reduction ratio is considered at every cross-section of the blade.

Every step of the inner iterative procedure consists of the following sub-steps; (i) the beam properties of the blade are determined based on the primary BTC design parameters and the secondary laminate thicknesses, (ii) the ultimate resultant loads along the blade span are computed through simulation of a subset of the certification envelope and (iii) stresses distributions and Tsai-Hill failure criterion values over every cross-section of the blade are evaluated. Calculations of steps (i) and (ii) are performed using the cross-sectional analysis tool, while calculation of ultimate loads is based on simulations performed with hGAST aero-elastic solver. When the iteration is concluded, the values of the failure criterion are compared with those of the reference blade and if they are found different a new iteration is initiated considering new thicknesses. In fact, a less conservative approach would be to consider unit as the maximum allowable value of Tsai-Hill criterion (i.e. equal to 1). In this case, the comparison between the reference and modified blade would not be fair (note that maximum calculated Tsai-Hill values of the reference blade, on the simulated conditions do not reach the limit value of 1). The procedure is repeated until convergence of the thickness reduction ratios is achieved. It is noted that before calculating loads, the BTC blades are re-twisted in order to restore power losses due to non-optimum twist distribution (see 3.2.2.1. for more details). The above steps are schematically shown in the flowchart of Fig. 3.10.

The most time-consuming part of the optimization process is the estimation of the design loads through the time domain aero-elastic analysis. Thus, in the present work the IEC 61400-1 design load case (DLC-1.3, extreme turbulent wind conditions in normal operation), at the wind speed of 13 m/s , is only considered with the aim to retain computational cost manageable. In [68] and [67] the above DLC was found to result in maximum flap-wise blade loads. In addition, and in order to further reduce computational cost, every simulation is performed for a shorter period of time (for example, only 150sec duration). The above duration is centered around the time instant that ultimate load of the reference blade occurs. Given that the overall blade shape is not altered, peak loads are expected to occur at neighboring time instants. Even though this might not be the ultimate load of the new design it will definitely correspond to a peak load. Hence, reduction of a peak load is already a strong indication that overall the new design exhibits lower loads.

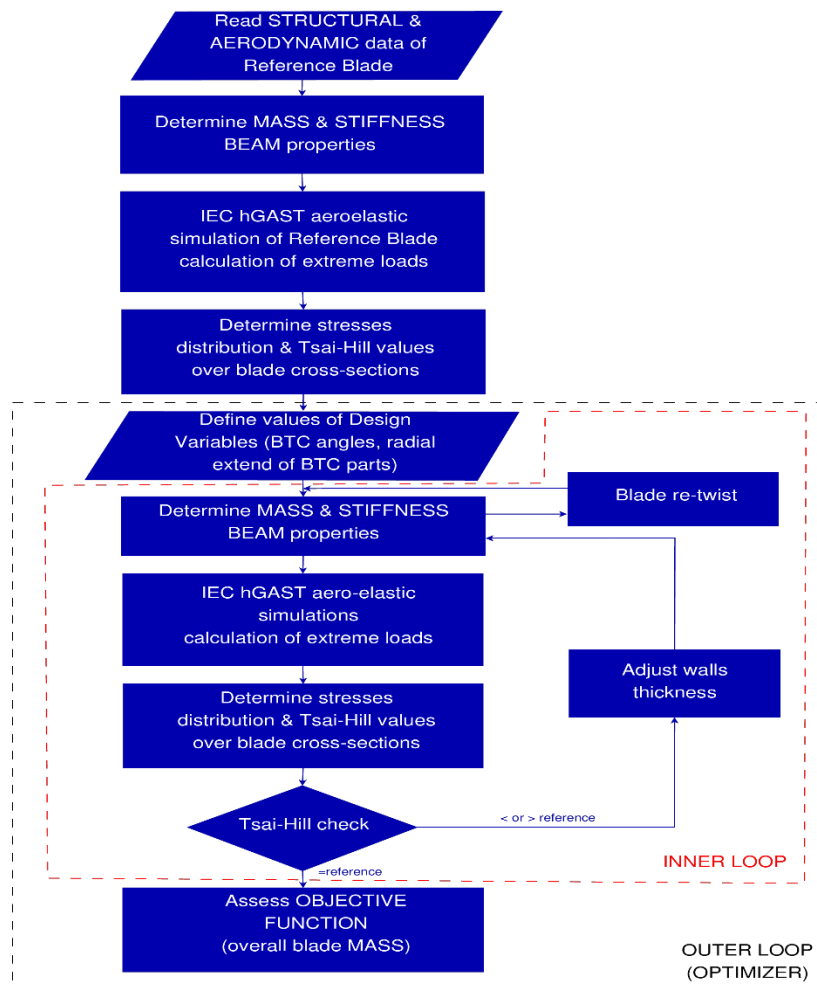


Figure 3.10: Flow-chart presenting the procedure for estimating the optimal BTC distribution in terms of maximum blade mass reduction while maintaining the same maximum Tsai-Hill values with the reference blade, The dashed red box contains the steps of inner loop.

3.4. Application examples

In the previous sub-section, the load alleviation capability of the two passive control techniques, namely the BTC and FEC has been assessed. Reduction of loads allows us to reduce blades' wall thicknesses and therefore the mass of the blade structure. With respect to the framework described in section 3.3., in the present section the margins for reducing the mass of the blade of DTU-10MW RWT are explored [100] based on three scenarios. In the first and second scenarios, the possibility to reduce the mass of the blades is assessed through i) optimal distribution of blade sweeping and ii) segmented application of the ply offset angle of the uni-directional material over the spar-caps of the blade. Finally, in the last scenario BTC is combined with FEC, the latter realized through a 3% shifting of the spar caps. Mass reduction potential is explored using various optimization methods. Both fatigue and ultimate loads in normal operation are considered in the analyses. Fatigue loads are assessed on the basis of IEC-61400-1 DLC-1.2 (normal operation with normal turbulence conditions NTM), while ultimate loads are calculated through DLC-1.3 (normal operation with extreme turbulence conditions ETM) and DLC-6.x (parked/idling rotor in storm conditions) – for more information, see appendix A.

3.4.1. Lightweight rotor using sweep

In sub-section 3.2.2.3., the technique of the geometric BTC, through sweeping the pitch axis has been described. It has already been discussed that due to blade curvature, the mass of the blade inevitably increases if the blade radius and the thicknesses of the inner structure walls are maintained. However, the relief in loads, allows for the reduction of the thickness of the walls, according to the procedure described in the section 3.3. (see the flow-chart of Fig. 3.10).

3.4.1.1. Manual tailoring of sweep and optimization studies

In the first step, the potential of reducing blade mass by applying blade sweep is investigated. Blade sweep following Eq. 3.2 is considered, while the analysis is performed for different values of the tip deflection lying in the range $[0 - 8m]$ considering a $1m$ step in the variation of S_{tip} .

In Table 3.7, it follows that the greatest mass reduction is achieved for $S_{tip} = 6m$ (so-called 'sweep- $6m'$). It is observed that as the value of S_{tip} increases, the flap-wise bending moment decreases, while the torsion moment increases. This is in line with the observations in section 3.2.2.3. On the other hand, the edge-wise bending moment does not exhibit a clear trend. This is because it depends on two factors: (i) the overall blade length and (ii) the eccentricity of the blade sections with respect to the pitch axis. Both increase with increasing S_{tip} leading to increased edgewise bending moments. Edgewise bending moment decreases for moderate values of S_{tip} up to $6m$ as a result of the lower wall thicknesses, while increases for higher values. In the latter cases, it is dominated by the factors i) and ii) described above.

In Pavese et al. [150], various blade sweep geometries are evaluated. In the parametric studies presented in [150], three features of sweep are addressed: (i) the starting point for blade sweeping along the blade span, (ii) maximum sweep deflection and (iii) blade forward sweep. In the current thesis, a similar configuration is approximated through a Bezier curve of four equidistant (in terms of their radial position) control points. It is reasonable to assume that at the root of the blade the sweep should be zero. Therefore, the first two control points are placed at the root of the blade and at an intermediate radial station respectively, both on the pitch axis of the blade (considering zero sweep deflection). The co-ordinates of the last two control points (v_1 and v_2 in Fig. 3.11) were considered as design variables of the optimization loop. An optimization process based on quasi-Newton BFGS (see section 2.4.3.), has been established. Besides v_1 and v_2 , the wall thicknesses of the inner structure are also considered as design variable (inner loop), while blade overall mass is considered as objective function.

Table 3.7: Effect of sweep on blade mass and loads.

$S_{tip}[m]$	Blade mass [kg]	Flap-wise [kNm]	Edge-wise [kNm]	Torsion [kNm]
0	40089	69256	23237	384
1	-0.67%	-0.26%	-2.12%	+34.83%
2	-1.34%	-0.73%	-3.37%	+137.03%
3	-1.99%	-1.39%	-4.00%	+271.58%
4	-2.72%	-2.17%	-4.16%	+405.12%
5	-3.62%	-3.06%	-4.19%	+530.87%
6	-3.74%	-3.93%	+1.38%	+662.68%
7	-2.18%	-3.92%	+0.39%	+805.72%
8	+0.11%	-4.04%	+12.26%	+961.98%

This optimization method requires the estimation of the starting Hessian matrix. Typically, this matrix is either calculated using finite differences or the identity matrix assumption is made. In the current work, the approach of computing only the on-diagonal elements of the Hessian matrix has been adopted. The

final shape (so-called ‘sweep-opt’) of the blade sweep (i.e. the result of the optimization design process), which has 8.6% less mass relative to the reference configuration, is shown in the Fig. 3.11.

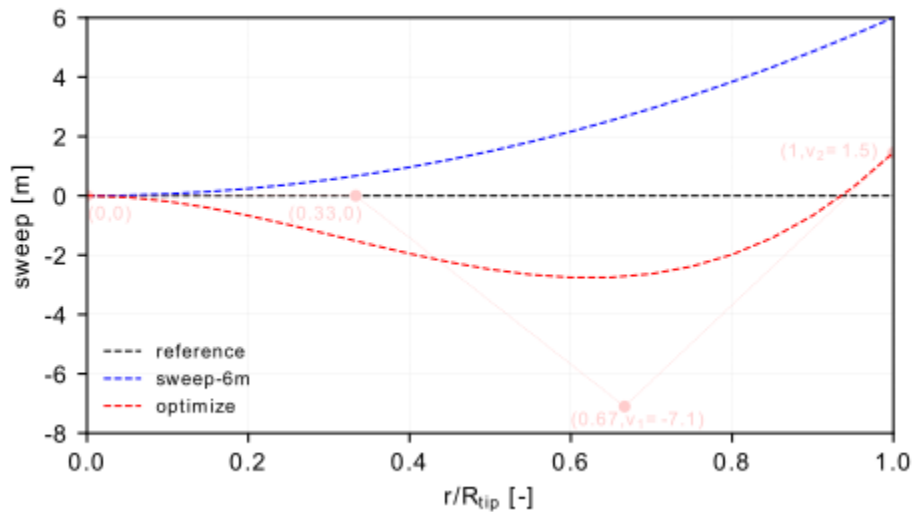


Figure 3.11: Sweep configuration of: (i) reference blade, (ii) sweep-6m and (iii) sweep-opt.

3.4.1.2. Verification of sweep-6m and sweep-opt

The verification step consists of performing detailed aero-elastic simulations of a representative and extended sub-set of IEC 61400-1 (comparing the reference wind turbine to two swept configurations: the sweep-6m and the sweep-opt). These simulations for an extended range of wind speeds, considering a wider simulation window are performed aiming at further assessing the swept blade designs. Fig. 3.12 and 3.13 present the combined bending and the torsional moment at the blade root. The results are obtained through three full 10min simulations (different wind seeds), at extreme turbulence condition (corresponding to DLC-1.3). Both swept configurations (sweep-6m and sweep-opt) appear to have lower combined bending moment (see Fig. 3.12) compared to the straight blade, with the greatest reduction observed in the optimized blade sweep-opt. A relief in the bending moment is observed in all wind speed, with the highest reduction obtained for the sweep-opt blade at 25 m/s (−10.6%). According to the Fig. 3.13, the introduction of sweep increases significantly the torsional moment. However, the optimized shape, gives rise to the lowest increase in this moment due to its forward sweep at its inner part. As an example, at 13 m/s wind speed, sweep-6m presents a 509% increase in the torsional moment, while the optimized configuration a 364% increase.

It is noted that sweeping is not addressed in the optimization studies of the following chapter 4 for the reasons that:

- the curved shape may affect blade's flexibility in relation to buckling behavior, which is not studied in this thesis.
- the cost model described in chapter 2, does not include the cost of: (i) a curved mold, (ii) fabrication and (iii) transportation of curved blades.

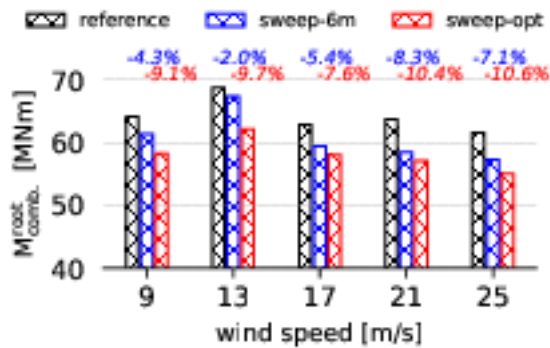


Figure 3.12: Combine moment at the blade root, for various wind speed. The study includes the configurations of: (i) reference, (ii) sweep-6m and (iii) sweep-opt.

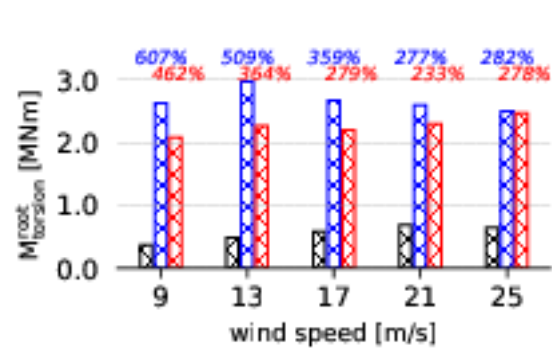


Figure 3.13: Torsional moment at the blade root for various wind speed. The study includes the configurations of : (i) reference, (ii) sweep-6m and (iii) sweep-opt.

3.4.2. Lightweight rotor using BTC technique

Compression of the capital cost – CAPEX (by reducing the mass of the blades) of the DTU-10MW RWT, is the purpose of the present study. At first, BTC parameters (i.e. uniform ply offset angle all along the blade span and its starting position) are manually tailored. Then, optimal segmental application of BTC control (the blade is divided into segments over which different ply offset angles are considered) is tackled using the optimization framework described in section 3.3. through application of the COBYLA optimization method (see section 2.4.1.). The study is concluded through a full evaluation of the optimum design configurations both in terms of ultimate and fatigue loading. In this final evaluation the full range of the encountered by the turbine wind conditions is scanned. Three realizations of 10min duration each are simulated for every wind speed considered in the analysis.

3.4.2.1. Manual search and optimization

A first estimate of the mass reduction capabilities of the BTC blades is shown in the left plot of Fig. 3.14, obtained by considering fixed values of the ply angles equal to 5° , 7.5° and 10° respectively. In addition, to assess the effect of the ply offset angle starting position (partially coupled blades) ply angle re-orientation is applied at various starting radial positions from the blade root up to about the 2/3 of

the span. Every point on the left plot corresponds to a different value of the ply offset angle starting radius. The presented results are obtained within the inner optimization loop of the procedure presented in section 3.3. for fixed values of the ply angles. They correspond to sixty different design points (3 ply angles \times 20 starting positions). The maximum mass reduction of the blades is about 8%, obtained for ply angle of 7.5° and the starting positions spanning from 25 – 40% of the blade span. It is noted that positive relative differences correspond to increase in the blade mass (with respect to the reference blade), as for example seen in the 10° ply angle case for a starting position near the blade root. The explanation of this increase in mass lies in the fact that flap-wise bending stiffness decreases with the increase of the ply angles and therefore the thickness of the blade walls must also increase to maintain Tsai-Hill criterion values at the same level as those of the reference blade. The right plot of Fig. 3.14 demonstrates the convergence of the blade mass reduction with the number of iterations performed. It is found that 4 – 5 iterations of the inner optimization loop (sets of aero-elastic simulations) are required for convergence.

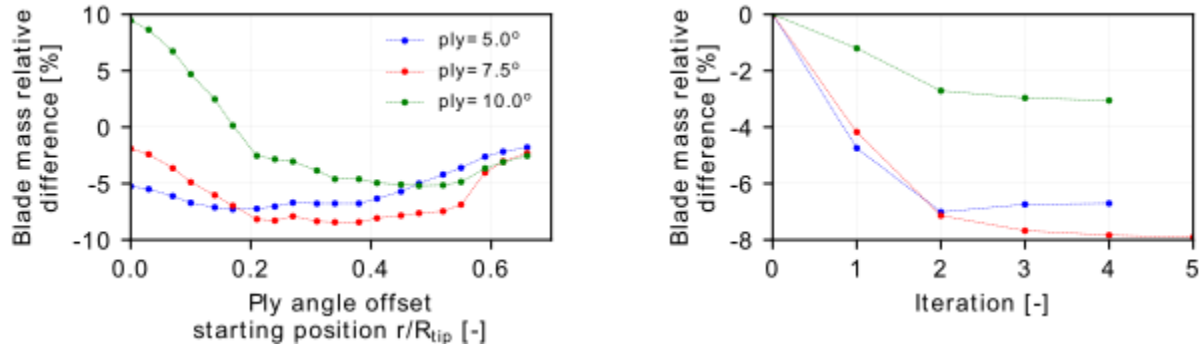


Figure 3.14: Mass reduction of BTC blades as a function of the ply angle (i.e. 5° , 7.5° and 10°) and ply angle offset starting positions (points on the curves correspond to different values of starting position) – *left plot*. Convergence of the inner optimization loop for ply angle starting position=0.3 – *right plot*. Mass reduction is estimated for given BTC blade parameters (ply angle & starting position) to maintain the Tsai-Hill value of the reference blade.

Next, in order to obtain the optimum BTC configuration in terms of mass reduction, the full optimization methodology is employed (i.e. the outer loop is activated as well). Four cases are considered regarding the span-wise distribution of the ply angles. In the first three cases the blade is divided into 2, 3 or 4 segments respectively (symbol N denotes the number of segments) of constant ply angle. In every case the ply angle of the first part is set to zero. The fourth case corresponds to a theoretical, continuous ply angle distribution defined by the following three-parameter spatial function:

$$ply(r; ply_{tip}; r_s; \gamma) = ply_{tip} \left[1 - \left(1 - \frac{r - r_s}{1 - r_s} \right)^\gamma \right] \quad (3.3)$$

where r is the independent variable denoting the non-dimensional radial position (normalized with the blade radius) and the three parameters ply_{tip} , r_s , γ denote the ply angle at the tip of the blade, the non-dimensional position at which offset angle is applied to material plies and the order of the function respectively. Design variables in the first three cases are the discrete values of the ply angle and the starting positions of the $N - 1$ last segments, while in the latter case design variables are the three parameters of the space function.

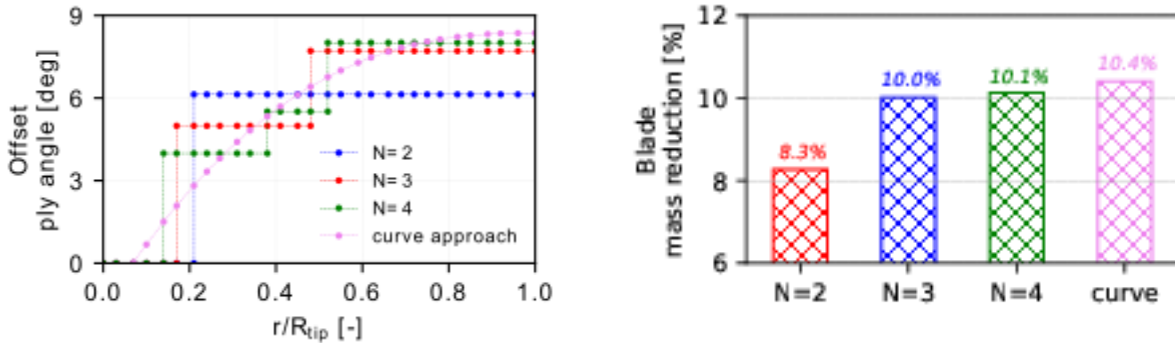


Figure 3.15: Optimum (in terms of mass reduction) ply angle span-wise distribution – *left plot* and maximum blade mass reduction – *right plot* of the BTC configurations considered.

Fig. 3.15 shows the converged (optimum) values of the design variables and of the corresponding cost function. Specifically, the left plot provides the optimum ply angle distribution along the blade span (design variables), while the right plot presents the corresponding maximum mass reduction percentage of the considered BTC blade configurations (cost function). For $N = 2$, maximum mass reduction is 8.3% for 6° offset ply angle starting at 22% of the blade span. For $N = 3$, maximum mass reduction increases to 10% for offset ply angles of 5° and 7.8° starting at 20% and 50% of the blade span respectively. For $N = 4$ no further significant improvement is obtained. Furthermore, the continuous theoretical distribution defines the upper mass reduction limit for a BTC blade. The maximum mass reduction achieved is 10.5%, while the estimated optimum values of the parameters of Eq. 3.3 are $ply_{tip} = 8.36^\circ$, $r_s = 6.9\%$ and $\gamma = 2.5$. It is thus concluded that the configuration with $N = 3$ approaches the maximum theoretical limit. It is also remarkable that the optimum ply angle values of the first three cases are a more or less piece-wise constant approximations of the continuous function of case 4 as shown in the left plot of Fig. 3.15. The layout of the optimized BTC blade for the case $N = 2$ is shown in Fig. 3.16.

Fig. 3.17 shows the optimum span-wise distribution of the wall thickness ratio. This ratio indicates the maximum allowable reduction in the thickness of the walls of the BTC blade for which the Tsai Hill values of the baseline configuration are not exceeded. In Fig. 3.18 the convergence of the outer optimization loop is shown for the case $N = 2$. The values of the design variables and cost function are presented

versus the performed optimization iterations. It is noted that a higher number of iterations is required in order to reach a converged solution, as the number of design variables increase. For the case of $N = 3$, thirty-five optimization iterations are required to obtain the optimum design parameters, while for $N = 2$ about twenty-five iterations are required which consistent that the number of the design variables is reduced and its design configuration is significantly simpler.

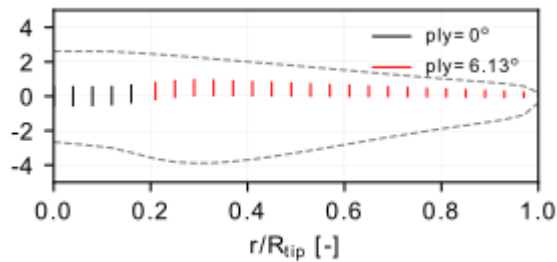


Figure 3.16: Layout of the optimized BTC blade in case $N = 2$. The plot provides the ply angle span-wise distribution of the UD material of the spar cap.

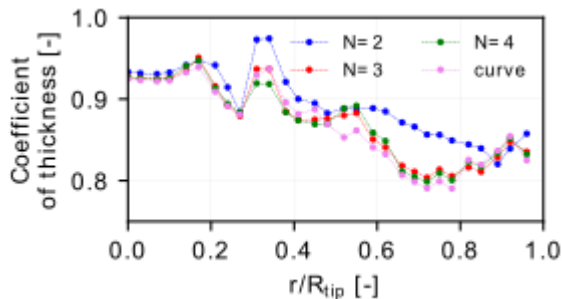


Figure 3.17: Optimum span-wise distribution of the wall thickness multiplier which specifies the reduction of the BTC blades mass, while maintaining the Tsai-Hill value of the reference configuration.

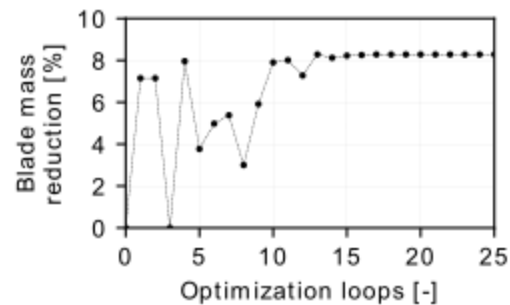
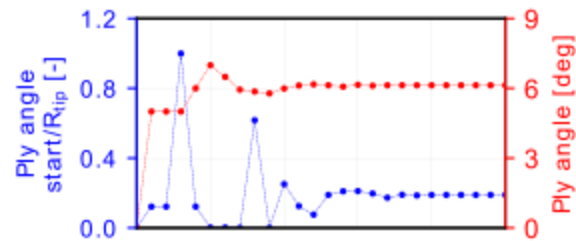


Figure 3.18: Convergence of the design variables (*upper plot*) and of the cost function (*bottom plot*) of the outer optimization loop for the case $N = 2$.

3.4.2.2. Verification of the $N = 2$ and $N = 3$ designs

The BTC designs with $N = 2$ and $N = 3$ are verified in this section. The first ($N = 2$) is the standard BTC option addressed in the existing literature, with a uniform ply angle offset starting at 22% of the span. The second ($N = 3$) is a slightly more complex design with lower ply offset angle at the blades inner part and higher at the outer (see Fig. 3.15, left plot), which however allows for almost 2% additional mass reduction. Manufacturing of both design is considered feasible. As also demonstrated in section 3.4.1.2., the verification step consists of performing detailed aero-elastic simulations of a representative and

extended subset of IEC 61400-1 (as compared to the one considered in the optimization process) for the optimized designs. This includes performing full $10min$ simulations for the turbulent wind cases considering three realizations of the turbulent wind inflow. In this section, the design configurations are assessed, both in terms of ultimate loading considering extreme turbulence conditions at various wind speeds, as well as in terms of fatigue loading considering normal turbulence conditions at various wind speeds.

Before proceeding with the time domain analyses, the natural frequencies of the coupled DTU-10MW RWT at stand still are checked for the different BTC configurations considered. Comparison of the natural frequencies of the reference configuration against the BTC ones is performed on the basis of the eight lowest frequencies. Frequencies of the reference configuration and of the two BTC designs (with $N = 2$ and $N = 3$) are compared in Table 3.8. For the BTC designs, the percentage relative frequency difference with respect to the reference turbine is also provided. Tower side-side and fore-aft frequencies slightly increase due to the lower rotor mass. The increase in the frequencies of the first tower modes is in the order of 1%. As concerns rotor modes, the frequency of the symmetric edge-wise mode increases by 5% and 6.2%, while the frequency of the symmetric flap-wise mode increases by 2.7% and 2.8% for $N = 2$ and $N = 3$ respectively. Rotor asymmetric flap-wise modes increase by 3.3 – 4.6% and asymmetric edge-wise modes by 3.3 – 4.1%. It is hence concluded that the change of the laminate thickness and the ply angle re-orientation does not significantly alter the dynamic behavior of the turbine.

Table 3.8: Standstill natural frequencies comparison between the DTU-10MW RWT and $N = 2$ and $N = 3$ configurations. Absolute frequencies (in Hz) are provided for the reference turbine and relative percentage differences with respect to the reference configuration are provided for the modified designs.

mode shape	reference	$N = 2$	$N = 3$
1 st tower bending side-side	0.249	1.2%	1.6%
1 st tower bending fore-aft	0.252	0.8%	1.2%
1 st symmetric rotor edge-wise/drive-train	0.515	5.0%	6.2%
1 st asymmetric rotor flap-wise (yaw)	0.539	3.9%	4.6%
1 st asymmetric rotor flap-wise (tilt)	0.580	3.3%	3.6%
1 st symmetric rotor flap-wise	0.633	2.7%	2.8%
1 st asymmetric rotor edge-wise (vertical)	0.958	3.4%	4.1%
1 st asymmetric rotor edge-wise (horizontal)	0.972	3.3%	3.8%

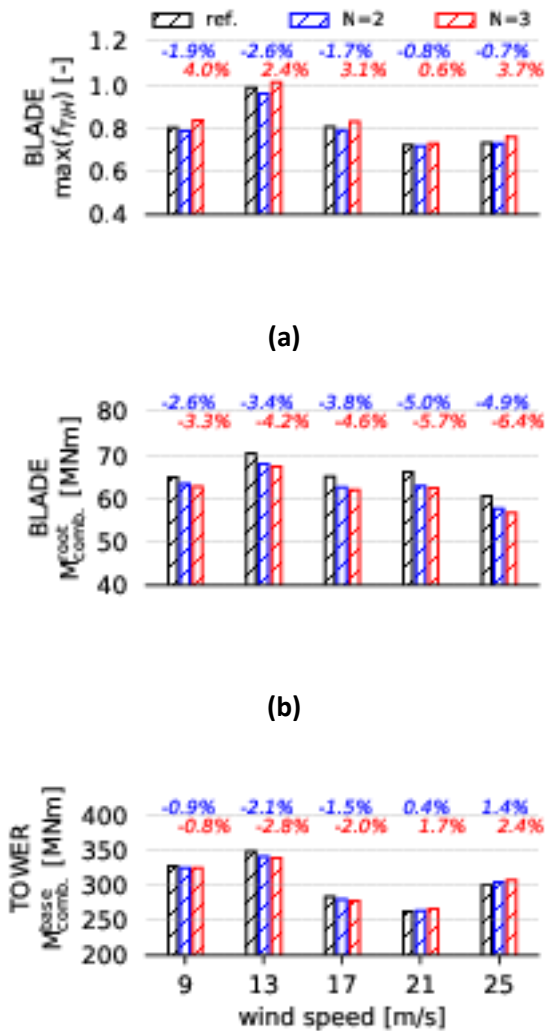


Figure 3.19: Ultimate load assessment of the DTU-10MW RWT and BTC configurations with $N = 2$ and $N = 3$ considering the DLC-1.3. (a) Blade maximum Tsai-Hill values, (b) maximum combined bending moment at the blade root and (c) maximum combined bending moment at the tower.

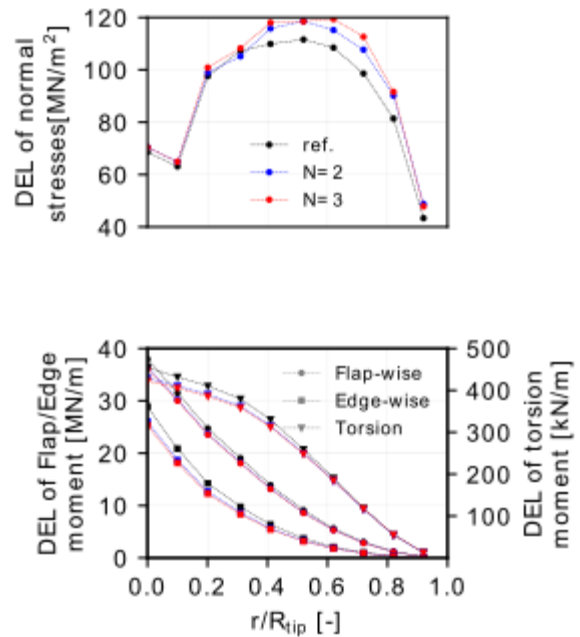


Figure 3.20: Fatigue load assessment of the reference DTU-10MW RWT and the BTC configurations with $N = 2$ and $N = 3$ considering the DLC-1.2. (a) DELs span-wise distribution of the spar mean normal stress and (b) of the blade moments.

Fig. 3.19 presents the results of the ultimate loads assessment. Comparisons between the reference DTU-10MW RWT and BTC configurations with $N = 2$ and $N = 3$ are presented. Plots on the left present the results of the ultimate load analysis that correspond to IEC DLC-1.3, while plots on the right present the results of the fatigue analysis, through DLC-1.2. The maximum Tsai-Hill values (failure occurs for values > 1) of the blade are shown in the upper plot, the maximum combined bending moment at the blade root in the middle plot and maximum combined bending moment at the base of the tower in the

lower plot. Maximum Tsai-Hill values are obtained for DLC-1.3 at 13 m/s for all designs, corresponding to the wind conditions considered in the optimization process. It is noted that for wind speeds higher than the rated, the pitch mechanism is activated giving rise to reduced blade loads. The maximum Tsai-Hill value along the whole blade span is shown in the plots.

Table 3.9: DELs of the tower base moments of the reference DTU-10MW RWT and relative percentage difference of the BTC configurations, with $N = 2$ and $N = 3$ considering the DLC-1.2.

	reference	$N = 2$	$N = 3$
Fore-aft moment	123449	-0.77%	-0.74%
Side-side moment	53748	-4.04%	-4.53%
Yawing moment	32037	-4.49%	-5.38%

Fatigue loads are assessed based on the Damage Equivalent Loads (DELs) calculated assuming twenty years lifetime Weibull parameters $C = 11 m/s$ and $k = 2$, $N_{ref} = 10^7$ reference cycle and Wöhler coefficients $m = 10$ for the blades and $m = 4$ for the steel tower. Fig. 3.20, presents the results of the fatigue load assessment, providing comparisons between the reference DTU-10MW RWT and the BTC configurations with $N = 2$ and $N = 3$. The upper plot corresponds to the DELs of the spar cap mean normal stress along the span, while the bottom plot to the DELs of the three blade moments along the span. In Table 3.9, the DELs of the tower base moments are shown. BTC designs exhibit reduced tower moment DELs by 0.8% and blade moment DELs by up to 10% (reduction increases towards the root). On the contrary, DEL of the mean stress increases up to 14% at the 75% of the blade span due to the thickness reduction, while near the root it increases by only 2.7%. This indicates that lower mass reductions than those reported in the previous section are foreseen in case the design of the blades is driven by fatigue. However, many recent studies as for example in the INNWIND.EU project (see section 1.1.2.) and optimization developments indicate that the design of modern large composite blades is driven by ultimate loading. This implies that within the time span of 20 years (or 25 years for offshore turbines) the blade that has been designed to withstand extreme loads will also withstand the resulting fatigue spectrum, maintaining a sufficient residual life margin.

3.4.3. Lightweight rotor using combination of BTC and FEC control

In section 3.2.2.2. and 3.2.2.4. of this chapter, the load reduction capacity of BTC and FEC passive load control methods was independently assessed. In the present application, the possibility to combine the two passive load control methods with the aim to reduce the mass of the blade and at the same time to minimize vibrations during idling/parked operation, is investigated. It is noted that reduction of the mass

of the blades by some percentage (i.e. reducing the amount of material used in manufacturing the blades) reduces the overall cost of the wind turbine but not by the same percentage, as the cost of the rotor amounts $\sim 25\%$ of the overall cost of the turbine for onshore wind turbines and $\sim 15\%$ for offshore. The design of the new “*modified*” blade is performed in the context of an aero-elastic optimization loop in which the objective function is the blade mass (minimum mass), as also considered in the previous application example, while design variables are the ply offset angle of BTC, by keeping FEC constant to 3% and the thickness of the inner structure walls. A uniform thickness reduction factor is applied over every cross-section of the blade, which is though varied independently among the different cross-sections (twenty-one cross-sections along the blade span are considered in the present analysis). Moreover, the lamination sequence and the properties of the materials used, are kept fixed in all segments of every cross-section (see appendix A, for more information). The offset of the “UNIAX” plies begins at the span-wise position of $r/R_{tip} = 20\%$ and extends up to the blade tip, following the analysis of section 3.2.2.2. Furthermore, a fixed relative displacement of caps is considered, equal to 3% of the chord based on the FEC assessment of section 3.2.2.4. The minimization of the blade mass is performed under the constraint that the maximum Tsai-Hill failure criterion value of every cross-section along the blade span does not exceed the value of the corresponding section of the reference blade, thereby ensuring a fair comparison.

It is important to note that rationalization of the computational cost is absolutely critical at this point. To this end, the duration of the time domain simulation is limited to 150sec (CPU time of 45min). The simulation window is centered around the time instant for which maximum loads of the reference rotor in a simulation with a total duration of 30min is obtained for most of the cross-sections. It is noted that even for the cross-sections that maximum load occurs at a different time instant, still the load within the selected window is very close to its maximum. The above choice, dictated by the requirement for affordable computational cost, does not ensure that ultimate load is always tracked down. However, practice has shown that following the above approach, loads do not significantly deviate from the actual ultimate loads. Besides, optimized designs are eventually verified on the basis of detailed turbulent wind simulations over a range of wind and operation conditions, as performed in the previous applications.

3.4.3.1. Rotor mass minimization through various optimization methods

The above optimization problem is treated using three different optimization algorithms: (i) the COBYLA: a gradient-free optimizer based on evolution algorithms, (ii) the SLSQP: a sequential least squares programming optimizer, using the Jacobian matrix (calculated based on central differences using two-points) and (iii) Newton’s method: in which an iterative method for finding the critical point of derivative and estimating the Hessian matrix (by using central differences of three-points) is necessary. Table 3.10 shows the number of calls of the routine that calculates the objective function for each of the above three methods. The computational cost is proportional to the number of calls, needed for the assessment of the candidate solutions and the computation of the Jacobian/Hessian matrix (depending on the employed optimization algorithm). It is seen that Newton’s method is the most cost effective

choice, while computational time can be further suppressed if the Hessian matrix computation is parallelized.

Table 3.10: Number of objective function calls for the tested optimization algorithms.

Number of objective function calls	COBYLA	SLSQP	Newton
For assessing the candidate solution	23	14	0
For estimating the Jacobian/Hessian matrix	0	12	15
Total number of calls without parallelization	24	26	15
Total number of calls with parallelization	23	20	5

All tested methods converge to the same optimum. The final result of the optimization process is a “modified blade” with 8.3% lower mass as compared to the reference blade, attained by introducing 5.8° offset angle on the uni-directional material over the caps. In Fig. 3.21, the span-wise distribution of the predicted thickness reduction factor of the optimal blade is shown. It is seen that an average thickness reduction factor of about 92% is achieved.

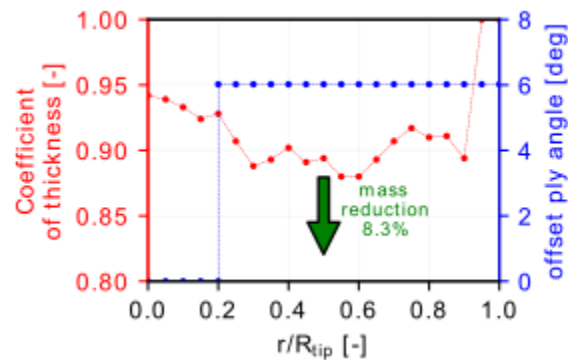


Figure 3.21: Span-wise distribution of the thickness coefficient (inner optimization loop) and offset ply angle of the uni-directional material (outer optimization loop), as a result of the mass minimization process.

3.4.3.2. Verification of the BTC 5° , FEC 3% and “modified” designs

The verification step consists of performing detailed aero-elastic simulations of representative and extended sub-set of IEC 61400-1. The strength and fatigue characteristics of the turbine with the “modified” rotor are verified through detailed, time domain aero-elastic simulations of a selected subset

of load cases of the IEC standard. The “*modified*” design is compared against those with the reference rotor, with a rotor consisting of blades having 5° ply offset on their caps, starting at 20% of the blade radius and with a rotor consisting of blades having 3% of the chord displacement of their caps. The last two constitute the best compromise for pure BTC and FEC according to the parametric studies of sections 3.2.2.2. and 3.2.2.4. respectively. Apart from the rotor, the rest of the turbine, i.e. drive train, generator, nacelle and tower, as well as the control system are the same in all configurations. The blade mass and the mean power output of the rotor variants compared in the present study are listed in Table 3.12. It is seen that the mass of the FEC 3% blade is 0.3% higher than that of the reference and BTC 5° blade because of the inclined placement of the webs (longer shear webs). Furthermore, the annual mean power loss due to application of BTC is only 0.3% thanks to the blade re-twisting.

Table 3.11: List of DTU-10MW RWT designs studied with passive control techniques (Weibull parameters $C = 11 \text{ m/s}$ and $k = 2$ considered for the mean annual power calculation).

design	Ply angle [°]	Caps displacement [% of the chord]	Blade mass [tn]	Mean power [MW]	Reduce loads of
reference	0	0	39.97	6.13	-
<i>BTC</i> 5°	5	0	39.97	6.11	DLC-1.3
<i>FEC</i> 3%	0	3	40.10	6.13	DLC-6.x
<i>modified</i>	5.8	3	36.69	6.11	DLC-1.3 & 6.x

A sub-set of the most critical DLCs of the IEC 61400-1 standard for class IA (the design class of the reference turbine) are simulated using hGAST. Both extreme and fatigue DLCs are addressed in the analysis. The reduced test matrix of the simulated DLCs is provided in appendix A. A list of power production (normal operation) cases, covering a wide range of wind velocities are considered in 1.x-series. In the Table A.6, NTM and ETM refer to the Normal and Extreme Turbulence Models. DLC-1.2 corresponds to normal operation of the wind turbine in normal turbulence conditions (NTM) and determines the Fatigue Limit State (FLS). Simulations are performed for wind speeds in the range [5 – 25 m/s] with a step of 2 m/s. DLC-1.3 corresponds to extreme wind conditions and determines the Ultimate Limit State (ULS). Simulations are performed for wind speeds in the range [9 – 25 m/s] with a step of 4 m/s. DLCs-6.x are chosen as the most unfavourable non-operating DLCs. In the present analysis 0° wind direction is considered in DLC-6.1 (normal idling operation), while ±30° and ±60° wind yaw angles are considered in DLC-6.2 (idling operation combined with loss of grid). Three wind seeds (of 10min duration each) are simulated in every FLS and ULS test case.

As in the previous example, the natural frequencies at standstill of the four turbine variants are first compared in Table 3.12. As expected, a slight reduction (0.5%) in the frequency of the symmetric flap-wise mode is noted for the BTC rotor. This is due to the fact that rotation of the plies reduces the stiffness of the flap-wise direction. A slight decrease in the order of 1% is noted at the frequencies of the asymmetric flap-wise modes of the FEC blade and a 1.2% reduction at the frequency of the symmetric edge-wise mode. Finally, the maximum recorded difference is the 2.1% increase in the frequency of the symmetric edge-wise mode of the optimized (“*modified*”) rotor which is due to the reduced mass of the blades. The frequency comparison of Table 3.12, demonstrates that the performed modifications are not expected to significantly affect the overall dynamic behavior of the coupled wind turbine system. It is clarified that in the optimization process no constraints are set on the values of the natural frequency.

Table 3.12: Standstill natural frequencies comparison between the DTU-10MW RWT and the variants with passive load control techniques. Absolute frequencies (in *Hz*) are provided for the reference turbine and relative percentage differences with respect to the reference configuration are provided for the modified designs.

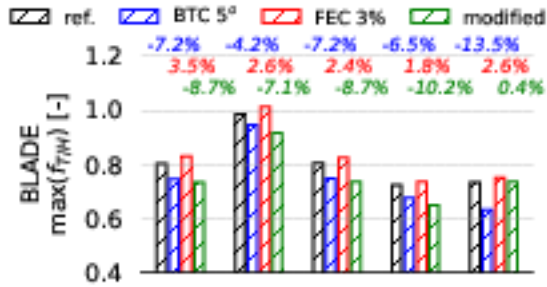
mode shape	reference	BTC 5 ⁰	FEC 3%	modified
1 st tower bending side-side	0.250	0.0%	0.0%	1.2%
1 st tower bending fore-aft	0.253	0.0%	0.0%	0.8%
1 st symmetric rotor edge-wise/drive-train	0.519	0.0%	-1.2%	2.1%
1 st asymmetric rotor flap-wise (yaw)	0.551	-0.4%	-1.1%	-0.2%
1 st asymmetric rotor flap-wise (tilt)	0.596	-0.3%	-1.2%	-1.2%
1 st symmetric rotor flap-wise	0.657	-0.5%	0.0%	-0.6%
1 st asymmetric rotor edge-wise (vertical)	0.965	0.2%	-0.2%	0.5%
1 st asymmetric rotor edge-wise (horizontal)	0.981	0.2%	0.6%	1.0%

Next, ultimate loads results of the four configurations are compared in Fig. 3.21&3.22, (results for DLC-1.3 and 6.x respectively). In Fig. 3.21, the maximum Tsai-Hill failure criterion values of the four blade configurations are compared over the whole range of simulated wind speeds. The results of Fig. 3.21 confirm that the most unfavorable wind velocity is that of 13 *m/s*. In Fig. 3.21a, it is noted that although a constraint is set on the maximum equivalent stresses of the optimized “*modified*” blade which should not exceed those of the reference design, a 7.1% reduction is achieved for the optimized design. A reduction in the maximum stress of the optimized blade is also achieved at all other wind speeds (maximum reduction of 10.2% is noted at the wind velocity of 21 *m/s*), except at the wind speed of

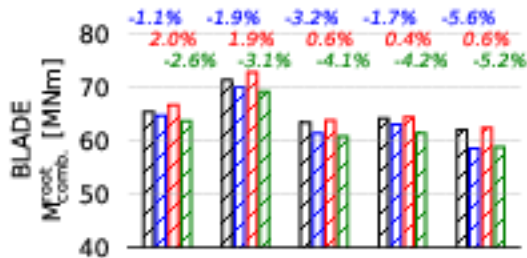
25 m/s where a 0.4% increase is obtained. It is important to note through that only at the wind velocity of 13 m/s the Tsai-Hill value approaches the failure limit of 1, while at all other wind speeds remains close to 0.8, for both, the reference and the “*modified*” blade. The 5° ply offset angle of the pure BTC configurations was selected based on the parametric study of section 3.2.2.2. in which simulations were performed at the wind velocity of 13 m/s . It is seen that the maximum Tsai-Hill value of the pure BTC blade is indeed below the value of reference not only at the wind velocity of 13 m/s (4.2% reduction), but also at all other simulated wind velocities (reductions of ~7% at 9 m/s , 17 m/s and 21 m/s and 13.7% at 25 m/s). The somewhat lower reduction noted at the wind velocity of 13 m/s as compared to that reported in appendix A (4.2% vs 7.1%) is because in the present analysis three seeds (3 × 10min) of turbulent wind are simulated, while in the analysis of/in appendix A only one (10min simulation). The pure FEC configuration exhibits slightly maximum Tsai-Hill values at all simulated wind velocities (it exceeds the failure limit of 1 at 13 m/s).

The same holds for the blade root combined bending moment (Fig. 3.22b) and the tower base combined bending moment (Fig. 3.22c) of the pure FEC blade as compared to the reference one. The above is attributed to the fact that FEC focuses on stall induced vibrations of the parked rotor and not on operational loads. Present results indicate that the effect of FEC on operational loads is unfavorable, though the resulting increase in stresses and loads is marginal. As seen in Fig. 3.22b&c, pure BTC leads to reduced blade loads, while its effect on tower loads is mixed and depends on wind velocity. However, the ultimate tower bending moment, obtained at 13 m/s , remains unchanged. For the optimized blade reduced blade and tower bending moments are obtained. A slight increase of 0.8% is only noted on tower base combined bending moment at the wind speed of 25 m/s . Furthermore, the reduction in the rotor mass of the “*modified*” blade implies benefits for the “*downstream*” components, which are expected to lead to additional cost reductions.

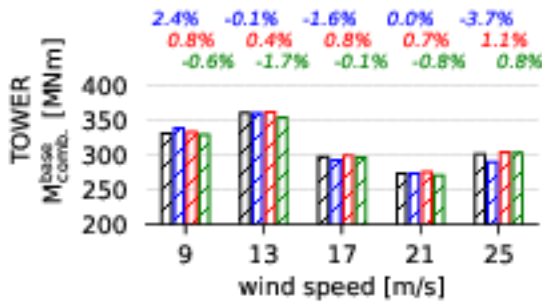
In Fig. 3.23 the DLC-6.x loads are compared for the four blade configurations. In line with the results of section 3.1.2.2., maximum blade loads for the reference blade (blade root edge-wise and combined bending moment) are obtained at the yaw angle of +30°. The same happens with the tower base combined moment. Application of pure BTC (5° ply offset angle) does not significantly alter the loads. Only a slight reduction of maximum blade and tower loads is observed. On the other hand (as also discussed in section 3.1.2.2.), application of pure FEC, results in substantially lower blade moments. This is due to the suppression of the stall induced vibrations and the subsequent reduction in edge-wise bending moments by 66%. The effect of pure FEC on tower base moment is neutral. Finally, integration of a 3% of the chord displacement of the caps in the optimized blade geometry leads to an almost equal with the pure FEC reduction in the blade edge-wise and combined bending moment (63.3% and 23.5% respectively) plus a 4.9% reduction in the maximum tower base bending moment. It is therefore concluded that the overall effect of FEC on ultimate design loads is beneficial despite its slightly unfavorable effect on operational loads.



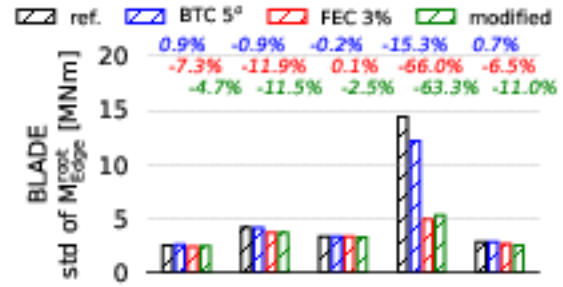
(a)



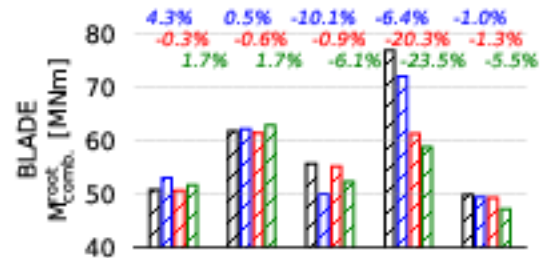
(b)



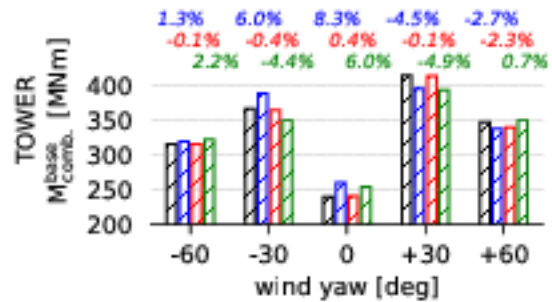
(c)



(a)



(b)



(c)

Figure 3.22: DLC-1.3 ultimate loads vs wind speed of different configurations (with safety factors) (a) Blade maximum value of Tsai-Hill failure criterion, (b) maximum combined bending moment at blade root and (c) maximum combined bending moment at tower base. Percentage relative differences with respect to the reference configuration are shown above the bars.

Figure 3.23: DLC-6.x ultimate loads vs wind yaw of different configuration (with safety factors) (a) standard deviation (std) of edge-wise bending moment at blade root, (b) maximum combined bending moment at blade root and (c) maximum combined bending moment at tower base. Percentage relative differences with respect to the reference configuration are shown above the bars.

In addition to ULS, verification of the final optimized blade and pure BTC and FEC variants also includes FLS. FLS assessment of the four wind turbine designs is performed on the basis of DLC-1.2 of IEC 61400-

1. Lifetime fatigue Damage Equivalent Loads (DELs) are calculated from the load time series of DLC-1.2 simulations, for all operational wind velocities (range 5 – 25 m/s) assuming twenty years lifetime, Weibull parameters $C = 11 \text{ m/s}$, $k = 2$, $N_{ref} = 10^7$ reference cycles and Wöhler coefficients of $m = 10$ for the blades and $m = 4$ for the (steel) tower. Table 3.13 provides the DELs of reference turbine, at the root of the blade and at the tower base, as well as the percentage difference of their change in the pure BTC and FEC and the optimized blade. The application of pure BTC, with 5° ply offset angle, leads to reduction of fatigue loads of the blade and tower. Maximum is the reduction in the flap-wise bending moment (5.1% reduction). In contrast, pure FEC slightly increases the DELs of all components. Slight is the increase in all of them (order of magnitude of 1%), but the blade pitching moment which increases by 10.7%. The increase in the pitching moment is due to the increased offset of the mass center over all blade sections, which is obtained as a result of the displacement of the caps. The optimized blade, which combines both passive load control techniques, combines pros and cons of both. The DEL of the flap-wise moment of the optimized blade is slightly lower than that of the pure BTC blade (5.5% compared to 5.1% reduction of the pure BTC). The DEL of the edge-wise moment is reduced by $\sim 9 - 10\%$ as compared to the other blade designs as result of the mass reduction. Slightly lower is also the reduction in the tower fatigue loads as compared to the pure BTC configuration. Finally, lower is the increase in the DEL of the pitching moment as compared to the pure FEC configuration (1.9% of the optimized vs. 10.7% of the pure FEC).

Table 3.13: DLC-1.2 fatigue loads comparison between the DTU-10MW RWT and its variants with passive load control techniques. DELs calculated for twenty years lifetime with Wöhler coefficient $m = 10$ for the blades and $m = 4$ for the tower and $N_{ref} = 10^7$ cycles and Weibull parameters $C = 11 \text{ m/s}$ and $k = 2$. Absolute load (in kNm) are provided for the reference turbine and relative percentage difference with respect to the reference configuration are provided for the modified designs.

designs	Blade Root			Tower Base		
	M_{flap}	M_{pitch}	M_{edge}	$M_{fore-aft}$	M_{yaw}	$M_{side-side}$
<i>reference</i>	25045	420	27791	111751	24460	33549
BTC 5°	-5.1%	-3.6%	-0.3%	-3.3%	-3.9%	-2.0%
FEC 3%	+0.7%	+10.7%	+0.4%	+0.7%	+0.6%	+1.8%
<i>modified</i>	-5.5%	+1.9%	-8.9%	-1.3%	-5.2%	-0.5%

3.5. Summary

Although active control techniques have been thoroughly examined by the scientific community, a brief review has nevertheless been carried out in the present chapter. The exhaustion of their potential has

turned the interest of the scientific community towards passive techniques. These techniques have proven to be equally or even more effective.

So, a preliminary evaluation of the possibility of reducing the loads developing on wind turbine blades, using passive (through BTC and FEC) control techniques, is investigated in this chapter. The load alleviation capabilities of passive load control methods are compared against those of their active control counterparts (based on conventional IPC and IFC) The analysis is performed for the reference DTU-10MW RWT. Preliminary optimization simulations, aiming at suppressing the mass of the blades are performed using independently and jointly BTC and FEC. In order to serve the present optimization study the preliminary testing of the coupling of the servo-aero-elastic solver hGAST with the thin lamination cross sectional tool have been established.

Active load control techniques achieve an 25% reduction of the blade flap-wise fatigue bending load with both IPC and combined IPC&IFC strategies. Overall, tower fatigue loads slightly increase by 2% because the proposed control loops have only been designed for alleviation of the blade loads while they are not aiming at tower loads. Moderate is the effect on ultimate loads by both control concepts. As a result of the combined applications of IPC&IFC a 7.4% reduction of the blade ultimate flap-wise load is obtained.

The design space of material and geometric BTC and FEC is scanned in order to identify the limits of their application and the anticipated benefits in terms of load reduction. Aero-elastic simulations of various material BTC configurations indicated that for the blade considered in the analysis, ply offset angles higher than 7.5° could result in deteriorated strength of the blade due to the weakening of the blade stiffness in the flap-wise direction. Likewise, extreme sweep application (in geometric BTC) can exacerbate the blade loads. However, the anticipated level of reduction of the ultimate loads and stresses in both cases is $\sim 7\%$. Application of FEC is found necessary for the mitigation of the idling operation blade loads of the DTU-10MW RWT blade at the yaw angle of $+30^\circ$. The anticipated reduction in the extreme idling operation load is 20% for a moderate shift of the caps by 3% of the blade chord.

In the last part of the chapter, an iterative process for reducing the thickness of the walls of the blades is established. This process has been included in a minimization environment, where the passive control parameters (e.g. the offset ply angle) are the optimization variables and the objective function is the capital cost – CAPEX (through blade mass). Three application examples have been addressed:

- In the first example, the application of appropriate sweep curvature to minimize blade mass, has been studied. The result is a sickle-shaped sweep, where the tip deflection is $S_{tip} = 1.5m$ and at around the 3/4 of the blade length, a maximum forward sweep of about $3m$, occurs. The main conclusion of the above design configuration is that through blade sweep an 8% lower blade mass can be achieved.
- In the second example, it is concluded that for the DTU-10MW RWT blades, ply angle in the range of $5^\circ - 7.5^\circ$ starting at 15 – 30% of the blade span, can provide overall mass reduction of about 8%. Moreover, a hybrid BTC design in which the ply angles gradually increase toward the tip is tested

(max ply angle $\sim 8^\circ$). Mass reduction of 10% is obtained for the above hybrid configuration, when the blade reduction of combined bending is 5 – 7% and of the tower base, 6.6 – 8.1%, for every configuration.

- In the last example, a BTC design with an additional 3% displacement of the spar beam caps (FEC 3%) is tested. The reduction of the mass of the blade is similar to that of the first application example (or with the second example, in its simplest form) about 8%, however the modified configuration has now been tested in extreme conditions beyond extreme turbulence in normal operation (i.e. DLC-6.x, where substantial loads and vibrations are usually observed). The aforementioned optimization was performed using all optimization algorithms presented in section 3.3. Thus, it was made possible to evaluate these methods in terms of convocation speed and stability.

Finally, due to computer cost limitations during the optimization processes, the duration of the time domain aero-elastic simulations was kept low (only 150sec). Thus, although the simulation window is centered around the interval of interest, within which ultimate loads are anticipated, a final design verification step is considered indispensable. In this step, the optimized blade geometry is verified by much more detailed simulations of several DLCs at various wind speeds, which in addition include assessment of the turbine fatigue loads. The simulations of the verification step substantiate that ultimate Tsai-Hill values of the optimized blade remain below the constrain values determined by the reference design.

This page intentionally left blank

Chapter 4

4. Multi-disciplinary aero-elastic optimization of DTU-10MW RWT

The current trend in the design of modern wind turbines, which also extends to the aeronautical sector, is to apply integrated aero-elastic optimization methods [42] that consider both the aerodynamic performance of the rotor and the structural characteristics of the system components within the same optimization loop. Usually some specific cost parameters or even the overall Levelized Cost of Electricity (LCoE) is set as objective function of the optimization process [105]. The European project Innwind.EU [18], which was concluded some years ago, explored the potential to integrate innovative features (passive and active control methods, smart add-on devices, alternative structural designs etc.) in the design of large offshore turbines that either enhance energy yield or mitigate loads and consequently reduce LCoE. This project came to the conclusion that the optimum mix of such features can be effectively determined only if integrated design tools are largely deployed. The reason being that in many cases the above solutions act in an antagonistic manner, while the solution that provides maximum load reduction is not necessarily the most effective in terms of cost. It is noted that the need for integrating technology breakthrough solutions within current designs does not only stem from the necessity of suppressing existing turbines' cost. It is also linked to the market demand for up scaled turbines.

The optimization framework described in section 2.5. and utilized in the previous chapter for the minimization of the mass of the blade (see section 3.3. and 3.4.), is now employed with the aim to minimize LCoE. The CAPital EXPenditure (CAPEX) of the turbine is evaluated on the basis of the cost model described in section 2.3. Optimization is carried out by simultaneously evaluating the full set of

conditions (see appendix A, DLC-1.3 and DLC-6.x) that can determine ultimate loads. The main innovation of the current chapter is the complete multi-disciplinary design optimization employed, in which the structural (i.e. the thicknesses of the inner structure walls and parameters of the two passive control techniques – Bend-Twist-Coupling and Flap-Edge-Coupling) and the aerodynamic (i.e. the blade radius, the chord and the twist distributions) characteristics of the rotor are evaluated in the same loop concurrently.

4.1. Alternatives to FEC control of loads – combined application of passive control methods

Aero-elastic simulations of idling rotors indicate that maximum blade loads (combined bending moments) appear at yaw angles in the ranges $[-40^\circ, -15^\circ]$ or $[+15^\circ, +40^\circ]$ [47]. Yaw misalignment angles of $\pm 15^\circ$ are likely to occur even in normal idling operation (DLC-6.1), while higher yaw angles can only be encountered as a result of some fault in the wind-tracking system (DLC-6.2), for more information see appendix A. So, when manufacturer come across the abovementioned problem, i.e. that DLC-6.x loads exceed the strength limits of their design, they usually apply ad hoc, local modifications, e.g. locally reinforcing the inner-blade structure in order to increase strength margins. Such modifications, despite solving the problem, they increase the weight of the blade, which is by no means optimum. Even if the designer increases the blade structural twist (see section 2.2.5.) in order to increase edge-wise damping, this is not done necessarily in an optimum fashion when local interventions in the inner structure of the blade are employed (e.g. by increasing the thickness of the composite material towards the leading edge over the suction side and towards the trailing edge on the pressure side). However, an unbounded increase in FEC could entail implications in the operational loads. Blades with enhanced FEC, under the action of extreme flap-wise loads, usually tend to undergo high leading edge-wise deflections, which make the blade behave as a virtually forward swept blade. As a result of the forward sweep, the blade tends to twist towards stall and therefore will further increase flap-wise loading in normal operation.

A consistent and effective way to tailor wind turbine blades is to determine the design parameters within the course of an optimization process. The best combination of design variables is sought that mitigates stall-induced vibrations without deteriorating normal operation loading, using as objective function, some design cost parameter. This is the approach adopted in the present thesis. Two different FEC methods are employed for the idling DTU-10MW RWT in order to mitigate stall-induced edge-wise vibrations. The first FEC method considered, is the one typically employed by wind turbine manufacturers. The thicknesses of the blade section walls are varied asymmetrically between the suction and the pressure side. Higher thicknesses of uniaxial (UNIAX) and triaxial (TRIAX) layers are considered towards the Leading Edge (L/E) of the section on its suction side (segment “Leading” of Low Pressure - L/P side in Fig. 4.1, left) – while the thickness of the walls on the pressure side is reinforced towards the Trailing Edge (T/E) (segment “trailing” of High Pressure - H/P side in Fig. 4.1, left). The

second method is addressed in section 3.2.2.4. and 3.4.3. (previous chapter) and by the authors in [49]. It consists of shifting the two spar caps in opposite directions. The main difference of the present study is that the displacement of the caps is not fixed along the blade span but a distribution is sought having parameters that are design variables in the optimization process.

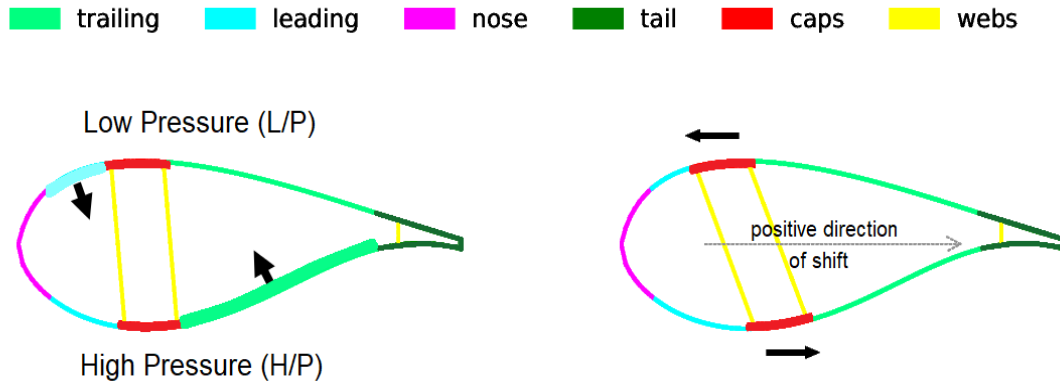


Figure 4.1: Definition of blade cross-section, demonstrating the material (left) and geometrically (right) based FEC through appropriate asymmetric thickness increase or displacement of the spar caps.

The design parameters in both methods are optimized within a complete Multi-Disciplinary Aero-elastic Optimization (MDAO) loop, in which the objective function is the overall LCoE of the wind turbine. The assessment of the potential design solutions considers both the critical survival wind load cases but also the most critical operational load cases, with the aim to ensure that design modifications that improve the loading of the idling rotor do not entail a deterioration in the operational loading characteristics. The last step of the optimization analyses is to combine both FEC methods and at the same time, apply a moderate material BTC [67],[100] through the introduction of an offset angle to the composite plies of the uniaxial (UNIAX) material over the spar caps of the blade, aiming at compensating any increase in the operational loads due to FEC. It is required that the maximum obtained Tsai-Hill criterion values in the optimum design [98] do not exceed those of the reference blade under operational ultimate loads, which is included as constraint in the optimization process. This is a deliberate choice, which entails a more conservative design than the one that satisfies the requirement that Tsai-Hill values do not exceed the unit failure threshold. However, it is a choice that avoids the excessive increase in safety factors (material γ_m or/and loads γ_L) and ensures that the optimum blade design is directly comparable to the reference blade.

The minimization problem is divided into two loops with the aim to moderate the computational cost of the optimization loop [49],[100], as also done in section 3.3. The outer loop specifies the parameters of FEC and BTC. In the present work, these parameters are (i) the thickness distribution along the blade

span of the L/P “leading” and H/P “trailing” segments of the cross-sections in the FEC method (see Fig. 4.1, left), (ii) the displacement of the caps in the geometrical FEC method (see Fig. 4.1, right) and (iii) the ply offset angle of the material BTC blades. Furthermore, the outer loop adjusts the geometric characteristics of the blade (blade planform, i.e. the twist angle or/and chord distribution) and evaluates the cost function (LCoE). The inner loop specifies an overall, uniform thickness coefficient for the walls of every cross-section that varies along the span. Its purpose is to estimate the thickness of the blade walls in such a way as to maintain the maximum values of Tsai-Hill criterion of the reference blade (constraint of the optimization process). This part of the optimization process is the most time consuming because it includes the computation of the ultimate resultant loads using hGAST, as well as the calculation of the beam properties and stress distributions of the “*modified*” blades based on the FEC and BTC with the cross-section tool.

4.2. Application examples

In Chapter 3, passive load control techniques led to the reduction of the thicknesses of the blades’ inner structure walls and by that to the reduction of the overall mass of the blade, keeping the maximum values of Tsai-Hill criterion along the blade unchanged - relative to the reference wind turbine (see appendix A). Such intervention has direct effect on the CAPEX of the rotor and thereby on LCoE. However, several studies [18] have indicated that a more effective way for suppressing LCoE is to capitalize reduced loading for enhancing energy yield by increasing the rotor radius (keeping the same rated power – reducing rotor specific power). So, the first application example of the present chapter evaluates the possibility of increasing the rotor diameter, by applying material BTC. In this case, as in the applications of the previous chapter, the research focuses on the Extreme Turbulence Model (ETM), i.e. DLC-1.3 at 13 m/s - while again a short simulation window of 150sec has been adopted during the optimization procedure. However, as also done in the application examples of the previous chapter, the final optimized designs are verified in the last step through three 10min simulations. In the second application example, the research has focused on the combined application of the two FEC methods (geometric and material) as well as of material BTC in view of further reducing LCOE by alleviating idling operation loads. The above design requires the aero-elastic evaluation of the designs both for normal operation conditions with extreme turbulence (DLC 1.3, at 13 m/s) and for idling operation (DLC-6.2, at $+30^\circ$ yaw angle – see appendix A). It is noted that in the idling state, edgewise instabilities may be triggered long after the initiation of the simulation. So, a larger time span (of about 300sec) is considered during the optimization process.

4.2.1. LCoE minimization through MDAO, using BTC techniques

The design of the new “*modified*” blade is performed in the context of a MDAO loop in which the objective function is the LCoE (minimum LCoE). Design variable are:

- The thickness of the inner structure walls: a uniform thickness reduction factor is applied over every cross-section of the blade, which is though varied independently among the different cross-sections. As mentioned earlier, this is exclusively handled by the inner optimization loop.
- The ply offset angle of BTC: a constant offset of the UD plies is considered that begins at the fixed span-wise position $r/R_{tip} = 20\%$ and extends up to the blade tip, following the findings in [49],[67].
- The blade radius and planform (chord/twist span-wise distribution): the reference span-wise chord distribution is only allowed to vary uniformly, while the twist distribution is approximated through three Bezier controls-points (C/P) from which only the last point is allowed to change with respect to y -axis.

The choice to maintain a low number of design variables in the parametrization of some of the design parameters is justified by the fact that small variations of the reference design (i.e. DTU-10MW RWT) are foreseen as a result of the application of BTC. It is noted that the thickness of all cross-sections is scaled proportionally with the chord to maintain constant relative thickness.

4.2.1.1. Description of the optimization procedure and results

Minimization of the LCoE is performed under the assumption that the rated power of $10MW$ remains fixed and the maximum Tsai-Hill failure criterion value of every cross-section along the blade span does not exceed the value of the corresponding section of the reference blade. During the optimization, all other components of the DTU-10MW RWT but the blades, remain unchanged (e.g. tower and drive train). Unchanged also remain the airfoil type distribution, the lamination sequence and the properties of the materials used in all blade sections. In every optimization iteration, the generator characteristic for optimum speed control is adjusted in order to ensure that C_p^{max} tracking is effectively performed. It is noted that as a result of the variation of the blade shape, the $C_p - \lambda$ curve of the rotor changes and that entails a possible change slightly in the optimum tip speed ratio value. Rated rotor speed is linearly reduced with the radius to keep a constant tip speed of $\sim 90 m/s$ (the tip speed of the DTU-10MW RWT).

Results of the MDAO process are presented next. The converged design is a “*modified*” blade with increased radius and weight by 3.7% and 1% respectively and with 5.9° offset ply angle on the uni-directional material over the caps. It produces 2.4% higher Annual Energy Production (AEP) and reduces LCoE by 0.71%, as compared to the reference design, with Weibull parameters of $C = 11 m/s$, $k = 2$ and availability of 99%. Table 4.1 compares the main characteristics between the reference and the “*modified*” design, including also in this comparison the configuration proposed in the Lightweight Rotor – L/R (the simpler case of $N = 2$) of the section 3.4.2., in which the design variables were the wall thickness and the offset ply angle.

Table 4.1: Comparison between the DTU-10MW RWT, the Lightweight Rotor – L/R from section 3.4.2. and the “modified” design with the optimized rotor for reduced LCoE.

parameter	reference	L/R	“modified”
Rated power [MW]	10.0	10.0	10.0
Rated omega [rpm]	9.6	9.6	9.3
Radius [m]	89.2	89.2	92.5
Blade mas [tn]	40.0	36.8	40.4
Combined moment at blade root [MNm]	64.0	59.9	70.9
AEP [GWh]	45.1	50.2	51.4
W/T cost [\$]	14.67	14.59	14.95
LCoE [\$/MWh]	44.96	44.77	44.64

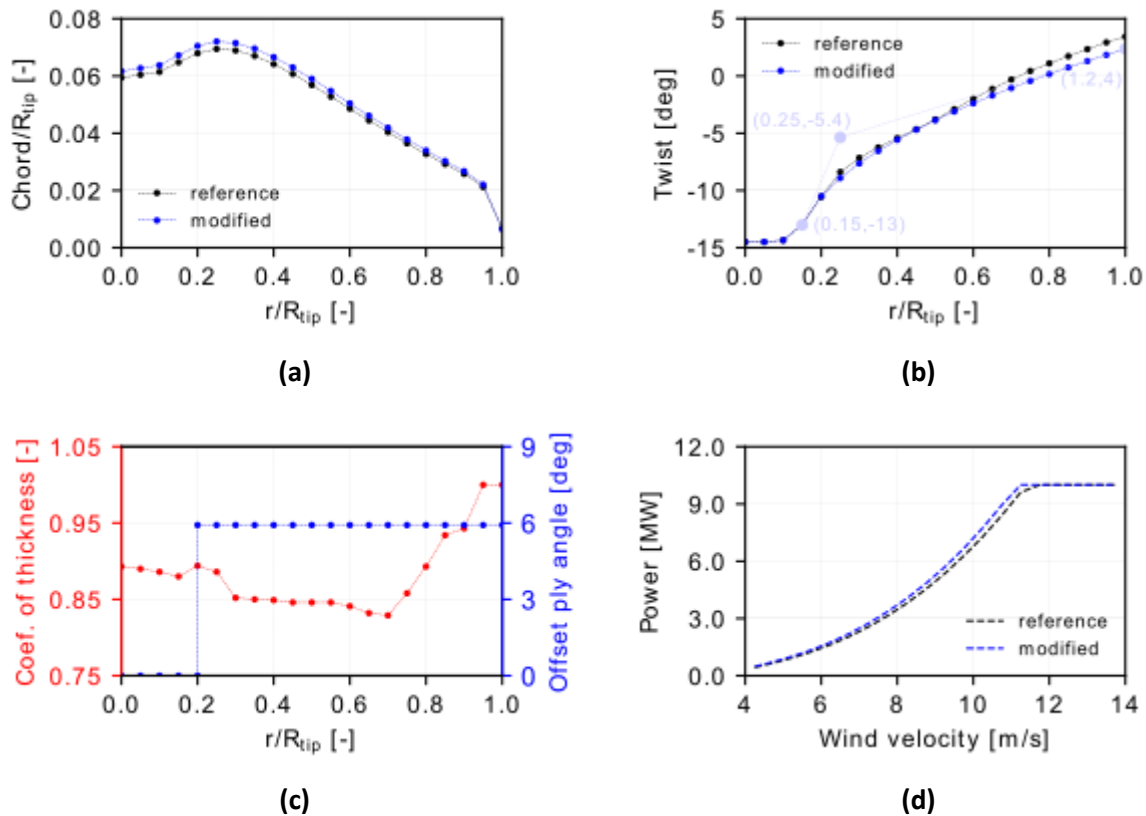
**Figure 4.2:** Comparison of the design variables between the reference and the “modified” blade design with $R_{tip} = 92.49m$, (a) Chord distribution, (b) twist distribution, (c) distribution of thickness coefficient and offset ply angle and (d) power curve comparisons.

Fig. 4.2 compares the values of the design variables between the reference and the “*modified*” rotor design. In Fig. 4.2a and Fig. 4.2b the chord and twist distributions are provided. The chord of the “*modified*” design is increased by 7.6%. This is half the increase in radius, which implies that a more slender “*modified*” blade is obtained. The twist distribution presents a slight increase of about 1° at the tip. The faint blue marks in Fig. 4.2b indicated the three Bezier C/Ps considered as design variables for determining twist distribution. Fig. 4.2c shows the span-wise distribution of the predicted thickness reduction factor of the optimum blade. It is seen that an average thickness decrease of about 11 – 12% is obtained. In the same figure, the constant ply angle distribution of 5.9° , starting at $r/R_{tip} = 20\%$ is also included. Finally, Fig. 4.2d compares the power curves of the “*modified*” blade against the reference. Obviously, the “*modified*” design produces more power below rated as a result of the reduced specific power of the new rotor design.

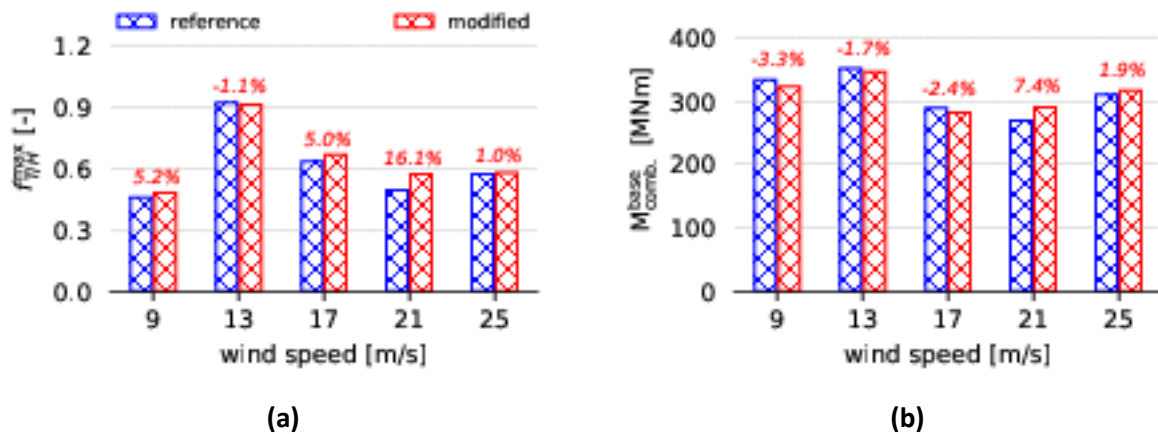
4.2.1.2. Assessment of “*modified*” design

Verification simulations of the newly designed rotor are presented in this section. These include modal characterization of the new wind turbine and more detailed aero-elastic simulations for a wider range of conditions (in accordance with IEC 61400-1 [53] specifications). At first, the eight first natural frequencies at standstill of the reference and the modified turbine are compared in Table 4.2. The frequencies obtained through the direct up-scaling of the reference turbine with Scaling Factor $S/F = 1.037$ are also provided as a fairer basis of comparison with the modified configuration. As mentioned, the rated rotor speed is set to be inversely proportional to the radius. It is seen that the modifications performed are not expected to significantly affect the overall dynamic behavior of the coupled wind turbine system, as the maximum frequency difference between the up-scaled and the “*modified*” rotor is limited to 3.7%.

Next, ultimate loads results of the two configurations are compared. The results stem from time domain aero-elastic simulations for the IEC 61400-1 DLC-1.3, which is the DLC considered in the MDAO process. Three wind speeds (of 10min duration each) are simulated considering the wind speed range [9 – 25 m/s]. In Fig. 4.3a, the maximum Tsai-Hill failure criterion values recorded along the span of the two blade configurations are compared. The results confirm that the most load-challenging wind velocity is that of 13 m/s. It is noted that although a constraint is set on maximum equivalent stresses, the maximum stresses of the optimized “*modified*” blade do not exceed those of the reference design. Furthermore, a 1.1% reduction is eventually achieved for the optimized design. A reduction in the maximum stress of the optimized blade is also achieved at all other wind speeds. It is also important to note that only at the wind velocity of 13 m/s the Tsai-Hill value approaches the failure limit of 1, while at all other wind speeds remains within the range of [0.45 – 0.70] both for the reference and for the “*modified*” blade.

Table 4.2: Standstill natural frequencies of the DTU-10MW RWT, the up-scaled $S/F = 1.037$ and the “modified” design.

mode shape	reference	up-scaled	“modified”
1 st tower bending side-side	0.250	0.241	0.250
1 st tower bending fore-aft	0.253	0.244	0.253
1 st symmetric rotor edge-wise/drive-train	0.521	0.502	0.513
1 st asymmetric rotor flap-wise (yaw)	0.550	0.530	0.540
1 st asymmetric rotor flap-wise (tilt)	0.595	0.574	0.584
1 st symmetric rotor flap-wise	0.651	0.628	0.638
1 st asymmetric rotor edge-wise (vertical)	0.969	0.934	0.964
1 st asymmetric rotor edge-wise (horizontal)	0.982	0.947	0.975

**Figure 4.3:** Ultimate loads analysis resulting from aero-elastic simulations of DLC-1.3 for various wind speeds: (a) maximum value of Tsai-Hill criterion ($f_{T/H}^{max}$) along the blade span and (b) maximum value of the combined bending moment at the tower base. Percentage relative differences with respect to the reference configuration are shown above the bars.

In Fig. 4.3b, the tower based ultimate combined bending moment of the two configurations is compared. As seen in the plot, tower maximum load of the “modified” configuration is lower (by 1.7%, obtained at 13 m/s) than that of the reference turbine. It is noted that the design of the tower is out of the scope of the present work and therefore no constraint on rotor thrust has been imposed in the optimization loop. Presently we aim on interventions only at the rotor level, which entail reduction of

the LCoE. It is rather incidental that tower loads remain almost unchanged and this is due to the fact that although the rotor disk area of the optimized rotor increases, the newly design blades are more slender and rotate at a lower angular velocity (constraint on linear tip speed). Therefore, as long as the ultimate tower loads are not exceeding the maximum values of the reference turbine, the introduction of the tower in the design process is not considered necessary. However, in future studies, tower wall thicknesses can be also introduced as design variables and this could lead to even lower LCoE values.

4.2.2. LCoE minimization through MDAO, focusing on storm conditions

In this section, the different optimization scenarios addressed in the present work are detailed, while further specific information concerning the simulations performed for the assessment of candidate optimum solutions is provided.

4.2.2.1. Description of the design cases

In Table 4.3, the five optimization cases (CASE A, B, C, D and E) examined in this section are listed along with the passive control methods applied.

Table 4.3: DTU-10MW RWT passive control designs aimed at minimizing the LCoE.

design	material FEC	geometrical FEC	re-twist	material BTC	Comments
reference					DTU-10MW RWT
CASE A	√				FEC control
CASE B	√	√			FEC control
CASE C	√	√			FEC control
CASE D	√	√	√		FEC with re-twist
CASE E	√	√	√	√	FEC&BTC with re-twist

- **CASE A:** concerns material FEC which is based on thickening the L/P “leading” and the H/P “trailing” element of the cross-section walls, respectively (see Fig. 4.1, left). In this optimization study, a different coefficient for the wall thickness increase is applied to each element that varies along the span of the blade. The radial distributions of the two coefficients (i.e. for the L/P and H/P sides) are parameterized using global Bezier interpolation functions with three C/Ps per distribution. In the optimization process, three parameters per distribution (six in total) are considered as design

variables: (i) the value of the coefficient of the first C/P, which is fixed at the blade root, (ii) the value of the coefficient of the second C/P and (iii) its radial position. The third C/P is considered fixed at the blade tip with a fixed value of one (i.e. no thickness change is performed). In addition to the above two coefficients applied to specific segments of the cross-section, a global thickness coefficient is also considered for all the elements in the cross-section. It varies radially, in a discrete manner at the twenty-one radial sections analyzed. In CASE A the planform of the blade is considered fixed and identical to that of the reference blade.

- CASE B: concerns geometric FEC which is based on the displacement of the spar caps of the two sides of the cross-section in opposite directions (see Fig. 4.1, right). In this case study, a different percentage shifting (relative to the section chord length) of every cap is considered that varies along the span of the blade. The radial distributions of the percentage displacements (for the L/P and H/P sides) are parameterized using again global Bezier interpolation functions with three C/Ps. As previously, the same three parameters in each distribution are considered as design variables and the remaining three parameters are kept fixed. Further, a global thickness coefficient is applied to all the elements in the cross-section at twenty-one radial stations while the planform of the blade is considered fixed.
- CASE C: concerns the combined application of both the above two methods. It is sought whether a combination of the two methods could be more flexible in tailoring the structural twist angle distribution. In order to reduce the total number of design variables (of the combined application of the two methods) from twelve to eight, the radial positions of the intermediate (mid-span) Bezier C/Ps of all curves are maintained fixed to the positions that simulations of CASE A and B converged to. The above choice implies that the overall shapes of the radial distribution curves would be quite insensitive to the exact radial placement of the intermediate C/P.
- CASE D: concerns the combined application of both the above two methods (i.e. CASE C) in conjunction with the re-design of the blade twist. As mentioned in the introduction section of his chapter, FEC entails an indirect, unfavourable BTC effect, induced by the forward sweep deflection. The above BTC effect causes a nose-up twisting of the blade sections that gives rise to increased flap-wise loads. Re-twisting of the blade could be a means for mitigating the above effect. The twist distribution of the blade is parameterized using global Bezier interpolation functions with three C/Ps. The radial position and the twist of the first C/P are fixed at $r/R_{tip} = 0.15$ and $\theta = -13.1^\circ$. The radial position of the second and third C/P are fixed at $r/R_{tip} = 0.25$ and 1, respectively, while the twist angle of these C/Ps is considered as a design variable.
- CASE E: concerns the combined application of both the above two methods (i.e. CASE D) in conjunction with material BTC (application of offset angle theta to the UD plies over the spar caps, see Fig. 3.1). The aim of BTC in this case is to alleviate any negative effects of FEC on operational loads. BTC begins at $r/R_{tip} = 0.20$ and consists of only one design variable (a constant ply offset angle which is applied from $r/R_{tip} = 0.20$ up to the blade tip). The mechanism through which BTC alleviates loads is the nose-down twist rotation that takes place whenever the blade is subjected to excessive flap-wise deflections, acting as a passive control of the flap-wise loads of the blade [67].

The induced torsional deformation due to BTC suggests that effective optimization of the loading and of the performance requires a re-design of the blade aerodynamic twist. The same parameterization of the blade twist distribution, as well as of the FEC parameters is employed as in CASE D.

4.2.2.2. Material and geometric FEC (CASE A and B)

The optimization results of CASE A and B are presented in this section. In those two scenarios, the two FEC methods for the suppression of stall-induced vibrations are implemented and assessed separately, the one from the other.

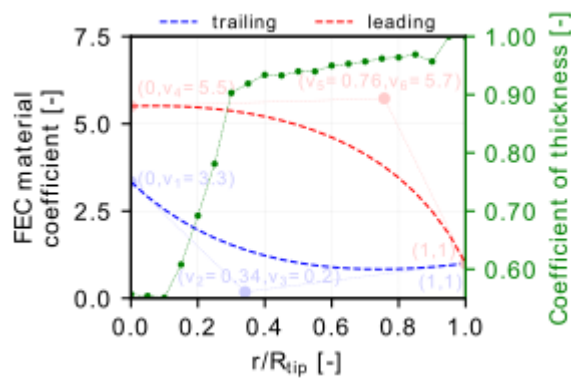


Figure 4.4: Material FEC (CASE A): coefficients of change in thickness of the materials “TRIAx” and “UNIAX”, for the regions H/P “trailing” and L/P “leading” and global coefficient of the cross-section thickness (with green color). Cyan and orange symbols depict control points, connected with straight lines.

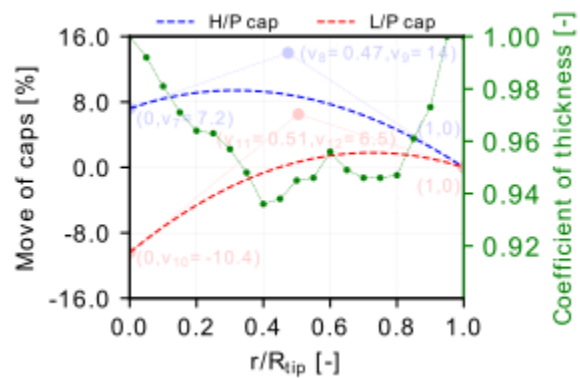


Figure 4.5: Geometric FEC (CASE B): span-wise distributions of percentage shift in the caps relative to the chord and global coefficient for the cross-section thickness (with green color). Cyan and orange symbols depict control points, connected with straight lines.

In Fig. 4.4, the optimum values of the six design variables ($v_1 - v_6$) of CASE A (material FEC) that define the radial distribution of the thickness increase coefficients in the walls of the L/P “leading” and H/P “trailing” elements are presented along with the corresponding Bezier curves. In the same figure, the global thickness variation coefficient of all the walls is also shown. As seen in the figure, a higher increase in the thickness is required for the “leading” element, all along the blade span. At the root of the blade, the thickness increase coefficient is equal to 5.5 for the “leading” element and 3.3 for the “trailing” one. This high increase in the thickness of the two elements is accompanied by a global reduction coefficient for the thickness of all walls of about 0.5. Beyond $r/R_{tip} = 0.30$, the global thickness coefficient returns to values slightly lower than 1, while the thickness increases coefficient for

the “leading” element still obtains high values (close to 5) that gradually decrease towards the blade tip. The thickness increase coefficient for the “trailing” element, beyond $r/R_{tip} = 0.30$, drops to values close to 1. Application of material FEC reduces blade mass by 10.3% and overall LCoE by 0.82%. A marginal increase in AEP of 0.12% is also obtained, which is due to the indirect twisting effect caused by FEC in normal operation. The virtual forward sweeping of the blade due to FEC cause nose-up twisting of the blade sections, which leads to slightly higher power output of the blade.

In Fig. 4.5, the optimum values of the six design variables ($v_7 - v_{12}$) of CASE B (geometric FEC) that define the radial distribution of the shift in the spar caps are presented along with the corresponding Bezier curves. The positive shift is the one towards the trailing edge T/E. In the same figure, the global thickness variation coefficient for all the walls is also shown. As seen in the figure, the L/P cap is shifted towards the leading edge by 10.4% at the blade root, while the displacement of the H/P is somewhat lower (7.2%) and it is towards the T/E. The displacement of the L/P cap decreases towards zero with the increase in the radial position. Some small positive displacements in the order of 1% are noted for radial positions higher than 0.5. It is important to point out that the effect on the cross-bending stiffness is obtained as a result of the motion of the tow caps and not as a result of their absolute position per se. This can be seen in Fig. 4.5, where although for $r/R_{tip} > 0.50$, the L/P cap moves towards the T/E, its relative displacement with respect to the H/P cap remains in the same direction. The displacement of the H/P cap remains high (7 – 10%) up to the radial station $r/R_{tip} = 0.50$ and thereafter, drops toward zero.

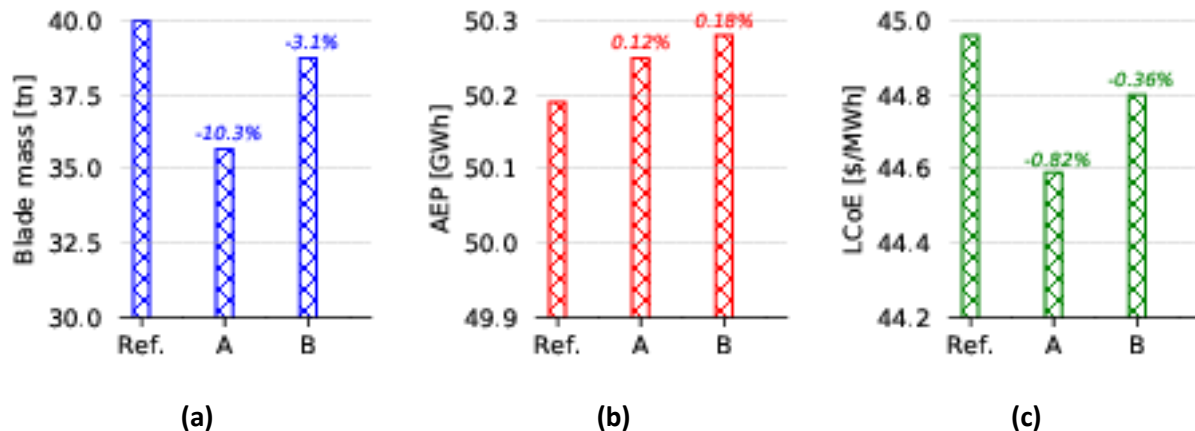


Figure 4.6: (a) Blade mass, (b) annual energy production and (c) Levelized Cost of Energy, of the material FEC (CASE A) and the geometric FEC (CASE B) designs and relative percentage differences with respect to the reference configuration.

A notable difference between the two methods is that while the material FEC attains the increase in cross-bending stiffness by intervening on the thickness of the L/P side (L/P “leading” element), in the geometric FEC, the increase in the cross-bending stiffness is mainly achieved by the backwards

displacement of the H/P cap. Therefore, it is a result of an intervention mainly on the H/P side. It should also be noted that the global thickness coefficient in the geometric FEC method remains close to 1 all along the blade span (minimum value ~ 0.94). Application of the geometric FEC reduces mass by 3.1% and LCoE by 0.36% (substantially lower reductions than those for the material FEC). Similar to CASE A, a marginal increase in AEP of 0.18% is also obtained, as shown in Fig. 4.6.

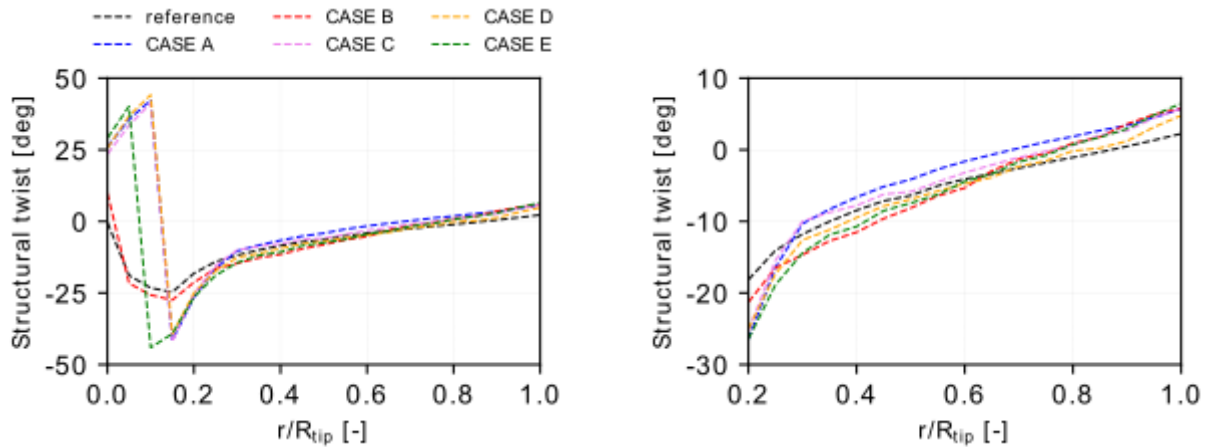


Figure 4.7: Structural twist distribution of the design configurations: on the left plot shows the full distribution and on the right the range 0.2 – 1.0 (zoom).

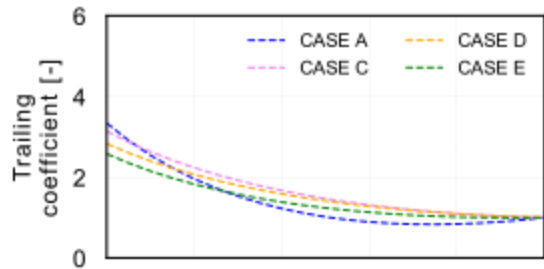
In Fig. 4.7, the structural twist distribution (see definition of structural twist in [49]) of CASE A and B is depicted (along with all other configurations analyzed in the next section). It is seen that material FEC gives rise to high local increase in the structural twist to feather direction (negative twist values) in a radial range of 0.10 – 0.20. On the other hand, geometric FEC causes an almost constant and much smaller shift in the structural twist all along the span. The positive structural twist angles at the innermost sections ($r/R_{tip} < 0.10$) do not affect the stability characteristics of the blade. They are obtained as a result of the re-distribution by the optimizer of the material over the root sections in a way that loads are supported. The minor effect of the geometric FEC on the structural twist justifies its limited capability to reduce blade mass and LCoE.

4.2.2.3. Combined application of passive control methods (CASE C, D and E)

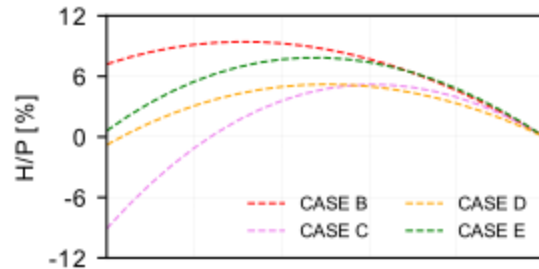
In the present section, CASE C, D and E, in which combined application of different passive load control methods is performed, are addressed.

In CASE C, combined application of the two FEC methods (material and geometric) is performed. Fig. 4.8 and 4.9 provide the radial distributions of the material thickness coefficients and of the caps' displacement, respectively for CASE C and all other configurations analyzed. It is seen that the combined

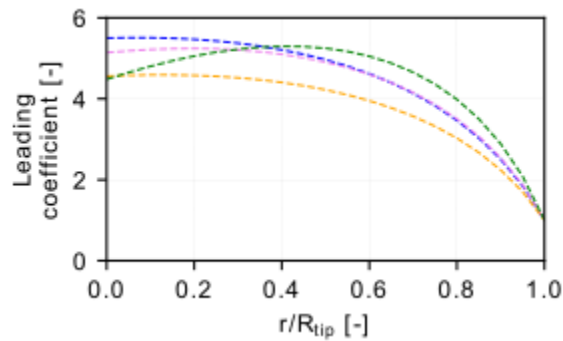
application of the two methods does not significantly alter the design parameters of the material FEC. On the other hand, the radial distributions of the caps' displacement appear to be much more sensitive (see Fig. 4.9). This is justified by the observation made in section 4.2.2.2. that the material FEC is far more effective in adjusting the structural twist. Thus, while the predominant design variable that affects structural twist exhibits similar behavior with that of CASE A, the secondary parameter, which only has an additive effect, is let free by the optimizer to vary a lot more (i.e. the optimum is rather flat). It is interesting to note that, in particular in CASE C, the optimizer finds that the optimum displacement for the H/P cap is towards the L/E, while the L/P cap remains almost un-displaced. Although this seems to be a paradox on first reading, it is explained by the fact that moving the H/P cap towards the leading edge leads to an increase in the H/P "trailing" element, leaving more space for material FEC to adjust the cross-bending stiffness. The reduction in the mass achieved by CASE C is 13.3%, which is more or less, the summation of the reductions achieved in CASE A and B. The reduction in the LCoE in CASE C is 1.02%, slightly lower than the sum of the reductions attained in CASE A and CASE B. Similar to CASES A and B, a very small increase in AEP of 0.16% is obtained.



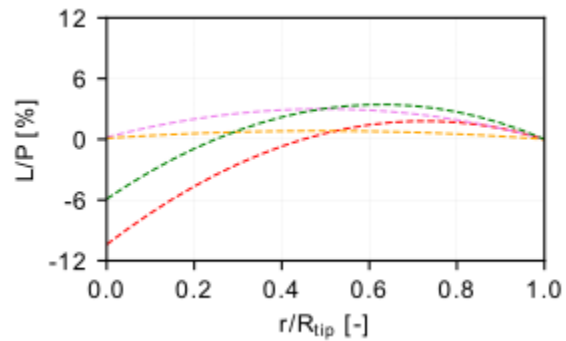
(a)



(a)



(b)



(b)

Figure 4.8: Distribution of the material FEC coefficient for the (a) leading and (b) trailing region of the cases: A, C, D and E.

Figure 4.9: Distribution of the geometric FEC coefficient for the (a) high-pressure and (b) low-pressure cap of the cases: B, C, D and E.

In CASE D, the re-twist of the blade acts as an additional mechanism for adjusting structural twist. As seen in Fig. 4.7, the structural twist distribution of CASE D configuration resembles that of CASE A. This means that, as in CASE C, the structural twist distribution is dictated by material FEC. Further, the re-twisting of the blade at its tip towards the feather direction, as shown in Fig. 4.10, enhances the cross-bending stiffness at the tip region of the blade. As in CASE C, the thickness coefficients of material FEC are similar to those of CASE A and C (see Fig. 4.8). Slightly smaller thickness increase coefficients are noted for the H/P “leading” element, which are compensated by the slightly higher displacement of the H/P cap towards the L/E, as compared to CASE C (see Fig. 4.9). CASE D has an incremental effect on mass reduction as compared to CASE C (14% mass reduction vs. 13.3% for CASE C) and it has a neutral effect on LCoE (reduction of 1.02% as in CASE C). As in all previous cases, a marginal increase in AEP of 0.14% is noted.

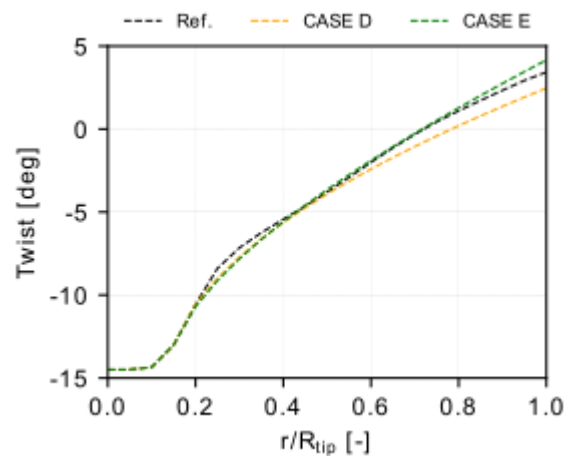


Figure 4.10: Twist distribution of the cases: reference (A-C), D and E.

The results of CASE E, in which all interventions are combined together, are summarized in Fig. 4.11. The figure provides the optimum distributions of the design parameters in the passive control modifications considered. The optimum ply offset angle obtained by the optimizer is 6.2° , as shown in Fig. 4.11b, being totally aligned with previous studies [67],[100],[98]. Furthermore, BTC allows for much higher global sectional thickness reduction coefficients as compared to CASES A and B. As seen in Fig. 4.11d, the average value of the global thickness coefficient is ~ 0.75 . The result of the blade re-twist is a twist to feather at the inner part of the blade and a twist to stall at the tip region (see Fig. 4.10 and 4.11c). The aim of the first is to increase the structural twist at the inboard sections. The aim of the latter is to compensate the twisting of the blade towards the tip due to the BTC effect. As in CASES C and D, the structural twist distribution is dictated by the material FEC (see Fig. 4.7). Moreover, the distributions of the thickness coefficients of the material FEC are very similar to those of all previous cases (see Fig. 4.8 and 4.11a). As opposed to CASES C and D, a notable shift in the L/P cap towards the L/E is obtained in

this case (-5.9% at the root of the blade), while the displacement distribution of the H/P cap is very similar to the one in CASE D (see Fig. 4.11b).

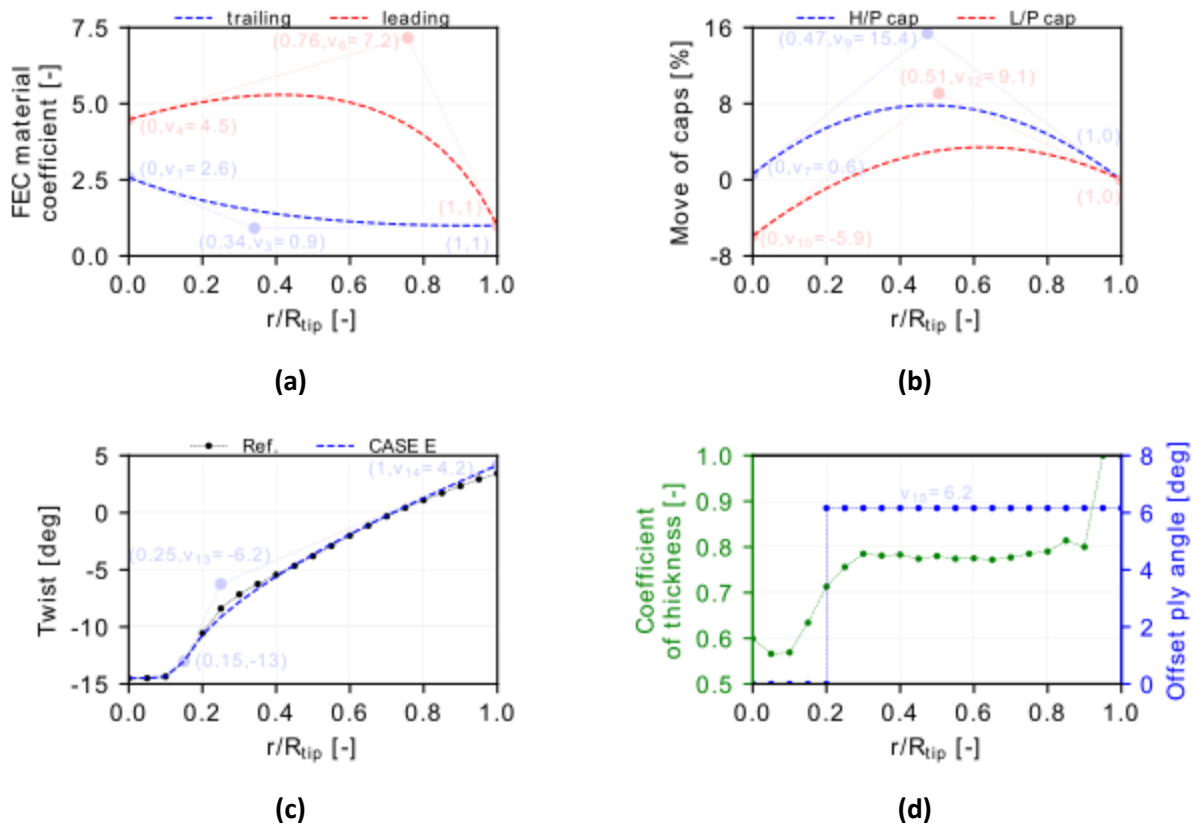


Figure 4.11: CASE E: distribution of (a) FEC material approach, (b) FEC geometrical approach, (c) twist and (d) offset ply angle of ‘UNIAX’ material and coefficient of wall thickness.

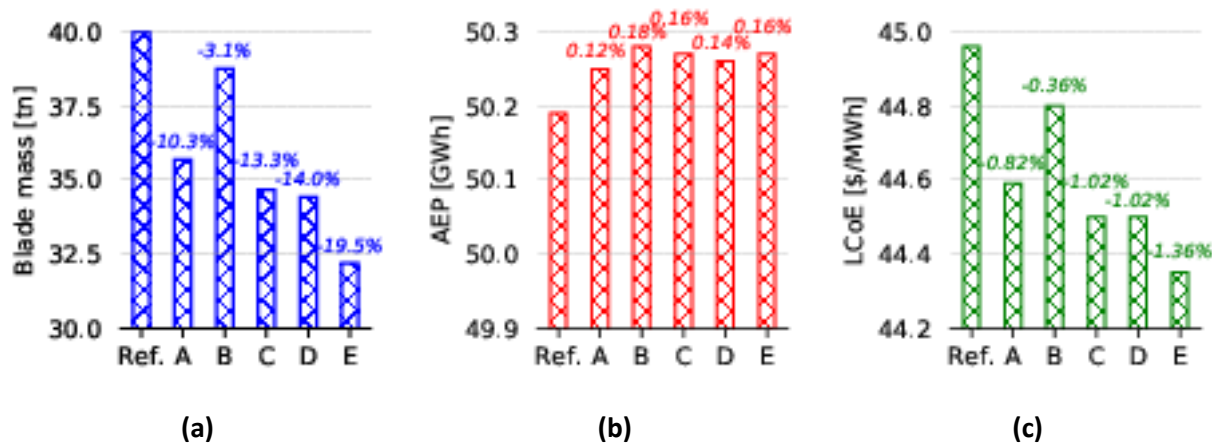


Figure 4.12: (a) Blade mass, (b) annual energy production and (c) levelized cost of energy of the different designs and relative percentage differences with respect to the reference configuration.

CASE E has a substantial additional mass reduction effect as compared to CASE D (19.5% vs. 14% of CASE D), which is obviously due to the application of the BTC. The LCoE reduction in CASE E is 1.36%, the highest of all studied cases. Again, a marginal increase in AEP of 0.16% is attained. Fig. 4.12 summarizes the optimum value of the blade mass, AEP and LCoE, obtained with the MDAO process for the considered designs (CASES A-E). For the sake of completeness, all designs are shown in the figure, including CASES A and B that have already been presented in Fig. 4.6.

Table 4.4: Results for the design variables of the considered configurations. Numbers in red correspond to design variable values that remain fixed in the simulation.

	CASE A	CASE B	CASE C	CASE D	CASE E
V1 (trailing/root C/P in y-axis)	3.34	-	3.14	2.83	2.58
V2 (trailing/interm. C/P in x-axis)	0.34	-	0.34	0.34	0.34
V3 (trailing/interm. C/P in y-axis)	0.18	-	1.18	1.18	0.91
V4 (leading/root C/P in y-axis)	5.50	-	5.14	4.56	4.48
V5 (leading/interm. C/P in x-axis)	0.76	-	0.76	0.76	0.76
V6 (leading/interm. C/P in y-axis)	5.73	-	5.90	4.92	7.17
V7 (H/P cap/root C/P in y-axis)	-	7.20	-9.10	-0.80	0.60
V8 (H/P cap/interm. C/P in x-axis)	-	0.47	0.47	0.47	0.47
V9 (H/P cap/interm. C/P in y-axis)	-	14.00	13.80	10.80	15.40
V10 (L/P cap/root C/P in y-axis)	-	-10.40	0.20	0.10	-5.90
V11 (L/P cap/interm. C/P in x-axis)	-	0.51	0.51	0.51	0.51
V12 (L/P cap/interm. C/P in y-axis)	-	6.50	5.90	1.60	9.10
V13 (twist/interm. C/P in y-axis)	-	-	-	-5.54	-6.24
V14 (twist/tip C/P)	-	-	-	2.47	4.16
V15 (BTC angle)	-	-	-	-	6.16
Number of design variables	6	6	8	10	11

Finally, Table 4.4 details the design variables considered per design (CASES A-E). In the table, the optimum value per design variable is provided for all the cases considered. The horizontal lines are introduced to distinguish the various design interventions performed, i.e. the material FEC, the geometric FEC, the re-twist and the material BTC.

4.2.2.4. Verification of optimum designs

In the present section, verification of the optimum design A, B and E, from sections 4.2.2.2. and 4.2.2.3., is performed. The strength characteristics of the optimum, tailored turbines are verified – as in any design configuration that has been developed (see section 3.4.1.2., 3.4.2.2., 3.4.3.2. and 4.2.1.2.) through detailed, time domain aero-elastic simulations of a selected subset of ultimate load cases for the IEC 61400-1 standard, simulated using hGAST. The blade and tower loads in the tailored, optimized configurations are compared against those of the reference wind turbine. The aim of the verification step is to perform a thorough check of the final optimum designs (the two FEC configurations and the configuration that combines all design interventions), which consists of a more extended list of DLCs and conditions and wider evaluation windows (in terms of simulated time series lengths) compared to those considered within the optimization loop.

Table 4.5: Standstill natural frequencies of the reference DTU-10MW RWT and FEC designs. Relative percentage differences with respect to the reference configuration are also provided.

mode shape	reference	CASE A	CASE B	CASE E
1 st tower bending side-side	0.250	0.8%	0.4%	2.0%
1 st tower bending fore-aft	0.253	0.8%	0.4%	1.6%
1 st symmetric rotor edge/drive-train	0.521	-3.5%	-0.4%	0.8%
1 st asymmetric rotor flap-wise (yaw)	0.550	-3.3%	-1.8%	-2.0%
1 st asymmetric rotor flap-wise (tilt)	0.595	-3.9%	-2.7%	-3.9%
1 st symmetric rotor flap-wise	0.651	-2.0%	-1.1%	-1.4%
1 st asymmetric edge-wise (vertical)	0.969	-9.1%	-0.8%	-5.7%
1 st asymmetric rotor edge-wise (horizontal)	0.982	-8.5%	0.1%	-5.0%

Before assessing the loads in the different designs, a comparison of the natural frequencies of the variants A, B and E with the reference turbine is performed in Table 4.5, in order to identify possible critical changes in the dynamic characteristics of the new designs. As a result of the increased structural coupling in the flap-wise and edge-wise directions and the material re-distribution over the cross-sections, the frequencies of the root bending modes drop (both the flap-wise and edge-wise). Higher reductions, in the order of 8 – 9%, are noted in the frequencies of the asymmetric edge-wise modes, in the application of material FEC. The maximum frequency reduction in the flap-wise modes is in the order of 3.5 – 4% and it is again, obtained for configuration A (material FEC). On the other hand,

geometric FEC entails a lower reduction in the natural frequencies. Finally, the reduction in the frequencies noted in CASE E is similar to that in CASE A, most probably dictated by the material FEC. A slight increase is noted in the frequencies of the tower modes as a result of the lower-rotor mass achieved by all tailored designs. The frequency comparisons in Table 4.5 indicate that the performed structural modifications are not expected to significantly alter the overall dynamic behavior of the coupled wind turbine system.

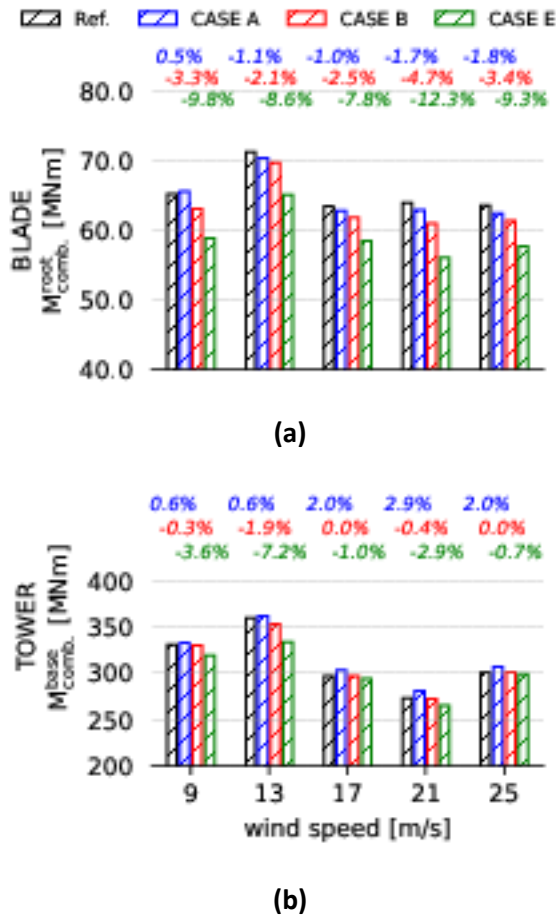


Figure 4.13: DLC-1.3 ultimate loads vs. wind speed of examined configurations (including safety factors) maximum combined bending moment (a) at the blade root and (b) at the tower base.

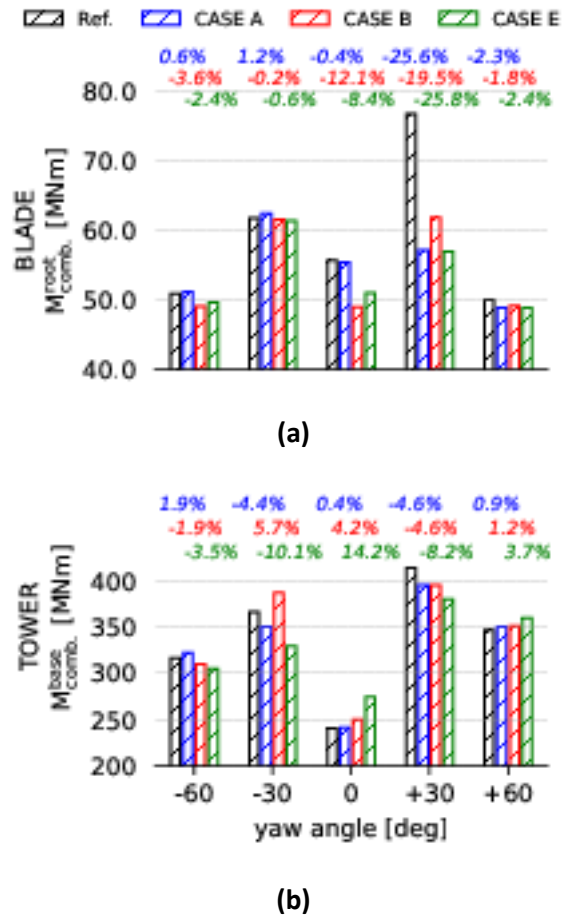


Figure 4.14: DLC-6.x ultimate loads vs. yaw angle of examined configurations (including safety factors) maximum combined bending moment (a) at the blade root and (b) at the tower base.

In Fig. 4.13 and 4.14, the ultimate loads of the blades and the tower of the three turbine configurations (A, B and E) are presented as a function of the wind speed for DLC-1.3 and as a function of the yaw angle

for DLC-6.1 and 6.2. The first important observation in Fig 4.14a is that the ultimate blade load of DLCs-6.x (yaw angle of $+30^\circ$) is effectively reduced in all configurations. A maximum reduction of 25.8% is achieved for configuration E. A similar reduction is achieved with configuration A (25.6%), while a reduction of 19.5% is obtained for configuration B. In fact, the ultimate loads of DLCs-6.x even drop below the ultimate load of DLC-1.3 (obtained at a wind speed of 13 m/s) in all optimized designs. The suppression of stall-induced vibrations in the rotor edge-wise modes in idling operation indirectly affects tower loads (see Fig. 4.14b). The ultimate tower load decreases by 4.6% in configurations A and B and by 8.2% in configuration E. Furthermore, the optimized application of FEC, as well as the combined application of FEC and BTC, does not incur any increase in the blade loads in normal operation. As seen in Fig. 4.13a, ultimate blade loads of all configurations are lower than those of the reference blade. Tower normal operation loads are also moderated, except for those in configuration B, for which a slight increase of 0.6% is noted in the maximum normal operation load while an increase up to 2.9% is seen at a wind speed of 21 m/s (see Fig. 4.13b). However, it should be stressed that normal operation tower loads are far less than idling operation tower loads. DLC-6.2 is definitely the design-driving load case, both before and after the structural and aerodynamic interventions performed in the present study.

4.3. Summary

The present chapter focused on the complete multi-disciplinary design of 10MW wind turbine blades. By complete multi-disciplinary is meant that all disciplines of the physical system are considered in the analysis (servo-aero-elastic simulations of the full wind turbine system are performed for determining design loads), while design variables include both structural and aerodynamic parameters of the system including the parameters of the passive control methods addressed. The assessment of the candidate solutions is performed on the basis of LCoE using the cost model presented in section 2.3.2. In the above context the following application examples are considered:

- First, the rotor radius, the planform of the blade, the thickness of the composite material walls and the parameters of the material BTC (ply offset angle), are considered as design variables of the optimization study. The results of the analysis indicate that an overall 0.71% reduction in LCoE ($0.32\text{ \$/MWh}$) can be achieved if the reference blade is elongated by 3.7%. A moderate optimum material ply offset angle of 5.9° is obtained while the optimized blade design has 1% higher mass as compared to the reference (note that geometric similarity, power 3-law, would imply a 12% increase in mass). The increase in energy production by the newly designed rotor design is 2.4%.
- Then, design modifications of the blade inner structure that lead to suppression of the stall-induced edge-wise vibrations in idling operation are assessed. The design parameters of two FEC methods (material and geometric) are tested following a step-wise approach, in which the two methods were first evaluated separately, then in combination and finally, they were blended with material BTC and re-twist of the blade. Optimization studies indicated that material FEC, which is based on the asymmetrical increase in the thickness of the walls of the L/P side towards the section nose and of

the H/P side towards the T/E, is more effective in suppressing stall-induced instabilities and reducing LCoE than the geometric FEC, which is based on the displacements of the spar caps of the L/P and H/P sides in opposite directions. Geometric FEC leads to an almost constant shift in the structural twist angle all along the blade span, while material FEC results in a high local increase in the cross-bending stiffness and the corresponding structural twist angle in the inboard part of the blade. The latter turns out to give a mass reduction in the blade of 10.3% and a corresponding decrease in LCoE of 0.82%, while the former gives rise to a reduction in mass of 3.1% and of LCoE of 0.36%. Combined of the two methods appears to have an accumulative effect, while additional application of BTC with a parallel re-twisting of the blade provides a maximum reduction in mass and LCoE of 19.5% and 1.36%, respectively.

This page intentionally left blank

Chapter 5

5. Conclusions

This is the concluding chapter of the PhD thesis, which briefly discusses the most significant conclusions and outcomes of the work. Among others, in the following paragraphs the published articles produced by the thesis, are listed and briefly discussed. Finally, some unanswered questions that arose from this work and which could feed future research work are recorded.

5.1. General concluding remarks

The overall target set by the present thesis, is the development of an Multi-Disciplinary Aero-elastic Optimization (MDAO) framework for the optimal design of wind turbine systems. The multi-disciplinarity of the developed optimization framework consists in the concurrent treatment of the aerodynamics of the rotor, the structural and aero-elastic response of the full wind turbine as well as the feedback of the controller, within the same simulation environment which also serves the simultaneous optimization of the external shape and the inner structure of the blades. In addition, the possibility of suppressing Levelized Cost of Electricity (LCoE) through the combined application of Bend-Twist-Coupling (BTC) and Flap-Edge-Coupling (FEC) passive load control techniques is assessed, by optimally designing the offset angle of the plies of the UD material on the caps of the blades, the sweep angle of the blades, the geometry of the shear webs/caps and the thickness of the blade skin.

5.1.1. Summary of thesis

The thesis begins with the description of the underlying theory of each individual numerical module that has been used by the current work in order to compose an MDAO framework for the design optimization of large wind turbines. The toolbox employed by the present thesis consists of i) in-house

tools developed in previous theses, which have been thoroughly used and validated by the laboratory of aerodynamic of NTUA in the context of several EU and national projects in the past years, ii) existing publicly available tools and iii) newly developed tools which have been specifically designed and realized in order to meet the requirements of the developed optimization framework. The toolbox of the MDAO framework developed by the thesis consists of:

- hGAST: an in-house multibody, FEM, servo-aero-elastic tool. In this solver, the full wind turbine is considered as a multi-component dynamic system having as components the blades, the drive train and the tower, all approximated as Timoshenko beam structures. Assembly of the above components into the full system is carried out in the framework of the so-call multibody approach. hGAST has been thoroughly validated in the framework of numerous EU and national projects in the past. The purpose of hGAST within the optimization framework is to provide the resultant design loads at every location on the wind turbine. These design loads are obtained by simulating the operational envelope of the wind turbine as it is specified by the IEC standard.
- Cross-sectional analysis tool: an in-house cross-sectional analysis tool based on thin lamination theory. The departure point for the development of this tool was an existing tool by University of Patras, which provides the equivalent beam stiffness and mass characteristics of wind turbine blades' cross-sections, while it is capable of treating the anisotropic behavior of material plies. The existing tool was extended and upgraded to be able to compute fully populated stiffness matrices, taking into account all material driven coupling effects in order to be able to be used for the modeling of BTC or/and FEC blades. In addition, the tool was upgraded to be able to provide stresses and Tsai-Hill failure criterion distributions over the cross-sections of the blades, based on the resultant design loads provided by hGAST. Mass and stiffness properties predictions by the model as well as stresses results are compared against results of the publicly available BECAS tool for the DTU-10MW RWT. The purpose of the thin lamination tool within the optimization framework is to provide equivalent beam properties of the candidate blade designs to hGAST for the aero-elastic analyses and to evaluate stresses distributions along the blade span based on the design loads predicted by hGAST.
- Cost model: a cost model of the full wind turbine was set up by combining models from the literature that estimate the cost of the materials of the various components along with the cost of the manufacturing processes. The detailed cost model by NREL (in the thesis it is called as NREL-2019) is adopted for the blades, while the cost of the other parts of the rotor (i.e. hub, spinner and pitch mechanism) is based on empirical expressions. The cost estimation for the generator, the gearbox and the tower is derived through the up-scaling of the data of a reference wind turbine of nominal power of $1.5MW$. The validation of the aforementioned model has been performed both against the detailed cost model of NREL for various blades which is available through the numerical tools of WISDEM, as well as against bibliographic data of complete wind turbine systems. The cost model constitutes the objective function of the optimization framework.
- Optimization methods: a number of state-of-the-art optimization methods have been tested in the present thesis. Each method presents some advantages, such as for example the ease of application

to each problem, the absence of the need of computing gradients and/or the speed of convergence. In the current thesis, three optimization methods have been employed: (i) the gradient-free COBYLA, (ii) the gradient based SLSQP and (iii) Hessian based Newton. The first two methods are publicly available in the SciPy library of Python, while the Newton's method has been programmed and utilized in two forms: the traditional one where the Hessian matrix is calculated in every iteration of the optimization process and the quasi-approach of BFGS, where the Hessian matrix is evaluated through a re-cursive relationship.

5.1.2. Application examples and main conclusions

The developed MDAO framework considers as design variables i) the aerodynamic shape of the blade (i.e. blade length, chord and twist distribution) ii) the geometry (e.g. position of spar caps, thickness of blade skin) and the material distribution of the blade inner structure (e.g. offset angle of UD plies on caps). A global, span-wise parameterization of the geometry is defined on the basis of Bezier curves for inner-structure parameters, such as the thickness of the skin walls or the position/orientation of the shear webs. A similar parameterization routine is defined for the representation of the external blade shape. A number of geometric constraints (e.g. maximum deflection of the blades) and loading constraints (maximum value of Tsai-Hill criterion along the blade span) are set and eventually MDAO environment provides optimal wind turbine designs, evaluated on the basis of the LCoE. It is fact that the the proposed designs, minimizing LCoE tend towards longer and lighter rotors (per unit length), which is in agreement with the literature [42],[105]. Also, when stall induced edgewise instability is considered in the optimization process, a blade with higher Flap-Edge-Coupling (larger value of structural twist – along the span) is designed, as expected from previous developments [47].

At first, a preliminary evaluation of the capabilities both of active and passive load control techniques is performed through parametric studies aimed at tentatively exploring the design space of the possible solutions. These parametric studies aim at identifying the limits of their application and the anticipated benefits in terms of load reduction. In this context, passive load control methods are compared against their commonly used active load control counterparts. Evaluation studies of the combined application of IPC and IFC, performed in the framework of the present work indicated that active load control techniques can reduce the blade flap-wise fatigue load by about 25% (sole application of IPC leads to slightly lower reduction percentage). On the other hand, the tower fatigue loads slightly increase by 2% because in the design of the proposed control loops no provision was made on tower loads alleviation. As a result of the combined application of IPC and IFC a 7.4% reduction of the blade ultimate flap-wise load is obtained.

On the other hand, scanning of the design space for BTC and FEC indicated that for the blade considered in the analysis, ply offset angles higher than 7.5° could cause weakening of the blade stiffness in the flap-wise direction. The anticipated level of reduction of the ultimate loads and stresses is $\sim 7\%$, like that obtained through the application of active load control methods. Application of FEC is found necessary for the mitigation of the DTU-10MW RWT blade loads in idling operation at the yaw angle of

+30°. The anticipated reduction in the extreme idling operation load is 20% for a moderate shift of the caps by 3% of the blade chord.

Based on the aforementioned alleviation of the ultimate loads, an optimization study, aimed at reducing the blades' walls thickness (and therefore blade mass) was established. The optimization process consists in minimizing CAPital EXpenditure (CAPEX) by optimally designing the ply offset angle of the UD material on the caps of the blade (material BTC) and the radial position wherefrom this offset angle begins or by specifying the optimal swept blade geometry (geometric BTC). Three application examples are considered, two focusing on pure BTC (geometric and material) and addressing only operational loads and another one combining FEC with material BTC and addressing both normal and idling operation loads:

- In the first application example focusing on the use of sweep. The shape of the elastic axis is approximated by a Bezier curve, with the control points being the design variables of the optimization process. In this case, a "sickle-shape" configuration (forward swept at the inner part and backwards swept towards the tip) for the blade has been provided by the optimization loop, which has 8.6% less mass than the conventional straight blade.
- In the second application example, the material BTC through an offset ply angle in UD material over the 'caps' has been studied. It is found that for the DTU-10MW RWT blades, ply angle in the range of $5^\circ - 7.5^\circ$ starting at 15 – 30% of the blade span, can provide overall mass reduction of about 8%. Moreover, a hybrid BTC design in which the ply angles gradually increase toward the tip is addressed (max ply angle $\sim 8^\circ$). Mass reduction of 10% is obtained for the above hybrid configuration. In addition, BTC blades reduce the combined banding moment at the root of the blade by 5 – 7% and at the tower base by 6.6 – 8.1%. In the analyses of the aforementioned application example, only normal operation cases (DLC 1.3) are considered in specifying the design loads of the blade.
- In the last application example, the reference design has a 3% of the chord displacement of the spar caps (FEC 3%) while the appropriate ply offset angle is searched that will provide maximum reduction in the overall mass of the blade. The result on the mass blade is similar to that of the previous examples, however in this modified configuration, apart from normal operation conditions, reduction of loads under extreme wind conditions is addressed (i.e. DLC-6.x, where the larger vibrations are usual observed). This optimization study is performed using different optimization methods. All optimization methods mentioned above have been evaluated in terms of convocation and stability.

As a final step of each optimization study, a verification of the modified designs has been performed through detailed time domain simulations of an extended subset of DLCs at various wind speed, which in addition, in most of the cases, include the assessment of the turbine fatigue loads. These simulations substantiate that maximum Tsai-Hill values of the optimized blade designs remain below the limit values.

Next, a multi-disciplinary design of the 10MW wind turbine rotor, integrating passive load control techniques and considering as design variables not only structural parameters but also aerodynamic

ones, is performed. In this study, along with the previously analyzed structural design variables (e.g. passive control parameters, geometry of the spar caps and shear webs), the chord and twist distributions and the blade length are also addressed. In contrast to the previously reported analyses, the present optimization studies focus on the minimization of the LCoE. Two application examples are considered one addressing only normal operation conditions and a second one addressing also extreme winds and idling operation mode of the wind turbine.

Table 5.1: DTU-10MW RWT passive control designs parametrization aimed at minimizing the LCoE.

design	material	geometrical	re-twist	material	Blade mass [<i>tn</i>]	AEP [<i>GWh</i>]	LCoE [<i>\$/MWh</i>]
	FEC	FEC		BTC			
reference					40.0	45.1	44.96
<i>modified</i>				√	1.0%	14.0%	-0.7%
CASE A	√				10.3%	0.1%	-0.8%
CASE B	√	√			-3.1%	0.2%	-0.4%
CASE C	√	√			-13.3%	0.2%	-1.0%
CASE D	√	√	√		-14.0%	0.1%	-1.0%
CASE E	√	√	√	√	-19.5%	0.2%	-1.4%

A summary of the parameters and the value of LCoE, is presented in Table 5.1, while each application example is described below:

- In the first application example (so-call as '*modified*'), the rotor radius, the planform of the blade, the thickness of the composite material walls and the parameters of the material BTC, are considered as design variables of the optimization study. The result of the analysis indicated that an overall 0.71% reduction in LCoE (0.32 *\$/MWh*) can be achieved if the reference blade is elongated by 3.7%. A moderate optimum material ply offset angle of 5.9° is obtained while the optimized blade design has 1% higher mass as compared to the reference (note that geometric similarity, power 3-law, would imply a 12% increase in mass). The increase in energy production by newly designed rotor design is 2.4%.
- In the second application example (CASES A-E), design modifications of the blade inner structure, which lead to suppression of stall-induced edge-wise vibrations in idling operation and therefore reduce design-driving loads, have been also assessed. The design parameters of two FEC methods (material and geometric) have been tested on a step-wise approach, in which the two methods were first evaluated separately, then in combination and finally, they were blended with material BTC and blade re-twisting. Optimization studies indicated that material FEC, which is based on the

asymmetrical increase in the thickness of the walls of the L/P side towards the section nose and of the H/P side towards the T/E, is more effective in suppressing stall-induced instabilities and reducing LCoE than the geometric FEC, which is based on the displacements of the spar caps of the L/P and H/P sides in opposite directions. Geometric FEC leads to an almost constant shift in the structural twist angle all along the blade span, while material FEC results in a high local increase in the cross-bending stiffness and the corresponding structural twist angle in the inboard part of the blade. The latter turns out to give a mass reduction for the blade of 10.3% and a corresponding decrease in LCoE of 0.82%, while the former gives rise to a reduction in mass of 3.1% and of LCoE of 0.36%. Combination of the two methods appears to have an accumulative effect, while concurrent application of BTC with a parallel re-twisting of the blade provides a maximum reduction in mass and LCoE of 19.5% and 1.36%, respectively.

5.2. Future research topics

In the last decade, research on innovative wind turbine design concepts has experienced explosive growth. According to Adam Chehouri et al. [151], the rate of publications of articles on wind turbine design and optimization, has been doubled in five years. This interest of the scientific community is also shared by the industry, which in recent years has adopted many of the innovations and disruptive design modification that have been proposed in the scientific literature [152] and [153]. Although the present thesis aspires to contribute in this direction, some issues remained un-addressed. So, the topics that could be subjects for future research are listed below:

- Thorough re-design of a wind turbine: studying the case of the complete re-design of the 10MW reference wind turbine, the research could focus on the evaluation/optimization of every sub-component such as: the blades, the tower, the gearbox etc. The implementation of the above design requires the adoption of an accurate and validated cost model, for each component separately and the simultaneous evaluation of the loading conditions of every component including: ultimate loads, buckling and fatigue loads. For examples, the INNWIND.EU project [18] has demonstrated that blades' design is driven by the ultimate loads, while the design of the tower is driven by buckling and fatigue loads. Such research could be easily accommodated within the developed optimization framework by simply considering only few additional simulation modules and design variables along with an appropriate parameterization. The large computational cost that such research requires, presupposes the parallelization of the simulations.
- 3D FEM analysis: although the beam model is quite reliable, nevertheless in the context of the complete design optimization of a wind turbine of 10MW (including the blades, the tower, the gearbox etc.), enhancing the design verification step through a 3D analysis, is considered crucial. This can be done by employing 3D commercial packages (e.g. ANSYS or ABAQUS) which can assess the buckling behavior and modes of the blades/tower, after the issue of aero-elastic tailoring is primarily addressed.

- New disruptive wind turbine designs: Following the up-scaling trend suggested by the scientific community of wind energy, in a future work it would be interesting to design new up-scaled wind turbines exceeding 20MW. These turbines could be designed for offshore installations (e.g. bottom fixed or floating), taking into account, among others, the hostile marine environment and the hydrodynamic loading. Previous works performed with hGAST [22] have evaluated various substructure designs for offshore wind turbines (e.g. monopile, jacket, different types of floaters etc.). The parameterization and optimization of the above substructures could be the subject of this research. Such research would open new horizons for future wind farms installations in the sea.
- New cost model: Finally the development of a new cost model, which will include the modeling of the various active and passive control techniques described in the current work, is considered critical. In this case, empirical relationships (those are absent today from the literature) should be developed in relation to the costs of manufacturing and transporting curved molds, through the use of sweeping or the extra cost of introducing an offset ply angle in the uni-directional material over the 'caps'. Moreover, such a model could include offshore applications, facilitating their development.

5.3. Dissemination of results

The most important results of this thesis have been published in eight articles and the main conclusions have been presented in three international conference/seminar (five posters in total).

5.3.1. Published papers

During the current thesis, eight publications have been made, which are listed below in chronological order:

- Manolas D., Serafeim G., Chaviaropoulos P., Riziotis V. and Voutsinas S. (2018) *“Assessment of load reduction capabilities using passive and active control methods on a 10MW-scale wind turbine”*, J. of Physics: Con. Ser. 1037 (2018) 032042, doi: 10.1088/1742-6596/1037/3/032042.
- Manolas D., Spyropoulos N., Serafeim G., Riziotis V., Chaviaropoulos P. and Voutsinas S. (2018) *“Inflow-based flap control on a 10MW-scale wind turbine using a spinner anemometer”*, J. of Physics: Con. Ser. 1037 (2018) 032045, doi: 10.1088/1742-6596/1037/3/032045.
- Latoufis K., Serafeim G., Chira K., Riziotis V., Voutsinas S. and Hatziargyriou N. (2020) *“Holistic Design of Small-scale StandAlone Wind Energy Conversion Systems Using Locally Manufactured Small Wind Turbines”*, J. of Physics: Con. Ser. 1618 (2020) 042012, doi: 10.1088/1742-6596/1618/4/042012.
- Serafeim G., Manolas D., Riziotis V., Chaviaropoulos P. (2020) *“Lightweight optimal rotor design of a 10MW-scale wind turbine using passive load control methods”*, J. of Physics: Con. Ser. 1618 (2020) 022061, doi: 10.1088/1742-6596/1618/2/022061.
- Schinas P., Serafeim G., Manolas D., Riziotis V., Voutsinas S., Philippidis T. and Chaviaropoulos P. (2020) *“Assessment of extreme stresses and deflections on wind turbine blades with stochastic*

material properties using statistical extrapolation methods” J. of Physics: Con. Ser. 1618 (2020) 052029, doi: 10.1088/1742-6596/1618/5/052029.

- Serafeim G., Manolas D., Riziotis V. and Chaviaropoulos P. (2022) “*Multidisciplinary aeroelastic optimization of a 10MW-scale wind turbine rotor targeting to reduced LCoE*”, J. of Physics: Con. Ser. 2265 (2022) 042051, doi: 10.1088/1742-6596/2265/4/042051.
- Serafeim G., Manolas D., Riziotis V. and Chaviaropoulos P. (2022) “*Optimized blade mass reduction of a 10MW-scale wind turbine via combined application of passive control techniques based on flap-edge and bend-twist coupling effects*”, J. of Wind Engineering and Industrial Aerodynamics 225:105002, doi: 10.1016/j.jweia.2022.105002.
- Serafeim G., Manolas D., Riziotis V. and Chaviaropoulos P. (2022) “*Wind Turbine Blade Design Optimization for Reduced LCoE, Focusing on Design –Driving Loads Due to Storm Conditions*”, J. of Fluids 7(8):280, doi: 10.3390/fluids/7080280.

5.3.2. Participation in seminars and conferences

Participation in conferences:

- International conference “Torque-2022”, poster title «*Multidisciplinary aero-elastic optimization of a 10MW-scale wind turbine rotor targeting to reduced LCoE*», 1-3 June 2022, Delft-Holland.
- International conference “Torque-2020”, poster title «*Lightweight optimal rotor design of a 10MW-scale wind turbine using passive load control methods*», 28 September – 2 October 2020, Delft-Holland.
- International wind energy seminar “14th EAWC PhD seminar”, poster title «*Assessment of load cost reduction capabilities of a 10MW-scale wind turbine through ply angle orientation*», 18-22 September 2018, Brussels-Belgium.
- International conference “Torque-2018”, poster title «*Assessment of load reduction capabilities using passive and active control methods on 10MW-scale wind turbine*», 20-22 June 2018, Milan-Italy.
- International conference “Torque-2018”, poster title «*Inflow-based flap control on a 10MW-scale wind turbine using a spinner anemometer*», 20-22 June 2018, Milan-Italy.

5.4. Acknowledgements

The current thesis has been financially supported by the following sources:

- The Hellenic Foundation for Research and Innovation (HFRI) under the HFRI PhD Fellowship grant (Fellowship Number: 867).



- Greece and European Union (European Social Fund-ESF) through the Operational Programme «Human Resources Development, Education and Lifelong Learning» in the context of the Act “Enhancing Human Resources Research Potential by undertaking a Doctoral Research” Sub-action 2: IKY Scholarship Programme for PhD candidates in the Greek Universities (Fellowship Number: 2022-050-0502-52636).



- Renewable energy research company of “iWind” (for more information visited the <https://www.iwind.gr> or e-mail: info@iwind.gr).



This page intentionally left blank

Appendix A

A. Description of RWT

During the last two decades, the design of turbines with lighter and higher diameters rotors has become the main challenge for the wind energy community. This challenge was the main objective of the Light Rotor project [154] launched as a cooperation between DTU Wind Energy and the OEM company Vestas [155]. The result of the above collaboration was the design of a $10MW$ wind turbine, the design of which was inspired by the conceptual NREL-5MW [71]. Among the objectives set by the project was the design of an optimized conventional three bladed horizontal axis wind turbine [52]. Optimization of the wind turbine concerned both its aerodynamic and structural characteristics. In the following years the DTU-10MW RWT became the reference turbine of many scientific studies and published papers [156],[157],[158] while it was also considered as reference turbine in other recent projects beyond the Light Rotor project, such as the INNWIND.EU [18]. The DTU-10MW RWT serves as the reference turbine of the present thesis, therefore presentation of its main characteristics is provided for the sake of completeness. A full description of the basic geometrical, aerodynamics and structural characteristics of the DTU-10MW RWT is provided herein, summarizing minor modifications (such as the thickness of walls, near the tip) adopted as well as details of fabrication materials obtained from various literature sources.

A.1. Overall

The DTU-10MW RWT is a conventional three-bladed, upwind $10MW$ offshore turbine designed based on the provisions of class 1A of the IEC standard (see Fig. A.1). The main characteristics of the wind turbine are provided in Table A.1. In this table also data from the direct up-scaling of the NREL-5MW RWT are shown. Most of the structural parameters of the turbine were based on the up-scaling of the above turbine applying classical geometric similarity rules [159]. So, for example, the steel tower of the

wind turbine follows the geometric rule of $H_{tower}^{5MW} \sqrt{P_{10MW}/P_{5MW}}$, where H_{tower}^{5MW} is the height of the tower of 5MW-RWT and P indicates the rated power of each turbine.

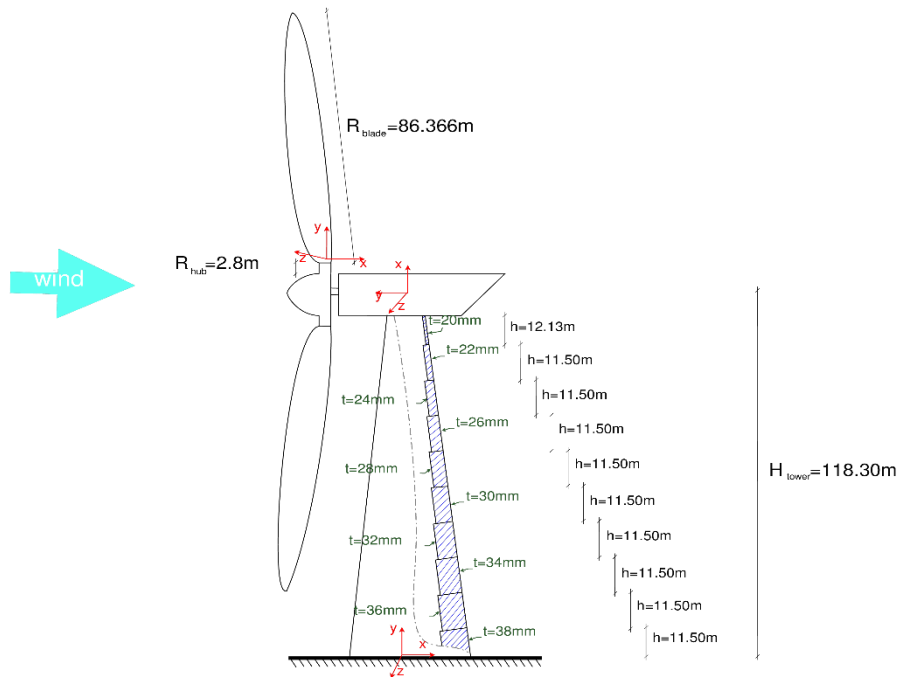


Figure A.1: A sketch of DTU-10MW RWT.

Table A.1: Key parameters of the DTU-10MW RWT compared to a direct up-scale of the NREL-5MW RWT.

parameter	DTU-10MW RWT	Up-scaled NREL-5MW
Wind Regime	IEC Class 1A	IEC Class 1B
Rotor Orientation Control	Clockwise rotation - Upwind	Same
Control	Variable Speed/Collective Pitch	Same
Operational wind speed	4-25m/s	Same
Rated wind speed	11.4m/s	Same
Rated power	10MW	Same
Number of blades	3	Same
Rotor and hub diameter	178.3m, 5.6m	178.3m, 4.24m
Hub Height	119.0m	127.0m
Drivetrain	Medium Speed, Multiple-Stage Gearbox	High Speed, Multiple-Stage Gearbox
Range of rotor speed	6.0-9.6rpm	4.9-8.6rpm
Maximum Generator Speed	480.0rpm	1173.7rpm
Gearbox Ratio	50	97
Maximum Tip Speed	90.0m/s	79.9m/s
Hub Overhang	7.1m	Same
Shaft Tilt and rotor precone angle	5.0deg, -2.5deg	Same
Blade Prebend	3.332m	0.0m
Blade, Nacelle and Tower mass	227962kg, 446036kg, 628442kg	311127kg, 678823kg, 982765kg

A.2. Airfoils and geometric parameters of the blade

The blade was designed based on one airfoil family all along its span, namely the FFA-W3-xxx [160]. This airfoil family is frequently used in modern mega-watt wind turbine designs. Because the FFA airfoils are available for relative thicknesses ranging between 21.2% to 36.0%, extrapolation of the profile shapes is performed up to the thickness of 60% while transition sections were produced for the inner most part of the blade, from 60% thickness up to the 100% thickness of the circular section of the blade root. In Fig. A.2, the distribution of the different airfoils (of different relative thickness) along the span of the blade is shown. This distribution is the result of the aerodynamic optimization performed by DTU. Furthermore, in Table A.2, the main geometric characteristics of the DTU-10MW RWT blade, as the prebend, chord and twist distributions are provided. In addition to the above, this table gives information about the topology of each cross-section. It provides the position of the moving key-points (KP) that define the location of the ‘caps’ as well as the number of shear webs the different cross section are composed of. The position of the key point is provided in a non-dimensional manner, as percentage of the local chord. This percentage corresponds to non-dimensional distance of the point from the Leading Edge (L/E) point of the section. As shown in Fig. A.3, the positions of certain key-points is preset while the number of the required webs is derived through local buckling analysis performed by DTU.

Table A.2: Geometric characteristics of the wind turbine blade of DTU-10MW RWT. The non-dimensional distance of KP are counting from L/E.

r/R_{tip}	prebend [m]	chord [m]	twist [deg]	pitch axis [-]	KP-03 [-]	KP-04 [-]	KP-07 [-]	KP-08 [-]	num. of webs
0.00	0.000	5.300	-14.500	0.500	0.73	0.53	0.29	0.49	2
0.05	-0.013	5.300	-14.492	0.499	0.72	0.52	0.29	0.49	2
0.10	-0.041	5.480	-14.351	0.488	0.68	0.51	0.29	0.48	2
0.15	-0.071	5.777	-13.013	0.448	0.60	0.44	0.28	0.46	2
0.20	-0.110	6.059	-10.558	0.407	0.53	0.37	0.27	0.44	2
0.25	-0.153	6.193	-8.392	0.380	0.47	0.32	0.25	0.41	3
0.30	-0.217	6.146	-7.155	0.364	0.40	0.26	0.22	0.37	3
0.35	-0.291	5.978	-6.244	0.355	0.39	0.25	0.22	0.36	3
0.40	-0.380	5.722	-5.435	0.350	0.37	0.23	0.21	0.35	3
0.45	-0.485	5.415	-4.656	0.350	0.37	0.23	0.22	0.36	3
0.50	-0.613	5.070	-3.801	0.350	0.37	0.23	0.22	0.36	3
0.55	-0.758	4.708	-2.909	0.350	0.38	0.23	0.23	0.37	3
0.60	-0.929	4.335	-2.007	0.350	0.38	0.23	0.23	0.38	3
0.65	-1.125	3.965	-1.133	0.350	0.38	0.23	0.23	0.38	3
0.70	-1.330	3.603	-0.314	0.350	0.38	0.23	0.23	0.38	3
0.75	-1.594	3.252	0.433	0.350	0.38	0.23	0.23	0.38	3
0.80	-1.876	2.920	1.099	0.350	0.38	0.23	0.23	0.38	3
0.85	-2.185	2.605	1.724	0.350	0.38	0.23	0.23	0.38	3
0.90	-2.533	2.299	2.335	0.350	0.38	0.23	0.23	0.38	3
0.95	-2.915	1.893	2.928	0.350	0.38	0.23	0.23	0.38	3
1.00	-3.331	0.601	3.428	0.350	0.38	0.23	0.23	0.38	0

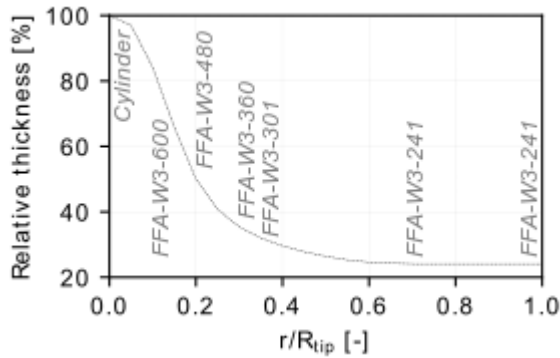


Figure A.2: Relative thickness distribution, with airfoils positions along the blade.

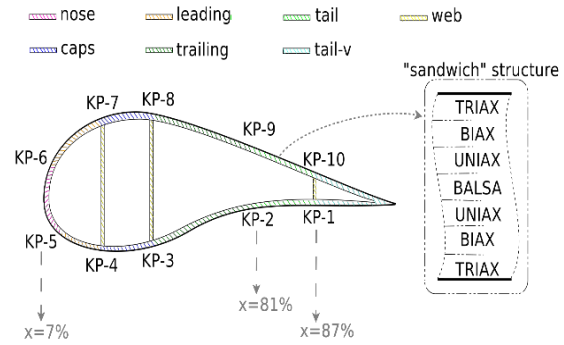


Figure A.3: Cross-section of the wind turbine blade with three webs and qualitative description of the different regions.

A.3. Structural design of blade

Looking at the internal structure of the blade, this is typically made of fiberglass in sandwich-type, as qualitatively depicted in Fig. A.3. Specifically, ‘TRIAX’, ‘BIAx’ and ‘UNIAX’ are used as base materials surrounding a core of ‘BALSa’ symmetrically - with their mechanical properties presented in Table A.3 [50]. In the same table, the characteristics of the minor materials used in the fabrication of the blade, and are considered in the cost model analysis are also provided. In general, the quadrilateral defined by the two ‘caps’ and the two main webs constitutes the so-called ‘caps-box’. This box undertakes the main part of the loading developing during the operation of the wind turbine – while the main role of the remaining regions is to provide the shape of local airfoil section.

Table A.3: RWT blade material cost and structural properties.

	TRIAX	BIAx	UNIAX	BALSa	Resin/Hardener	Adhesive	Painting
Price[\$/Kg]	2.86	3.00	1.87	7.23	3.63	9.00	7.23
Density[Kg/m ³]	1845	1845	1916	110	1200	1200	1150
F _{FV} [%]	72.5	72.5	72.5	72.5	-	-	-
E ₁₁ [N/m ²]	21.8E+9	13.9E+9	41.6E+9	50.0E+6	-	-	-
E ₂₂ [N/m ²]	14.7E+9	13.9E+9	14.9E+9	50.0E+6	-	-	-
G ₁₂ [Nm/m ²]	9.4E+9	11.5E+9	5.1E+9	16.7E+9	-	-	-
G ₁₃ [Nm/m ²]	4.5E+9	4.5E+9	5.1E+9	15.0E+7	-	-	-
G ₂₃ [Nm/m ²]	4.5E+9	4.5E+9	5.5E+9	15.0E+7	-	-	-
V ₁₂ [-]	0.48	0.49	0.24	0.49	-	-	-
X _c [N/m ²]	1.8E+8	9.5E+7	2.8E+8	1.8E+5	-	-	-
X _t [N/m ²]	2.2E+8	1.0E+8	4.0E+8	3.1E+5	-	-	-
Y _c [N/m ²]	6.9E+7	9.5E+7	8.6E+7	1.8E+5	-	-	-
Y _t [N/m ²]	4.1E+7	1.0E+8	3.4E+7	3.1E+5	-	-	-
S[N/m ²]	3.1E+7	5.0E+7	3.1E+7	5.0E+5	-	-	-

Table A.4: Thickness of material distribution in [mm], per region of blade cross-section.

r/R_{tip}	nose			leading			caps			trailing		
	TRIAX	UNIAX	BALSA	TRIAX	UNIAX	BALSA	TRIAX	UNIAX	BALSA	TRIAX	UNIAX	BALSA
0.00	8.0	8.0	10.0	8.0	8.0	10.0	8.0	8.0	0.0	8.0	8.0	10.0
0.05	7.8	7.9	15.0	7.8	7.8	15.0	6.7	11.8	0.0	7.9	7.8	20.0
0.10	6.7	7.2	20.0	6.7	6.1	20.0	4.0	20.2	0.0	6.8	6.1	35.0
0.15	5.1	5.9	30.0	5.1	3.9	30.0	1.0	30.9	0.0	5.4	3.9	60.0
0.20	3.8	3.7	35.0	3.8	2.0	35.0	0.0	35.8	0.0	4.2	2.0	70.0
0.25	3.0	2.1	35.0	3.0	1.0	35.0	0.0	37.5	0.0	3.5	1.0	70.0
0.30	2.4	1.0	35.0	2.4	0.0	35.0	0.0	39.3	0.0	2.9	0.0	70.0
0.35	2.0	1.0	30.0	2.0	0.0	30.0	0.0	40.8	0.0	2.7	0.0	70.0
0.40	1.9	1.0	30.0	1.9	0.0	30.0	0.0	41.5	0.0	2.6	0.0	65.0
0.45	1.8	1.0	30.0	1.8	0.0	30.0	0.0	41.5	0.0	2.5	0.0	65.0
0.50	1.7	1.0	25.0	1.7	0.0	25.0	0.0	40.9	0.0	2.5	0.0	65.0
0.55	1.6	1.0	25.0	1.6	0.0	25.0	0.0	39.6	0.0	2.4	0.0	60.0
0.60	1.5	0.0	20.0	1.5	0.0	20.0	0.0	38.4	0.0	2.3	0.0	55.0
0.65	1.5	0.0	20.0	1.5	0.0	20.0	0.0	36.7	0.0	2.2	0.0	45.0
0.70	1.4	0.0	15.0	1.4	0.0	15.0	0.0	33.4	0.0	2.1	0.0	35.0
0.75	1.3	0.0	15.0	1.3	0.0	15.0	0.0	30.5	0.0	2.1	0.0	30.0
0.80	1.3	0.0	15.0	1.3	0.0	15.0	0.0	26.1	0.0	2.0	0.0	25.0
0.85	1.2	0.0	10.0	1.2	0.0	10.0	0.0	19.8	0.0	1.9	0.0	20.0
0.90	1.2	0.0	10.0	1.2	0.0	10.0	0.0	13.8	0.0	1.8	0.0	15.0
0.95	1.2	0.0	5.0	1.2	0.0	5.0	0.0	8.6	0.0	1.7	0.0	15.0
1.00	1.2	0.0	5.0	1.2	0.0	5.0	0.0	1.5	10.0	1.6	0.0	10.0

Table A.4: Thickness of material distribution in [mm], per region of blade cross-section (*continue*).

r/R_{tip}	tail			tail-v			webs	
	TRIAX	UNIAX	BALSA	TRIAX	UNIAX	BALSA	BIAX	BALSA
0.00	8.0	8.0	10.0	8.0	8.0	10.0	2.6	26.0
0.05	7.9	7.9	20.0	7.9	7.9	20.0	2.6	24.0
0.10	6.8	7.0	35.0	6.8	7.0	35.0	2.6	24.0
0.15	5.4	6.0	60.0	5.4	6.0	30.0	2.8	22.0
0.20	4.2	5.5	70.0	4.2	5.5	25.0	3.4	22.0
0.25	3.5	5.4	66.7	3.5	5.4	30.0	2.8	20.0
0.30	2.9	5.1	60.0	2.9	5.1	30.0	4.3	18.0
0.35	2.7	4.8	50.0	2.7	4.8	30.0	4.6	16.0
0.40	2.6	4.4	41.7	2.6	4.4	27.5	4.7	14.0
0.45	2.5	4.2	35.0	2.5	4.2	25.0	4.7	14.0
0.50	2.5	3.8	31.7	2.5	3.8	22.5	4.6	12.0
0.55	2.4	3.4	23.3	2.4	3.4	15.0	4.5	8.0
0.60	2.3	3.2	21.7	2.3	3.2	7.5	4.4	8.0
0.65	2.3	2.9	15.0	2.3	2.9	7.5	4.3	6.0
0.70	2.2	2.5	11.7	2.2	2.5	3.5	4.0	6.0
0.75	2.1	2.2	10.0	2.1	2.2	3.0	3.9	4.0
0.80	2.0	1.9	8.3	2.0	1.9	2.5	3.6	4.0
0.85	2.0	1.4	6.7	2.0	1.4	2.0	3.3	4.0
0.90	1.9	1.0	5.0	1.9	0.0	1.5	2.9	2.0
0.95	1.9	1.0	3.3	1.9	0.0	1.0	2.2	2.0
1.00	1.8	0.0	1.7	1.0	0.0	0.0	1.3	2.0

The selection of each material, as well as its thickness (occurs as a result of the layers of fiberglass), was carried out based on the reinforcement of each region of the cross-section, taking into account the cost of each material. In the extended Table A.4, the thicknesses of the different materials, in each region along the DTU-10MW RWT blade are presented. As can be clearly seen in the aforementioned table, the region of the 'caps', which is expected to receive the largest axial stresses, consists mainly of the uni-directional material (UNIAX), in contrast to the other regions of the cross-sections containing significantly greater thicknesses of Balsa. Balsa is a significantly cheaper material, but it does not directly contribute to the reinforcement of the walls. In practice the core does not receive any loads (so it is not taken into account in the stresses analysis), however its placement determines the distance between the fiberglass on either side of it, thus affecting the bending loads at a local level and the mass/frequencies of the blade at a macroscopic level.

A.4. Control

A controller with partial and full load operation capabilities has been adopted. This controller is based on classical proportional-integral control theory, while additional filters (e.g. filter mitigating) and drive train damper that ensure a smooth transition, are available. The generator speed is the main feedback signal, as the reference generator power is used to smooth the switching between partial and full load operation. The rotational speed of the rotor, is largely determined by the natural frequencies of the wind turbine, setting the range of its variation between $6\sim 9.6rpm$. The eigen-frequency analysis of the full wind turbine system reveals that the first two tower modes are approximately $0.25Hz$ (see Table A.7), not interfering with the $3p$ and $6p$ harmonics. The maximum rotational speed is obtained at the rated wind speed, beyond which pitch control takes place with the pitch angle reaching a maximum of 26° , when the cut-out wind speed of $25 m/s$ is reached. The reader can refer to the manual of DTU Wind Energy Control [161], for more information.

A.5. Power curve analysis

The power produced by the wind turbine, at various wind speeds in the range of $5\sim 25 m/s$ (i.e. during normal operation of the turbine), is calculated using Blade Element Momentum Theory (BEMT) analysis. The range $5\sim 11.4 m/s$ is called the partial-load region, where the pitch angle is set to zero value – while for higher wind speeds the generated power is maintained by introducing pitch control at the command of the control system. In Table A.5, the computed power curve of the wind turbine is presented. Also, in this table, the annual power production estimate is provided, considering a uniform mechanical and electrical losses coefficient of $\eta = 0.94$ and Weibull parameters: $C = 11 m/s$ and $k = 2$.

Table A.5: Integrated of pitch angle, probability and power produced, as function of wind speed.

speed [m/s]	pitch [deg]	prob. [-]	power [MW]	speed [m/s]	pitch [deg]	prob. [-]	power [MW]	speed [m/s]	pitch [deg]	prob. [-]	power [MW]
5	0.0	0.034	0.81	12	3.5	0.030	10.00	19	16.0	0.008	10.00
6	0.0	0.037	1.44	13	7.0	0.027	10.00	20	17.0	0.006	10.00
7	0.0	0.039	2.32	14	9.0	0.023	10.00	21	18.0	0.005	10.00
8	0.0	0.039	3.47	15	11.0	0.019	10.00	22	20.0	0.003	10.00
9	0.0	0.038	4.94	16	12.5	0.016	10.00	23	22.0	0.002	10.00
10	0.0	0.036	6.77	17	14.0	0.013	10.00	24	24.0	0.002	10.00
11	0.0	0.033	9.00	18	15.0	0.010	10.00	25	26.0	0.001	10.00
Annual Power Produced [GWh]											47.18

A.6. RWT loads analysis

In this section, results of the aero-elastic analyses of DTU-10MW RWT are presented. Aero-elastic simulations are performed using the in-house servo-aero-elastic solver hGAST (see section 2.1.). First, the eigen-value analysis results are discussed and then fatigue and ultimate load analyses both for the blade and the tower are presented. Furthermore, a comparison of the results of the two dynamic stall models employed in this thesis, the ONERA [79] and the Beddoes-Leishman [80] is performed. In the following table, the simulated design load cases and the safety factors considered in each one of them (in accordance with the provisions of the IEC-61400 standard [53]) are listed.

Table A.6: DLCs definition for loads assessment.

DLC	conditions	wind speeds [m/s]	yaw angle [deg]	safety factor (η_L)
1.2	NTM	5-25, step 2	0	-
1.3	ETM	11-25, step 2	0	1.35
6.1	EWM	50	0,±8	1.35
6.2	EWM	50	±15,±30,±45,±60	1.10

A.6.1. Eigen-value analysis

The full wind turbine system that includes the three blades, the nacelle and the tower, is treated as a single coupled structure. The eigen-value analysis usually precedes any aero-elastic time domain analysis, since it determines the natural frequencies of the structure. Using the in-house aero-elastic solver hGAST, the eight lowest frequencies of the DTU-10MW RWT are presented in the Table A.7.

Table A.7: Standstill natural frequencies of DTU-10MW RWT, in [Hz].

mode shape		mode shape	
1st tower bending side-side	0.250	1 st asymmetric rotor flap-wise (tilt)	0.596
1 st tower bending fore-aft	0.253	1 st symmetric rotor flap-wise	0.657
1 st symmetric rotor edge-wise/drivetrain	0.519	1 st asymmetric rotor edge-wise (vert.)	0.965
1 st asymmetric rotor flap-wise (yaw)	0.551	1 st asymmetric rotor edge-wise (horiz.)	0.981

A.6.2. Fatigue analysis

In the present section, the life time equivalent fatigue loads for the blades and tower of DTU-10MW RWT are assessed. The fatigue loads are based on $11 \times 600sec$ time domain simulations, considering different turbulent seeds and yaw misalignments (in total thirty-three load cases are considered per each turbulence seed). Simulations for different wind speeds are performed with a step of $2 m/s$ in the range of $5 - 25 m/s$, see Table A.8. DLC-1.2, is the design load case that has been used to estimate the value of Damage Equivalent Load (DEL), for $N_{ref} = 10^7$ cycles, corresponding to twenty years life time damage based on Palmgren-Miner's summation rule [162]:

$$DEL = \left[\frac{1}{N_{ref}} \sum_1^i p_i \left(\sum_1^k N_{i,k} S_{i,k}^m \right) \right]^{1/m} \quad (A.1)$$

where $N_{i,k}$ are the number of cycles at load range $S_{i,k}$ determined with rainflow counting, p_i is the probability of the wind speed and the Wöhler exponent takes the value of $m = 10$ in the case of the blades analysis and $m = 4$ in the tower analysis.

Table A.8: Lifetime DELs of the DTU-10MW RWT cross-sections (absolute values [kNm]), based on DLC-1.2, calculated for twenty years lifetime with Weibull parameters $C = 11 m/s$ and $k = 2$, Wöhler coefficient $m = 10$ for the blades and $m = 4$ for the tower and $N_{ref} = 10^7$ cycles.

BLADE				TOWER			
r/R_{tip}	Flap	Pitch	Edge	h/H	Side-side	Yaw	Fore-aft
0.0	25727.8	426.7	27834.8	0.0	35011.8	25298.0	113784.1
0.1	21384.1	399.2	20122.6	0.1	30582.4	25288.1	99231.7
0.2	17210.5	373.6	14200.4	0.2	26378.2	25258.7	85887.0
0.3	13349.9	336.7	9696.4	0.3	22590.4	25170.5	73569.9
0.4	9877.7	273.7	6301.7	0.4	19436.8	25184.6	62649.7
0.5	6853.8	209.4	3824.6	0.5	16529.3	25170.6	52896.2
0.6	4355.8	148.2	2107.8	0.6	13622.9	25133.7	43639.7
0.7	2429.3	91.3	1005.8	0.7	10618.0	25031.6	35465.5
0.8	1050.7	46.2	364.7	0.8	7731.7	25018.3	28936.1
0.9	234.4	13.7	65.9	0.9	5159.7	24983.1	25321.7

A.6.3. ONERA Vs Beddoes-Leishman dynamic stall model

The uncertainty in the prediction of the aerodynamic loads in dynamic stall is a well-known fact within the wind energy sector and it is the main cause of the consequent uncertainty in the prediction of the stall-induced edgewise vibrations. Different state-of-the-art dynamic stall models can give significantly different load results in the onset of dynamic stall due to the quite different aerodynamic damping predicted by the stall models. Several dynamic stall models are proposed by the literature, with the most commonly used by the wind energy community being the ONERA and the Beddoes-Leishman

models. In the current section, the load predictions of the two models for the DTU-10MW RWT are compared both in normal and idling operation.

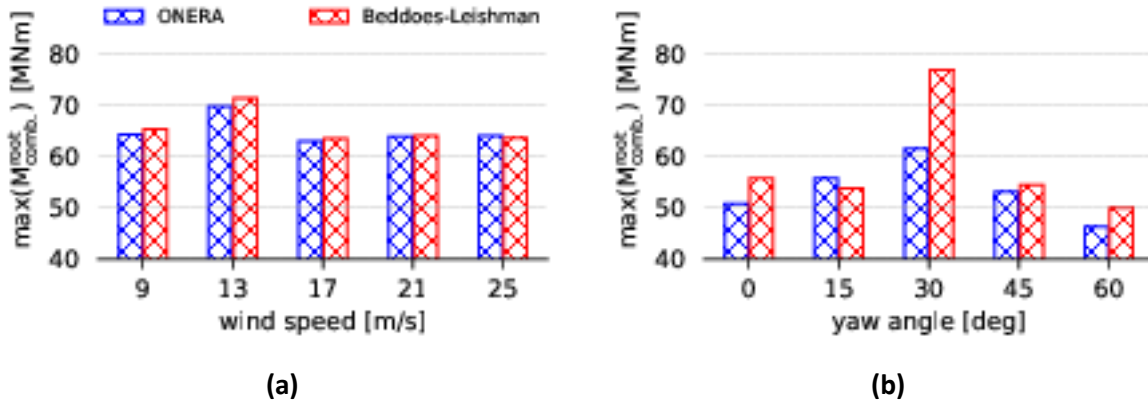


Figure A.4: Maximum combined bending moment at the blade root, using ONERA and Beddoes-Leishman aerodynamic model, for: (a) DLC-1.3 and (b) DLC-6.x, for various wind speeds and wind yaw angles respectively.

According to Fig. A.4, when idling operation simulations are performed using the ONERA dynamic stall model, substantially lower ultimate loads are obtained at a yaw angle of $+30^\circ$. Predictions of the two models notably deviate only at this particular yaw angle i.e. at the onset of the stall flutter, while similar load predictions are obtained by the two models in the operational case (DLC-1.3). This notable difference in the two models around the onset of the instability leads to the following mismatch: when Beddoes-Leishman model is employed, the design-driving DLC is 6.2 at $+30^\circ$ yaw, while when the ONERA model is used, DLC-1.3 at 13 m/s wind speed determines the design load. Given that it is by no means straightforward to conclude which of the models is more accurate, in the application examples studied in the present thesis the following approach has been adopted: when the analysis includes only the assessment of the extreme turbulent conditions (i.e. pure BTC studies considering operational loads), the ONERA model has been employed – in any other case (i.e. FEC studies, alone or in combination with BTC), the Beddoes-Leishman has been employed. In the Table A.9, the dynamic stall model adopted in each application of the thesis is presented.

Table A.9: Dynamic stall model that has been adopted in each application of the thesis.

application	dynamic stall model
3.4.1.	ONERA
3.4.2.	ONERA
3.4.3.	Beddoes-Leishman
4.2.1.	ONERA
4.2.2.	Beddoes-Leishman

A.6.4. Ultimate loads and stresses analysis

The ultimate loads both at the blade root and at the tower base, are obtained through time domain aero-elastic simulations for DLC-1.3 and DLC-6.x. According to IEC-61400 standard specifications, the first DLC simulates normal operation of the turbine under extreme turbulence conditions, while the second considers the situation that the wind turbine experiences extreme (survival) wind speeds and it is in parked or idling mode. In Fig. A.5, the maximum combined bending moment at the blade root and tower base, are illustrated, using the Beddoes-Leishman stall model. It is clear that ultimate loads, both for the tower and the blades, occurs in DLC-6.2, at $+30^\circ$ yaw angle. It is noted that, in the current thesis, the loads of DLC 1.3 at 13 m/s are considered as design loads either the investigation has been focused on BTC or FEC techniques.

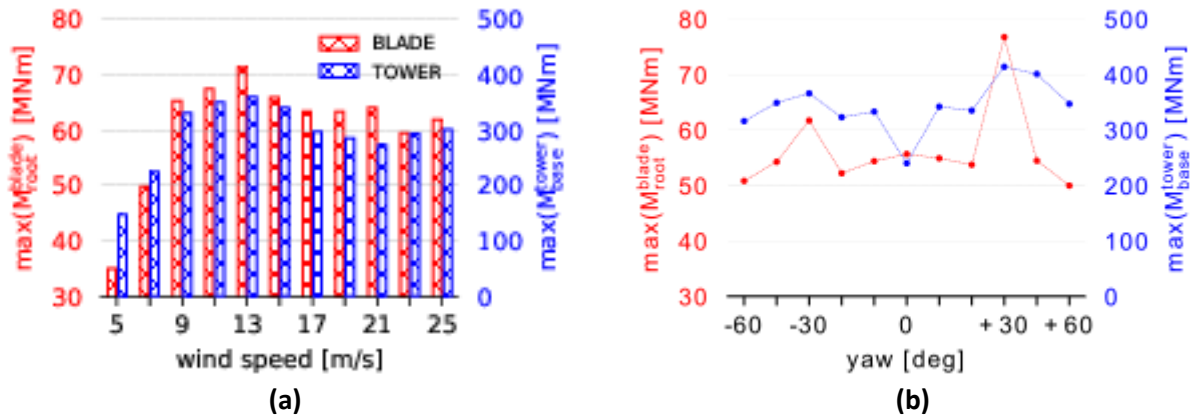


Figure A.5: Maximum combined bending moment at the blade root (red color) and tower base (blue color), for the cases: (a) DLC-1.3 for various wind speeds and (b) DLC-6.x yaw angles.

For the maximum combined bending moments of DLC-1.3 at 13 m/s , the simultaneous loads along the blade and tower (three forces and three moments in all directions) are reported in the Table A.10. Using the cross-sectional analysis tool, described in section 2.2., the maximum value of the Tsai-Hill failure criterion is calculated. This value is obtained taking into account the load safety factor reported in Table A.6 and the material safety factor ($\gamma_m = 1.20$, uniform for all materials). It is seen that the cross-section exhibiting maximum equivalent stress is that at 40% of the blade span.

Table A.10: Operational ultimate loads distribution along the blade and tower, for DTU-10MW RWT.

BLADE							
r/R_{tip}	$F_x[kN]$	$F_y[kN]$	$F_z[kN]$	$M_x[kNm]$	$M_y[kNm]$	$M_z[kNm]$	Tsai-Hill [-]
0.00	-661.9	1755.9	1343.6	67969.0	323.0	21359.6	0.286
0.10	-543.4	1599.9	1241.9	56753.7	338.1	15356.8	0.418
0.20	-446.4	1444.0	1244.6	46134.1	316.5	11153.3	0.719
0.30	-328.5	1251.5	1153.7	35895.8	309.4	7481.3	0.892
0.40	-265.8	1029.1	1098.5	26648.3	247.8	5019.6	0.981
0.50	-199.7	787.4	968.9	18407.4	215.0	3131.4	0.936
0.60	-143.6	556.9	795.6	11457.2	151.2	1765.8	0.838
0.70	-72.6	267.7	548.4	6298.3	92.1	883.1	0.833
0.80	-52.2	139.4	387.1	2705.1	44.2	385.7	0.562
0.90	-27.1	57.0	172.4	578.4	10.4	93.0	0.209
TOWER							
h/H	$F_x[kN]$	$F_y[kN]$	$F_z[kN]$	$M_x[kNm]$	$M_y[kNm]$	$M_z[kNm]$	$M_c[kNm]$
0.00	2924.0	-17177.4	241.4	42184.9	-3252.8	-358013.4	360490.2
0.10	2919.1	-15889.7	242.3	39302.1	-3246.4	-323227.4	325608.1
0.20	2884.5	-14867.4	183.8	35540.6	-4657.7	-288467.2	290648.4
0.30	2627.3	-13849.4	243.3	33586.6	490.9	-254028.2	256238.9
0.40	2704.4	-12886.3	246.7	30537.6	505.4	-221448.4	223544.0
0.50	2784.0	-12021.5	236.1	27489.2	516.7	-187654.5	189657.3
0.60	2387.4	-11300.0	102.1	20440.5	2863.0	-155191.1	156531.5
0.70	2472.4	-10612.0	95.9	19088.2	2849.4	-124787.9	126239.4
0.80	2541.0	-10007.0	90.8	17777.9	2839.8	-93293.0	94971.7
0.90	1298.4	-8915.5	155.7	16748.3	12.8	-63490.4	65662.3

Appendix B

B. Cross-sectional analysis

The current appendix provides the necessary information on the methodology followed in the analysis of the cross sections of the blade. The calculation of the full mass and stiffness matrices of every cross-section of the blade is based on Thin Lamination Theory (L/T) and an in-house Python code has been developed to support it. Given the above matrices as well as a loads set, the code can calculate the local stress tensor that develops at the level of the material layer.

L/T has been adopted by several research developments in the past [96],[97],[163], which have guided the present work. In the updated version of L/T presented herein, i) the effect of the shape of the cross-section geometry of shear rigidity properties and ii) an additional shear web (three in total) have been considered. The fullness of the derived stiffness matrix makes the present methodology suitable for modelling aero-elastically tailored blades exploiting passive load mitigation techniques (such as bend-twist or tension-twist coupling).

The approach presented herein focuses on the analysis of 2D sections, assuming that the blade is assembled by a sequence of cross-sections, each of which is expressed by a pair of full mass and stiffness matrices. The main publication containing the theoretical background on which the present implementation relies on is [96]. The stiffness properties of the cross-section are estimated through the integration over the laminates' thickness and along the section's periphery. The main difference of the current approach with respect to the "classical theory", is that it offers the possibility to evaluate the effect of non-symmetric layers.

B.1. Layer stiffness analysis

As can be seen in the appendix A, the blades of modern wind turbines are fabricated by fiberglass. In the case of DTU-10MW RWT, the primary materials used are: UNIAX, BIAX and TRIAX and are placed

symmetrically in a “sandwich” type structure on either side of the BALSA core. Each material is described by the list of its properties (see Table A.3, appendix A), referring on the material coordinate system $[Ox_m y_m z_m]$ of Fig. B.1. For example, for a uni-directional layer (UNIAX), where all fibers are aligned with the major x -axis (e.g. zero offset angle), the following material properties should be provided:

- ρ : material density $[kg/m^3]$
- E_{xx} : longitudinal elasticity modulus $[N/m^2]$
- E_{yy} : in-plane transverse elasticity modulus $[N/m^2]$
- ν_{xy} : in-plane Poisson ratio $[-]$
- G_{xy} : in-plane shear modulus $[N/m^2]$
- G_{xz} : out-of-plane-longitudinal shear modulus $[N/m^2]$
- G_{yz} : through-the-thickness shear modulus $[N/m^2]$
- X_c : compression longitudinal strength $[N/m^2]$
- X_t : tension longitudinal strength $[N/m^2]$
- Y_c : compression shear strength $[N/m^2]$
- Y_t : tension shear strength $[N/m^2]$

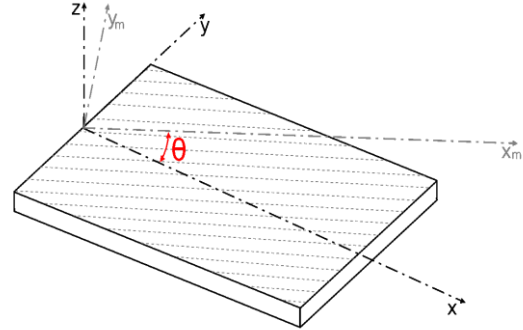


Figure B.1: Material $[Ox_m y_m z_m]$ and local $[Oxyz]$ coordinate system and example of layer with off-set ply angle.

The material coordinate system is related to the local system $[Oxyz]$, through the off-axis rotation around the z_m -axis. At the layer stiffness level, linear elasticity is assumed and involves the estimation of the material stiffness on the local system. Because a zero offset ply angle of the layer causes the physical paradox of greater longitudinal stiffness, the following cases are distinguished:

B.1.1. Layer stiffness without offset ply angle

At the layer level, the linear elasticity can be expressed by the mathematical expression:

$$\begin{Bmatrix} \sigma_x \\ \sigma_{xz} \\ \sigma_{xy} \end{Bmatrix} = \underbrace{\begin{bmatrix} E_{xx} & 0 & 0 \\ 0 & G_{xz} & 0 \\ 0 & 0 & G_{xy} \end{bmatrix}}_{q_{3 \times 3}} \begin{Bmatrix} \varepsilon_x \\ \varepsilon_{xz} \\ \varepsilon_{xy} \end{Bmatrix} \quad (\text{B.1})$$

where ε and σ correspond to the strain and stress tensors in vectorial form and the subscript x , y and z represent the coordinates of the local layer system (see Fig. B.1).

B.1.2. Layer stiffness with offset ply angle

In the special case where a layer is placed at an offset angle θ (see Fig. B.1), a special approach is adopted. According to this approach, the two layer stiffness matrices are defined as follows:

- layer stiffness matrix of 3×3 :

$$q_{3 \times 3} = \left\{ R_{3 \times 3}^{-T} \begin{bmatrix} 1/E_{xx} & 0 & 0 \\ 0 & 1/G_{xz} & 0 \\ 0 & 0 & 1/G_{xy} \end{bmatrix} R_{3 \times 3}^{-1} \right\}^{-1} \quad (\text{B.2})$$

where,

$$R_{3 \times 3} = \begin{bmatrix} \cos^{-1} \theta & 0 & 2 \cos \theta \sin \theta \\ 0 & \cos \theta & 0 \\ -\cos \theta \sin \theta & 0 & \cos^2 \theta - \sin^2 \theta \end{bmatrix}$$

- layer stiffness matrix of 5×5 :

$$q_{5 \times 5} = \left\{ R_{5 \times 5}^{-T} \begin{bmatrix} 1/E_{xx} & -v_{xy}/E_{xx} & 0 & 0 & 0 \\ -v_{xy}/E_{xx} & 1/E_{yy} & 1/G_{yz} & 0 & 0 \\ 0 & 0 & 0 & 1/G_{xz} & 0 \\ 0 & 0 & 0 & 0 & 1/G_{xy} \end{bmatrix} R_{5 \times 5}^{-1} \right\}^{-1} \quad (\text{B.3})$$

where,

$$R_{5 \times 5} = \begin{bmatrix} \cos^2 \theta & \sin^2 \theta & 0 & 0 & 2 \cos \theta \sin \theta \\ \sin^2 \theta & \cos^2 \theta & 0 & 0 & -2 \cos \theta \sin \theta \\ 0 & 0 & \cos \theta & -\sin \theta & 0 \\ 0 & 0 & \sin \theta & \cos \theta & 0 \\ -\cos \theta \sin \theta & \cos \theta \sin \theta & 0 & 0 & \cos^2 \theta - \sin^2 \theta \end{bmatrix}$$

Thus, the corresponding to Eq. B.1, 3×3 stiffness matrix is defined as follows for the case of offset ply angle:

$$q_{3 \times 3} = \begin{bmatrix} q_{3 \times 3}(1,1) & 0 & q_{5 \times 5}(1,5) \\ 0 & q_{5 \times 5}(4,4) & 0 \\ q_{5 \times 5}(5,1) & 0 & q_{5 \times 5}(5,5) \end{bmatrix} \quad (\text{B.4})$$

B.2. Laminate stiffness analysis

By integrating the stiffness properties along the thickness of the skins and webs (under the assumption of a sufficiently thin shell) the following 3×3 stiffness matrices associated with extension A^j , bending D^j and their coupling B^j of the j -th element of a laminate are obtained:

$$A^j = \sum_{k=1}^{N_{layer}} q_{3 \times 3}^k h_k \quad D^j = \sum_{k=1}^{N_{layer}} q_{3 \times 3}^k h_k \left(\frac{h_k^2}{12} + \bar{t}_k^2 \right) \quad B^j = \sum_{k=1}^{N_{layer}} q_{3 \times 3}^k h_k \bar{t}_k \quad (\text{B.5})$$

In Eq. B.5, h_k is the thickness of k -th layer and is the distance of the mid-line of the k -th layer from the mid-line of the skin (see Fig. B.2) given by:

$$\bar{\tau}_k = \begin{cases} \frac{h_k - H}{2} \\ \bar{\tau}_{k-1} + \frac{h_{k-1} + h_k}{2} \end{cases} \quad (\text{B.6})$$

where H denotes the total thickness of the laminate.

B.3. Sectional configuration of cross-section

The cross-sections of the blades of modern wind turbines are generally thin-walled with two or three vertical webs (see Fig. B.2). These webs form internal cells that affect the torsional behavior of the cross-section, while the outer shape determines the values of Timoshenko shear factors. In the current section, management of the above parameters as well as the estimation of the full stiffness matrix of the cross-section are described. Finally, following the reverse course and applying the internal loads, the stresses developed on any point of the cross-section are calculated.

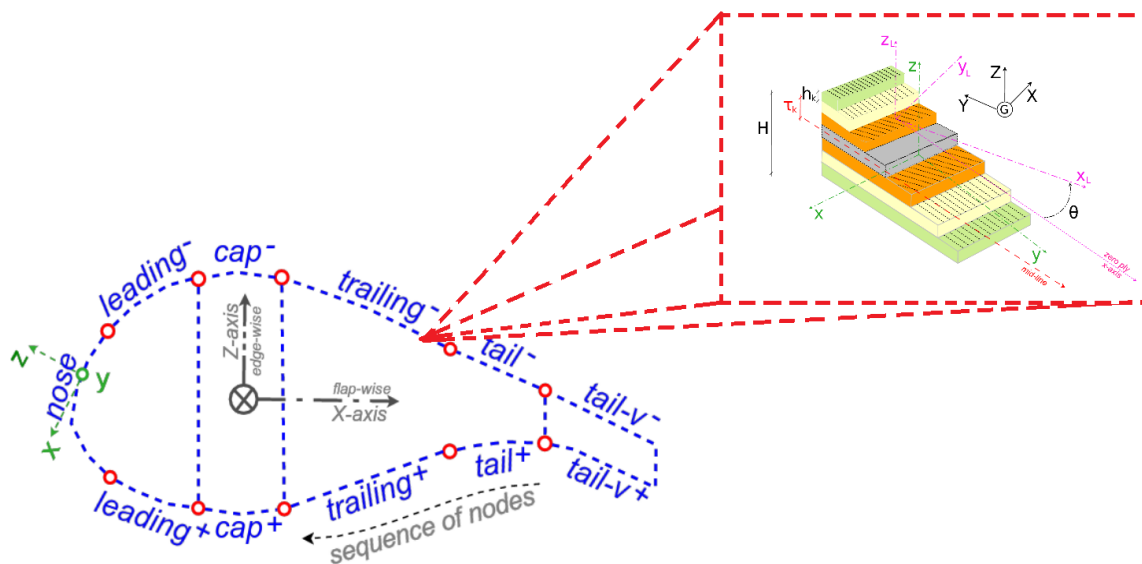


Figure B.2: Cross-section regions and focus on a point (layers structure of fiberglass).

B.3.1. Theory for torsion

According to [164], due to the multi-cell configuration addressed, a geometry factor [97] must be defined, which mainly scales the torsional stiffness properties of the blade. By applying torsion moment equilibrium (integrating shear stresses flow over the skins and the webs of the section) for all the cells shaping the cross-section (e.g. four cells for a cross-section with three webs), the following linear system of equations is obtained:

$$\begin{bmatrix} \lambda_1^{skin} & \lambda_{12}^{web} & 0 & 0 \\ -\lambda_{12}^{web} & \lambda_2^{skin} & -\lambda_{23}^{web} & 0 \\ 0 & -\lambda_{23}^{web} & \lambda_3^{skin} & -\lambda_{34}^{web} \\ 0 & 0 & -\lambda_{34}^{web} & \lambda_4^{skin} \end{bmatrix} \begin{Bmatrix} Cah_1 \\ Cah_2 \\ Cah_3 \\ Cah_4 \end{Bmatrix} = \begin{Bmatrix} \alpha_1 \\ \alpha_2 \\ \alpha_3 \\ \alpha_4 \end{Bmatrix} \quad (B.7)$$

where its solution Cah_i defines the geometric parameters, needed for the estimation of the geometry factor, as detailed next. The unknown coefficient matrix of system Eq. B.7 is symmetric. The coefficients of the matrix stem from the integration of the shear properties over the parts of the skin and the webs that form every cell and are given by:

$$\begin{aligned} \lambda_i^{skin} &= \sum_{j \in skin} \frac{\ell_j}{A_{33}^j}, i = 1, 2, \dots, N_{cell} \\ \lambda_{i,i+1}^{web} &= \sum_{j \in web} \frac{\ell_j}{A_{33}^j}, i = 1, 2, \dots, N_{cell} - 1 \end{aligned} \quad (B.8)$$

Indices $i, i + 1$ in the second expression denote the two cells adjacent to a web. Coefficients λ are calculated through summation over all segmented elements of the cell, while the vector of the right hand side represents the circulation integral over the i^{th} cell and is given by:

$$\alpha_i = - \sum_{j \in cell} \ell_j sng_j (-Z_j \cos \theta_j + X_j \sin \theta_j) - 2 \sum_{j \in cell} \ell_j \frac{B_{33}^j}{A_{33}^j} \quad (B.9)$$

where, ℓ_j is the length of the element, X_j and Z_j are the coordinates of the center of the element and $\cos \theta_j$ and $\sin \theta_j$ are the directional cosine and sine of the element. sng_j equals 1 for elements belonging to skin laminates and to the right web of the cell, while equals -1 for the element of the left web of the cell. Then, the geometry factor A_h^j for the j^{th} segmented element (taking into account in which cell/cells it belongs) is given by:

$$A_h^j = \begin{cases} \frac{Cah_i - 2B_{33}^j}{A_{33}^j} & , \text{for skin elements} \\ \frac{Cah_i - Cah_{i+1} - 2B_{33}^j}{A_{33}^j} & , \text{for web segments} \end{cases} \quad (B.10)$$

B.3.2. Geometry of cross-section and shear factors

The outer geometry, i.e. the shape of the cross-section affects various elements of the 6×6 full stiffness matrix. In this section, the Timoshenko shear factors estimation process is described, based on the theory that has been adopted by Kosmatka in [99].

B.3.2.1. Theory of Timoshenko shear factors

Let's consider a cantilever prismatic beam of length L with an arbitrary full cross-section of area A composed of a homogeneous, isotropic material, as depicted in Fig. B.3. As this figure shows, the beam

is subjected to two in-plane forces (F_x and F_z), which are applied at the centroid of the tip cross-section, as well as a torsional moment M_y . So, the following equations are satisfied:

$$F_x = \int_A \tau_{xy} dA \quad F_z = \int_A \tau_{zy} dA \quad M_y = \int_A x\tau_{zy} - z\tau_{xy} dA \quad (\text{B.11})$$

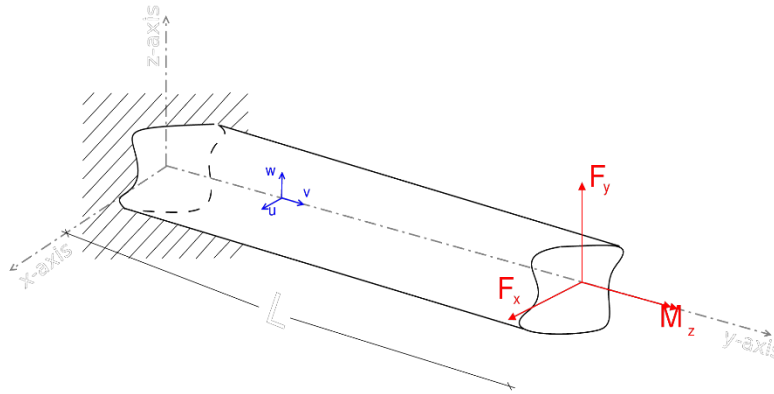


Figure B.3: Prismatic cantilever beam.

By considering that the in-plane stresses (σ_{xx} , σ_{zz} and τ_{xz}) are negligible, in respect to Saint-Venant's assumptions [165] and applying the principle of minimum potential energy, the governing equations can be derived. Therefore, according to the kinematics of a compatible one-dimension theory [166], a set of linear equations can be developed:

$$P \begin{Bmatrix} F_x \\ F_z \\ M_y \end{Bmatrix} = Q \begin{Bmatrix} \frac{\partial u}{\partial z} - \Phi_x \\ \frac{\partial v}{\partial z} + \Phi_z \\ \frac{\partial \theta}{\partial z} \end{Bmatrix} \Rightarrow \begin{Bmatrix} F_x \\ F_z \\ M_y \end{Bmatrix} = \begin{bmatrix} GAk_x & GA & -GA_{\bar{y}} \\ GA & GAk_z & GA_{\bar{x}} \\ -GA_{\bar{y}} & GA_{\bar{x}} & GJ \end{bmatrix} \begin{Bmatrix} \frac{\partial u}{\partial z} - \Phi_x \\ \frac{\partial v}{\partial z} + \Phi_z \\ \frac{\partial \theta}{\partial z} \end{Bmatrix} \quad (\text{B.12})$$

where,

$$P = \begin{bmatrix} 1 - \frac{G}{EI_{zz}} \int_A \frac{\partial \Psi_{y1}}{\partial x} dA & -\frac{G}{EI_{xx}} \int_A \frac{\partial \Psi_{y2}}{\partial x} dA & 0 \\ -\frac{G}{EI_{zz}} \int_A \frac{\partial \Psi_{y1}}{\partial z} dA & 1 - \frac{G}{EI_{xx}} \int_A \frac{\partial \Psi_{y2}}{\partial z} dA & 0 \\ -\frac{G}{EI_{zz}} \int_A x \frac{\partial \Psi_{y1}}{\partial z} - z \frac{\partial \Psi_{y1}}{\partial x} dA & -\frac{G}{EI_{zz}} \int_A x \frac{\partial \Psi_{y2}}{\partial z} - z \frac{\partial \Psi_{y2}}{\partial x} dA & 1 \end{bmatrix}$$

$$Q = \begin{bmatrix} GA & 0 & G \int_A \frac{\partial \Psi_{y3}}{\partial x} - z dA \\ 0 & GA & G \int_A \frac{\partial \Psi_{y3}}{\partial z} + x dA \\ 0 & 0 & G \int_A x \left[x + \frac{\partial \Psi_{y3}}{\partial z} \right] - z \left[\frac{\partial \Psi_{y3}}{\partial x} - z \right] dA \end{bmatrix}$$

where, E is Young's modulus of the material, ν is the Poisson ratio, G is the shear modulus that satisfies (in the case of isotropic material) $G = \frac{E}{2(1+\nu)}$, k_x, k_z are the shear correction coefficients in the two shear directions required by Timoshenko beam theory [167], Ψ is the out-of-plane warping function and finally (u, v, w) and (Φ_x, Φ_z, θ) represent the displacements and rotations about the centroid of the cross section respectively.

The warping function Ψ_i , $i = 1, 2, 3$, is an input quantity in which indices 1, 2 correspond to shear-dependent warping, while the index 3 is the Saint-Venant torsion function. This function, can be written in matrix form as:

$$\Psi_i(x, z) = [N(x, z)]\{\varphi_i\} \quad (\text{B.13})$$

where $\{\varphi_i\}$ is a column-matrix of unknown coefficients and $N(x, z)$ is a row-matrix of the power terms which are usually selected a polynomial order like Pascal's triangle of nine terms:

$$[N(x, z)] = [x \quad z \quad x^2 \quad xz \quad z^2 \quad x^3 \quad x^2z \quad xz^2 \quad z^3] \quad (\text{B.14})$$

This function, is mainly affected by the cross-section shape as well as the material properties and it can be determined by calculating the coefficients φ_i , through solving a set of linear algebraic equations:

$$[K]\{\varphi_i\} = [[F_w] - [F_c]]\{Q_i\} \quad (\text{B.15})$$

where,

$$[K] = GL \int_A \frac{\partial [N(x, z)]^T}{\partial x} \frac{\partial [N(x, z)]}{\partial x} + \frac{\partial [N(x, z)]^T}{\partial z} \frac{\partial [N(x, z)]}{\partial z} dA$$

$$[F_w] = EL \left[\int_A x [N(x, z)]^T dA, \int_A z [N(x, z)]^T, 0 \right]$$

$$[F_c] = GL \int_A \left[\frac{\partial [N(x, z)]^T}{\partial z}, \frac{\partial [N(x, z)]^T}{\partial x} \right] \begin{bmatrix} -vxz & -\frac{\nu}{2}(z^2 - x^2) & x \\ -\frac{\nu}{2}(x^2 - z^2) & -vxz & -z \end{bmatrix} dA$$

$$Q_i = \begin{cases} [1 \quad 0 \quad 0]^T, & \text{if } i = 1 \\ [0 \quad 1 \quad 0]^T, & \text{if } i = 2 \\ [0 \quad 0 \quad 1]^T, & \text{if } i = 3 \end{cases}$$

B.3.2.2. Procedure for Timoshenko shear factors calculation

The procedure for calculating the Timoshenko shear factors is briefly described through five steps:

- during the integrations, the elements of the skin (outer elements of cross-section) are taken into account (not the webs).
- the row-matrix $N(x, z)$, is adopted from Eq. B.14.
- calculation of φ_i , through the Eq. B.15.
- estimation of 3×3 matrices P and Q of Eq. B.12.
- solving Eq. B.12 and determining the coefficients k_x and k_z .

B.3.2.3. Application of Timoshenko shear factors

Predictions of the shear factors by L/T model are compared to results from references [168] and [165] for two different cross-section shapes (see Fig. B.4). The two sections tested are a full elliptical section with uniform, isotropic material and Poisson ratio $\nu = 0.333$, having as parameter the semi-axes ratio (r_2/r_1) and a hollow circular section of uniform, isotropic material with varying Poisson ratio. It is noted that, as indicated in the literature [168], the shape of the cross section and Poisson ratio are both important parameters that drive variations in the value of the shear factor. The results of the comparisons for both sections are provided in Table B.1. The percentage differences with respect to the predictions reported in the literature are provided in the table, along with the predicted values of the shear factors.

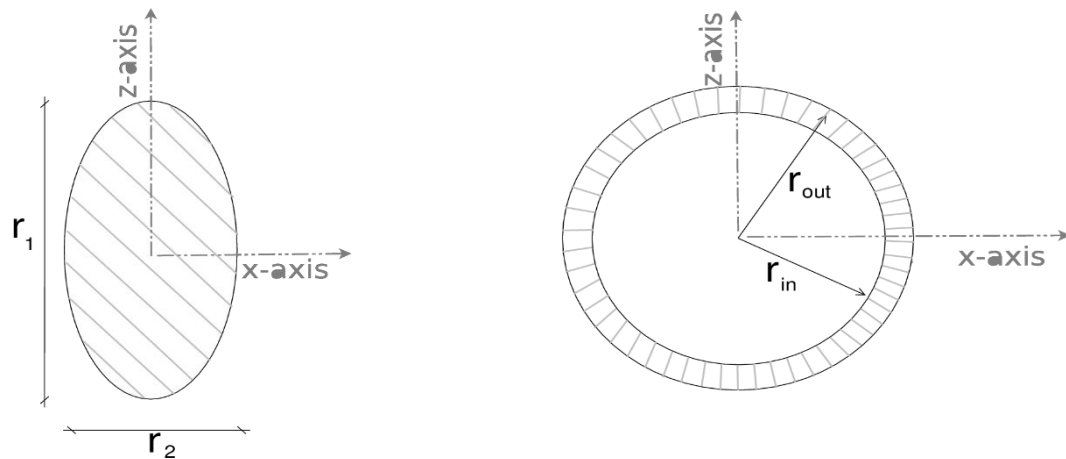


Figure B.4: Sketch of simple geometric shapes (ellipse and hollow circle), used for determining the Timoshenko shear factors.

As seen in Table B.1, the differences between the predictions of the current method and those reported in [168] and [99] do not exceed 2%. In the case of the elliptical section, they appear to be slightly higher in the predictions of k_x , in particular for the semi-axes ratios of 0.1 and 0.2. Much smaller differences (order of 0.2%) are noted in the prediction of k_z for the elliptical section but also in the prediction of the shear factor ($k_x = k_z = k$) of the circular section for all Poisson ratios. The predicted trend by both

models is that k_x , increases with the increase in the semi-axes ratio of the elliptical section, while k slightly increases with the increase in the Poisson ratio.

Table B.1: Timoshenko shear factors for a) full elliptical cross-section ($\nu = 0.333$), for various semi-axis ratios r_2/r_1 and b) hollow circle with ratio of inner over outer radius of 0.9, for various Poisson's ratios. Comparison between present work (L/T) and results in [168] and [99].

r_2/r_1	Ellipse						ν	Hollow circle		
	Shear factor k_x [-]			Shear factor k_z [-]				Shear factor k [-]		
	Ref. [99]	L/T	diff.	Ref. [99]	L/T	diff.		Ref. [168]	L/T	diff.
0.01	0.005	0.005	0.0%	0.917	0.915	-0.2%	0.1	0.514	0.515	0.2%
0.10	0.310	0.304	-1.9%	0.917	0.915	-0.2%	0.2	0.524	0.525	0.2%
0.20	0.602	0.596	-1.0%	0.916	0.914	-0.2%	0.3	0.533	0.534	0.2%
0.50	0.830	0.827	-0.4%	0.909	0.907	-0.2%	0.4	0.541	0.542	0.2%
1.00	0.889	0.889	0.0%	0.889	0.889	0.0%	0.5	0.548	0.549	0.2%

B.3.3. Cross-sectional stiffness analysis

By integrating laminate stiffness properties of Eq. B.5 along the skins and the webs of the cross-section, the stiffness matrix \mathbf{K} , relating resultant section forces and moments \mathbf{F} , \mathbf{M} with global strain and curvature characteristics $\boldsymbol{\varepsilon}$, $\boldsymbol{\kappa}$ is obtained with respect to the cross-section coordinate system $OXYZ$:

$$\begin{Bmatrix} \mathbf{F} \\ \mathbf{M} \end{Bmatrix} = \mathbf{K} \begin{Bmatrix} \boldsymbol{\varepsilon} \\ \boldsymbol{\kappa} \end{Bmatrix} \Rightarrow \begin{Bmatrix} F_x \\ F_y \\ F_z \\ M_x \\ M_y \\ M_z \end{Bmatrix} = \begin{bmatrix} \text{sub-matrix A} & & \\ & \text{sub-matrix B} & \\ & & \text{sub-matrix D} \end{bmatrix} \begin{Bmatrix} \varepsilon_x \\ \varepsilon_y \\ \varepsilon_z \\ \kappa_x \\ \kappa_y \\ \kappa_z \end{Bmatrix} \quad (\text{B.16})$$

sub-matrix A contains $K_{11}^A, K_{12}^A, K_{13}^A, K_{22}^A, K_{23}^A, K_{33}^A$.
 sub-matrix B contains $K_{11}^B, K_{12}^B, K_{13}^B, K_{21}^B, K_{22}^B, K_{23}^B, K_{31}^B, K_{32}^B, K_{33}^B$.
 sub-matrix D contains $K_{11}^D, K_{12}^D, K_{13}^D, K_{22}^D, K_{23}^D, K_{33}^D$.
 sub-matrix B^T is the transpose of sub-matrix B. The diagonal elements of sub-matrix A and D are labeled as $K_{11}^A, K_{33}^A, K_{11}^D, K_{33}^D$.

where, in the special case of uniform, isotropic material (i.e. standard Timoshenko beam model) the elements in the boxes may zero values. In the above symmetric stiffness matrix, the diagonal elements K_{11}^A and K_{33}^A represent transverse shear rigidity, K_{22}^A axial stiffness, K_{11}^D and K_{33}^D flexural stiffness in the flap-wise and edge-wise directions respectively and K_{22}^D torsional stiffness. The off-diagonal elements K_{21}^B and K_{23}^B represent bending-torsion couplings due to the offset of the elastic center with respect to the cross-section coordinate system. Similarly, terms K_{12}^B and K_{32}^B represent shear-torsion couplings due

to the offset of the shear center with respect to the cross-section coordinate system. The cross bending coupling term K_{13}^D introduces the FEC effect, whereas the elements K_{12}^D and K_{23}^D shown in blue are responsible for the activation of BTC between flap or edge direction and torsion. Finally, the terms affected by Timoshenko shear factors, are shown in red color.

In the following the equations describing each term of the full stiffness matrix are provided:

- sub-matrix A:

$$K_{11}^A = \sum_{j=1}^{N_{el}} \ell_j (A_{33}^j \cos^2 \theta_j + A_{22}^j \sin^2 \theta_j) \quad (\text{B.17a})$$

$$K_{12}^B = \sum_{j=1}^{N_{el}} \ell_j A_{13}^j \cos \theta_j \quad (\text{B.17b})$$

$$K_{13}^A = \sum_{j=1}^{N_{el}} \ell_j (A_{33}^j \sin \theta_j \cos \theta_j - A_{22}^j \cos \theta_j \sin \theta_j) \quad (\text{B.17c})$$

$$K_{22}^A = \sum_{j=1}^{N_{el}} \ell_j A_{11}^j \quad (\text{B.17d})$$

$$K_{23}^A = \sum_{j=1}^{N_{el}} \ell_j A_{13}^j \sin \theta_j \quad (\text{B.17e})$$

$$K_{33}^A = \sum_{j=1}^{N_{el}} \ell_j (A_{33}^j \sin^2 \theta_j + A_{22}^j \cos^2 \theta_j) \quad (\text{B.17f})$$

- sub-matrix B:

$$K_{11}^B = \sum_{j=1}^{N_{el}} \ell_j (B_{13}^j \cos \theta_j - A_{13}^j Z_j) \cos \theta_j \quad (\text{B.17g})$$

$$K_{12}^B = z_{sc} K_{11}^A + x_{sc} K_{13}^A \quad (\text{B.17h})$$

$$K_{13}^B = \sum_{j=1}^{N_{el}} \ell_j (A_{13}^j X_j + B_{13}^j \sin \theta_j) \cos \theta_j \quad (\text{B.17i})$$

$$K_{21}^B = \sum_{j=1}^{N_{el}} \ell_j (B_{11}^j \cos \theta_j - A_{11}^j Z_j) \quad (\text{B.17j})$$

$$K_{22}^B = - \sum_{j=1}^{N_{el}} \ell_j (A_{13}^j A h^j + 2B_{13}^j) \quad (\text{B.17k})$$

$$K_{23}^B = \sum_{j=1}^{N_{el}} \ell_j (A_{11}^j X_j + B_{11}^j \sin \theta_j) \quad (\text{B.17l})$$

$$K_{31}^B = \sum_{j=1}^{N_{el}} \ell_j (B_{13}^j \cos \theta_j - A_{13}^j Z_j) \sin \theta_j \quad (\text{B.17m})$$

$$K_{32}^B = z_{sc}K_{13}^A + x_{sc}K_{33}^A \quad (\text{B.17n})$$

$$K_{33}^B = \sum_{j=1}^{N_{el}} \ell_j (A_{13}^j X_j + B_{13}^j \sin \theta_j) \sin \theta_j \quad (\text{B.17o})$$

- sub-matrix D:

$$K_{11}^D = \sum_{j=1}^{N_{el}} \ell_j (A_{11}^j Z_j^2 - 2B_{11}^j Z_j \cos \theta_j + D_{11}^j \cos^2 \theta_j) \quad (\text{B.17p})$$

$$K_{12}^D = x_{sc}K_{11}^B - z_{sc}K_{31}^B + \sum_{j=1}^{N_{el}} \ell_j [B_{13}^j (Ah^j \cos \theta_j - 2X_j) - A_{13}^j Ah^j Z_j + 2D_{13}^j \cos \theta_j] \quad (\text{B.17q})$$

$$K_{13}^D = \sum_{j=1}^{N_{el}} \ell_j [D_{11}^j \sin \theta_j \cos \theta_j - A_{11}^j X_j Z_j - B_{11}^j (Z_j \sin \theta_j - X_j \cos \theta_j)] \quad (\text{B.17r})$$

$$K_{22}^D = z_{sc}K_{11}^B + x_{sc}K_{13}^B + \sum_{j=1}^{N_{el}} \ell_j [A_{33}^j (Ah^j)^2 + 4B_{33}^j Ah^j + 4D_{33}^j] \quad (\text{B.17s})$$

$$K_{23}^D = \sum_{j=1}^{N_{el}} \ell_j [A_{13}^j Ah^j X_j + B_{13}^j (Ah^j \sin \theta_j + 2X_j) + 2D_{13}^j \sin \theta_j] \quad (\text{B.17t})$$

$$K_{33}^D = \sum_{j=1}^{N_{el}} \ell_j (A_{11}^j X_j^2 + 2B_{11}^j X_j \sin \theta_j + D_{11}^j \sin^2 \theta_j) \quad (\text{B.17u})$$

B.3.4. Shear center

Assuming the thin walled and three-cell ellipsis of Fig. B.5,

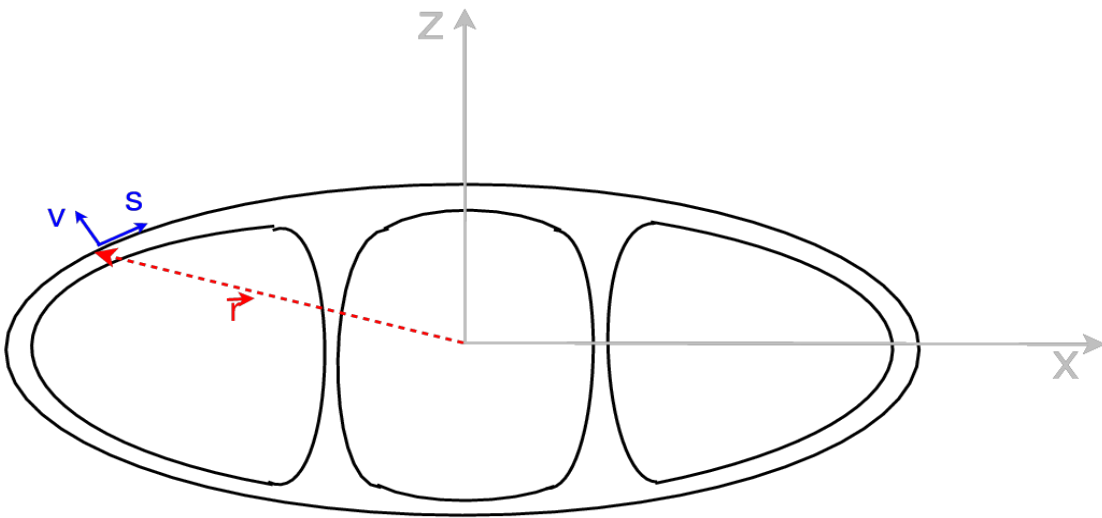


Figure B.5: Assumed section with coordinate system and notations used in appendix B.

The shear center coordinates are calculated employing the compatibility condition for the stresses:

$$\sigma_{y,y} + \sigma_{ys,s} + \sigma_{yv,v} = 0 \quad (\text{B.18})$$

Integrating over the laminate thickness (from 0 to h) and assuming that: $\int_0^h \sigma_{yv,v} dv = \sigma_{yv}(h) - \sigma_{yv}(0) \approx 0$ one gets $\int_0^h \sigma_{ys,s} dv + \int_0^h \sigma_{y,y} dv = 0$ or $\frac{d[\int_0^h \sigma_{ys} dv]}{ds} + \frac{d[\int_0^h \sigma_y dv]}{dy} = 0$.

Using the notation $q(s) = \int_0^h \sigma_{ys} dv$, $N_y(s, y) = \int_0^h \sigma_y dv$ and integrating along s the compatibility condition reads:

$$\Delta q = q(s_2) - q(s_1) = - \int_{s_1}^{s_2} N_{y,y}(s, y) ds \quad (\text{B.19})$$

Eq. B.19 is the starting relation that provides the so-called “basic shear flow” of all similar simplified methods used to non-FSM (Full Stiffness Matrix) formulations.

To calculate $N_{y,y}$ we assume that we already know the shear center coordinates and that the analysis is done using the $OXYZ$ coordinate system located at the shear center of the section.

The expressions of the strains in this system are given by:

$$\varepsilon_y(s, v, y) = \varepsilon_{0y} - k_x(y)[z_0 - x_{0,s}v] + k_z(y)[x_0 + z_{0,s}v] + k_{y,y}\Psi(s, v) \quad (\text{B.20a})$$

$$\varepsilon_{y,s}(s, v, y) = \varepsilon_{0yz}(y)z_{0,s} + \varepsilon_{0yx}(y)x_{0,s} + \varepsilon_{0ys}^t(s, y) - 2k_y(y)v \quad (\text{B.20b})$$

$$\varepsilon_{yv}(s, v, y) = -\varepsilon_{0yz}(y)x_{0,s} + \varepsilon_{0yx}(y)z_{0,s} \quad (\text{B.20c})$$

Then, the normal stress σ_y can be expressed through the equation:

$$\sigma_y(s, v, y) = q_{11}\varepsilon_y(s, v, y) + q_{13}\varepsilon_{ys}(s, v, y) \quad (\text{B.21})$$

Substituting the strain expressions from Eq. B.20, integrating over the thickness of the laminate and neglecting the higher order warping term, we derive $N_y(s, y)$ as:

$$\begin{aligned} N_y(s, y) = & A_{11}[\varepsilon_{0y}(y) - k_x(y)z_0 + k_z(y)x_0] + B_{11}[k_x(y)x_{0,s} + k_z(y)z_{0,s}] \\ & + A_{13}[\varepsilon_{0yz}(y)z_{0,s} + \varepsilon_{0yx}(y)x_{0,s} + \varepsilon_{0ys}^t(s, y)] - 2B_{13}k_y(y) \end{aligned} \quad (\text{B.22})$$

Neglecting $k_{y,y}$ as a higher order term, $N_{y,y}$ is written as:

$$\begin{aligned} N_{y,y}(s, y) = & A_{11}[\varepsilon_{y,y}(y) - k_{x,y}(y)z_0 + k_{z,y}(y)x_0] + B_{11}[k_{x,y}(y)x_{0,s} + k_{z,y}(y)z_{0,s}] \\ & + A_{13}[\varepsilon_{yz,y}(y)z_{0,s} + \varepsilon_{yx,y}(y)x_{0,s}] - 2B_{13}k_{y,y}(y) \end{aligned} \quad (\text{B.23})$$

The needed values of the strain and curvature derivatives may be obtained by inverting the full stiffness matrix and applying pure bending at the x and z directions respectively. Given that the bending moment derivatives $M_{z,y}$, $M_{x,z}$ are connected to the (y -independent) shear components Q_z , Q_x through $M_{z,y} = Q_x$ and $M_{x,z} = -Q_z$, the strain-curvature derivatives in the $N_{y,y}$ formula are expressed as:

$$\begin{Bmatrix} \varepsilon_{y,y} \\ \varepsilon_{yx,y} \\ \varepsilon_{yz,y} \\ k_{x,y} \\ k_{z,y} \\ k_{y,y} \end{Bmatrix} = \begin{bmatrix} K_{24}^{-1} & K_{26}^{-1} \\ K_{14}^{-1} & K_{16}^{-1} \\ K_{34}^{-1} & K_{36}^{-1} \\ K_{44}^{-1} & K_{46}^{-1} \\ K_{64}^{-1} & K_{66}^{-1} \\ K_{54}^{-1} & K_{56}^{-1} \end{bmatrix} \begin{Bmatrix} -Q_z \\ +Q_x \end{Bmatrix} \quad (\text{B.24})$$

where K_{ij}^{-1} are the entries of the inverted full stiffness matrix.

Introducing Eq. B.24 into Eq. B.23 $N_{y,y}$ can be now expressed as:

$$N_{y,y} = Q_z f_z + Q_x f_x \quad (\text{B.25})$$

where f_z, f_x are functions of K_{ij}^{-1} , the geometry and the material properties expressed through A_{11}, B_{11}, A_{13} and B_{13} .

Having the basic shear flow through Eq. B.19 one may proceed to the calculation of the “rectified basic shear flow” with exactly the same formulation used in the non-FSM approaches.

There is still another detail that one has to account for the proper calculation of the constant shear flow $q(0)$, which ensures the equilibrium of the shear flow at nodes connecting more than two elements.

The constant derives from the enforcement of $\oint_{C_L} \varepsilon_{ys} ds = 0$ at all closed loops of the section, where ε_{ys} is the circumferential shear strain at the laminate center. $\varepsilon_{ys}(s)$ is connected to the local shear flow $q(s)$ through the formula $\varepsilon_{ys}(s) = q(s)/A_{33}^M$, where $A_{33}^M = A_{33} - A_{13}^2/A_{11}$.

The proposed formulation is therefore using A_{33}^M in the place of A_{33} (of the classical theory) to account for A_{13} effects.

Besides the alternative formulation for $N_{y,y}$ and the introduction of A_{33}^M there are no more changes required for the application of the proposed theory.

The above theory can be used for the calculation of the shear flow around the section as soon as the coordinates of shear center (x_{sc}, z_{sc}) are known. It is therefore evident that its application in calculating the shear center coordinates cannot be done in one shot and an iterative procedure is required. This is because the shear center coordinates not only indirectly appear in the $N_{y,y}$ expression (through the airfoil coordinates) but also affect the K_{ij}^{-1} terms. The iterative scheme comprises the following steps:

- assume initial (x_{sc}, z_{sc}) values.
- translate the airfoil coordinate system to the shear center.
- set-up the full stiffness matrix Eq. B.16 and invert it to calculate K_{ij}^{-1} .
- calculate $N_{y,y}$ using equations Eq. B.23 and Eq. B.24 and from that the basic shear flow from Eq. B.19.
- make the next steps to re-calculate the shear center location.
- go back to the first step until convergence.

B.3.5. Cross-sectional stresses analysis

Finally, the cross-sectional analysis tool can estimate the developing stresses, produced for a given set of internal loads $\{F \ M\}^T$, through inversion of Eq. B.16 and calculation of the generalized strains $\{\varepsilon \ \kappa\}^T$. Then, the distribution of normal (σ_n) and shear (σ_s) stresses are calculated over the material laminates through application of Hooke’s law. The above two stresses are consolidated and related with the material strength (S_1 -longitudinal strength and S_2 -shear strength) through the Tsai-Hill failure

criterion [98], by considering a material safety factor of $\gamma_m = 1.2$. Failure occurs for criterion values exceeding 1, whereas the criterion is given by:

$$f_{T/H} = \frac{\sigma_n^2}{S_1^2} - \frac{|\sigma_n \sigma_s|}{S_1^2} + \frac{\sigma_s^2}{S_2^2} \quad (\text{B.26})$$

B.4. Thin lamination model application example – static cantilever

In the present section, predictions by the thin lamination model of the sectional properties of a cantilever composite beam are compared against those of BECAS tool [55]. In this case, a $1m$ long, thin-walled, composite beam with elliptical cross-section (with semi-axes ratio 1:2) and uniform wall thickness of $0.01m$, has been considered. The beam is clamped at one end and a vertical force $F = 10000N$ is applied at the free end. As shown in Fig. B.6, the beam walls consist of two layers of fiberglass triaxial (TRIAX) or uni-directional (UNIAX) with a $3mm$ thickness, on either side of the Balsa core which is $4mm$ thick, forming a *sandwich-type configuration*. The UNIAX material is used in the $0.3m$ wide upper and lower regions marked with dashed lines in Fig. B.6, which are called ‘caps’ and the TRIAX is the reinforcement material used in the skin. Information about the properties of the above materials, are provided in Table A.3 of the appendix A.

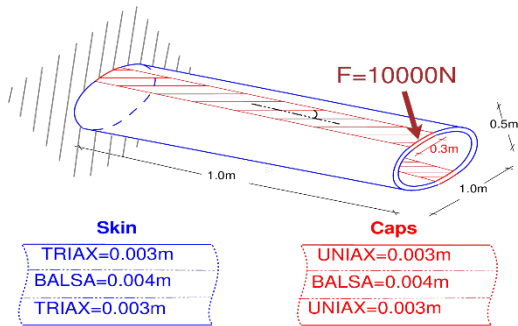


Figure B.6: Sketch of the tubular composite cantilever of $1m$ long. The cross-section of beam has elliptical shape, with ratio 1:2 and it consists by different lay-up configuration between ‘caps’ and skin region.

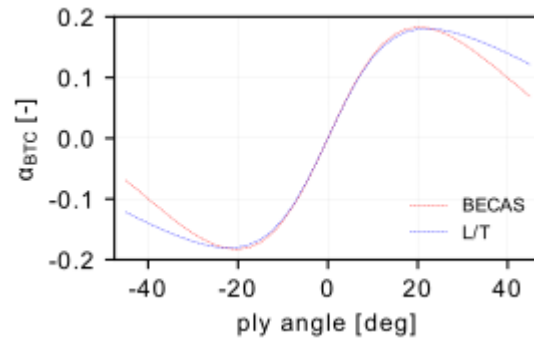


Figure B.7: Distribution of the coupling factor α_{BTC} , of the tubular cross-section, relative to the offset ply angle of the UNIAX material. The comparison is performed using BECAS and L/T tools.

By introducing an offset angle in the UNIAX on the caps, it is possible to activate Bend Twist Coupling (BTC) of the cantilever, see Fig. B.6. The above technique has been used extensively in the last decades by the wind energy community as a passive control to alleviate the operational loads of the wind turbine blades [67]. According to the definition by Lobitz and Laino [146] the local material BTC coefficient α_{BTC} between flap-wise bending and torsion is given by:

$$\alpha_{BTC} = \frac{K_{12}^D}{\sqrt{K_{11}^D \times K_{22}^D}} \quad (\text{B.27})$$

The magnitude of α_{BTC} is the measure of the BTC potential of the beam and the sign of it is related to the twist direction. In the case of the elliptical beam studied in this section, a prediction of the above quantity, has been obtained for various offset ply angles in the range $[-45^\circ, +45^\circ]$. Computations are performed using both BECAS and the L/T tool. As depicted in the Fig. B.7, predictions by the L/T model perfectly agree, in the range of ply angles $[-20^\circ, +20^\circ]$. For larger/smaller angles, deviations in the predictions of the two tools increase gradually, reaching 77% in the case of 45° ply angle. In practice, application of the material BTC is limited to ply offset angles not higher than $\pm 10^\circ$, because as ply offset angle increases, the capability of the caps to carry bending moments is reduced (strength of the material is weakened as a result of the rotation of the fibers).

Table B.2: Diagonal stiffness characteristics and maximum stress of the ellipse section, provided by BECAS, L/T and Analytic approach.

	Analytic	BECAS	diff.	L/T	diff.
$K_{11}[MN]$	73.15	68.99	-5.7%	77.23	5.6%
$K_{22}[MN]$	390.01	389.71	-0.1%	390.01	0.0%
$K_{33}[MN]$	31.32	31.03	-0.9%	25.03	-20.1%
$K_{44}[MN/m^2]$	15.77	15.80	0.2%	15.78	0.1%
$K_{55}[MN/m^2]$	11.28	12.00	6.4%	12.00	6.4%
$K_{66}[MN/m^2]$	34.31	34.25	-0.2%	34.31	0.0%
$\sigma_{normal}^{max}[MN/m^2]$	6.78	6.53	-3.7%	6.38	-5.9%

In Table B.2, the value of the most important terms of the stiffness matrix of the 2D elliptical section, are presented, for the case where the material BTC is switched off (i.e. ply angle is zero). The aforementioned terms, following the indices of Eq. B.16, correspond to the on-diagonal elements of the 6×6 stiffness matrix. Each term is calculated using the BECAS tool and L/T and the results are compared with the analytical approach, in which Timoshenko shear factors of $k_x = 0.65$ and $k_z = 0.45$, have been applied. As seen in Table B.2, a very good agreement between BECAS, L/T and the analytic approach is obtained. This is especially true for the terms that contribute to the moments, i.e. indices 4 – 6. In the configuration of Fig. B.6, the cross-section at the root of the cantilever is of great interest. As expected, maximum normal stress develops on the outer surface (UNIAX material) of the ‘caps’ region and is calculated by:

$$\sigma_{normal}^{max} = \frac{Mz_{max}}{I} \quad (B.28)$$

where, M : calculated bending moment ($M = F L$)

z_{max} : vertical distance away from the natural axis

I : moment of inertia around the natural axis

This is also confirmed by the two numerical tools (BECAS and L/T), showing, however, a slight deviation in the value of the maximum normal stress - relative to the analytical solution, of the order of -3.7% and -5.9% respectively.

References

- [1] Blyth J. **(2005)** *'Britain's First Modern Wind Power Pioneer'*, Wind Engineering, 29(3), 191-200, doi: 10.1260/030952405774354921
- [2] Fleming P. and Proderst S. **(1984)** *'The Evolution Of Wind-Turbines: An Historical Review'*, Applied Energy, 18(3), 163-177, doi: 10.1016/0306-2619(84)90007-2
- [3] *'History Of Wind Power'*, https://handwiki.org/wiki/Engineering:History_of_wind_power
- [4] Chel A. and Kaushik G. **(2011)** *'Renewable Energy For Sustainable Agriculture'*, Agronomy for Sustainable Development, 31(1), 91-118, doi: 10.1051/agro/2010029
- [5] Kumar A., Khan M. and Pandey B. **(2018)** *'Wind Energy: A Review Paper'*, Gyancity Journal of Engineering and Technology, Vo. 4, no. 2, pp. 29-37, ISSN: 2456-0065, doi: 10.21058/gjet.2018.42004
- [6] *'Our World In Data'*, <https://ourworldindata.org/>
- [7] Blair N., Bolinger M., Elliott D., George R., Goldberg M., Hand M., Heimiller D., Hem T., Miller B., O'Connell R., Schwartz M., Tegen S. and Wiser R. **(2008)** *'20% Wind Energy By 2030: Executive Summary'*, DOE/GO-102008-2578, <http://www.nrel.gov/docs/fy08osti/41869.pdf>
- [8] Zygierewicz A. and Sanz L. **(2018)** *'Renewable Energy Directive: Revision Of Directive (EU) 2018/2001'*, European Parliamentary Research Service, PE 662.619
- [9] REPowerEU Plan **(2022)** *'Communication From The Commission To The European Parliament, The European Council, The Council, The European Economic And Social Committee And The Committee Of The Regions'*, COM(2022) 230 final
- [10] Luo X., Wang J., Dooner M. and Clarke J. **(2015)** *'Overview Of Current Development In Electrical Energy Storage Technologies And The Application Potential In Power System Operation'*, Applied Energy, 137, 511-536, doi: 10.1016/j.apenergy.2014.09.081
- [11] Borah R., Hughson F., Johnston J. and Nann T. **(2020)** *'On Battery Materials And Methods'*, Materials Today Advances, 6, 100046, doi: 10.1016/j.mtadv.2019.100046
- [12] Kumar A. and Sehgal M. **(2018)** *'Hydrogen Fuel Cell Technology For A Sustainable Future: A Review'*, SAE Technical Paper Servies, doi: 10.4271/2018-01-1307

-
- [13] *'Electricity From Renewable Sources On The Rise'*, <https://ec.europa.eu/eurostat/web/products-eurostat-news/w/ddn-20230127-1>
- [14] Sieros G., Chaviaropoulos P., Sørensen D., Bilder H. and Jamieson P. **(2012)** *'Upscaling Wind Turbines Theoretical And Practical Aspects And Their Impact On The Cost Of Energy'*, *Wind Energy*, 15(1),3-17, doi: 10.1002/we.527
- [15] Chaviaropoulos P., Politis E., Lekou D., Sørensen N., Hansen M., Bulder B., Winkelaar D., Lindenburg C., Saravanos D., Philippidis T., Galiotis C., Hansen M. and Kossivas T. **(2006)** *'Enhancing The Damping Of Wind Turbine Rotor Blades, The Dampblade Project'*, *Wind Energ.* 2006; 9:163-177, doi: 10.1002/we.183
- [16] *'STABCON'*, <https://cordis.europa.eu/project/id/ENK5-CT-2002-00627>
- [17] *'UpWind'*, <https://cordis.europa.eu/project/id/19945>
- [18] *'INNWIND.EU'*, <https://cordis.europa.eu/project/id/308974>
- [19] *'AVATAR'*, <https://cordis.europa.eu/project/id/608396>
- [20] Papadakis G. and Voutsinas S. **(2019)** *'A Strongly Coupled Eulerian Lagrangian Method Verified In 2D External Compressible Flows'*, *J. of Comput. Fluids* 2019, 195, 104325
- [21] Manolas D., Riziotis V., Papadakis G. and Voutsinas S. **(2020)** *'Hydro-servo-aero-elastic Analysis of Floating Offshore Wind Turbines'*, *J. of Fluids*, 5(4), 200, special issue on Wind and Wave Renewable Energy Systems, doi: 10.3390/fluids5040200
- [22] Manolas D. **(2015)** *'Hydro-Aero-Elastic Analysis Of Offshore Wind Turbines'*, PhD thesis, <http://dx.doi.org/10.26240/heal.ntua.2154>
- [23] Bossanyi E. **(2003)** *'Individual Blade Pitch Control For Load Reduction'*, *Wind Energy*, 6(2), 119-128, doi: 10.1002/we.76
- [24] Lackner M. and Kuik G. **(2010)** *'A Comparison Of Smart Rotor Control Approaches Using Trailing Edge Flaps And Individual Pitch Control'*, *Wind Energy*, 13(2-3), 117-134, doi: 10.1002/we.353
- [25] Menon M. and Ponta F. **(2022)** *'Aero-Elastic Response Of Wind Turbine Rotor Under Rapid Actuation Of Flap-Based Flow Control Devices'*, *Fluids* 2022, 7, 129, <https://doi.org/10.3390/fluids7040129>
- [26] Ashwill T., Kanaby G., Jackson K. and Zuteck M. **(2010)** *'Development Of The Swept Twist Adaptive Rotor (STAR) Blade'*, 48th AIAA Aerospace Sciences Meeting Including the New Horizons Forum and Aerospace Exposition, doi: 10.2514/6.2010-1582
- [27] Knight & Carve Wind Group **(2009)** *'Sweep-Twist Adaptive Rotor Blade'*, Final Project Report, SAND2009-8037, Sandia National Laboratories, Albuquerque, NM, December 2009, <https://www.osti.gov/servlets/purl/973353>
- [28] Larwood S., Dam C. and Schow D. **(2014)** *'Design Studies Of Sweep Wind Turbine Blades'*, *Renewable Energy*, 71, 563-571, doi: 10.1016/j.renene.2014.05.050
- [29] Brøndsted P., Lilholt H. and Lystrup A. **(2005)** *'Composite Materials For Wind Power Turbine Blades'*, *Annual Review of Materials Research*, 35(1), 505-538, doi: 10.1146/annurev.matsci.35.100303.110641

-
- [30] Hyer W. (1982) '*Unsymmetrically Laminated Composites*', Progress in science and engineering of composites, 4th International Conference on Composite Materials, Tokyo, ID: 19830058945
- [31] Chordis D. (2012) '*Structural Analysis Of Composite Wind Turbine Blades*', PhD thesis, ISBN: 978-3-319-00863-9, doi: 10.1007/978-3-319-00864-6, <http://www.springer.com/series/11859>
- [32] Campbell A. (1912) '*On Vibration Galvanometers With Unifilar Torsional Control*', Proceedings of the Physical Society of London, 25(1), 203-205, doi: 10.1088/1478-7814/25/1/320
- [33] Pealing H. (1913) '*XLII. On An Anomalous Variation Of The Rigidity Of Phosphor Bronze*', Philosophical Magazine Series 6, 25:147, 4180427, doi: 10.1080/14786440308634177
- [34] Rohde S., Ifju P., Sankar B. and Jenkins D. (2015) '*Experimental Testing Of Bend-Twist Coupled Composite Shafts*', Experimental Mechanics 55(9), 1613-1625, doi: 10.1007/s11340-015-0050-0
- [35] Nicholls-Lee R., Boyd S. and Turnock S. (2009) '*Development Of High Performance Composite Bend-Twist Coupled Blades For A Horizontal Axis Tidal Turbine*', <https://www.researchgate.net/publication/240623016>
- [36] Ozbay S. (2006) '*Extension-Twist Coupling Optimization In Composite Rotor Blades*', PhD thesis, <http://hdl.handle.net/1853/10422>
- [37] DiPalma M., Ferede E. and Gandhi F. (2018) '*Optimization of Extension-Twist Coupling Composite Blades For High-Speed Rotorcraft*', Proceedings of the 74th American Helicopter Society Annual Forum, Phoenix, Arizona, May 15-17, 2018
- [38] Mansfield E. and Sobey A. (1979) '*The Fibre Composite Helicopter Blade, Part 1: Stiffness Properties And Part 2: Prospects For Aeroelastic Tailoring*', <https://doi.org/10.1017/S0001925900008623>
- [39] Chopra I. and Hong C. (1985) '*Aero-Elastic Stability Analysis Of A Composite Rotor Blade*', J. of the American Helicopter Society, 30(2), 57-67, doi: 10.4050/jahs.30.57
- [40] Sundar D., Narasimalu S. and Yaiwen Y. (2018) '*Study Of Bend To Twist Coupling Of Composite Laminates For Passive Load Alleviation Of A Wind Turbine Blade*', 2018 Asian Conference on Energy, Power and Transportation Electrification (ACEPR), doi: 10.1109/accept.2018.8610671
- [41] Meng H., Lien F., Glinka G. and Geiger P. (2018) '*Study On Fatigue Life Of Bend-Twist Coupling Wind Turbine Blade Based On Anisotropic Beam Model And Stress-Based Fatigue Analysis Method*', Composite Structures, 208, 678-701, doi: 10.1016/j.compstruct.2018.10.032
- [42] Croce A., Sartori L., Lunghini M., Clozza L., Bortolotti P. and Bottasso C. (2016) '*Lightweight Rotor Design By Optimal Spar Cap Offset*', J. of Phys.: Conf. Ser., 753, 062003, doi: 10.1088/1742-6596/753/6/062003
- [43] Lobitz D., Veers P. and Migliore P. (1996) '*Enhanced Performance Of HAWTS Using Adaptive Blades*', Proceedings of the Wind 1996 ASME Wind Energy Symposium, January 29-February 2 1996
- [44] Fedorov V. (2012) '*Bend-Twist Coupling Effects In Wind Turbine Blades*', PhD thesis, https://backend.orbit.dtu.dk/ws/portalfiles/portal/54637711/PhD_Thesis_Vladimir_Fedorov.pdf

-
- [45] Stäblein R. and Hansen H. **(2016)** *'Effect Of Turbulence On Power For Bend-Twist Coupled Blades'*, J. of Phys.: Conf. Ser., 753, 042018, doi: 10.1088/1742-6596/753/4/042018
- [46] Roeleven N. **(2018)** *'Optimal Design Of Wind Turbine Blades For Bend Twist Coupling Effects'*, DTU Wind Energy-M-0223
- [47] Wang K., Riziotis V. and Voutsinas S. **(2016)** *'Aero-Elastic Stability Of Idling Wind Turbines'*, J. of Phys.: Con. Ser., 753, 042008, doi: 10.1088/1742-6596/753/4/042008
- [48] Ashuri T., Zaaijer M., Martins J. and Zhang J. **(2016)** *'Multi-disciplinary Design Optimization Of Large Wind Turbines – Technical, Economic And Design Challenges'*, Energy Conversion and Management, 123, 56-70, doi: 10.1016/j.enconman. 2016.06.004
- [49] Serafeim G., Manolas D., Riziotis V., Chaviaropoulos P. and Saravanos D. **(2022)** *'Optimized Blade Mass Reduction Of A 10MW-scale Wind Turbine Via Combined Application Of Passive Control Techniques Based Of Flap-Edge And Bend-Twist Coupling Effects'*, J. of Wind Engineering & Industrial Aerodynamics 225 (2022) 105002, <https://doi.org/10.1016/j.jweia.2022.105002>
- [50] Serafeim G., Manolas D., Riziotis V. and Chavaropoulos P. **(2022)** *'Multi-disciplinary Aeroelastic Optimization Of A 10MW-scale Wind Turbine Rotor Targeting To Reduced LCoE'*, J. of Phys.: Con. Ser. 2265 (2022) 042051, doi: 10.1088/1742-6596/2265/4/ 042051
- [51] Virtanen P., Gommers R., Oliphant T. et al. **(2020)** *'SciPy 1.0: Fundamental Algorithms For Scientific Computing In Python'*, Nature Methods 17, 261-272 (2020), <https://doi.org/10.1038/s41592-019-0686-2>
- [52] Bak C., Zahle F., Bitsche R., Kim T., Yde A., Henriksen L., Natarajan A. and Hansen M. **(2013)** *'Description Of The DTU 10MW Reference Wind Turbine'*, DTU Wind Energy Report-I-0092, https://backend.orbit.dtu.dk/ws/portalfiles/portal/55645274/The_DTU_10MW_Reference_Turbine_Christian_Bak.pdf
- [53] IEC 61400-1, IEC, 2003. 188184CDV, Edited by TC88-MT1 25-26, May **2004**, 3rd edition, pp. 26-29
- [54] Riziotis V. **(2003)** *'Aerodynamic And Aeroelastic Analysis Of Dynamic Stall On Wind Turbine Rotors'*, PhD Thesis, NTUA - Athens
- [55] Blasques A. **(2012)** *'User's Manual For BECAS: A Cross Section Analysis Tool For Anisotropic And Inhomogeneous Beam Sections Of Arbitrary Geometry'*, Risø DTU – National Laboratory for Sustainable Energy, Denmark, Forskningscenter Risoe, Risoe-R No. 1785 (EN)
- [56] *'WISDEM'*, [github.com/WISDEM.WISDEM](https://github.com/WISDEM/WISDEM)
- [57] Thirstrup J. **(1990)** *'Kinematically Non-linear Finite Element Model Of A Horizontal Axis Wind Turbine. Part 1'*, Risoe National Lab., Meteorology and Wind Energy (Denmark), Technical Report NEI-DK-994, <https://www.osti.gov/etdeweb/biblio/7146832>
- [58] Chaviaropoulos P. **(1996)** *'Development Of A State-of-the Art Aero-elastic Simulator For Horizontal Axis Wind Turbines – Part 1: Structural Aspects'*, Wind Engineering, vol. 20, No. 6, pp. 4005-421, <https://www.jstor.org/stable/43749809>
- [59] Hansen M., Sørensen J., Voutsinas S., Sørensen N. and Madsen H. **(2006)** *'State Of The Art In Wind Turbine Aerodynamics And Aeroelasticity'*, Progress in Aerospace Sciences, 42(4), pp. 285-330, doi: 10.1016/j.paerosci.2006.10.002

-
- [60] Oye S. (1996) *'FLEX4 Simulation Of Wind Turbine Dynamics'*, Proceedings of 28th IEA Meeting of Experts Concerning State of the Art of Aero-elastic Codes for Wind Turbine Calculations, Lyngby 1996
- [61] Jonkman J. and Buhl J. (2005) *'FAST User's Guide'*, National Renewable Energy Laboratory (U.S.A.), Technical Report NREL/TP-500-38230, <http://wind.nrel.gov/designcodes/simulators/fast/FAST.pdf>
- [62] Riziotis V. and Voutsinas S. (2006) *'Advanced Aero-elastic Modeling Of Complete Wind Turbine Configurations In View Of Assessing Stability Characteristics'*, Conference: EWEC 2006, <https://www.researchgate.net/publication/279531138>
- [63] Chortis D., Chrysochoidis N. and Saravanos D. (2007) *'Damped Structural Dynamics Models Of Large Wind-turbine Blades Including Material And Structural Damping'*, J. of Phys.: Con. Der. 75 (2007) 012076, doi: 10.1088/1742-6596/75/1/012076
- [64] Bottasso C., Croce A., Savini B., Sirchi W. and Trainelli L. (2006) *'Aero-servo-elastic Modeling And Control Of Wind Turbines Using Finite-element Multibody Procedures'*, Multibody Syst Dyn (2006) 16:291-308, doi: 10.1007/s11044-006-9027-1
- [65] Hodges D. (2006) *'Non-linear Composite Beam Theory'*, ISBN: 978-1-56347-697-6, <https://doi.org/10.2514/4.866821>
- [66] Riziotis V. and Voutsinas S. (1998) *'A General Aerodynamic And Structural Prediction Tool For Wind Turbines'*, European wind energy conference: 448-452, ISBN: 0953392201
- [67] Bagherpour T., Li X., Manolas D. and Riziotis V. (2018) *'Modeling Of Material Bend-Twist Coupling On Wind Turbine Blades'*, J. of Composite Structures 193 (2018) 237-246, <https://doi.org/10.1016/j.compstruct.2018.03.071>
- [68] Manolas D., Serafeim G., Chaviaropoulos P., Riziotis V. and Voutsinas S. (2018) *'Assessment Of Load Reduction Capabilities Using Passive And Active Control Methods On A 10MW-scale Wind Turbine'*, J. of Phys.: Con. Ser. 1037 (2018) 032042, doi: 10.1088/1742-6596/1037/3/032042
- [69] Manolas D., Riziotis V. and Voutsinas S. (2015) *'Assessing The Importance Of Geometric Non-linear Effects In The Prediction Of Wind Turbine Blade Loads'*, J. of Computational and Nonlinear Dynamics, 10(4), 041008-1, doi: 10.1115/1.4027684
- [70] Lansen T. and Hansen A. (2019) *'How 2 HAWC2, The User's Manual'*, DTU Wind Energy HAWC2 Development Team, Risø-R-1597, ISBN 978-87-550-3583-6
- [71] Jonkman J., Butterfield S., Musial W. and Scott G. (2009) *'Definition Of A 5-MW Reference Wind Turbine For Offshore System Development'*, Technical Report NREL/TP-500-38060
- [72] Madsen H., Riziotis V., Zahle F., Larsen J., Politis E., Hanses L., Snel H. and Grasso F. (2012) *'BEMT Modeling Of Inflow With Shear In Comparison With Advanced Model Results'*, Wind Energy 2012, 15, 63-81, doi: 10.1002/we.493
- [73] Voutsinas S. (2006) *'Vortex Methods In Aeronautics: How To Make Things Work'*, International Journal of Computational Fluid Dynamics, 20(1), 3-18, doi: 10.1080/10618560600566059
- [74] Wilcox D. (2006) *'Turbulence Modeling For CFD'*, ISBN 978-1-928729-08-2

-
- [75] Spyropoulos N., Papadakis G., Prospathopoulos J. and Riziotis V. **(2021)** *'Investigating The Level Of Fidelity Of An Actuator Line Model In Predicting Loads And Deflections Of Rotating Blades Under Uniform Free-Stream Flow'*, Applied Sciences, 19;11(24):12097, <https://doi.org/10.3390/app112412097>
- [76] Glauert H. **(1935)** *'Airplane Propellers. In: Aerodynamic Theory'*, Springer p. 169-360, https://doi.org/10.1007/978-3-642-91487-4_3
- [77] Van Grol H., Snel H. and Schepers J. **(1991)** *'Wind Turbine Benchmark Exercise On Mechanical Loads'*, Vo. 1, part A & B. A state of the art report in ECN-C-91-031
- [78] Schepers J. and Snel H. **(1994)** *'Joint Investigation Of Dynamic Inflow Effects And Implementation Of An Engineering Method For Response Analysis'*, in ECN Report ECN-C-94-107, The Netherlands
- [79] Petot D. **(1989)** *'Differential Equation Modeling Of Dynamic Stall'*, La Recherche Aérospatiale (English Edition), p. 59-72
- [80] Leishman J. and Beddoes T. **(1986)** *'A Generalized Model For Airfoil Unsteady Aerodynamic Behavior And Dynamic Stall Using The Indical Method'*, In Proceedings of the 42nd Annual forum of the American Helicopter Society, Washington DC
- [81] Glauert H. and Committee A. **(1926)** *'A General Theory Of The Autogyro'*, Vo. 11111, HM Stationery Office
- [82] Coleman P., Feingold A. and Stempin C. **(1945)** *'Evaluation Of The Induced-Velocity Field Of An Idealized Helicopter Rotor'*, DTIC Document
- [83] Burton T., Sharpe D., Jenkins N. and Bossanyi E. **(2001)** *'Wind Energy Handbook'*, John Wiley & Sons ISBN: 9780471489979, doi: 10.1002/0470846062
- [84] Øye S. **(1992)** *'Induced Velocities For Rotors In Yaw'*, In Proceedings of the Sixth IEA Symposium, ECN, Netherlands
- [85] Drees M. **(1949)** *'A Theory Of Airflow Through Rotors And Its Application To Some Helicopter Problems'*, J. of the Helicopter Association of Great Britain 3(2): p. 79-104
- [86] Stäblein A. and Morten H. **(2016)** *'Timoshenko Beam Element With Anisotropic Cross-Sectional Properties'*, In Proceedings of the VII European Congress on Computational Methods in Applied Sciences and Engineering European Community on Computational Methods in Applied Sciences
- [87] Bauchau O., Bottasso C. and Nikishkov Y. **(2001)** *'Modeling Rotor Dynamics With Finite Element Multibody Procedures'*, Mathematical and Computer Modelling, 33(10-11), 1113-1137, doi: 10.1016/s0895-7177(00)00303-4
- [88] Resor B. **(2013)** *'Definition Of A 5MW/61.5m Wind Turbine Blade Reference Model'*, Sandia Report SAND2013-2569, <https://www.osti.gov/servlets/purl/1095962>
- [89] 'ANSYS', <https://www.ansys.com/>
- [90] 'ABAQUS', <https://www.3ds.com/products-services/simulia/products/abaqus/>
- [91] Brbero E., Lopez R. and Davalos J. **(1993)** *'On The Mechanics Of Thin-Walled Laminated Composite Beams'*, J. of Composite Materials 27:806, doi: 10.1177/002199839302700804

-
- [92] Massa J. and Barbero E. **(1998)** 'A Strength Of Materials Formulation For Thin Walled Composite Beams With Torsion', *J. of Composite Materials*, 32(17), 1560-1594, doi: 10.1177/002199839803201702
- [93] Chandra R. and Chopra I. **(1992)** 'Structural Behavior Of Two-Cell Composite Rotor Blades With Elastic Couplings', *AIAA Journal*, 30(12), 2914-2921, doi: 10.2514/3.11637
- [94] Yu W., Volovoi V., Hodges D. and Hong X. **(2002)** 'Validation Of The Variational Asymptotic Beam Section Analysis', *AIAA Journal*, 40(10), 2105-2112, doi: 10.2514/2.1545
- [95] Johnson E., Vasiliev V. and Vasiliev D. **(2001)** 'Anisotropic Thin-Walled Beams With Closed Cross-Sectional Contours', *AIAA Journal* 39(12):2389-2393, doi: 10.2514/2.1247
- [96] Sravanos D., Varelis D., Plagianakos T. and Chrisochoidis N. **(2006)** 'A Shear Beam Finite Element For The Damping Analysis Of Tubular Laminated Composite Beams', *J. of Sound and Vibration* 291 (3-5), 802-823, doi: 10.1016/j.jsv.2005.06.045
- [97] Chordis D., Varelis D. and Saravanos D. **(2012)** 'Prediction Of Material Coupling Effect On Structural Damping Of Composite Beams And Blades', *J. of Composite Structures*, 94(5), 1646-1655, doi: 10.1016/j.compstruct.2011.12.004
- [98] Wu W., Cheng H. and Kang C. **(2000)** 'Random Field Formulation Of Composite Laminates', *J. of Composite Structures*, 49(1), 87-93, doi: 10.1016/s0263-8223(99)00128-2
- [99] Kosmatka J. **(1992)** 'The Use Of Cross-Section Warping Functions In Composite Rotor Blade Analysis', NASA, Report SSRP-92/11
- [100] Serafeim G., Manolas D., Riziotis V. and Chaviaropoulos P. **(2020)** 'Lightweight Optimal Rotor Design Of A 10W-scale Wind Turbine Using Passive Load Control Methods', *J. of Phys.: Con. Ser.* 1618, 022061, doi: 10.1088/1742-6596/1618/2/011061
- [101] Aquilina M., Sant T. and Farrugia R. **(2014)** 'Cost Modelling Of Floating Wind Farms With Up-scaled Rotors In Maltese Waters', Conference: Annual Seminar organized by the institute for Sustainable Energy, Malta, <https://www.researchgate.net/publication/281480875>
- [102] Jamieson P. **(2018)** 'Innovation In Wind Turbine Design', 2nd Edition, Wind Energy, ISBN: 978-1-119-13790-0
- [103] Harrison R. and Jenkins G. **(1994)** 'Cost Modelling Of Horizontal Axis Wind Turbines', Technical Report, ETSU-W-34/00170/REP
- [104] Bortolotti P., Johnson N., Abbas N., Anderson E., Camarena E. and Paquette J. **(2021)** 'Land-based Wind Turbines With Flexible Rail-transportable Blades – Part 1: Conceptual Design And Aeroservoelastic Performance', *J. of Wind Energ. Sci.*, 6, 1277-1290, <https://doi.org/10.5194/wes-6-1277-2021>
- [105] Wanke G., Bergami L., Zahle F. and Verelst D. **(2021)** 'Redesign Of An Upwind Rotor For A Downwind Configuration: Design Changes And Cost Evaluation', *J. of Wind Energ. Sci.*, 6, 203-220, <https://doi.org/10.5194/wes-6-203-2021>
- [106] Serafeim G., Manolas D., Riziotis V. and Chaviaropoulos P. **(2022)** 'Wind Turbine Blade Design Optimization For Reduced LCoE, Focusing On Design-driving Loads Due To Storm Conditions', *J. of Fluids* 2022, 7, 280, <https://doi.org/10.3390/fluids7080280>

-
- [107] Burton T., Jenkins N., Sharpe D. and Bossanyi E. **(2011)** *'Wind Energy Handbook'*, Second Edition, ISBN: 9780470699751, doi: 10.1002/9781119992714
- [108] Fingersh L., Hand M. and Laxson A. **(2006)** *'Wind Turbine Design Cost And Scaling Model'*, Technical Report, NREL/TP-500-40566
- [109] Bortolotti P., Berry D., Murray R., Gearthner E., Jenne D., Damiani R., Barter G. and Dykes K. **(2019)** *'A Detailed Wind Turbine Blade Cost Model'*, Golden, CO: National Renewable Energy Laboratory, NREL/TP-5000-73585, <https://www.nrel.gov/docs/fy19osti/73585.pdf>
- [110] Bergeles G. **(2005)** *'Wind Turbine'* 1st edition, ISBN: 960-7888-57-x
- [111] *'EASY'*, <http://velos0.ltt.mech.ntua.gr/EASY/>
- [112] Gray J., Hwang J., Martins J., Moore K. and Naylor B. **(2019)** *'OpenMDAO: An Open-source Framework For Multidisciplinary Design, Analysis And Optimization'*, J. of Structural and Multidisciplinary Optimization, doi: 10.1007/s00158-01902211-z
- [113] Nelder J. and Mead R. **(1965)** *'A Simplex Method For Function Minimization'*, The Computer Journal, 7(4), 308-313, doi: 10.1093/comjnl/7.4.308
- [114] Powell **(1994)** *'A Direct Search Optimization Method That Models The Objective And Constraint Functions By Linear Interpolation'*, Advances in Optimization and Numerical Analysis, 51-67, doi: 10.1007/978-94-0158330-5_4
- [115] Powell M. **(2007)** *'A View of Algorithms For Optimization Without Derivatives'*, Department of Applied Mathematics and Theoretical Physics, Center for Mathematical Sciences, 2007/NA03, http://www.damtp.cam.ac.uk/user/na/NA_papers/NA2007_03.pdf
- [116] Bartoli N., Lefebvre T., Dubreuil S., Olivanti R., Bons N., Martins R. and Bouhlel M. **(2017)** *'An Adaptive Optimization Strategy Based On Mixture Of Experts For Wing Aerodynamic Design Optimization'*, AIAA 2017-4433, <https://doi.org/10.2514/6.2017-4433>
- [117] Bös J. **(2006)** *'Numerical Optimization Of The Thickness Distribution Of Three-dimensional Structures With Respect To Their Structural Acoustic Properties'*, J. of Struct Multidisc Optim (2006) 32:12-30, doi: 10.1007/s00158-005-0560-y
- [118] Annoni J., Bay C., Taylor T., Pao L., Fleming P. and Johnson K. **(2018)** *'Efficient Optimization Of Large Wind Farms For Real-time Control'*, 2018 Annual American Control Conference (ACC), doi: 10.23919/acc.2018.8430751
- [119] Barr S. and Jaworski J. **(2019)** *'Optimization Of Tow-steered Composite Wind Turbine Blades For Static Aeroelastic Performance'*, Renewable Energy, 139, 859-872, doi: 10.1016/j.renene.2019.02.125
- [120] Li J. and Zhang M. **(2021)** *'Data-based Approach For Wing Shape Design Optimization'*, Aerospace Science and Technology, 112, 106639, doi: 10.1016/j.ast.2021.106639
- [121] Kraft D. **(1988)** *'A Software Package For Sequential Quadratic Programming'*, Technical Report. DFVLR-FB 88-28, DLR German Aerospace Center – Institute for Flight Mechanics, Koln - Germany

- [122] Wu H. (2007) *'The Karush-Kuhn-Tucker Optimality Conditions In An Optimization Problem With Interval-valued Objective Function'*, European Journal of Operational Research 176(1), 46-59, doi: 10.1016/j.ejor.2005.09.007
- [123] Hanson R. and Lawson C. (1969) *'Extensions And Applications Of The Householder Algorithm For Solving Linear Least Squares Problems'*, Mathematics of Computation, 23(108), 787, doi: 10.2307/2004965
- [124] K. Giannakoglou (2006) *'Optimization Methods In Aerodynamics'*, NTUA in-house book, 4th edition, Athens 2006
- [125] Davidon W. (1991) *'Variable Metric Method For Minimization'*, SIAM journal on Optimization, 1(1), 1-17, doi: 10.1137/0801001
- [126] Fletcher R. and Powell M. (1963) *'A Rapidly Convergent Descent Method For Minimization'*, The Computer Journal, 6(2), 163-168, doi: 10.1093/comjnl/6.2.163
- [127] Fiacco A. and McCormick G. (1968) *'Nonlinear Programming Sequential Unconstrained Minimization Techniques'*, Society for Industrial and Applied Mathematics, ISBN: 9780898712544, <https://doi.org/10.1137/1.9781611971316.fm>
- [128] Broyden C. (1970) *'The Convergence Of A Class of Double-rank Minimization Algorithms'*, IMA Journal of Applied Mathematics, 6(3), 222-231, doi: 10.1093/imamat/6.3.222
- [129] Fletcher R. (1970) *'A New Approach To Variable Metric Algorithms'*, The Computer Journal, 13(3), 317-322, doi: 10.1093/comjnl/13.3.317
- [130] Goldfarb D. (1970) *'A Family Of Variable-metric Methods Derived By Variational Means'*, Mathematics of computation, 24(109), 23, doi: 10.2307/2004873
- [131] Shanno D. (1970) *'Conditioning Of Quasi-newton Methods For Function Minimization'*, Mathematics of Computation, 24(111), 647-647, doi: 10.1090/s0025-5718-1970-0274029-x
- [132] Asrul M., Ibrahim H., Mamat M. and Leong W. (2014) *'BFGS Method: A New Search Direction'*, J. of Sains Malaysia 43(10): 1593-1599, <https://www.researchgate.net/publication/287267638>
- [133] Bossanyi E. (2003) *'Wind Turbine Control For Load Reduction'*, Wind Energ. 2003; 6:229-24, doi: 10.1002/we.95
- [134] Bergami L. and Poulsen N. (2015) *'A Smart Rotor Configuration With Linear Quadratic Control Of Adaptive Trailing Edge Flaps For Active Load Alleviation'*, Wind Energ. 2015; 18:625-641, doi: 10.1002/we.1716
- [135] Gonzalez A., Enevoldsen P., Barlas A. and Madsen H. (2021) *'Field Test Of An Active Flap System On A Full-scale Wind Turbine'*, WES 6, 33-43, <https://doi.org/10.5194/wes-6-33-2021>
- [136] Lobitz D. and Veers P. (2003) *'Load Mitigation With Bending/Twist-Coupled Blades On Rotors Using Modern Control Strategies'*, Wind Energ. 2003; 6:105-117, doi: 10.1002/we.74
- [137] Bottasso C., Campagnolo F., Croce A. and Tibaldi C. (2012) *'Optimization-Based Study Of Bend-Twist Coupled Rotor Blades For Passive And Integrated Passive/Active Load Alleviation'*, Wind Energy: Published online in Wiley Online Library (wileyonlinelibrary.com), doi: 10.1002/we.1543

-
- [138] Riziotis V., Voutsinas S., Manolas D., Politis E. and Chaviaropoulos P. **(2010)** *'Aero-elastic Analysis Of Pre-curved Rotor Blades'*, <https://www.researchgate.net/publication/268417271>
- [139] Stettner M., Reijerkerk J., Lünenschloß A., Riziotis V., Croce A., Sartori L., Riva R. and Peeringa J. **(2016)** *'Stall-Induced Vibrations Of The AVATAR Rotor Blade'*, J. of Phys.: Conf. Ser., 753, 042019, doi: 10.1088/1742-6596/753/4/042019
- [140] Heinz C., Sørensen N., Riziotis V., Schwarz M., Gomez-Iradi S. and Stettner M. **(2016)** *'Aerodynamics Of Large Rotors'*, WP4. Deliverable 4.5; Technical Report; ECN Wind Energy: Petten, The Netherlands 2016, <https://repository.tudelft.nl/islandora/object/uuid%3Af1ee9368-ca44-47ca-abe2-b816f64a564f>
- [141] Loubeyres J., Pfister J., Blondel F. and Guy N. **(2022)** *'Stall Flutter Instabilities On The IEA-15 Reference Wind Turbine In Idling Conditions: Code-To-Code Comparisons And Physical Analyses'*, J. of Phys.: Con. Ser. 2265, 032019
- [142] Hansen H. **(2007)** *'Aero-elastic Instability Problems For Wind Turbines'*, Wind Energy, 10(6), 551-577, doi: 10.1002/we.242
- [143] Tsiantas T., Manolas D., Machairas T., Karakalas A., Riziotis V., Saravanos D. and Voutsinas S. **(2016)** *'Assessment Of Fatigue Load Alleviation Potential Through Blade Trailing Edge Morphing'*, J. of Phys.: Con. Ser. 753 042020, doi: 10.1088/1742-6596/753/4/042020
- [144] Bæk P. **(2011)** *'Unsteady Flow Modeling And Experimental Verification Of Active Flow Control Concepts For Wind Turbine Blades'*, PhD Thesis, DTU RISOE.
- [145] Stäblein A. **(2016)** *'Analysis And Design Of Bend-Twist Coupled Wind Turbine Blades'*, MARE-WINT, New Materials and Reliability in Offshore Wind Turbine Technology (pp. 67-80), Springer, https://doi.org/10.1007/978-3-319-39095-6_5
- [146] Lobitz D. and Laino D. **(1999)** *'Load Mitigation With Twist-Coupled HAWT Blades'*, 37th Aerospace Sciences Meeting and Exhibit, doi: 10.2514/6.1999-33
- [147] Thresher R., Hock S., Laxson A. and Smith B. **(2002)** *'Low Wind Speed Technology Deleopment In The U.S. Department Of Energy Wind Energy Research Program'*, presented at the American Wind Energy Association (AWEA) WINDPOWER 2002 Conference Portland, Oregon
- [148] Verelst D., Larsen T. and Wingerden J. **(2014)** *'Wind Tunnel Test Of A Free Yawing Downwind Wind Turbine'*, J. of Phys.: Con. Ser. 555, 012103, doi: 10.1088/1742-6596/555/1/012103
- [149] Riziotis V., Manolas D. and Voutsinas S. **(2011)** *'Advanced Aeroelastic Modelling Of Swept Rotor Blades'*, J. of Conference: EWEA 2011, Brussels, Belgium, <https://www.researchgate.net/publication/273380627>
- [150] Pavese C., Kim T. and Murcia J. **(2017)** *'Design Of A Wind Turbine Swept Blade Through Extensive Load Analysis'*, Renewable Energy, 102, 21-34, doi: 10.1016/j.renene.2016.10.039
- [151] Chehoury A., Younes R., Ilinca A. and Perron J. **(2016)** *'Wind Turbine Design: Multi-Objective Optimization'*, Wind Turbines – Design, Control and Application, doi: 10.5772/63481
- [152] *"Aeroelastically Tailored Blades"*, <https://pdf.archiexpo.com/pdf/siemens-gamesa/aeroelastically-tailored-blades/88089-134505.html>

-
- [153] "Turbine Load Control", <https://pdf.archiexpo.com/pdf/siemens-gamesa.turbine-load-control/88089-134495.html>
- [154] Bak C., Bitsche R., Yde A., Kim T., Hansen M., Zahle F., Gaunaa M., Blasques J., Pedro A., Dossing M., Wdel H. and Behrens T. (2012) 'Light Rotor: The 10MW Reference Wind Turbine', In Proceedings of EWEA 2012 –European Wind Energy Conference & Exhibition European Wind Energy Association (EWEA)
- [155] 'Vestas', <https://www.vestas.com/en>
- [156] Muggiasca S., Taruffi F., Fontanella A., Carlo S., Giberti H., Facchinetti A. and Belloli M. (2021) 'Design Of An Aeroelastic Physical Model Of The DTU 10MW Wind Turbine For A Floating Offshore Multipurpose Platform Prototype', Journal of Ocean Engineering 239 (2021) 109837, <https://doi.org/10.1016/j.oceaneng.2021.109837>
- [157] Zhenye S., Wei Z., Wen S., Wei Z., Jiufa C. and Qiuhan T. (2020) 'Aerodynamic Analysis Of Coning Effects On The DTU 10MW Wind Turbine Rotor', Journal of Energies 2020, 13(21), 5753, doi:10.3390/en13215753
- [158] McWilliam M., Barlas T., Madsen H. and Zahle F. (2018) 'Aero-elastic Wind Turbine Design With Active Flaps For AEP Maximization', Journal of Wind Energ. Sci., 3, 231-241, 2018, <https://doi.org/10.5194/wes-3-231-2018>
- [159] Chaviaropoulos P. (2007) 'Similarity Rules For W/T Up-scaling', <https://www.studeersnel.nl/nl/document/technische-universiteit-delft/wind-turbine-design/similarity-rules-for-wt-upscaling-2007/13331510>
- [160] Bjork A. (1990) 'Coordinates And Calculations For The FFA-W1-xxx, FFA-W1-xxx And FFA-W3-xxx Series Of Airfoils For Horizontal Axis Wind Turbines', Technical Report FFA TN 1990-15, FFA, Stockholm, Sweden, 1990
- [161] Hansen H. and Henriksen C. (2013) 'Basic DTU Wind Energy Controller', DTU Wind Energy, 2013, DTU Wind Energy E No. 0028
- [162] Kauzlarich J. (1981) 'The Palmgren-Miner Rule Derived', Tribological Design of Machine Elements, Proceedings of the 15th Leeds-Lyon Symposium on Tribology held at Boodington Hall, The University of Leeds Volume 14, (1989) 175-179, doi: 10.1016/S0167-8922(08)70192-5
- [163] Chaviaropoulos P. (2016) 'Full Stiffness Matrix Calculation For Composite Blade Sections', IWind.DR.001.2016
- [164] Stere M. (2010) 'The Torsion Of Multicell Sections', INCAS Bulletin 2 (3), 99-105, <https://doi.org/10.13111/2066-8201.2010.2.3.11>
- [165] Mindlin R. (1975) 'Solution Of St. Venant's Torsion Problem By Power Series', International Journal of Solids and Structures, Vo. 11, Iss. 3, 1975, pp. 321-328, doi:10.1016/0020-7683(75)90071-2
- [166] Ruta G., Pignataro M. and Rizzi N. (2006) 'A Direct One-Dimensional Beam Model For The Flexural-Torsional Buckling Of Thin-walled Beams', J. of Mechanics of Materials and Structures, Vol. 1, No. 8, 2006, pp. 1479-1496, doi:10.2140/jomms.2006.1.1479

- [167] Timoshenko S. **(1921)** *'On The Correction For Shear Of The Differential Equation For Transverse Vibrations Of Prismatic Bars'*, Philosophical Magazine and Journal of Science: Vol. 41, No. 245, pp. 744-746, doi:10.1080/14786442108636264
- [168] Cowper G. **(1966)** *'The Shear Coefficient In Timoshenko's Beam Theory'*, J. of Applied Mechanics, 33(2), 335, doi:10.1115/1.3625046

ΕΘΝΙΚΟ ΜΕΤΣΟΒΙΟ ΠΟΛΥΤΕΧΝΕΙΟ



ΣΧΟΛΗ ΜΗΧΑΝΟΛΟΓΩΝ ΜΗΧΑΝΙΚΩΝ

ΕΡΓΑΣΤΗΡΙΟ ΑΕΡΟΔΥΝΑΜΙΚΗΣ

ΔΙΔΑΚΤΟΡΙΚΗ ΔΙΑΤΡΙΒΗ

ΠΕΡΙΛΗΨΗ ΣΤΑ ΕΛΛΗΝΙΚΑ

Πολυ-πεδιακή βελτιστοποίηση πτερυγίων
ανεμογεννητριών με ενσωμάτωση τεχνικών
παθητικού ελέγχου φορτίων

Γιάννης Σεραφείμ

27 Σεπτεμβρίου 2023



ΕΘΝΙΚΟ ΜΕΤΣΟΒΙΟ ΠΟΛΥΤΕΧΝΕΙΟ
ΣΧΟΛΗ ΜΗΧΑΝΟΛΟΓΩΝ ΜΗΧΑΝΙΚΩΝ
ΤΟΜΕΑΣ ΡΕΥΣΤΩΝ
ΕΡΓΑΣΤΗΡΙΟ ΑΕΡΟΔΥΝΑΜΙΚΗΣ

Πολυ-πεδιακή βελτιστοποίηση πτερυγίων ανεμογεννητριών με ενσωμάτωση τεχνικών παθητικού ελέγχου φορτίων

ΔΙΔΑΚΤΟΡΙΚΗ ΔΙΑΤΡΙΒΗ

ΤΟΥ

Γιάννη Ανδρέου-Σεραφείμ

Χρηματοδότηση:

Η έρευνα έχει υποστηριχθεί απ'το Ελληνικό Ίδρυμα Έρευνας & Καινοτομίας (ΕΛ.ΙΔ.Ε.Κ.) στο πλαίσιο της 2^{ης} Προκήρυξης Υποτροφιών ΕΛ.ΙΔ.Ε.Κ. για Υποψήφιους Διδάκτορες (Αριθμός Αίτησης: 867).



Η υλοποίηση της διδακτορικής διατριβής συγχρηματοδοτήθηκε απ'την Ελλάδα και την Ευρωπαϊκή Ένωση (Ευρωπαϊκό Κοινωνικό Ταμείο) μέσω του Επιχειρησιακού Προγράμματος «Ανάπτυξη Ανθρώπινου Δυναμικού, Εκπαίδευση και Διά Βίου Μάθηση», 2014-2020, στο πλαίσιο της Πράξης «Ενίσχυση του ανθρώπινου δυναμικού μέσω της υλοποίησης διδακτορικής έρευνας Υπόδραση 2: Πρόγραμμα χορήγησης υποτροφιών ΙΚΥ σε υποψήφιους διδάκτορες των ΑΕΙ της Ελλάδας». (Αριθμός Σύμβασης: 2022-050-0502-52636).



Ευρωπαϊκή Ένωση
Ευρωπαϊκό Κοινωνικό Ταμείο

Επιχειρησιακό Πρόγραμμα
Ανάπτυξη Ανθρώπινου Δυναμικού,
Εκπαίδευση και Διά Βίου Μάθηση

Με τη συγχρηματοδότηση της Ελλάδας και της Ευρωπαϊκής Ένωσης



ανάπτυξη - εργασία - αλληλεγγύη

Συγγραφέας: Γιάννης Ανδρέου-Σεραφεΐμ

Τίτλος: Πολυ-πεδιακή βελτιστοποίηση πτερυγίων ανεμογεννητριών με ενσωμάτωση τεχνικών παθητικού ελέγχου φορτίων

Ερ. Κέντρο: Εργαστήριο Αεροδυναμικής Ε.Μ.Π.

Περίληψη: Αντικείμενο της διατριβής είναι ο βέλτιστος σχεδιασμός πτερυγίου ανεμογεννήτριας DTU-10MW RWT, με στόχο την ελαχιστοποίηση του σταθμισμένου κόστους ενέργειας (LCoE), συνδυάζοντας τεχνικές παθητικού ελέγχου φορτίων. Σε αυτή τη διατριβή, έχουν αξιολογηθεί τέτοιες τεχνικές με εφαρμογή δομικής και γεωμετρικής σύζευξης κάμψης/στρέψης (BTC) και κάμψεων πτερύγισης/περιστροφής (FEC). Η πολυ-πεδιακή βελτιστοποίηση περιλαμβάνει σε κοινό βρόχο τα αεροδυναμικά (π.χ. κατανομή χορδής και συστροφής) και δομικά (π.χ. πάχη τοιχωμάτων) χαρακτηριστικά καθώς και τις παραμέτρους παθητικού ελέγχου φορτίων. Στο πλαίσιο της έρευνας, έχουν αξιολογηθεί (και συγκριθεί) διάφορες τεχνικές βελτιστοποίησης όπως: COBYLA, SLSQP και η μέθοδος Newton.

Αναφορά: Εθνικό Μετσόβιο Πολυτεχνείο

Δημοσίευση: 27 Σεπ. 2023

Εξεταστική επιτροπή:

1. Δημήτριος Σαραβάνος*, καθηγητής, Τμήμα Μηχανολόγων Μηχανικών - Πανεπιστήμιο Πατρών
2. Σπυρίδων Βουτσινάς*, καθηγητής, Σχολή Μηχανολόγων Μηχανικών Ε.Μ.Π.
3. Βασίλιος Ριζιώτης (επιβλέπων)*, Αναπληρωτής καθηγητής, Σχολή Μηχανολόγων Μηχανικών Ε.Μ.Π.
4. Κυριάκος Γιαννάκογλου, καθηγητής, Σχολή Μηχανολόγων Μηχανικών Ε.Μ.Π.
5. Νικόλαος Χρυσοχοΐδης, καθηγητής, Τμήμα Μηχανολόγων Μηχανικών – Πανεπιστήμιο Πατρών
6. Μαρίνος Μανωλέσος, επίκουρος καθηγητής, Σχολή Μηχανολόγων Μηχανικών Ε.Μ.Π.
7. Εμμανουήλ Αγγέλου, επίκουρος καθηγητής, Σχολή Ναυπηγών Μηχανολόγων Μηχανικών Ε.Μ.Π.

*μέλος τιμελούς επιτροπής

Σελίδες: 80

Σχήματα: 41

Πίνακες: 10

Αναφορές: 56

Εθνικό Μετσόβιο Πολυτεχνείο,
Σχολή Μηχανολόγων Μηχανικών
Ηρώων Πολυτεχνείου 9 15780
Ζωγράφου - Αθήνα
Ελλάδα
seraf@fluid.mech.ntua.gr

Αυτή η σελίδα μένει κενή

© Copyright 2023

Απαγορεύεται η αναδημοσίευση, η αναπαραγωγή, ολική, μερική ή περιληπτική, ή η απόδοση κατά παράφραση ή διασκευή του περιεχομένου του βιβλίου με οποιονδήποτε τρόπο, μηχανικό, ηλεκτρονικό, φωτοτυπικό, ηχογράφησης ή άλλο, χωρίς προηγούμενη γραπτή άδεια του συγγραφέα. Νόμος 2121/1993 και κανόνες του Διεθνούς Δικαίου που ισχύουν στην Ελλάδα.

Αυτή η σελίδα μένει κενή

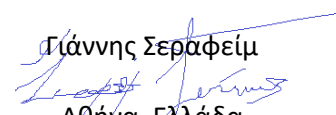
Ευχαριστίες

Η διδακτορική εργασία πραγματοποιήθηκε στο εργαστήριο Αεροδυναμικής επί πεντέμισι χρόνια, σε πλήρη απασχόληση. Για 29 μήνες, χρηματοδοτήθηκε απ'το Ελληνικό Ίδρυμα Έρευνας και Καινοτομίας (ΕΛ.ΙΔ.Ε.Κ.), ενώ τους τελευταίους 16 μήνες απ'το Ίδρυμα Κρατικών Υποτροφιών Ελλάδος (Ι.Κ.Υ.). Στο ενδιάμεσο χρονικό διάστημα, η οικονομική στήριξη προήλθε απ'την ιδιωτική εταιρεία έρευνας ανανεώσιμων πηγών ενέργειας iWind. Φυσικά, η οικονομική τους στήριξη εκτιμάται ιδιαίτερα!

Κίνητρο για τη διατριβή αυτή, αποτέλεσε τόσο το ενδιαφέρον μου για τα μαθηματικά και τις φυσικές επιστήμες, όσο και η προσωπική μου επιθυμία να συμβάλω έστω και λίγο, σε μια πιο πράσινη και οικολογική αλλαγή. Λοιπόν, νιώθω πολύ ευγνώμων για την ευκαιρία που είχα να συνεργαστώ με πολλούς έξυπνους, ευγενικούς και δημιουργικούς ανθρώπους. Ένας τέτοιος άνθρωπος, είναι ο επιβλέπων μου, ο αναπληρωτής καθηγητής Βασίλης Ριζιώτης ο οποίος πριν από περίπου έξι χρόνια μου έδωσε την ευκαιρία να ασχοληθώ με ένα τόσο ενδιαφέρον θέμα. Ήταν πάντα δίπλα μου, με στήριζε και με ενέπνεε, ενώ με τις γνώσεις και την εμπειρία του στα θέματα της αεροδυναμικής και των ανανεώσιμων πηγών, έδινε πάντα τις σωστές οδηγίες για την αντιμετώπιση οποιουδήποτε προβλήματος. Δυστυχώς, ο θαυμασμός μου για την προσωπικότητα του και τις γνώσεις του δεν εκφράζεται σε λίγες γραμμές... Φυσικά, θα ήταν παράλειψη μου να μην ευχαριστήσω τα άλλα δυο μέλη της συμβουλευτικής επιτροπής, τους καθηγητές Σπύρο Βουτσινά και Δημήτρη Σαραβάνο, για τα χρήσιμα σχόλια και τις παρατηρήσεις τους, που βοήθησαν στη διαμόρφωση της παρούσας διατριβής. Οι συζητήσεις μας τόσο για την πορεία της διατριβής όσο και για άλλα θέματα ήταν ατελείωτες. Οι συμβουλές τους ήταν τόσο χρήσιμες και το ενδιαφέρον τους επικεντρώνεται πραγματικά στην πρόοδο και τη βελτίωση όλων των φοιτητών τους. Επί τη ευκαιρία, θα ήθελα να εκφράσω τις ευχαριστίες μου σε όλα τα μέλη της εξεταστικής επιτροπής για την ανάγνωση της διατριβής και τη διατύπωση εποικοδομητικών σχολίων και παρατηρήσεων.

Ένα ξεχωριστό ευχαριστώ οφείλω στον Δημήτρη Μανωλά, για την ενθάρρυνση και υποστήριξη του σε κάθε βήμα αυτής της διατριβής. Γνωρίζω πόσο δύσκολο πράγμα είναι να αφιερώνεις έστω και λίγο χρόνο καθημερινά για συμβουλές και παρατηρήσεις – πάντα σε φιλικό ύφος, παρά το ήδη αυστηρό χρονοδιάγραμμα και τις ευθύνες που έχεις! Επιπλέον, ένα ιδιαίτερο ευχαριστώ οφείλω στον φίλο μου Θεολόγο Ανδρόνικο, με τον οποίο μοιράστηκα το ίδιο γραφείο στο μεγαλύτερο μέρος των τελευταίων ετών. Τέλος, θα ήθελα να εκφράσω τις ειλικρινείς μου ευχαριστίες σε όλους τους συναδέλφους μου στο εργαστήριο: Κώστα Διακάκη, Παναγιώτη Σχοινά, Νίκο Σπυρόπουλο, Δημήτρη Ντούρα και Δημήτρη Βλαστό, για το πολύ φιλικό περιβάλλον. Πραγματικά το εργασιακό περιβάλλον ήταν φανταστικό και είμαι ευγνώμων για την καλή παρέα και τις ωραίες συζητήσεις, τόσο σε επιστημονικό όσο και σε προσωπικό επίπεδο.

Τέλος, θα ήθελα να ευχαριστήσω την οικογένεια μου. Η αδελφή μου και κυρίως οι γονείς μου, που με στηρίζουν σε κάθε περίπτωση. Είναι πολύ σημαντικό να ξέρεις πως η οικογένεια σου είναι πάντα δίπλα σου! Λυπάμαι, που χρειάστηκε να με αντέξετε στις διακοπές όταν εγώ ήμουν πολύ απασχολημένος με την ολοκλήρωση του κειμένου της παρούσας διατριβής.

Γιάννης Σεραφείμ

Αθήνα, Ελλάδα
27 Σεπτεμβρίου 2023

Αυτή η σελίδα μένει κενή

Περίληψη: Αντικείμενο της διατριβής, είναι ο βέλτιστος σχεδιασμός πτερυγίων ανεμογεννήτριας. Ένα σύνολο από διάφορες σχεδιαστικές ιδέες έχουν δοκιμαστεί, με ιδιαίτερη έμφαση στις τεχνικές παθητικού ελέγχου φορτίων. Μεταξύ αυτών των τεχνικών, έχει αξιολογηθεί η δυνατότητα μείωσης τόσο των ακραίων φορτίων όσο και των φορτίων κόπωσης, με εφαρμογή σύζευξης κάμψης/στρέψης (BTC) ή/και πτερύγισης/περιστοφής (FEC). Η έρευνα έχει δείξει ότι για την ανεμογεννήτρια αναφοράς DTU-10MW RWT, μια μείωση 3 – 5% στα ακραία φορτία καθώς και 5 – 10% στα φορτία κόπωσης είναι εφικτή με την εφαρμογή τέτοιων τεχνικών. Η πιο πάνω ανακούφιση των φορτίων, επιτρέπει τη συμπίεση του κόστους, μέσω της μείωσης της μάζας των απαιτούμενων υλικών. Παρ’όλα αυτά, οι τεχνικές αυτές είναι δυνατό να δράσουν ανταγωνιστικά μεταξύ τους, ενώ η εφαρμογή τους επηρεάζει και την αντοχή της κατασκευής. Αυτό το πρόβλημα καλείται να λύσει η βελτιστοποίηση. Στη διατριβή, περιγράφεται ένα ολοκληρωμένο περιβάλλον σχεδιασμού και βελτιστοποίησης πτερυγίων, που περιλαμβάνει υπολογιστικά εργαλεία τα οποία είτε χρησιμοποιούνται ήδη απ’το εργαστήριο είτε αναπτύχθηκαν στο πλαίσιο της εργασίας αυτής. Αποτέλεσμα της πιο πάνω βελτιστοποίησης είναι ένα πτερύγιο με 8 – 10% λιγότερη μάζα. Το πτερύγιο αυτό, έχει μετατοπισμένα τα ‘καπάκια’ κατά 3% (FEC 3%), σε σχέση με το πτερύγιο αναφοράς – ενώ παρουσιάζει μια τμηματική στροφή $5^{\circ} - 7^{\circ}$ (BTC $5^{\circ} - 7^{\circ}$) στο μονο-κατευθυντήριο υλικό των ‘καπακιών’ (μετά το 20 – 30%). Στο τελευταίο μέρος της διατριβής, εφαρμόζεται πολυ-πεδιακή βελτιστοποίηση με στόχο την ελαχιστοποίηση του κόστους ενέργειας (LCoE). Στη περίπτωση αυτή, εκτός απ’τη μάζα του πτερυγίου και τις παραμέτρους του παθητικού ελέγχου, ως μεταβλητές βελτιστοποίησης θεωρούνται οι κατανομές χορδής και συστροφής καθώς και το μήκος του πτερυγίου. Η πιο πάνω προσέγγιση, οδήγησε σε ένα βαρύτερο (κατά 1%) πτερύγιο, με 3.7% μεγαλύτερο μήκος. Μια εναλλακτική προσέγγιση του παραπάνω σχεδιασμού, όπου εξετάζεται η συνδυαστική εφαρμογή BTC και FEC καθώς και η εκ νέου κατανομή της συστροφής, οδηγεί σε ένα δρομέα με 19.5% λιγότερη μάζα.

Αυτή η σελίδα μένει κενή

Περιεχόμενα

Ευχαριστίες	v
Περίληψη	vii
Περιεχόμενα	ix
Κατάλογος σχημάτων	xiii
Κατάλογος πινάκων	xvii
1. Εισαγωγή	1
1.1. Το ενεργειακό μείγμα και οι στόχοι για το μέλλον	1
1.2. Έλεγχος φορτίων ανεμογεννητριών	3
1.3. Αντικείμενο διατριβής και καινοτομίες	5
1.4. Ανασκόπηση	6
2. Υπολογιστικά εργαλεία	7
2.1. Αερο-ελαστικός επιλύτης hGAST	7
2.1.1. Αεροδυναμικό μοντέλο	8
2.1.2. Ελαστο-δυναμικό μοντέλο	9
2.2. Εργαλείο ανάλυσης διατομών	11
2.2.1. Πολυ-στρωματοποιημένη θεωρία	11
2.2.2. Ανάλυση τάσεων	13
2.3. Κοστολόγηση ενέργειας	14
2.3.1. Μοντέλο κόστους ανεμογεννήτριας	14
2.3.1.1. Κόστος πύργου, κιβωτίου ταχυτήτων και γεννήτριας	14
2.3.1.2. Κόστος εργατικών, πλήμνης, μηχανισμού βήματος και επιταχυνσιόμετρου	15

2.3.1.3. Κόστος κατασκευής πτερυγίου	15
2.3.2. Εκτίμηση LCoE	18
2.4. Μέθοδοι βελτιστοποίησης	18
2.4.1. Μέθοδος COBYLA	18
2.4.2. Μέθοδος SLSQP	19
2.4.3. Μέθοδος Newton και σχεδόν-Newton	19
2.5. Περιβάλλον βελτιστοποίησης	20
3. Ελαχιστοποίηση μάζας δρομέα ανεμογεννήτριας 10MW	23
3.1. Ενεργητικός και παθητικός έλεγχος φορτίων	24
3.2. Μέθοδος μείωσης μάζας πτερυγίων – εφαρμογή δομικής πολυ-πεδιακής βελτιστοποίησης	25
3.3. Εφαρμογές	27
3.3.1. Μείωση μάζας δρομέα, με τη χρήση κυρτών πτερυγίων	27
3.3.1.1. Αναζήτηση “χώρου” και βελτιστοποίηση, για κυρτά πτερύγια	27
3.3.1.2. Πιστοποίηση των διαμορφώσεων sweep-6m και sweep-opt	29
3.3.2. Μείωση μάζας δρομέα, με χρήση τεχνικών BTC	30
3.3.2.1. Αναζήτηση “χώρου” και βελτιστοποίηση, για πτερύγια με BTC	30
3.3.2.2. Πιστοποίηση των διαμορφώσεων $N = 2$ και $N = 3$	33
3.3.3. Μείωση μάζας δρομέα, με συνδυαστική εφαρμογή BTC και FEC	35
3.3.3.1. Μείωση μάζας με χρήση διάφορων μεθόδων βελτιστοποίησης	36
3.3.3.2. Πιστοποίηση σχεδιαστικών διαμορφώσεων BTC 5°, FEC 3% και “modified”	37
4. Πολυ-πεδιακή αερο-ελαστική βελτιστοποίηση DTU-10MW RWT	41
4.1. Βέλτιστος συνδυασμός BTC και FEC – και μια εναλλακτική προσέγγιση του FEC	41
4.2. Εφαρμογές	42

4.2.1. Ελαχιστοποίηση LCoE, με τεχνικές BTC	43
4.2.1.1. Περιγραφή διαδικασίας και αποτελέσματα	43
4.2.1.2. Αξιολόγηση τροποποιημένου σχεδίου	45
4.2.2. Ελαχιστοποίηση LCoE, εστιάζοντας σε συνθήκες “ρελαντί”	46
4.2.2.1. Περιγραφή σχεδίων	46
4.2.2.2. Υλικό και γεωμετρικό FEC (CASE A και B)	47
4.2.2.3. Συνδυαστική εφαρμογή τεχνικών παθητικού ελέγχου (CASE C, D και E)	48
4.2.2.4. Πιστοποίηση βέλτιστων σχεδίων	52
5. Συμπεράσματα	55
5.1. Γενικές παρατηρήσεις και συμπεράσματα	55
5.2. Μελλοντική έρευνα	56
5.3. Χρηματοδότηση	57
Βιβλιογραφία	59

Αυτή η σελίδα μένει κενή

Κατάλογος σχημάτων

Σχήμα 1.1	Πορεία εξέλιξης διάφορων πηγών ενέργειας για ηλεκτροπαραγωγή, την περίοδο 2000-2020, σε παγκόσμιο επίπεδο	2
Σχήμα 1.2	Το ενεργειακό μείγμα στην Ευρωπαϊκή Ένωση, για ηλεκτροπαραγωγή το 2020	2
Σχήμα 1.3	Σκαρίφημα ενεργητικού και παθητικού ελέγχου: (α) μετα-πτερύγιο και (β) κυρτά πτερύγια	3
Σχήμα 1.4	Μηχανισμοί σύζευξης σύνθετων δοκών: (α) σύζευξη-επέκτασης-στρέψης μέσω “ελικοειδούς” διάταξης και (β) σύζευξη-κάμψης-στρέψης μέσω “αντισυμμετρικής” διάταξης	4
Σχήμα 1.5	Εισαγωγή γωνίας στο μονο-κατευθυντήριο υλικό, που βρίσκεται στα “καπάκια”	5
Σχήμα 1.6	Κατευθύνσεις πτερύγισης (flap-wise) και περιστροφής (edge-wise), πτερυγίου ανεμογεννήτριας	5
Σχήμα 2.1	Συνθήκες πρόσπτωσης της ροής αέρα σε αεροτομή	8
Σχήμα 2.2	Μοντέλο πολλαπλών σωμάτων με τοπικά και καθολικά συστήματα συντεταγμένων	9
Σχήμα 2.3	Μοντέλο πολλαπλών σωμάτων σε επίπεδο υπο-σώματος	10
Σχήμα 2.4	Τυπική διάταξη στρωμάτων υλικού, μιας σύνθετης συστοιχίας, από το λεπτό-τοιχο κέλυφος της διατομής πτερυγίου	12
Σχήμα 2.5	Ορισμός των περιοχών διατομής πτερυγίου ανεμογεννήτριας DTU-10MW RWT	12
Σχήμα 2.6	Η βιομηχανική κατασκευή των σύγχρονων πτερυγίων βασίζεται στη μοντελοποίηση VARTM και περιλαμβάνει την τοποθέτηση στρώσεων υαλονημάτων με μείγμα ρητίνης και κόλλας σε καλούπια	16
Σχήμα 2.7	Διάγραμμα διαδικασίας σχεδιασμού και βελτιστοποίησης	21
Σχήμα 3.1	Εισαγωγή στροφής στο μονο-κατευθυντήριο υλικό (UD), που βρίσκεται στα ‘καπάκια’ - BTC	24
Σχήμα 3.2	Γεωμετρικό FEC. Στο πάνω μέρος φαίνεται η διατομή αναφοράς, ενώ στο κάτω μέρος η μετατόπιση των ‘καπακιών’	24

Σχήμα 3.3	Διάγραμμα ροής για την ελαχιστοποίηση της μάζας πτερυγίου, με διαμόρφωση BTC. Ο εξωτερικός βρόχος, περιλαμβάνει τις κύριες μεταβλητές σχεδιασμού (π.χ. κατανομή της γωνίας του UD υλικού) - ενώ ο εσωτερικός βρόχος καθορίζει την κατανομή του πάχους των τοιχωμάτων, ώστε να διατηρηθούν στα ίδια επίπεδα οι μέγιστες τιμές του κριτηρίου Tsai-Hill, κατά μήκος του πτερυγίου	26
Σχήμα 3.4	Διαμόρφωση κυρτότητας για: (i) πτερύγιο αναφοράς, (ii) sweep-6m και (iii) sweep-opt	29
Σχήμα 3.5	Συνισταμένη ροπή στη ρίζα πτερυγίου, για διάφορες ταχύτητες ανέμου: (i) πτερύγιο αναφοράς, (ii) sweep-6m και (iii) sweep-opt	30
Σχήμα 3.6	Ροπή στρέψης στη ρίζα πτερυγίου, για διάφορες ταχύτητες ανέμου: (i) πτερύγιο αναφοράς, (ii) sweep-6m και (iii) sweep-opt	30
Σχήμα 3.7	Μείωση μάζας πτερυγίων BTC, για τρεις γωνίες μονο-κατευθυντήριου υλικού: 5° , 7.5° και 10° . Εκτός από τη γωνία, αξιολογείται και το σημείο εκκίνησης (κάθε σημείο στις καμπύλες αντιστοιχεί σε διαφορετικό σημείο εκκίνησης) – <i>αριστερό σχήμα</i> . Πορεία σύγκλισης του εσωτερικού βρόχου βελτιστοποίησης, για σημείο εκκίνησης=0.3 – <i>δεξί σχήμα</i> . Η μείωση της μάζας, πραγματοποιείται για δεδομένες σχεδιαστικές παραμέτρους BTC (γωνία & θέση εκκίνησης) ώστε να διατηρηθεί η κατανομή των μέγιστων τιμών Tsai-Hill, σε σχέση με το πτερύγιο αναφοράς	31
Σχήμα 3.8	Βέλτιστη (ως προς τη μείωση μάζας) κατανομή γωνίας μονο-κατευθυντήριου υλικού – <i>αριστερό διάγραμμα</i> και μέγιστη μείωση μάζας πτερυγίων – <i>δεξί διάγραμμα</i> των διαμορφώσεων BTC που έχουν εξεταστεί	32
Σχήμα 3.9	Διάταξη βελτιστοποιημένου πτερυγίου, για την περίπτωση $N = 2$. Το σχήμα παρουσιάζει την κατανομή της γωνίας του μονο-κατευθυντήριου υλικού στα ‘καπάκια’	33
Σχήμα 3.10	Βέλτιστη κατανομή του συντελεστή μεταβολής πάχους τοιχωμάτων κατά μήκος του πτερυγίου. Ο συντελεστής αυτός, εγγυάται την ελαχιστοποίηση του πάχους των τοιχωμάτων κάθε διατομής, διατηρώντας τη μέγιστη τιμή του κριτηρίου Tsai-Hill στα ίδια επίπεδα με το πτερύγιο αναφοράς	33
Σχήμα 3.11	Σύγκλιση των μεταβλητών σχεδιασμού – <i>άνω διαγράμματα</i> και συνάρτησης κόστους – <i>κάτω διάγραμμα</i> του εξωτερικού βρόχου βελτιστοποίησης, για την περίπτωση $N = 2$	33
Σχήμα 3.12	Υπολογισμός ακραίων φορτίων για DTU-10MW RWT και σχεδιαστικών διαμορφώσεων $N = 2$ και $N = 3$, θεωρώντας έντονη τύρβη ανέμου DLC-1.3: (α) μέγιστη τιμή κριτηρίου Tsai-Hill, (β) μέγιστη συνισταμένη ροπή κάμψης στη ρίζα του πτερυγίου και (γ) μέγιστη συνισταμένη ροπή κάμψης στη βάση του πύργου	34

Σχήμα 3.13	Υπολογισμός φορτίου κόπωσης ανεμογεννήτριας DTU-10MW RWT και των σχεδιαστικών διαμορφώσεων $N = 2$ και $N = 3$ υιοθετώντας κανονική τύρβη ανέμου DLC-1.2: (α) κατανομή DELs της μέσης ορθής τάσης στα ‘καπάκια’ και (β) των ροπών του πτερυγίου	34
Σχήμα 3.14	Κατανομή του συντελεστή μεταβολής πάχους τοιχωμάτων (εσωτερικός βρόχος) και γωνίας μονο-κατευθυντήριου υλικού (εξωτερικός βρόχος)	36
Σχήμα 3.15	Ακραία φορτία DLC-1.3 σε σχέση με τις ταχύτητες ανέμου, για κάθε σχεδιαστική διαμόρφωση (με συντελεστές ασφαλείας): (α) μέγιστη τιμή κριτηρίου Tsai-Hill failure στο πτερύγιο, (β) μέγιστη συνισταμένη ροπή στη ρίζα πτερυγίου και (γ) μέγιστη συνισταμένη ροπή στη βάση του πύργου. Οι ποσοστιαίες διαφορές, καταγράφονται πάνω απ’τις μπάρες	38
Σχήμα 3.16	Ακραία φορτία DLC-6.x σε σχέση με τις γωνίες ανέμου, για κάθε σχεδιαστική διαμόρφωση (με συντελεστές ασφαλείας) (α) τυπική απόκλιση (std) της κάμψης περιστροφής στη ρίζα πτερυγίου, (β) μέγιστη συνισταμένη ροπή στη ρίζα πτερυγίου και (γ) μέγιστη συνισταμένη ροπή στη βάση του πύργου. Οι ποσοστιαίες διαφορές, καταγράφονται πάνω απ’τις μπάρες	38
Σχήμα 4.1	Διατομή πτερυγίου ανεμογεννήτριας, με εφαρμογή υλικού FEC (αριστερά) και γεωμετρικού FEC (δεξιά), μέσω ασύμμετρης μεταβολής στο πάχος των τοιχωμάτων και μετατόπισης ‘καπακιών’	42
Σχήμα 4.2	Σύγκριση των μεταβλητών σχεδίασης μεταξύ πτερυγίου αναφοράς και τροποποιημένης διαμόρφωσης με ακτίνα $R_{tip} = 92.49m$: (α) κατανομή χορδής, (β) κατανομή συστροφής, (γ) κατανομή πάχους τοιχωμάτων και γωνίας μονο-κατευθυντήριου υλικού και (δ) καμπύλη ισχύος	44
Σχήμα 4.3	Ανάλυση ακραίων φορτίων, κατόπιν αερο-ελαστικών προσομοιώσεων DLC-1.3 για διάφορες ταχύτητες ανέμου: (α) μέγιστη τιμή κριτηρίου Tsai-Hill ($f_{T/H}^{max}$) και (β) μέγιστη τιμή συνισταμένης ροπής στη βάση του πύργου. Οι ποσοστιαίες διαφορές σε σχέση με την ανεμογεννήτρια αναφοράς, καταγράφονται πάνω απ’τις μπάρες	45
Σχήμα 4.4	Υλικό FEC (CASE A): συντελεστές μεταβολής πάχους των υλικών “TRIAx” και “UNIAX”, για τις περιοχές “trailing” (υπερ-πίεσης) και “leading” (υπο-πίεσης), καθώς και ο συνολικός συντελεστής πάχους που αφορά όλη τη διατομή (πράσινο χρώμα)	47
Σχήμα 4.5	Γεωμετρικό FEC (CASE B): κατανομές ποσοστιαίας μετατόπισης των ‘καπακιών’ του πτερυγίου σε σχέση με τη χορδή, καθώς και ο συνολικός συντελεστής πάχους που αφορά όλη τη διατομή (πράσινο χρώμα)	47
Σχήμα 4.6	(α) μάζα πτερυγίου, (β) ετήσια παραγωγή ενέργειας και (γ) κόστος ενέργειας LCoE για τις περιπτώσεις υλικού FEC (CASE A) και γεωμετρικού FEC (CASE B), καθώς και οι ποσοστιαίες τους διαφορές	48

Σχήμα 4.7	Κατανομή συντελεστών υλικού FEC για τις περιοχές: (α) “leading” και (β) “trailing” των διαμορφώσεων: A, C, D και E	49
Σχήμα 4.8	Κατανομή συντελεστών γεωμετρικού FEC για τις επιφάνειες: (α) υπερ-πίεσης και (β) υπο-πίεσης των διαμορφώσεων: B, C, D και E	49
Σχήμα 4.9	CASE E: κατανομή (α) υλικού FEC, (β) γεωμετρικού FEC, (γ) συστροφής και (δ) γωνίας μονο-κατευθυντήριου υλικού καθώς και συνολικού συντελεστή μεταβολής πάχους τοιχωμάτων	50
Σχήμα 4.10	(α) μάζα πτερυγίου, (β) ετήσια παραγωγή ενέργειας και (γ) κόστος ενέργειας (LCoE), καθώς και οι ποσοστιαίες τους διαφορές	51
Σχήμα 4.11	Ακραία φορτία DLC-1.3 για διάφορες ταχύτητες ανέμου (περιλαμβάνονται οι συντελεστές ασφαλείας), για τη μέγιστη συνισταμένη ροπή: (α) στη ρίζα του πτερυγίου και β) στη βάση του πύργου	52
Σχήμα 4.12	Ακραία φορτία DLC-6.x για διάφορες γωνίες ανέμου (περιλαμβάνονται οι συντελεστές ασφαλείας), για τη μέγιστη συνισταμένη ροπή: (α) στη ρίζα του πτερυγίου και (β) στη βάση του πύργου	52

Κατάλογος πινάκων

Πίνακας 2.1	Βασικές παράμετροι ανεμογεννήτριας αναφοράς	15
Πίνακας 2.2	Κοστολόγηση αναλώσιμων υλικών	17
Πίνακας 3.1	Επίδραση κυρτότητας στη μάζα και τα φορτία πτερυγίου	28
Πίνακας 3.2	Κοπωτικά φορτία (DELs) ροπών στη βάση του πύργου, για την ανεμογεννήτρια αναφοράς DTU-10MW RWT καθώς και σχετική ποσοστιαία διαφορά των διαμορφώσεων $N = 2$ και $N = 3$, υιοθετώντας κανονική τύρβη DLC-1.2	35
Πίνακας 3.3	Αριθμός κλήσεων αντικειμενικής συνάρτησης, που απαιτεί κάθε μέθοδος	36
Πίνακας 3.4	Πίνακας εξεταζόμενων διαμορφώσεων και σύγκριση με την DTU-10MW RWT. Οι παράμετροι Weibull για τον υπολογισμό της ετήσιας ισχύος, είναι: $C = 11 \text{ m/s}$ και $k = 2$	37
Πίνακας 3.5	Σύγκριση φορτίων κόπωσης DLC-1.2 μεταξύ του DTU-10MW RWT και των διαμορφώσεων παθητικού ελέγχου που εξετάζονται. Τα DELs υπολογίζονται για διάστημα είκοσι ετών με συντελεστή Wöhler $m = 10$ για τα πτερύγια και $m = 4$ για τον πύργο, $N_{ref} = 10^7$ κύκλοι και παράμετροι Weibull: $C = 11 \text{ m/s}$ και $k = 2$. Τα απόλυτα φορτία (σε kNm) καταγράφονται για την ανεμογεννήτρια αναφοράς καθώς και η σχετική ποσοστιαία διαφορά των διαμορφώσεων	39
Πίνακας 4.1	Σύγκριση κύριων χαρακτηριστικών ανεμογεννήτριας DTU-10MW RWT, δρομέα L/R απ'την ενότητα 3.3.2. και τροποποιημένης διαμόρφωσης "modified"	44
Πίνακας 4.2	Παθητικός έλεγχος ανεμογεννήτριας, με στόχο την ελαχιστοποίηση του LCoE	46
Πίνακας 4.3	Αποτελέσματα των μεταβλητών σχεδιασμού των σχεδιαστικών διαμορφώσεων που εξετάστηκαν. Οι τιμές με κόκκινο χρώμα, αντιστοιχούν στις μεταβλητές σχεδιασμού με σταθερή τιμή	51

Αυτή η σελίδα μένει κενή

Κεφάλαιο 1

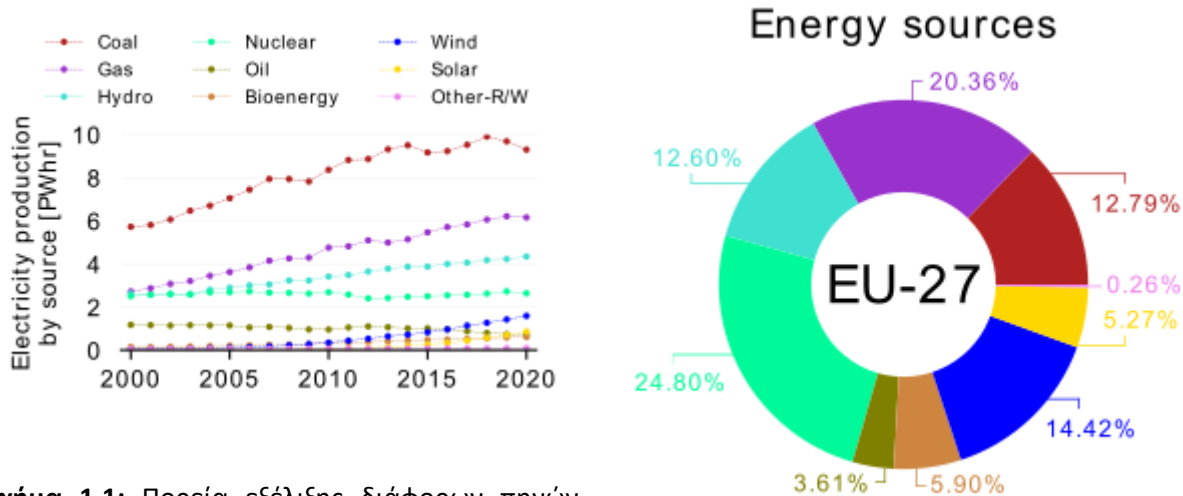
1. Εισαγωγή

Οι διαστάσεις των σύγχρονων ανεμογεννητριών παρουσιάζουν γεωμετρική αύξηση τις τελευταίες δεκαετίες, συμπιέζοντας με τον τρόπο αυτό το κόστος ηλεκτρικής ενέργειας (Levelized Cost of Electricity - LCoE), που παράγεται από τον άνεμο. Η αύξηση στο μέγεθος των ανεμογεννητριών, συνεπάγεται και αύξηση των φορτίων που αναπτύσσονται σε αυτές, με αποτέλεσμα να παρουσιάζονται αρκετές σχεδιαστικές προκλήσεις, οι οποίες απαιτούν καινοτόμες τεχνολογικές λύσεις. Τέτοιες καινοτομίες, περιλαμβάνουν: νέα και προηγμένα υλικά, υβριδικές μεθόδους κατασκευής, νέα σχέδια εσωτερικής δομής, νέες μεγάλου πάχους αεροτομές υψηλής απόδοσης και τεχνικές ενεργητικού ή/και παθητικού ελέγχου φορτίων. Μεταξύ των παραπάνω, οι μέθοδοι παθητικού ελέγχου έχουν αποδειχθεί πολλά υποσχόμενες στην ελάφρυνση των φορτίων και αποτελούν το κύριο αντικείμενο της παρούσας διατριβής. Στόχος, είναι ο βέλτιστος συνδυασμός τεχνικών παθητικού ελέγχου, που θα επιτρέψει τη συμπίεση του LCoE.

1.1. Το ενεργειακό μείγμα και οι στόχοι για το μέλλον

Αν και έχει γίνει πολλή συζήτηση για την ανάγκη μείωσης των εκπομπών CO_2 , σύμφωνα με τα διαθέσιμα δεδομένα [1] η παγκόσμια κοινότητα εξακολουθεί να στηρίζεται στα ορυκτά καύσιμα! Στο Σχ. 1.1, παρουσιάζεται η εξέλιξη της συμβολής κάθε πηγής στο παγκόσμιο ενεργειακό μείγμα, για ηλεκτροπαραγωγή από το 2000 έως το 2020. Σύμφωνα με το διάγραμμα αυτό, η συνολική ζήτηση ενέργειας αυξάνεται διαρκώς, χωρίς να παρουσιάζεται οποιαδήποτε ουσιαστική αλλαγή στη συμπεριφορά της παγκόσμιας κοινότητας, προς όφελος των ανανεώσιμων πηγών ενέργειας (αιολική, ηλιακή, άλλη). Όπως παρατηρούμε, η διείσδυση της αιολικής ενέργειας έκανε την εμφάνιση της μόλις τα τελευταία χρόνια, με τα έτη 2008 και 2016 να αποτελούν χρονιές “ορόσημα”, αφού ανέβηκε από την 7^η στην 6^η και από την 6^η στην 5^η θέση, αντίστοιχα. Από την άλλη, η Ευρωπαϊκή Ένωση, φαίνεται να

επιδεικνύει μεγαλύτερη συμμετοχή των «πράσινων» πηγών στο ενεργειακό μείγμα (βλέπε Σχ. 1.2). Συγκεκριμένα, η αιολική ενέργεια, βρίσκεται στην πρώτη θέση μεταξύ των ανανεώσιμων πηγών ενέργειας, ενώ μαζί με την ηλιακή και την υδροηλεκτρική ενέργεια, καταλαμβάνουν το $\frac{1}{3}$ της πίτας.



Σχήμα 1.1: Πορεία εξέλιξης διάφορων πηγών ενέργειας για ηλεκτροπαραγωγή, την περίοδο 2000-2020, σε παγκόσμιο επίπεδο.

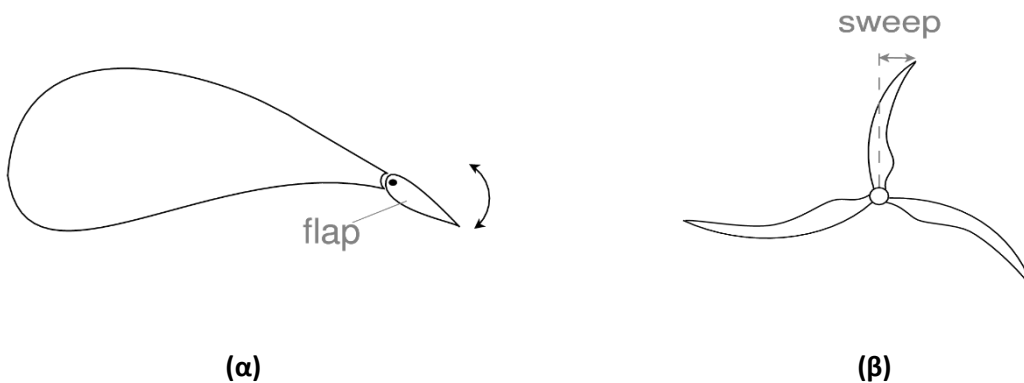
Σχήμα 1.2: Το ενεργειακό μείγμα στην Ευρωπαϊκή Ένωση, για ηλεκτροπαραγωγή το 2020.

Η αναζήτηση εναλλακτικών λύσεων και η μαζική υιοθέτηση πιο φιλικών προς το περιβάλλον πηγών ενέργειας είναι πλέον επιτακτική! Για τον λόγο αυτό, έχουν εφαρμοστεί διάφορες πολιτικές προς αυτή την κατεύθυνση και έχουν τεθεί στόχοι από τις κυβερνήσεις, για περιορισμό της χρήσης των ορυκτών καυσίμων. Για παράδειγμα, μέχρι το 2030 τουλάχιστον το 20% της ενέργειας των ΗΠΑ αναμένεται να προμηθεύεται από χερσαία και υπεράκτια αιολικά πάρκα [2] – ενώ η Ευρωπαϊκή Ένωση έχει δεσμευτεί για κάλυψη του 45% των αναγκών της από ανανεώσιμες πηγές [3]. Για να επιτευχθεί ο στόχος αυτός, θα απαιτηθεί τεράστια ανάπτυξη της αιολικής ενέργειας, τόσο στην ξηρά όσο και στη θάλασσα. Έμπρακτα, η Ευρωπαϊκή Ένωση έχει προωθήσει και στηρίζει οικονομικά την κοινότητα της αιολικής ενέργειας προκειμένου να αναπτυχθούν νέες τεχνολογίες και καινοτόμες εφαρμογές, που θα τροφοδοτήσουν τη βιομηχανία. Ξεχωρίζουν πέντε εμβληματικά ερευνητικά έργα στα οποία η ερευνητική κοινότητα έχει συνεργαστεί με τη βιομηχανία, για την ανάπτυξη νέων και επικυρωμένων εργαλείων καθώς και νέων τεχνολογιών, που σχετίζονται με την αιολική ενέργεια:

- DAMPBLADE [4] (2001-2004)
- STABCON [5] (2002-2006)
- UpWind [6] (2006-2011)
- INNWIND.EU [7] (2012-2017)
- AVATAR [8] (2013-2017)

1.2. Έλεγχος φορτίων ανεμογεννητριών

Η αύξηση του μεγέθους των ανεμογεννητριών, εμποδίζεται από το υψηλό κόστος κατασκευής, εργατικών, μεταφοράς και εγκατάστασης – ως αποτέλεσμα του κυβικού νόμου [9]. Νέα υλικά κατασκευής, καινούριες τεχνικές και καινοτομίες όπως είναι ο ενεργητικός/παθητικός έλεγχος των φορτίων, μπορούν να αποτελέσουν το «κλειδί» για την υπέρβαση τέτοιων εμποδίων. Για παράδειγμα, ο Bossanyi [10] μελέτησε τη δυνατότητα περιορισμού των φορτίων μέσω του ελέγχου βήματος - ενώ μια εναλλακτική προσέγγιση με χρήση μεταπτερυγίων, εμπνευσμένη από τις αεροπορικές εφαρμογές, έχει προταθεί από τους Matthew Lackner και Gijs Kuik το 2009 [11], όπου η χρήση των μετα-πτερυγίων εφαρμόζεται σε ανεμογεννήτρια 5MW (βλέπε Σχ. 1.3).

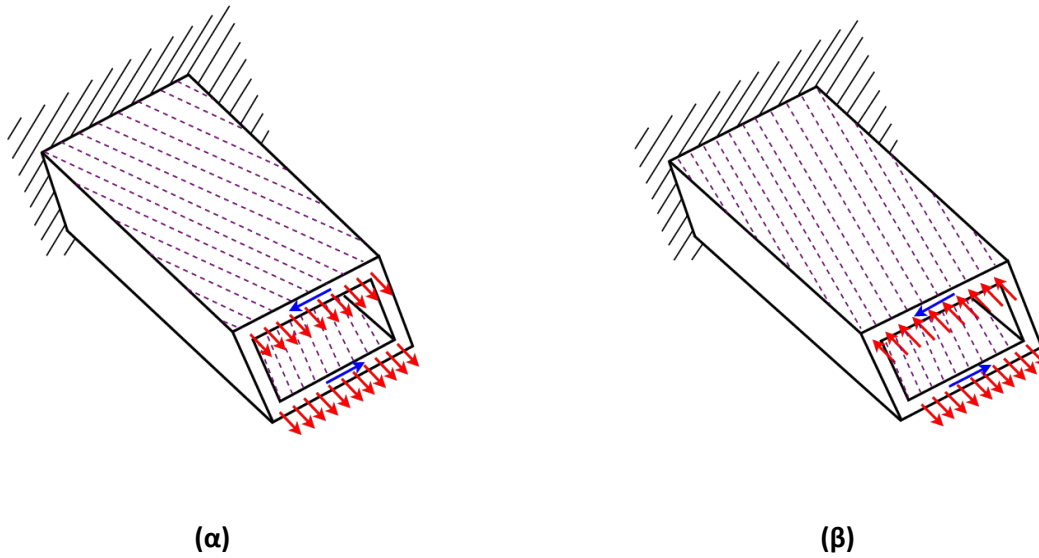


Σχήμα 1.3: Σκαρίφημα ενεργητικού και παθητικού ελέγχου: (α) μετα-πτερύγιο και (β) κυρτά πτερύγια.

Σε ότι αφορά τον παθητικό έλεγχο φορτίων, οι πιο συχνές εφαρμογές περιλαμβάνουν τη σύζευξη κάμψης-στρέψης (BTC). Μια από τις πρώτες εφαρμογές, πραγματοποιήθηκε από το εργαστήριο Sandia [12] και [13], όπου εξετάστηκε η δυνατότητα χρήσης κυρτών πτερυγίων (βλέπε Σχ. 1.3). Αποτέλεσμα της έρευνας ήταν ο σχεδιασμός της ανεμογεννήτριας STAR-27.1m, η οποία παρουσίαζε μειωμένα φορτία (στατικά και κόπωσης), πράγμα που επέτρεψε την αύξηση της διαμέτρου του δρομέα, παράγοντας 10 – 12% περισσότερη ενέργεια.

Τα πτερύγια των σύγχρονων ανεμογεννητριών, μεγάλης ισχύος – είναι μακριές λεπτές και εύκαμπτες κατασκευές από σύνθετα υλικά. Τέτοια υλικά, περιέχουν κυρίως ίνες γυαλιού ή άνθρακα καθώς και άλλα πλαστικά υλικά [14]. Συνήθως τα υλικά αυτά τοποθετούνται συμμετρικά, εκατέρωθεν ενός αφρώδους πυρήνα, σε δομή τύπου “σάντουιτς”. Η κλασική λεπτό-τοιχη πολυ-στρωματοποιημένη θεωρία (Lamination Theory – L/T) [15] και [16], είναι σε θέση να υπολογίσει τις μηχανικές ιδιότητες μιας διατομής, που αποτελείται από σύνθετα υλικά (πολλών στρωμάτων). Η “έξυπνη” τοποθέτηση των στρώσεων, όπως για παράδειγμα η τοποθέτηση του μονο-κατευθυντήριου (UD) υλικού υπό γωνία, είναι δυνατό να ενεργοποιήσει τη σύζευξη μεταξύ των κατευθύνσεων μιας διατομής. Γενικά, στην επιστήμη των υλικών έχουν εξεταστεί δυο πολύ γνωστές τεχνικές:

- Σύζευξη-Επέκτασης-Συστροφής (Extension-Twist-Coupling), βλέπε Σχ 1.4 (αριστερά).
- Σύζευξη-Κάμψης-Στρέψης (Bend-Twist-Coupling), βλέπε Σχ. 1.4 (δεξιά).

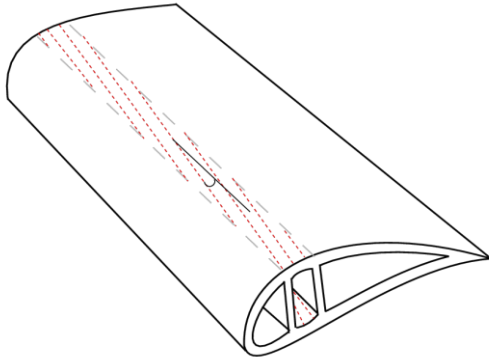


Σχήμα 1.4: Μηχανισμοί σύζευξης σύνθετων δοκών: (α) σύζευξη-επέκτσης-στρέψης μέσω “ελικοειδούς” διάταξης και (β) σύζευξη-κάμψης-στρέψης μέσω “αντισυμμετρικής” διάταξης.

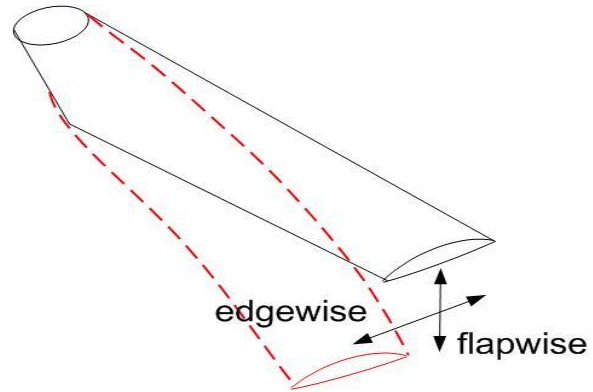
Σε περιπτώσεις όπου η κάμψη κυριαρχεί, μπορεί να χρησιμοποιηθεί η σύζευξη-κάμψης-στρέψης (BTC). Αν και η έννοια του BTC, προέρχεται από εφαρμογές ελικοπτέρων [17],[18], στη βιβλιογραφία αναφέρεται συχνά ως τεχνική παθητικού ελέγχου φορτίων [19],[20],[21]. Σύμφωνα με τον Lobitz [22], μια αύξηση 10 – 15% της διαμέτρου του δρομέα είναι εφικτή, εφαρμόζοντας μια μέτρια γωνία στο μονο-κατευθυντήριο υλικό που βρίσκεται πάνω απ’τις περιοχές των “καπακιών” ενός πτερυγίου ανεμογεννήτριας (βλέπε Σχ. 1.5). Αρκετές δημοσιεύσεις έχουν ασχοληθεί με την πιο πάνω τεχνική, είτε εστιάζοντας στη δοκιμή σύνθετων δοκών είτε πραγματικών πτερυγίων. Μεταξύ αυτών, ο Fedoron από το Πολυτεχνείο της Δανίας [23], αξιολόγησε τη δυνατότητα εφαρμογής BTC σε ένα τμήμα πτερυγίου ανεμογεννήτριας. Η μελέτη, επαλήθευσε τα θεωρητικά μοντέλα μέσω συγκρίσεων με πειραματικές μελέτες και διερεύνησε το εύρος κατά μήκος του πτερυγίου που μπορεί να εφαρμοστεί μια τέτοια τεχνική. Επιπλέον ο Stäblein [24], αξιολόγησε αριθμητικά τη δυνατότητα μείωσης των φορτίων. Μεταξύ άλλων, στην αναφορά του κάνει λόγο για μείωση περίπου 15% στα φορτία ροπής της ρίζας του πτερυγίου, με μια μικρή απώλεια ενέργειας.

Εκτός από την ανάγκη περιορισμού των φορτίων, ένα άλλο πρόβλημα που παρατηρείται συχνά κατά την εγκατάσταση ανεμογεννητριών, είτε όταν αυτές βρίσκονται σε κατάσταση “ρελαντί”, είναι η διαχείριση των ταλαντώσεων που παρατηρούνται κατά την πνοή ανέμου σε υψηλή γωνία απόκλισης. Ο Wang το 2016, δημοσίευσε μια εργασία [25] στην οποία αξιολογείται η ευστάθεια ενός δρομέα σε αργή λειτουργία “ρελαντί”, με βάση μη γραμμικές προσομοιώσεις στο πεδίο του χρόνου και γραμμική ανάλυση ιδιοτιμών. Αντικείμενο της μελέτης, αποτέλεσε η DTU-10MW RWT [26] και τα χαρακτηριστικά αστάθειας αξιολογήθηκαν χρησιμοποιώντας ένα γραμμικοποιημένο εργαλείο ανάλυσης ευστάθειας μέσω υπολογισμού των αερο-ελαστικών ιδιοτιμών καθώς και μέσω αερο-ελαστικών προβλέψεων

φορτίων. Πρακτικές λύσεις, του πιο πάνω προβλήματος, εξετάζονται στα κεφάλαια 3 και 4 της παρούσας διατριβής με χρήση τεχνικών σύζευξης-πτερύγισης-περιστροφής (Flap-Edge-Coupling - FEC), βλέπε Σχ. 1.6.



Σχήμα 1.5: Εισαγωγή γωνίας στο μονοκατευθυντήριο υλικό, που βρίσκεται στα “καπάκια”.



Σχήμα 1.6: Κατευθύνσεις πτερύγισης (flap-wise) και περιστροφής (edge-wise), πτερυγίου ανεμογεννήτριας.

1.3. Αντικείμενο διατριβής και καινοτομίες

Η παρούσας διατριβή στοχεύει στην ανάπτυξη βελτιστοποιημένων σχεδίων πτερυγίων ανεμογεννητριών ισχύος $10MW$, ελάχιστου LCoE. Η ανακούφιση των φορτίων, επιτυγχάνεται με την εφαρμογή τεχνικών παθητικού ελέγχου η οποία αποτελεί μέρος της παραπάνω στρατηγικής βελτιστοποίησης. Η συμπίεση του κόστους ενέργειας, μπορεί να υλοποιηθεί είτε με τη μείωση της κεφαλαιουχικής δαπάνης (CAPital EXpenditure - CAPEX) ή/και με την αύξηση της διαμέτρου του δρομέα. Η ανάπτυξη του υπολογιστικού πλαισίου σχεδιασμού και βελτιστοποίησης, απαιτεί την αξιοποίηση διαφόρων υπολογιστικών εργαλείων. Κάποια απ'τα εργαλεία που χρησιμοποιήθηκαν, αναπτύχθηκαν στο πλαίσιο της παρούσας διατριβής (συμβολή της εργασίας), άλλα τροποποιήθηκαν καταλλήλως, ενώ κάποια αξιοποιήθηκαν αυτούσια. Οι κύριοι στόχοι της εργασίας, συνοψίζονται πιο κάτω:

- Αρχικά, τα υπολογιστικά εργαλεία που χρησιμοποιούνται, έχουν πιστοποιηθεί μέσω σειράς παραδειγμάτων και εφαρμογών, τα αποτελέσματα των οποίων συγκρίνονται με τα αποτελέσματα άλλων/όμοιων υπολογιστικών εργαλείων και βιβλιογραφικών αναφορών.
- Έχει αναπτυχθεί ένα μοντέλο κόστους ανεμογεννήτριας. Το μοντέλο αυτό, περιλαμβάνει μια αναλυτική διαδικασία κοστολόγησης του πτερυγίου (κόστος υλικών, αναλώσιμων και εργατικών), ενώ τα υπόλοιπα τμήματα κοστολογούνται βάσει εμπειρικών σχέσεων. Παράλληλα, αξιολογήθηκαν διάφορες μέθοδοι βελτιστοποίησης. Οι περισσότερες απ'αυτές, διατίθενται από τη βιβλιοθήκη SciPy της Python, όπως η COBYLA και η SLSQP - ενώ άλλες όπως η μέθοδος Newton (και οι παραλλαγές της) απαιτούν την κωδικοποίησή τους.

- Οι διάφορες τεχνικές παθητικού ελέγχου, αξιολογούνται μεμονωμένα τόσο σε σχέση με τη δυνατότητα περιορισμού των αναπτυσσόμενων φορτίων, όσο και με τα περιθώρια συμπίεσης του CAPEX. Με τον τρόπο αυτό, γίνεται η “χαρτογράφηση” του χώρου των λύσεων και η αναζήτηση των πιθανών λύσεων του προβλήματος.
- Έχει αναπτυχθεί ένα ολοκληρωμένο περιβάλλον που συνδυάζει τα πιο πάνω υπολογιστικά εργαλεία, με στόχο την ελαχιστοποίηση του LCoE. Το περιβάλλον αυτό, εκτός από τις παραμέτρους που σχετίζονται με τις τεχνικές παθητικού ελέγχου, αξιολογεί και άλλες μεταβλητές που σχετίζονται με τη γεωμετρία του πτερυγίου (π.χ. κατανομή χορδής και συστροφής).
- Τόσο οι αεροδυναμικές μεταβλητές όσο και οι κατασκευαστικές, αξιολογούνται ταυτόχρονα σε κοινό βρόχο, στο πλαίσιο της πολυ-πεδιακής αερο-ελαστικής βελτιστοποίησης (Multi-Disciplinary Aero-elastic Optimization - MDAO). Στο πλαίσιο της MDAO, το αναλυτικό μοντέλο κόστους ανεμογεννήτριας παρέχει τη δυνατότητα ποσοτικοποίησης του κόστους της παραγόμενης ενέργειας LCoE, κάτι που αποτελεί άλλη μια καινοτομία της παρούσας εργασίας - αφού οι περισσότερες εργασίες μένουν μόνο στην εκτίμηση του CAPEX [27].

1.4. Ανασκόπηση

Η παρούσα εργασία, χωρίζεται σε πέντε κεφάλαια:

- Κεφάλαιο 2: Περιλαμβάνει μια σύντομη περιγραφή των υπολογιστικών εργαλείων που έχουν αναπτυχθεί και αξιοποιηθεί κατά τη διάρκεια της παρούσας εργασίας.
- Κεφάλαιο 3: Στο κεφάλαιο αυτό, αξιολογείται η δυνατότητα εφαρμογής τεχνικών παθητικού ελέγχου BTC και FEC, στην ανεμογεννήτρια αναφοράς DTU-10MW RWT. Ως αποτέλεσμα της, ανακούφισης των φορτίων που προκαλείται, αξιολογείται η δυνατότητα συμπίεσης του CAPEX μέσω εφαρμογής τεχνικών παθητικού ελέγχου.
- Κεφάλαιο 4: Στο κεφάλαιο αυτό, περιγράφεται η πολυ-πεδιακή διαδικασία ελαχιστοποίησης του LCoE, αξιολογώντας τόσο τις παραμέτρους που σχετίζονται με την εφαρμογή παθητικού ελέγχου όσο και τις γεωμετρικές παραμέτρους (π.χ. κατανομή χορδής και συστροφής). Στο τέλος του κεφαλαίου αυτού, προτείνεται ένα σύνολο βελτιστοποιημένων πτερυγίων.
- Κεφάλαιο 5: Περιλαμβάνει τα συμπεράσματα και τις προτάσεις για μελλοντική έρευνα.

Κεφάλαιο 2

2. Υπολογιστικά εργαλεία

Στο κεφάλαιο αυτό, παρουσιάζονται τα υπολογιστικά εργαλεία που αναπτύχθηκαν και αξιοποιήθηκαν στο πλαίσιο του πολυ-πεδιακού περιβάλλοντος σχεδιασμού και βελτιστοποίησης πτερυγίων ανεμογεννήτριας. Αρχικά, παρουσιάζεται ο αερο-ελαστικός επιλύτης hGAST [28] ο οποίος χρησιμοποιείται για τον υπολογισμό των φορτίων σχεδιασμού της ανεμογεννήτριας, με βάση τον κανονισμό IEC 61400-1 [29]. Στις επόμενες δυο ενότητες, περιγράφεται το υπολογιστικό εργαλείο ανάλυσης διατομών και το μοντέλο κόστους ανεμογεννήτριας. Τέλος, γίνεται μια περιγραφή των μεθόδων βελτιστοποίησης που χρησιμοποιήθηκαν στην εργασία καθώς και του ολοκληρωμένου περιβάλλοντος σχεδιασμού και βελτιστοποίησης. Ο αναγνώστης, μπορεί να βρει παραδείγματα πιστοποίησης των εργαλείων και σύγκρισης αποτελεσμάτων είτε με άλλα εργαλεία είτε με βιβλιογραφικές αναφορές, στο Αγγλικό κείμενο της διατριβής.

2.1. Αερο-ελαστικός επιλύτης hGAST

Ο ύδρο-σέρβο-αερο-ελαστικός επιλύτης hGAST, έχει αναπτυχθεί από το εργαστήριο αεροδυναμικής του Ε.Μ.Π., με σκοπό την αερο-ελαστική προσομοίωση υπεράκτιων/χερσαίων ανεμογεννητριών. Το αεροδυναμικό, το ελαστο-δυναμικό και το υδρο-δυναμικό (εάν υπάρχει) μοντέλο, λαμβάνονται χωριστά και στη συνέχεια συνδυάζονται επιβάλλοντας κατάλληλη μη-γραμμική σύζευξη στα σημεία αλληλεπίδρασης τους. Με τον hGAST πραγματοποιούνται οι απαραίτητοι υπολογισμοί στο πεδίο του χρόνου καθώς και η ιδιοδιανυσματική ανάλυση υπολογισμού των ιδιοσυχνοτήτων και ιδιομορφών της ανεμογεννήτριας. Καθορίζοντας την εξωτερική διέγερση (συνθήκες αέρα ή/και κυματισμού), οι υπολογισμοί στο πεδίο του χρόνου επιτρέπουν την εκτίμηση τόσο των κοπωτικών όσο και των ακραίων φορτίων.

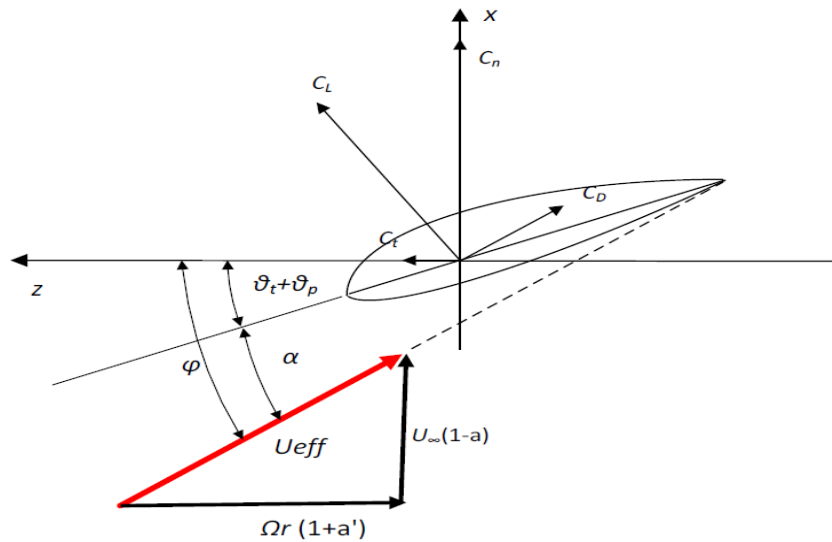
2.1.1. Αεροδυναμικό μοντέλο

Η πιο συνηθισμένη μέθοδος για τον υπολογισμό της αεροδυναμικής φόρτισης των πτερυγίων μιας ανεμογεννήτριας, είναι η θεωρία Δίσκου-Ορμής (Blade Element Momentum Theory - BEMT) [30] και στοιχείων πτερύγωσης. Ο συνδυασμός τους, καταλήγει σε δυο μη-γραμμικές εξισώσεις που επιλύονται επαναληπτικά:

$$dT = N_{blade} \frac{\rho U_{eff}^2}{2} (C_L \cos \varphi + C_D \sin \varphi) c dr = 4\pi\rho U_{\infty}^2 a(1-a)r dr \quad (2.1)$$

$$dQ = N_{blade} \frac{\rho U_{eff}^2}{2} (C_L \cos \varphi - C_D \sin \varphi) cr dr = 4\pi\rho U_{\infty} a'(1-a)r^3 dr \quad (2.2)$$

Όπου dT και dQ η ώση και η ροπή ενός δακτυλιοειδούς αγωγού ακτίνας dr , N_{blade} ο αριθμός των πτερυγίων, ρ η πυκνότητα του αέρα, U_{eff} η πραγματική ταχύτητα, U_{∞} η αδιατάρακτη ταχύτητα ανέμου, C_L και C_D οι συντελεστές άνωσης και οπισθέλκουσας αντίστοιχα, φ η γωνία μεταξύ της πραγματικής ταχύτητας και του επιπέδου του δρομέα, r η ακτινική θέση κάθε στοιχείου σε σχέση με τον άξονα περιστροφής, c το μήκος της τοπικής χορδής και Ω η ταχύτητα περιστροφής.



Σχήμα 2.1: Συνθήκες πρόπτωσης της ροής αέρα σε αεροτομή.

Ο συντελεστής αξονικής επαγωγής a , εκφράζει τη μείωση της ταχύτητας του ανέμου καθώς περνά μέσα απ'το δίσκο του δρομέα - ενώ ο συντελεστής περιφερειακής επαγωγής a' , την περιστροφή που προστίθεται στη ροή λόγω της περιστροφής του δρομέα. Η πραγματική ταχύτητα U_{eff} και η γωνία φ (βλέπε Σχ. 2.1) ορίζονται ως εξής:

$$U_{eff} = \sqrt{[U_{\infty}(1-a)]^2 + [\Omega r(1+a')]^2} \quad (2.3)$$

$$\varphi = \tan^{-1} \left[\frac{(1-a)U_{\infty}}{[(1+a')\Omega r]} \right] \quad (2.4)$$

Η γωνία πρόσπτωσης α που χρησιμοποιείται για να οριστούν οι συντελεστές C_L και C_D είναι:

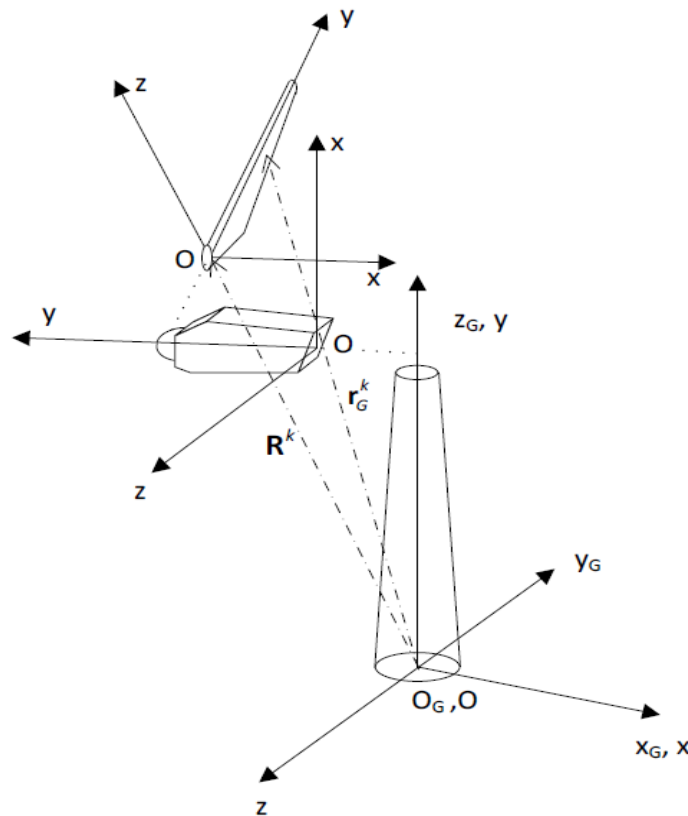
$$\alpha = \varphi - (\theta_t + \theta_p) \quad (2.5)$$

όπου θ_t και θ_p η τοπική γωνία συστρόφης και βήματος, αντίστοιχα.

2.1.2. Ελαστο-δυναμικό μοντέλο

Η ανεμογεννήτρια θεωρείται ως δυναμικό σύστημα πολλαπλών σωμάτων, η σύνθεση των οποίων πραγματοποιείται σύμφωνα με το μοντέλο πολλαπλών σωμάτων (multi-body model) [31]. Η ανάλυση της ελαστο-δυναμικής συμπεριφοράς της ανεμογεννήτριας συνίσταται στην εξέταση κάθε συνιστώσας της κατασκευής ξεχωριστά από τις υπόλοιπες και τη σύνδεση των συνιστωσών, μέσω της επιβολής καταλληλών κινηματικών συνθηκών καθώς και συνθηκών φόρτισης που επιβάλλονται στα σημεία σύνδεσης.

Η δομική μοντελοποίηση των ανεμογεννητριών, βασίζεται στην θεωρία δοκού (beam theory) [32]. Όλα τα εύκαμπτα τμήματα, θεωρούνται ως δοκοί Timoshenko που υπόκεινται σε κάμψη δυο κατευθύνσεων, διάτμηση, εφελκυσμό και στρέψη. Οι δοκοί χωρίζονται σε ένα αριθμό διασυνδεδεμένων “υπο-σωμάτων” (sub-bodies).



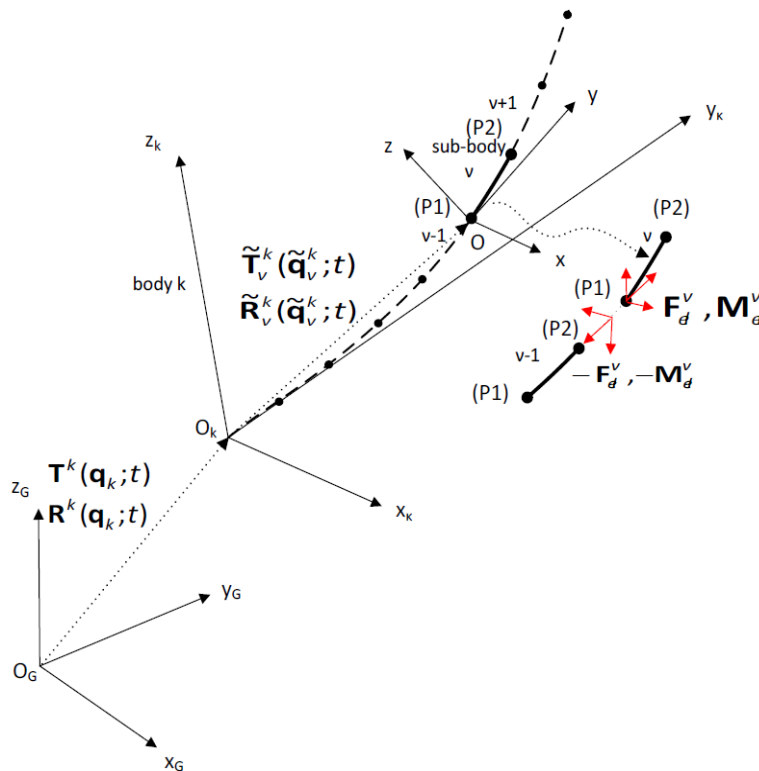
Σχήμα 2.2: Μοντέλο πολλαπλών σωμάτων με τοπικά και καθολικά συστήματα συντεταγμένων.

Κάθε υπο-τμήμα μπορεί να αντιπροσωπεύει μια συνιστώσα της ανεμογεννήτριας (δηλαδή τον πύργο, τον άξονα, το πτερύγιο) ή ένα μέρος αυτού. Ένα τοπικό σύστημα συντεταγμένων $[Oxyz]$ τίθεται στην αρχή κάθε συνιστώσας, ως προς το οποίο ορίζονται οι τοπικές ελαστικές παραμορφώσεις (βλέπε Σχ. 2.2). Έστω ότι το R^k δηλώνει το διάνυσμα θέσης της αρχής $[Oxyz]$ του στοιχείου “ k ” και το T^k το μητρώο περιστροφής απ’το τοπικό στο αδρανειακό σύστημα συντεταγμένων. Τότε, το διάνυσμα θέσης r_G^k ενός σημείου στο “ k ” σε σχέση με το αδρανειακό πλαίσιο $[Ox_Gy_Gz_G]$, ορίζεται ως:

$$r_G^k = R^k + T^k \cdot r^k \quad (2.6)$$

Η σύνθεση πολλαπλών σωμάτων μπορεί να επεκταθεί και στο επίπεδο των ίδιων των συνιστωσών. Με αυτό τον τρόπο, τα μεγάλα εύκαμπτα σώματα/συνιστώσες που υφίστανται σημαντικές παραμορφώσεις (όπως τα πτερύγια), χωρίζονται σε ένα αριθμό διασυνδεδεμένων υπο-σωμάτων, καθένα απ’τα οποία θεωρείται ως ξεχωριστό στοιχείο δοκού. Κάθε υπο-σώμα έχει το δικό του σύστημα συντεταγμένων $[Oxyz]$. Το πρώτο άκρο (P1) του υπο-σώματος θεωρείται ως η αρχή O , ενώ το δεύτερο άκρο (P2) θεωρείται ως ελεύθερο άκρο. Το σύστημα συντεταγμένων $[Ox_ky_kz_k]$ του υπο-σώματος “ v ” του σώματος “ k ” ορίζεται σε σχέση με το σύστημα συντεταγμένων $[Ox_ky_kz_k]$ του σώματος απ’το διάνυσμα θέσης της αρχής του \tilde{R}_v^k και ένα μητρώο περιστροφής \tilde{T}_v^k (βλέπε Σχ. 2.3). Το διάνυσμα θέσης ενός τυχαίου σημείου του υπο-σώματος “ v ” του σώματος “ k ” γράφεται σε σχέση με το αδρανειακό σύστημα συντεταγμένων $[Ox_Gy_Gz_G]$ ως:

$$r_{G,v}^k = R^k(q_k, t) + T^k(q_k, t) \cdot \{ \tilde{R}_v^k(\tilde{q}_v^k, t) + \tilde{T}_v^k(\tilde{q}_v^k, t) \cdot r_v^k \} \quad (2.7)$$



Σχήμα 2.3: Μοντέλο πολλαπλών σωμάτων σε επίπεδο υπο-σώματος.

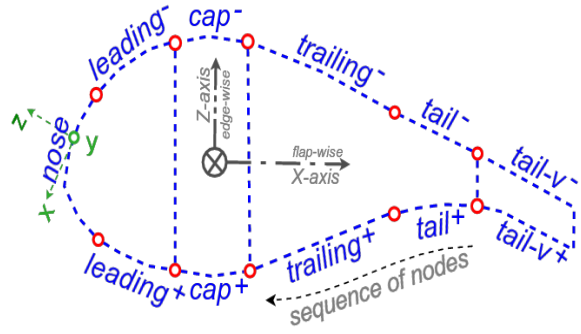
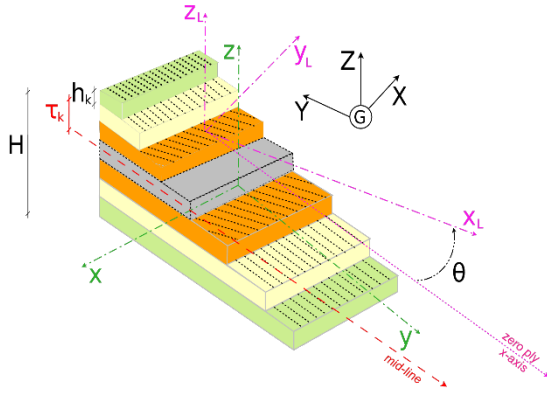
Εάν μία συνιστώσα/σώμα διαιρεθεί έναν αρκετά μεγάλο αριθμό υπο-σωμάτων, τότε οι μετατοπίσεις και οι περιστροφές - σε σχέση με το σύστημα του υπο-σώματος, θεωρούνται μικρές κι έτσι μπορούν να χρησιμοποιηθούν οι εξισώσεις γραμμικής δοκού. Μεγάλες παραμορφώσεις και περιστροφές “χτίζονται” σταδιακά και η μη-γραμμική δυναμική εισάγεται επιβάλλοντας σε κάθε υπο-σώμα τις μετατοπίσεις και τις περιστροφές των προηγούμενων ως κινήσεις άκαμπτου σώματος (rigid body motions). Η δυναμική σύζευξη των υπο-σωμάτων επιτυγχάνεται με την εισαγωγή των φορτίων αντίδρασης (3 δυνάμεις και 3 ροπές) του πρώτου κόμβου κάθε υπο-σώματος στον ελεύθερο κόμβο του προηγούμενου υπο-σώματος ως εξωτερικό φορτίο.

2.2. Εργαλείο ανάλυσης διατομών

Για τις ανάγκες της διατριβής αναπτύχθηκε ένα ολοκληρωμένο εργαλείο ανάλυσης διατομών. Βασίζεται στη θεωρία της λεπτό-τοιχης πολυ-στρωματοποιημένης διατομής [33],[34] και χρησιμοποιείται για τον υπολογισμό των μητρώων μάζας και δυσκαμψίας κάθε διατομής του πτερυγίου. Πρόκειται για αναβάθμιση υφιστάμενου κώδικα, που έχει αναπτυχθεί από κοινού μεταξύ του εργαστηρίου αεροδυναμικής-Ε.Μ.Π. και του Πανεπιστημίου Πατρών. Στην παρούσα εκδοχή, ο κώδικας είναι σε θέση να μοντελοποιήσει με μεγαλύτερη ακρίβεια τη γεωμετρία κάθε διατομής (δημιουργώντας δομικό πλέγμα), να λάβει υπόψη την εξωτερική γεωμετρία της διατομής (μέσω των συντελεστών Timoshenko) και να συμπεριλάβει μέχρι τρεις ιστούς (webs). Το ίδιο εργαλείο, μπορεί να πραγματοποιήσει ανάλυση τάσεων και να αξιολογήσει την αντοχή κάθε υλικού μέσω του κριτηρίου Tsai-Hill, υπό την επίδραση των εσωτερικών φορτίων της διατομής. Στο παράρτημα Β, παρουσιάζεται αναλυτικά η προσέγγιση που έχει υιοθετηθεί απ’το εργαλείο αυτό.

2.2.1. Πολυ-στρωματοποιημένη θεωρία

Τα πτερύγια των σύγχρονων ανεμογεννητριών, κατασκευάζονται από στρώσεις σύνθετων υλικών τα οποία σχηματίζουν δομή λεπτό-τοιχου κελύφους (βλέπε Σχ. 2.5). Κάθε πολυ-στρωματικό υλικό αποτελείται από ένα σύνολο στρωμάτων (π.χ. TRIAX, BIAx, UNIAx και BALSa), όπως φαίνεται στο Σχ. 2.4. Επιπλέον, κάθε διατομή αποτελείται από ένα πλήθος κελιών - ανάλογα με τον αριθμό των ιστών (webs). Για παράδειγμα, στη διατομή που παρουσιάζεται στο Σχ. 2.5, οι τρεις ιστοί ορίζουν συνολικά τέσσερα κελιά (κλειστοί βρόχοι). Κάθε κελί, σχηματίζεται από ένα σύνολο τμηματικών στοιχείων του εξωτερικού φλοιού της διατομής και των ιστών της. Έστω ότι με τους δείκτες i , j και k δηλώνονται το κελί, το στοιχείο και η στρώση υλικού – ενώ με N_{cell} , N_{el} και N_{layer} δηλώνεται το συνολικό πλήθος των κελιών, των στοιχείων και των στρώσεων, αντίστοιχα. Επίσης, ορίζονται τρία συστήματα συντεταγμένων (c.s.): i) το c.s. των στρώσεων των υλικών $x_L y_L z_L$ (x_L εκφράζει την κατεύθυνση της ίνας), ii) το c.s. της συστοιχίας/στοιχείου xyz και iii) το c.s. της διατομής XYZ , όπως φαίνεται στο Σχ. 2.5.



Σχήμα 2.4: Τυπική διάταξη στρωμάτων υλικού, **Σχήμα 2.5:** Ορισμός των περιοχών διατομής μιας σύνθετης συστοιχίας, από το λεπτό-τοιχο πτερυγίου ανεμογεννήτριας DTU-10MW RWT. κέλυφος της διατομής πτερυγίου.

Για κάθε υλικό, ο νόμος του Hooke, μπορεί να εκφραστεί σε σχέση με το σύστημα συντεταγμένων $x_L y_L z_L$, στη μορφή:

$$\boldsymbol{\sigma} = \mathbf{q}_L \cdot \boldsymbol{\varepsilon} = \begin{bmatrix} E_{11} & 0 & 0 \\ 0 & G_{13} & 0 \\ 0 & 0 & G_{12} \end{bmatrix} \cdot \boldsymbol{\varepsilon} \quad (2.8)$$

Στην πιο πάνω εξίσωση, το \mathbf{q}_L εκφράζει το μητρώο τοπικής δυσκαμψίας, $\boldsymbol{\varepsilon}$ είναι το διάνυσμα παραμορφώσεων, $\boldsymbol{\sigma}$ το διάνυσμα τάσεων, E_{11} το μέτρο ελαστικότητας κατά μήκος της ίνας, ενώ G_{13} και G_{12} είναι το μέτρο διάτμησης των δύο κατευθύνσεων.

Για τον προσδιορισμό των ιδιοτήτων δυσκαμψίας σε σχέση με το τοπικό σύστημα συντεταγμένων xyz , απαιτείται ο υπολογισμός του στραμμένου κατά γωνία θ μητρώου \mathbf{q}_c (για περισσότερες λεπτομερείς, βλέπε [34]). Με ολοκλήρωση των τοπικών ιδιοτήτων δυσκαμψίας, σε κάθε επιφάνεια του κέλυφους ή των ιστών, προκύπτουν τα 3×3 μητρώα δυσκαμψίας \mathbf{A}^j , \mathbf{D}^j και \mathbf{B}^j , για το j^{th} στοιχείο:

$$\mathbf{A}^j = \sum_{k=1}^{N_{layer}} \mathbf{q}_{ek} h_k \quad \mathbf{B}^j = \sum_{k=1}^{N_{layer}} \mathbf{q}_{ck} h_k \bar{\tau}_k \quad \mathbf{D}^j = \sum_{k=1}^{N_{layer}} \mathbf{q}_{ck} h_k \left(\frac{h_k^2}{12} + \bar{\tau}_k^2 \right) \quad (2.9)$$

Στην Εξ. 2.9, h_k είναι το πάχος της k^{th} στρώσης - ενώ η απόσταση της από τη μέση γραμμή του πάχους του στοιχείου (βλέπε Σχ. 2.4), δίνεται από:

$$\bar{\tau}_k = \begin{cases} \frac{h_k - H}{2} & , \text{για } k = 1 \\ \bar{\tau}_{k-1} + \frac{h_{k-1} + h_k}{2} & , \text{για } k = 2, 3, \dots, N_{layer} \end{cases} \quad (2.10)$$

όπου με H δηλώνεται το συνολικό πάχος του στοιχείου.

Με την ολοκλήρωση των ιδιοτήτων δυσκαμψίας του πολυ-στρωματικού στοιχείου της Εξ. 2.9, κατά μήκος του κελύφους και των ιστών της διατομής, λαμβάνεται το μητρώο δυσκαμψίας \mathbf{K} , που συνδυάζει τις δυνάμεις και τις ροπές \mathbf{F} , \mathbf{M} με τις συνολικές παραμορφώσεις και στροφές $\boldsymbol{\varepsilon}$, $\boldsymbol{\kappa}$, σε σχέση με το καθολικό σύστημα συντεταγμένων XYZ:

$$\begin{Bmatrix} \mathbf{F} \\ \mathbf{M} \end{Bmatrix} = \mathbf{K} \begin{Bmatrix} \boldsymbol{\varepsilon} \\ \boldsymbol{\kappa} \end{Bmatrix} \Rightarrow \begin{Bmatrix} F_x \\ F_y \\ F_z \\ M_x \\ M_y \\ M_z \end{Bmatrix} = \begin{bmatrix} K_{11}^A & K_{12}^A & K_{13}^A & K_{11}^B & K_{12}^B & K_{13}^B \\ & K_{22}^A & K_{23}^A & K_{21}^B & K_{22}^B & K_{23}^B \\ & & K_{33}^A & K_{31}^B & K_{32}^B & K_{33}^B \\ & & & K_{11}^D & K_{12}^D & K_{13}^D \\ & sym. & & & K_{22}^D & K_{23}^D \\ & & & & & K_{33}^D \end{bmatrix} \begin{Bmatrix} \varepsilon_x \\ \varepsilon_y \\ \varepsilon_z \\ \kappa_x \\ \kappa_y \\ \kappa_z \end{Bmatrix} \quad (2.11)$$

Ενδεικτικές εκφράσεις για τους όρους κάμψης και στρέψης του μητρώου δυσκαμψίας, παρατίθενται στη συνέχεια:

$$\begin{aligned} K_{11}^D &= EI_{xx} = \sum_{j=1}^{N_{el}} \ell_j (A_{11}^j Z_j^2 - 2B_{11}^j Z_j \cos \theta_j + D_{11}^j X_j^2) \\ K_{12}^D &= EI_{xy} = x_{sc} K_{14} - z_{sc} K_{34} + \sum_{j=1}^{N_{el}} \ell_j (-A_{13}^j A h^j Z_j + B_{13}^j (A h^j \cos \theta_j - 2Z_j) + 2D_{13}^j \cos \theta_j) \\ K_{13}^D &= EI_{xz} = \sum_{j=1}^{N_{el}} \ell_j (A_{11}^j X_j Z_j + B_{11}^j (Z_j \sin \theta_j - X_j \cos \theta_j) - D_{11}^j \sin \theta_j \cos \theta_j) \\ K_{22}^D &= GJ = z_{sc} G_x A_x + x_{sc} G_z A_z + \sum_{j=1}^{N_{el}} \ell_j (A_{33}^j (A h^j)^2 + 4B_{33}^j A h^j + 4D_{33}^j) \end{aligned} \quad (2.12)$$

όπου x_{sc} και z_{sc} δηλώνουν τη θέση του κέντρου διάτμησης ως προς τη διατομή.

2.2.2. Ανάλυση τάσεων

Τέλος, με αντιστροφή της Εξ. 2.11 και με δεδομένο ένα σύνολο εσωτερικών φορτίων $\{\mathbf{F} \quad \mathbf{M}\}^T$, μπορεί να γίνει μια εκτίμηση των ελαστικών παραμορφώσεων και καμπυλοτήτων $\{\boldsymbol{\varepsilon} \quad \boldsymbol{\kappa}\}^T$ της διατομής. Ακολούθως, οι ορθές (σ_n) και διατμητικές (σ_s) τάσεις που αναπτύσσονται πάνω σε κάθε υλικό της διατομής, μπορούν να υπολογιστούν με εφαρμογή του νόμου του Hook. Οι δυο τάσεις, ενοποιούνται και συσχετίζονται με την αντοχή του υλικού (S_1 -διαμήκης αντοχή και S_2 -αντοχή διάτμησης) μέσω του κριτηρίου αστοχίας Tsai-Hill [35], υιοθετώντας ένα συντελεστή ασφαλείας υλικών $\gamma_m = 1.2$. Σημειώνεται ότι η αστοχία του υλικού εμφανίζεται για τιμές κριτηρίου > 1 , ενώ η μαθηματική του έκφραση δίνεται από τη σχέση:

$$f_{T/H} = \frac{\sigma_n^2}{S_1^2} - \frac{|\sigma_n \sigma_s|}{S_1^2} + \frac{\sigma_s^2}{S_2^2} \quad (2.13)$$

2.3. Κοστολόγηση ενέργειας

Στην ενότητα αυτή, περιγράφεται ένα πλήρες μοντέλο κόστους ανεμογεννήτριας. Η ανάλυση περιλαμβάνει μια σύγχρονη και λεπτομερή προσέγγιση για τα πτερύγια, ενώ απλούστερες μαθηματικές εκφράσεις χρησιμοποιούνται για τις επιμέρους συνιστώσες της ανεμογεννήτριας (π.χ. πύργος, κιβώτιο ταχυτήτων και γεννήτρια). Τέλος, παρουσιάζεται ο υπολογισμός του κόστους παραγόμενης ενέργειας LCoE, σε δολάρια ΗΠΑ του 2019.

2.3.1. Μοντέλο κόστους ανεμογεννήτριας

Η βιβλιογραφία έχει προτείνει τρία μοντέλα κόστους, για ανεμογεννήτριες. Το απλούστερο έχει προταθεί απ'το Wind Energy Handbook [36] και χρησιμοποιεί απλές μαθηματικές εκφράσεις για την αναγωγή με βάση μια ανεμογεννήτρια αναφοράς. Το δεύτερο μοντέλο, έχει αναπτυχθεί απ'το NREL [37] το 2006 (εφεξής NREL-2006) και προσεγγίζει το κόστος των διαφόρων τμημάτων της ανεμογεννήτριας μέσω ημι-εμπειρικών εκθετικών εκφράσεων με βάση την ακτίνα του δρομέα. Τέλος, λόγω της πολυπλοκότητας κατασκευής των πτερυγίων, μια παραλλαγή της διαδικασίας κοστολόγησης που έχει περιγραφεί το 2019 απ'το NREL [38] (εφεξής NREL-2019), έχει ενσωματωθεί στην παρούσα ενότητα.

2.3.1.1. Κόστος πύργου, κιβωτίου ταχυτήτων και γεννήτριας

Το 2011, το Wind Energy Handbook πρότεινε την κοστολόγηση μιας ανεμογεννήτριας με βάση μια μηχανή αναφοράς (η οποία συμβολίζεται με *ref*). Στην παρούσα εργασία, η προσέγγιση αυτή έχει υιοθετηθεί για τα πιο ογκώδη τμήματα της ανεμογεννήτριας, δηλαδή τον πύργο, το κιβώτιο ταχυτήτων και τη γεννήτρια. Στη συνέχεια παρατίθενται οι μαθηματικές εκφράσεις:

$$Tower = Tower^{ref} \left[0.90 \times \left(\frac{R_{tip}}{R_{tip}^{ref}} \right)^{\gamma_{s-u}} + 0.10 \right] \quad (2.14)$$

$$Gearbox = Gearbox^{ref} \frac{P\Omega^{ref}}{P^{ref}\Omega} \quad (2.15)$$

$$Generator = Generator^{ref} \frac{P\Omega^{ref}}{P^{ref}\Omega} \quad (2.16)$$

όπου, P και Ω δηλώνεται η ονομαστική ισχύς και περιστροφή της μηχανής, ενώ ο εκθέτης παίρνει την τιμή $\gamma_{s-u} = 2.16$. Επίσης, ως ανεμογεννήτρια αναφοράς θεωρείται η μηχανή που περιγράφεται στον Πίνακα 2.1.

Πίνακας 2.1: Βασικές παράμετροι ανεμογεννήτριας αναφοράς.

<i>Parameters</i>	
Rated power	1.5MW
Rated omega	20.5rpm
Radius	35m
Hub height	65m
<i>Cost of components [in 2019 USA \$]</i>	
Rotor	336540
Tower	208740
Gearbox	217260
Generator	139160

2.3.1.2. Κόστος εργατικών, πλήμνης, μηχανισμού βήματος και επιταχυνσιομέτρου

Μια εναλλακτική προσέγγιση έχει προταθεί από το NREL-2006. Σε αυτή, το κόστος ενός πτερυγίου είναι ανάλογο του μήκους του υψωμένο στον κύβο. Στην παρούσα εργασία, η πιο πάνω προσέγγιση έχει υιοθετηθεί για το κόστος των εργατικών, με τον εκθέτη να παίρνει την τιμή $\gamma_{L\&O} = 2.52$.

$$Labor \ \& \ Others = 3.898 \times R_{tip}^{\gamma_{L\&O}} \quad (2.17)$$

Το μοντέλο αυτό (NREL-2006), παρέχει και μαθηματικές εκφράσεις και για τις επιμέρους συνιστώσες του δρομέα: πλήμνη, μηχανισμός βήματος και αεροδυναμική διαμόρφωση πλήμνης.

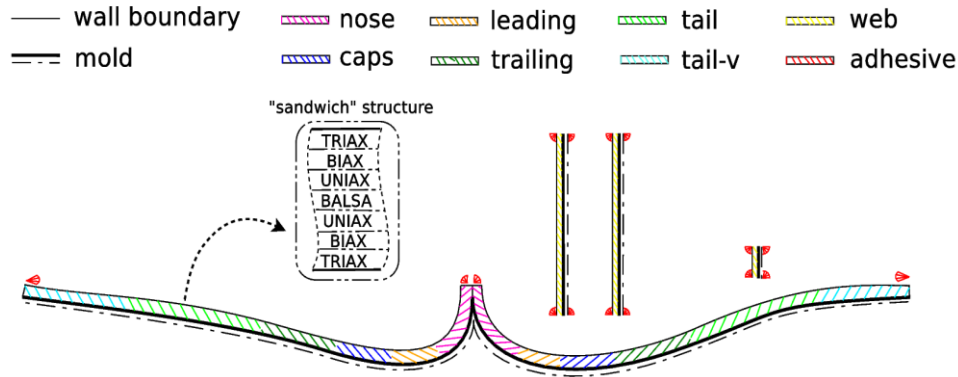
$$hub = 5.757 \times Blade \ Mass + 34280.61 \quad (2.18)$$

$$pitch \ mechanism = 4.303 \times R_{tip}^{2.658} \quad (2.19)$$

$$spinner = 292.65 \times R_{tip} - 4116.84 \quad (2.20)$$

2.3.1.3. Κόστος κατασκευής πτερυγίου

Η πολύπλοκη δομή των σύγχρονων πτερυγίων, οδήγησε το NREL το 2019 στην ανάπτυξη ενός λεπτομερούς μοντέλου κοστολόγησης πτερυγίων ανεμογεννητριών. Στο μοντέλο αυτό, εκτός από το κόστος των υλικών κατασκευής, γίνεται μια εκτίμηση των εργατο-ωρών που απαιτούνται, το κόστος κατασκευής καλουπιών κ.λπ. Εν πολλοίς, στην παρούσα εργασία έχει υιοθετηθεί η πιο πάνω προσέγγιση. Η παραλλαγή αυτή, περιλαμβάνει την ομαδοποίηση των αναλώσιμων σε τρεις κατηγορίες καθώς και απλοποιήσεις διαφόρων εκτιμήσεων και παραδοχών, όπως για παράδειγμα η διάκριση των κολλών που προορίζονται για το κέλυφος και τους ιστούς.



Σχήμα 2.6: Η βιομηχανική κατασκευή των σύγχρονων πτερυγίων βασίζεται στη μοντελοποίηση VARTM και περιλαμβάνει την τοποθέτηση στρώσεων υαλονημάτων με μείγμα ρητίνης και κόλλας σε καλούπια.

Τα πτερύγια των σύγχρονων ανεμογεννητριών αποτελούνται από διατομές λεπτών τοιχωμάτων, δύο ή τριών κελιών, βλέπε Σχ. 2.6. Το κέλυφος των πτερυγίων αποτελείται από δομή τύπου “σάντουιτς”, με τα TRIAX, BIAx και UNIAx να τοποθετούνται εκατέρωθεν ενός πυρήνα BALSa. Έτσι, η εκτίμηση της μάζας/κόστους των υλικών είναι εύκολη υπόθεση, αρκεί να είναι γνωστή η δομή του πτερυγίου. Ωστόσο, η κατασκευή του πτερυγίου περιλαμβάνει ένα καλούπι, ο όγκος του οποίου θεωρείται ότι είναι ίσος με το άθροισμα του όγκου των πρωτογενών υλικών πολλαπλασιασμένο επί ένα μείον το κλάσμα όγκου κάθε υλικού:

$$V_{matrix} = V_{fiberglass} \times (1 - F_{FV}) \quad (2.21)$$

Με βάση το σκίτσο του Σχ. 2.6, φαίνονται τα σημεία όπου εφαρμόζεται η κόλλα. Έτσι, λαμβάνεται μια 2D επιφάνεια $70mm \times 7mm$, πραγματοποιώντας με τον τρόπο αυτό μια εκτίμηση του κόστους της κόλλας, που απαιτείται για την κατασκευή. Το σύστημα αντικεραυνικής προστασίας είναι υποχρεωτικό και θεωρείται ότι κοστίζει $40 \$/m$. Επιπλέον, το μοντέλο αυτό υποθέτει ότι ένα ζεύγος μπουλόνια-παξιμάδια, κόστους 37% το κάθε ένα – τοποθετούνται ανά $\sim 15cm$ της περιμέτρου της ρίζας του πτερυγίου. Τέλος, ένα σύνολο από αναλώσιμα υλικά χρησιμοποιούνται για την κατασκευή του πτερυγίου. Στον Πίνακα 2.2, ο αναγνώστης θα βρει τις μαθηματικές εκφράσεις για καθένα απ’αυτά.

Το μοντέλο αυτό έχει συγκριθεί με το NREL-2019 και βιβλιογραφικές αναφορές (βλέπε Αγγλικό κείμενο της διατριβής), αποδεικνύοντας την υψηλή πιστότητα του μοντέλου, παρά τις όποιες απλουστεύσεις. Ωστόσο, κανένα μοντέλο δεν είναι σε θέση να παρέχει μια εκτίμηση του επιπλέον κόστους που προκύπτει απ’την εφαρμογή τεχνικών παθητικού ελέγχου. Για παράδειγμα, δεν μπορεί να υπολογιστεί το κόστος της τοποθέτησης του μονο-κατευθυντήριου υλικού υπό γωνία, ούτε το κόστος κατασκευής κυρτών πτερυγίων.

Πίνακας 2.2: Κοστολόγηση αναλώσιμων υλικών.

<u>αναλώσιμα</u>	<u>μαθηματική σχέση</u>	<u>ενδεικτικές τιμές</u>
	Proportional to R_{tip}	
Nonsand tape	$\frac{9 * Roll\ Width * R_{tip} * Unit\ Cost}{1 - waste}$	Roll Width = 0.127m Unit Cost = 1.67 \$/m ² waste = 10%
Chopped strand	$\frac{R_{tip} * Mass/Unit\ Length * Unit\ Cost}{1 - waste}$	Mas/Unit Length = 0.037 kg/m Unit Cost = 2.16 \$/kg waste = 5%
Tubing	$\frac{Length/Blade\ Length * R_{tip} * Unit\ Cost}{1 - waste}$	Length/Blade Length = 5 m/m Unit Cost = 0.23 \$/m waste = 5%
Tacky tape	$\frac{10 * R_{tip} * Roll\ Cost}{Roll\ Length * (1 - waste)}$	Roll Cost = 21.22 \$/roll Roll Length = 3.5m waste = 5%
Masking tape	$\frac{R_{tip} * Roll/Length * Roll\ Cost}{1 - waste}$	Roll/Length = 0.328m Roll Cost = 5.50 \$/roll waste = 10%
	Proportional to A_{molds}	
Peel ply	$\frac{A_{molds} * Unit\ Cost}{1 - waste}$	Unit Cost = 1.94 \$/m ² waste = 15%
Tackifier adhesive	$\frac{V.\ Bulk/Area * A_{molds} * Unit\ Cost}{1 - waste}$	V. Bulk/Area = $3.1 \times 10^{-5} m^3/m^2$ Unit Cost = 6762.8 \$/m ³ waste = 5%
Release agent	$\frac{V./Area * A_{molds} * Unit\ Cost}{1 - waste}$	V./Area = $2.57 \times 10^{-5} m^3/m^2$ Unit Cost = 15691.82 \$/m ³ waste = 5%
Flow medium	$\frac{0.70 * A_{molds} * Unit\ Cost}{1 - waste}$	Unit Cost = 0.646 \$/m ² waste = 15%
	Proportional to A_{out}	
Chop fibers	$\frac{Mass/Area * A_{out} * Unit\ Cost}{1 - waste}$	Mass/Area = 0.00976 kg/m ² Unit Cost = 6.19 \$/kg waste = 10%
White lightning	$\frac{V./Area * A_{out} * Unit\ Cost}{1 - waste}$	V./Area = $2.04 \times 10^{-5} m^3/m^2$ Unit Cost = 3006.28 \$/m ³ waste = 10%
Hardener	$\frac{Tubes/Area * A_{out} * Unit\ Cost}{1 - waste}$	Tubes/Area = 0.012 #/m ² Unit Cost = 1.65 \$/tube waste = 10%
Putty	$\frac{Mass/Area * A_{out} * Unit\ Cost}{1 - waste}$	Mass/Area = 0.0244 kg/m ² Unit Cost = 6.00 \$/kg waste = 10%
Putty catalyst	$\frac{Mass/Area * A_{out} * Unit\ Cost}{1 - waste}$	Mass/Area = 0.00488 kg/m ² Unit Cost = 7.89 \$/kg waste = 10%

2.3.2. Εκτίμηση LCoE

Σύμφωνα με το [39], το LCoE μπορεί να υπολογιστεί από τη σχέση:

$$LCoE = \frac{\overbrace{(ICC + BoP)}^{CAPEX} \frac{i}{1 - (1 + i)^{-N}} + OPEX}{AEP} \quad (2.21)$$

όπου το ICC δηλώνει το κεφαλαιουχικό κόστος με βάση το μοντέλο που προηγήθηκε, BoP στην εργασία αυτή λήφθηκε ίσο με $281\$/kW$, OPEX συνήθως εκτιμάται στο 5% του αρχικού κεφαλαιουχικού κόστους και το AEP μπορεί να υπολογιστεί μέσω αερο-ελαστικών προσομοιώσεων. Οι σύγχρονες ανεμογεννήτριες, σχεδιάζονται για $N = 20$ χρόνια και για ένα τυπικό επιτόκιο $i = 6\%$.

2.4. Μέθοδοι βελτιστοποίησης

Στην ενότητα αυτή, γίνεται μια σύντομη περιγραφή των πιο δημοφιλών πακέτων βελτιστοποίησης. Συγκεκριμένα, περιγράφονται: (i) COBYLA, (ii) SLSQP και (iii) Newton (μαζί με τη σχεδόν-Newton, BFGS). Οι δυο πρώτες μέθοδοι, είναι ελεύθερα διαθέσιμες από τη βιβλιοθήκη SciPy της Python [40], ενώ η τελευταία απαιτεί τον προγραμματισμό της.

2.4.1. Μέθοδος COBYLA

Πρόκειται για τον Constrained Optimization By Linear Approximation (COBYLA) [41],[42] που παρέχει τη δυνατότητα εύρεσης της ελάχιστης τιμής μιας αντικειμενικής συνάρτησης $F_{aim}(\vec{b})$, $\vec{b} \in R^n$ χωρίς να απαιτείται ο υπολογισμός των παραγώγων της, ενώ ταυτόχρονα επιδέχεται μη-γραμμικούς περιορισμούς της μορφής $C_i(\vec{b}) \geq 0$, $i = 1, 2, \dots, m$. Ο αλγόριθμος σχηματίζει γραμμικές πολυωνυμικές προσεγγίσεις των τιμών της συνάρτησης $F_{aim}(\vec{b})$ και των συναρτήσεων $C_i(\vec{b})$ με παρεμβολή μεταξύ των κορυφών ενός χωρίου simplex. Με τον όρο simplex n διαστάσεων περιγράφεται ένα κυρτό περίβλημα $n + 1$ σημείων, όπου n ο αριθμός των μεταβλητών της αντικειμενικής συνάρτησης. Ο αλγόριθμος απαιτεί οι τιμές της συνάρτησης $F_{aim}(\vec{b})$ να μπορούν να υπολογιστούν σε κάθε κορυφή \vec{b}^j , $j = 0, 1, \dots, n$ ενός μη εκφυλισμένου simplex διάστασης n . Αυτό επιτρέπει την εύρεση μοναδικών γραμμικών συναρτήσεων \hat{F} και \hat{C}_i , $i = 1, \dots, m$ που παρεμβάλλονται στην αντικειμενική συνάρτηση και τους περιορισμούς στις $n + 1$ κορυφές. Το πρόβλημα εύρεσης της ελάχιστης τιμής προσεγγίζεται έτσι με ένα πρόβλημα γραμμικού προγραμματισμού της μορφής:

$$\begin{aligned} \min_{\vec{b} \in R^n} F_{aim}(\vec{b}) \\ s. t.: \quad C_i(\vec{b}) \geq 0, i = 1, 2, \dots, m \end{aligned} \quad (2.22)$$

2.4.2. Μέθοδος SLSQP

Η αντιμετώπιση προβλημάτων βελτιστοποίησης με μεγάλο αριθμό παραμέτρων και η ανάγκη συμπίεσης του υπολογιστικού κόστους, καθιστά απαραίτητη τη χρήση τεχνικών που στηρίζονται στο διάνυσμα της κλίσης. Τέτοιες μέθοδοι έχουν αποδειχθεί στην πράξη πως εξασφαλίζουν τη σταθερότητα και οδηγούν σε συντομότερο χρονικό διάστημα στη βέλτιστη λύση. Η σχετική βιβλιοθήκη της Python, παρέχει μια εξαιρετικά δημοφιλή τεχνική, τη Sequential Least Squares Programming (SLSQP) που έχει προταθεί αρχικά από τον Dieter Kraft το 1963 [43]. Η μέθοδος αυτή, ελαχιστοποιεί μια συνάρτηση πολλών μεταβλητών με οποιονδήποτε συνδυασμό ορίων, περιορισμών ισότητας ή/και ανισότητας. Έτσι, το πρόβλημα μη-γραμμικής βελτιστοποίησης, έχει τη γενική μορφή:

$$\begin{aligned} \min_{\vec{b} \in \mathbb{R}^n} F_{aim}(\vec{b}) & \quad (2.23) \\ \text{s. t.}: \quad G_j(\vec{b}) = 0, j = 1, 2, \dots, k \\ G_j(\vec{b}) \geq 0, j = k + 1, \dots, m \\ \vec{b}_i^{lower} \leq \vec{b}_i \leq \vec{b}_i^{upper}, i = 1, 2, \dots, n \end{aligned}$$

όπου \vec{b} αποτελεί το διάνυσμα (μεγέθους n) των μεταβλητών βελτιστοποίησης, m είναι το πλήθος των περιορισμών ανισότητας και k είναι το πλήθος των περιορισμών ισότητας.

2.4.3. Μέθοδος Newton και σχεδόν-Newton

Η παραδοσιακή μέθοδος Newton, στηρίζεται στην ιδέα ότι το ακρότατο σημείο μιας εξίσωσης (ελάχιστο, μέγιστο, σημείο καμπής), χαρακτηρίζεται από μηδενική τιμή στην πρώτη παράγωγο. Συνεπώς, ως υποθέσουμε την προσέγγιση μιας συνάρτησης με την τετραγωνική συνάρτηση της μορφής:

$$F_{aim}(\vec{b}) = \frac{1}{2} \vec{b}^T A \vec{b} + B^T \vec{b} + a \quad (2.24)$$

Η προσέγγιση της μέσω της σειράς Taylor, έχει τη μορφή:

$$F_{aim}(\vec{b}) \cong F_{aim}(\vec{b}_*) + \nabla F_{aim}(\vec{b}_*)(\vec{b} - \vec{b}_*) + \frac{1}{2} (\vec{b} - \vec{b}_*)^T \nabla^2 F_{aim}(\vec{b}_*)(\vec{b} - \vec{b}_*) + \dots \quad (2.25)$$

όπου ο δείκτης "*" δηλώνει το σημείο αναφοράς και χωρίς δείκτη υποδεικνύεται ένα γειτονικό σημείο. Έτσι, η δεύτερη παράγωγος έχει τη μορφή:

$$\nabla F_{aim}(\vec{b}) \cong \nabla F_{aim}(\vec{b}_*) + \nabla^2 F_{aim}(\vec{b}_*)(\vec{b} - \vec{b}_*) \Rightarrow \vec{b} = \vec{b}_* - [\nabla^2 F_{aim}(\vec{b}_*)]^{-1} \nabla F_{aim}(\vec{b}_*) \quad (2.26)$$

Στην περίπτωση που η συνάρτηση είναι τετραγωνικής μορφής, απαιτείται ένα μόνο βήμα για την εύρεση της λύσης. Σε διαφορετική περίπτωση, απαιτούνται επαναλήψεις μέσω της αναδρομικής σχέσης:

$$\vec{b}_k = \vec{b}_k - \eta_k \underbrace{[\nabla^2 F_{aim}(\vec{b}_k)]^{-1}}_{\vec{p}} \nabla F_{aim}(\vec{b}_k) \quad (2.27)$$

όπου ο δείκτης “ k ” δηλώνει τον αριθμό της επανάληψης και το διάνυσμα \vec{p} καλείται “κατεύθυνση”.

Γενικά η μέθοδος Newton, θεωρείται μια παραδοσιακή τεχνική βελτιστοποίησης που σπάνια χρησιμοποιείται στις μέρες μας, λόγω του υψηλού υπολογιστικού κόστους εκτίμησης του Εσσιανού μητρώου (δηλαδή της ποσότητας $\nabla^2 F_{aim}(\vec{b}_k)$). Η βιβλιογραφία έχει προτείνει κατά καιρούς, πολλές εναλλακτικές προσεγγίσεις. Μια πολύ δημοφιλής παραλλαγή της μεθόδου Newton, είναι η τεχνική Broyden-Fletcher-Goldfarb-Shanno (BFGS) που προτάθηκε το 1970 [44-47]. Σύμφωνα με αυτή, ο υπολογισμός του Εσσιανού μητρώου (για απλότητα συμβολίζεται \hat{H}_{k+1}), υπολογίζεται με βάση το μητρώο του προηγούμενου βήματος μέσω της αναδρομικής σχέσης:

$$\hat{H}_{k+1} = \hat{H}_k - \frac{\hat{H}_k \vec{s}_k \vec{s}_k^T \hat{H}_k}{\vec{s}_k^T \hat{H}_k \vec{s}_k} + \frac{\vec{y}_k \vec{y}_k^T}{\vec{y}_k^T \vec{s}_k} \quad (2.28)$$

$$s. t.: \quad \vec{s}_k^T \vec{y}_k > 0$$

Η πιο πάνω σχέση, απαιτεί μια αρχική εκτίμηση του Εσσιανού μητρώου κατά το σημείο εκκίνησης. Αυτό μπορεί να γίνει, είτε με τον υπολογισμό του στο πρώτο βήμα της διαδικασίας βελτιστοποίησης (εάν είναι εύκολο κάτι τέτοιο) είτε πολλές φορές χρησιμοποιείται οποιοσδήποτε θετικά ορισμένος πίνακας (π.χ. ο μοναδιαίος).

2.5. Περιβάλλον βελτιστοποίησης

Ελαχιστοποίηση της συνάρτησης $f(\{v_S, v_A\}, \{c_S, c_A\})$ με μεταβλητές σχεδιασμού v_S, v_A και σταθερές παραμέτρους c_S, c_A , με τους γεωμετρικούς περιορισμούς:

$$g_A(v_A) \leq 0, g_S(v_S) \leq 0, g_{W/T}(v_A, v_S) \leq 0 \quad (2.74)$$

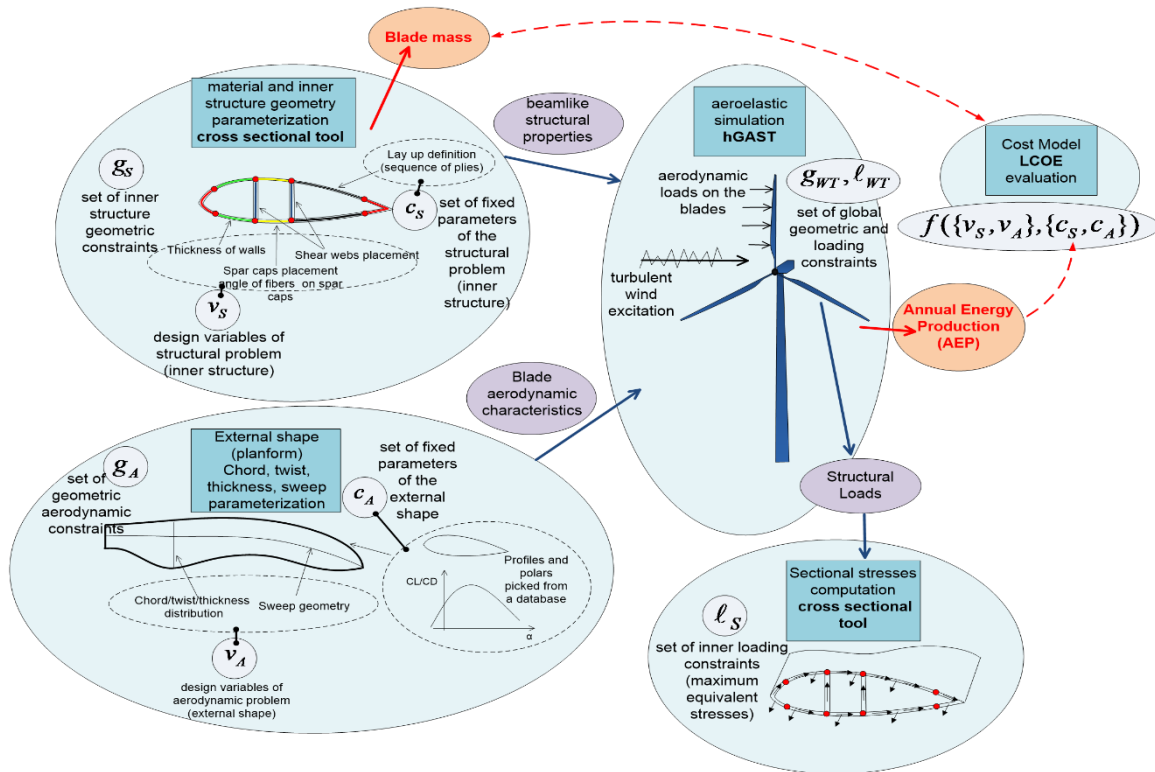
και τους περιορισμούς φορτίων:

$$l_S(v_A, v_S) \leq 0, l_{W/T}(v_A, v_S) \leq 0 \quad (2.75)$$

όπου με τον δείκτη A δηλώνονται οι αεροδυναμικές παράμετροι και με S οι κατασκευαστικές παράμετροι. Η αντικειμενική συνάρτηση f μπορεί να είναι είτε η συνολική μάζα της ανεμογεννήτριας, είτε το LCoE.

Η διαδικασία, περιλαμβάνει ένα σύνολο υπολογιστικών εργαλείων που έχουν παρουσιαστεί στο κεφάλαιο αυτό. Η ανάλυση της εσωτερικής δομής των πτερυγίων, τόσο για τον καθορισμό των μηχανικών ιδιοτήτων κάθε διατομής που συνθέτει το πτερύγιο της ανεμογεννήτριας (μητρώα μάζας και δυσκαμψίας) όσο και η ανάλυση των τάσεων (μέσω του κριτηρίου Tsai-Hill), πραγματοποιείται με το εργαλείο ανάλυσης διατομών. Η αερο-ελαστική προσομοίωση της μηχανής για την εκτίμηση των φορτίων που αναπτύσσονται σε διάφορες συνθήκες λειτουργίας, πραγματοποιείται με χρήση του επιλύτη hGAST, ενώ η κοστολόγηση της μηχανής πραγματοποιείται με το μοντέλο που έχει περιγραφεί

στην ενότητα 2.3. Τα βασικά χαρακτηριστικά της ανεμογεννήτριας όπως είναι η κατανομή χορδής και συστροφής, προσεγγίζονται με καμπύλες Bezier. Στον πυρήνα της διαδικασίας σχεδιασμού, βρίσκεται μια απ' τις μεθόδους βελτιστοποίησης που συναντήσαμε στην προηγούμενη ενότητα και σκοπός του είναι ο χειρισμός των μεταβλητών σχεδιασμού/βελτιστοποίησης.



Σχήμα 2.7: Διάγραμμα διαδικασίας σχεδιασμού και βελτιστοποίησης.

Αυτή η σελίδα μένει κενή

Κεφάλαιο 3

3. Ελαχιστοποίηση μάζας δρομέα ανεμογεννήτριας 10MW

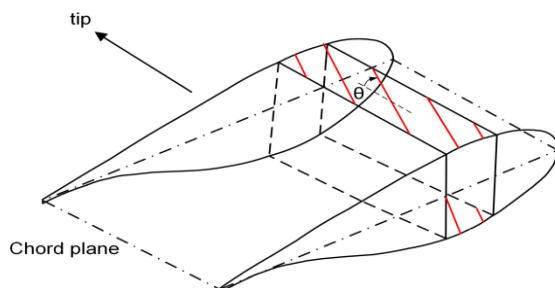
Ο στόχος κατασκευής ανεμογεννητριών πολύ μεγάλης ισχύος ($> 20MW$) και η συμπίεση του κόστους της παραγόμενης από αυτές ενέργειας (Levelized Cost of Electricity - LCoE), σε επίπεδα χαμηλότερα από τις συμβατικές πηγές ενέργειας, μπορεί να επιτευχθεί μόνο μέσω νέων τεχνολογικών ανακαλύψεων και την υιοθέτηση καινοτόμων ιδεών, οι οποίες θα καθιστούν τις ανεμογεννήτριες ελαφρύτερες και φθηνότερες. Τέτοιες καινοτόμες ιδέες, έχουν απασχολήσει τα τελευταία χρόνια την επιστημονική κοινότητα κυρίως μέσω της ανάπτυξης τεχνικών ελέγχου φορτίων. Οι τεχνικές αυτές, διακρίνονται σε δυο κατηγορίες: τον παθητικό και τον ενεργητικό έλεγχο. Σκοπός του κεφαλαίου αυτού, είναι η παρουσίαση τέτοιων τεχνικών με ιδιαίτερη έμφαση στην εφαρμογή παθητικών μεθόδων ελέγχου φορτίων – κάτι που τα τελευταία χρόνια έχει προσελκύσει το ενδιαφέρον του κλάδου της αιολικής ενέργειας. Η εργασία [48] και [49], έχουν αποδείξει πως η εφαρμογή τεχνικών παθητικού ελέγχου μπορεί να μειώσει σημαντικά τα ακραία φορτία που αναπτύσσονται στο πτερύγιο της ανεμογεννήτριας, τόσο κατά τη διάρκεια της λειτουργίας της όσο και κατά τη στάθμευση της (συνθήκες εκτός λειτουργίας). Η παραπάνω μείωση των φορτίων, επιτρέπει τη χρήση λιγότερης μάζας υλικών κατασκευής, περιορίζοντας έτσι την κεφαλαιουχική δαπάνη (CAPital EXpenditure - CAPEX) και κατ'επέκταση το κόστος ενέργειας. Με βάση το περιβάλλον σχεδιασμού και βελτιστοποίησης που περιγράφηκε στο τέλος του προηγούμενου κεφαλαίου, έχει αναπτυχθεί και παρουσιάζεται στη συνέχεια μια ολοκληρωμένη διαδικασία μείωσης του πάχους των τοιχωμάτων των πτερυγίων ανεμογεννήτριας. Τέλος, παρουσιάζονται τρεις εφαρμογές οι οποίες εξετάζουν τα περιθώρια μείωσης της μάζας των πτερυγίων, πετυχαίνοντας μια ελάφρυνση 8 – 10%.

3.1. Ενεργητικός και παθητικός έλεγχος φορτίων

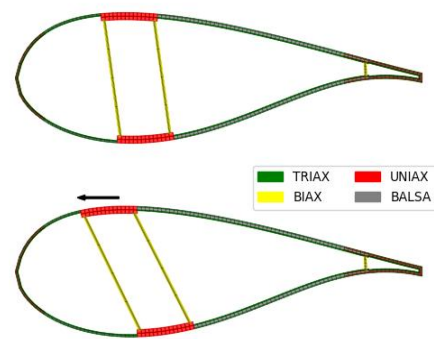
Οι πιο συνηθισμένες τεχνικές ελέγχου φορτίων, βασίζονται στις ενεργητικές μεθόδους. Ενεργητικός έλεγχος μπορεί να πραγματοποιηθεί είτε με τη ρύθμιση του βήματος (Individual Pitching Control - IPC) [10], είτε με χρήση μετα-πτερυγίων (Individual Flap Control – IFC) [50]. Τέτοιες τεχνικές, θεωρούνται πλέον δοκιμασμένες, αφού έχουν ήδη εξεταστεί από διάφορα ερευνητικά προγράμματα και δημοσιεύσεις [11] - ενώ έχουν εφαρμοστεί και σε εμπορικές ανεμογεννήτριες [51].

Απ'την άλλη, οι παθητικές μέθοδοι ελέγχου φορτίων έχουν περιγραφεί απ'την επιστημονική κοινότητα μέσω του όρου “Αερο-ελαστική Διαμόρφωση” (Aero-elastic Tailoring – A/T). Η A/T βασίζεται στην κατάλληλη διαμόρφωση της γεωμετρίας και των κατασκευαστικών/μηχανικών ιδιοτήτων των πτερυγίων, με τρόπο ώστε σε συνδυασμό και υπό την επίδραση της αεροδυναμικής διέγερσης να επιτυγχάνονται μειωμένα φορτία. Το θέμα της A/T και η εφαρμογή της στις νέες μεγάλες ανεμογεννήτριες, στα πλαίσια ενός ολιστικού περιβάλλοντος σχεδιασμού πτερυγίων, είναι ένα ιδιαίτερος επίκαιρο πεδίο της σύγχρονης επιστημονικής έρευνας και για τον λόγο αυτό αποτέλεσε και αποτελεί αντικείμενο πολλών ερευνητικών προγραμμάτων τα τελευταία χρόνια [21],[52] και [53]. Γενικά οι μέθοδοι A/T (BTC ή/και FEC), μπορούν να διακριθούν σε δυο κατηγορίες:

- Βάσει υλικών: μπορεί να επιτευχθεί με την εισαγωγή κατάλληλης γωνίας στην κατεύθυνση του μονο-κατευθυντήριου υλικού που βρίσκεται στην περιοχή των ‘καπακιών’ (βλέπε Σχήμα 3.1), επηρεάζοντας με τον τρόπο αυτό την ανισοτροπία του πτερυγίου.
- Βάσει γεωμετρίας: τόσο το εξωτερικό σχήμα της πτέρυγας όσο και η εσωτερική της γεωμετρία, είναι δυνατό να προσαρμοστούν με τέτοιο τρόπο ώστε να επιτυγχάνονται μειωμένα φορτία και περιορισμένες ταλαντώσεις. Έτσι, έχουν προταθεί πτερύγια ανεμογεννητριών με κατάλληλη κυρτότητα (sweep) και μετατοπισμένα ‘καπάκια’ (βλέπε Σχήμα 3.2).



Σχήμα 3.1: Εισαγωγή στροφής στο μονο-κατευθυντήριο υλικό (UD), που βρίσκεται στα ‘καπάκια’ - BTC.



Σχήμα 3.2: Γεωμετρικό FEC. Στο πάνω μέρος φαίνεται η διατομή αναφοράς, ενώ στο κάτω μέρος η μετατόπιση των ‘καπακιών’.

Ο σχεδιασμός των πτερυγίων μιας ανεμογεννήτριας, καθορίζεται από τα φορτία που προκύπτουν υπό ακραίες συνθήκες ανέμου (Design Loads Cases - DLC), σύμφωνα με το πρότυπο IEC 61400-1 [29]. Η πιο κοινή πηγή τέτοιων φορτίων, είναι οι συνθήκες έντονης τύρβης ανέμου (DLC-1.3), βλέπε Παράρτημα Α του Αγγλικού κειμένου. Σύμφωνα με την υπάρχουσα βιβλιογραφία [53],[54], οι τεχνικές παθητικού ελέγχου τύπου BTC (Bend-Twist-Coupling) είναι αποτελεσματικές για την αντιμετώπιση/ανακούφιση των ακραίων φορτίων που αναπτύσσονται σε τέτοιες συνθήκες. Παρά ταύτα, υπάρχουν και περιπτώσεις όπου τα μέγιστα φορτία παρατηρούνται όταν η μηχανική είναι σταθμισμένη (εκτός λειτουργίας) και σε κατάσταση “ρελαντί” (DLC-6.x). Μελέτες έχουν αποδείξει πως τα μεγαλύτερα φορτία παρατηρούνται σε πλευρικούς ανέμους γωνίας $[-40^\circ, -15^\circ]$ ή $[+15^\circ, +40^\circ]$ [25]. Μια λύση στο πιο πάνω πρόβλημα, είναι η ενίσχυση της απόσβεσης του πτερυγίου μέσω σύζευξης των δυο κατευθύνσεων πτερύγισης και περιστροφής (Flap-Edge-Coupling - FEC) [55].

3.2. Μέθοδος μείωσης μάζας πτερυγίων – εφαρμογή δομικής πολυ-πεδιακής βελτιστοποίησης

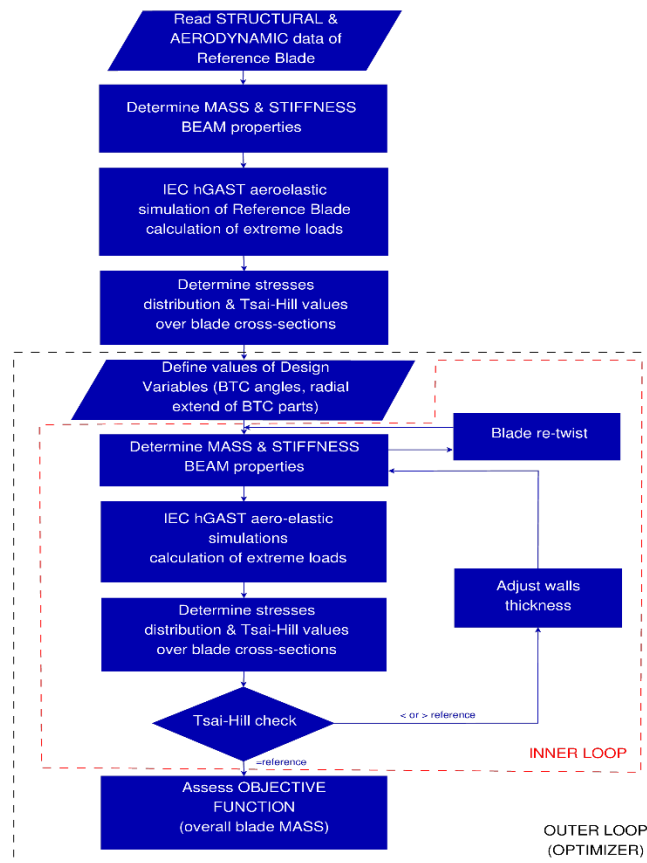
Η διαδικασία μείωσης της μάζας των πτερυγίων ανεμογεννήτριας, περιλαμβάνει δύο βρόχους. Ο διαχωρισμός της διαδικασίας, επιτρέπει τον χειρισμό μικρότερου πλήθους μεταβλητών σχεδιασμού και τη συμπίεση του απαιτούμενου υπολογιστικού κόστους.

- Τον εξωτερικό βρόχο, χειρίζεται ο βελτιστοποιητής και καθορίζει τις βασικές μεταβλητές σχεδιασμού αξιολογώντας τη συνάρτηση κόστους. Στις εφαρμογές που ακολουθούν, κύριες μεταβλητές σχεδιασμού αποτελούν οι γεωμετρικές παράμετροι του BTC (π.χ. οι κατανομή γωνίας του μονο-κατευθυντήριου υλικού), ενώ συνάρτηση κόστους θεωρείται η ποσοστιαία μείωση της μάζας του πτερυγίου, σε σχέση με το πτερύγιο αναφοράς.
- Τον εσωτερικό βρόχο, αποτελεί μια επαναληπτική διαδικασία που καθορίζει τις τιμές των δευτερευουσών μεταβλητών του προβλήματος. Με τον όρο δευτερεύουσες μεταβλητές, εννοούνται οι μεταβλητές που σχετίζονται με την κατανομή του πάχους του πολυ-στρωματικού υλικού, που συνθέτει το τοίχωμα του πτερυγίου της ανεμογεννήτριας. Συγκεκριμένα, ο βρόχος αυτός, αναζητάει τις ελάχιστες τιμές του πάχους για τις οποίες οι μέγιστες τιμές Tsai-Hill είναι στο ίδιο επίπεδο με τις αντίστοιχες τιμές του πτερυγίου αναφοράς. Σημειώνεται, ότι στις εφαρμογές που ακολουθούν έχει υποτεθεί μια ομοιόμορφη αναλογία μείωσης πάχους σε κάθε διατομή του πτερυγίου.

Κάθε βήμα της εσωτερικής διαδικασίας, περιλαμβάνει τα εξής: (i) οι μηχανικές ιδιότητες δοκού του πτερυγίου, προσδιορίζονται με βάση τόσο τις κύριες παραμέτρους σχεδιασμού (π.χ. η διαμόρφωση BTC που αξιολογείται) όσο και από τις δευτερεύουσες παραμέτρους (π.χ. τα πάχη των υλικών), (ii) τα ακραία φορτία προκύπτουν κατόπιν αερο-ελαστικών προσομοιώσεων ενός υπο-συνόλου του φακέλου πιστοποίησης της ανεμογεννήτριας και (iii) οι κατανομές τάσεων και οι τιμές του κριτηρίου αστοχίας Tsai-Hill, αξιολογούνται σε κάθε διατομή του πτερυγίου. Τα βήματα (i) και (iii) πραγματοποιούνται χρησιμοποιώντας το εργαλείο ανάλυσης διατομών, ενώ οι προσομοιώσεις - δηλαδή το βήμα (ii), με τη

χρήση του αερο-ελαστικού επιλύτη hGAST. Με το πέρας κάθε επανάληψης, οι τιμές του κριτηρίου αστοχίας συγκρίνονται με τις αντίστοιχες τιμές του περυγίου αναφοράς και στην περίπτωση σημαντικών διαφορών ξεκινάει μια νέα επανάληψη λαμβάνοντας υπόψη την κατανομή των νέων παχών. Η διαδικασία επαναλαμβάνεται έως ότου επιτευχθεί η σύγκλιση. Αξίζει να σημειωθεί, ότι στα περύγια με οποιαδήποτε διαμόρφωση BTC, είναι απαραίτητος ο επανα-σχεδιασμός της κατανομής συστροφής, ώστε να αποκατασταθούν οι απώλειες ισχύος. Τα πιο πάνω βήματα, περιγράφονται στο διάγραμμα ροής του Σχ. 3.3.

Φυσικά, το πιο χρονοβόρο τμήμα της διαδικασίας αποτελούν οι αερο-ελαστικές προσομοιώσεις στο πεδίο του χρόνου. Στην παρούσα εργασία, τα ακραία φορτία λαμβάνονται με βάση τις δυσμενέστερες συνθήκες που προκύπτουν από τον κανονισμό IEC 61400-1 (άνεμος με έντονη τύρβη DLC-1.3, στα 13 m/s), βλέπε [54] και [53]. Προκειμένου να μειωθεί ακόμα περισσότερο το υπολογιστικό κόστος, κάθε προσομοίωση διαρκεί περίπου 150sec, χρονικό διάστημα που θεωρείται ότι είναι αρκετό για να συμπεριλάβει τη χρονική στιγμή όπου παρατηρούνται τα ακραία φορτία.



Σχήμα 3.3: Διάγραμμα ροής για την ελαχιστοποίηση της μάζας περυγίου, με διαμόρφωση BTC. Ο εξωτερικός βρόχος, περιλαμβάνει τις κύριες μεταβλητές σχεδιασμού (π.χ. κατανομή της γωνίας του UD υλικού) - ενώ ο εσωτερικός βρόχος καθορίζει την κατανομή του πάχους των τοιχωμάτων, ώστε να διατηρηθούν στα ίδια επίπεδα οι μέγιστες τιμές του κριτηρίου Tsai-Hill, κατά μήκος του περυγίου.

3.3. Εφαρμογές

Η μείωση των φορτίων που προκύπτει ως αποτέλεσμα της εφαρμογής τεχνικών παθητικού ελέγχου φορτίων, επιτρέπει τη μείωση του πάχους των τοιχωμάτων των πτερυγίων της ανεμογεννήτριας. Με βάση τη διαδικασία που έχει περιγραφεί στην ενότητα 3.2, διερευνώνται τα περιθώρια μείωσης της μάζας του πτερυγίου της ανεμογεννήτριας DTU-10MW RWT. Στη συνέχεια, εξετάζονται τρεις περιπτώσεις: i) ο σχεδιασμός κυρτών πτερυγίων (sweep), ii) η τμηματική εισαγωγή γωνίας στο μονο-κατευθυντήριο υλικό των ‘καπακιών’ και iii) η εισαγωγή γωνίας στο μονο-κατευθυντήριο υλικό πτερυγίου που φέρει σταθερό παθητικό έλεγχο σύζευξης κάμψεων πτερυγίωσης και περιστροφής (FEC 3%) – συνδυασμός BTC και FEC.

3.3.1. Μείωση μάζας δρομέα, με τη χρήση κυρτών πτερυγίων

Παρόλο που ένα πτερύγιο λόγω κύρτωσης θα παρουσίαζε μεγαλύτερο μήκος, εντούτοις η ανακούφιση των φορτίων επιτρέπει τη μείωση του πάχους των τοιχωμάτων του, με βάση τη διαδικασία που έχει περιγραφεί στην ενότητα 3.2 και στο Σχ. 3.3. Η δυνατότητα χρήσης τέτοιων, κυρτών πτερυγίων εξετάζεται στην ενότητα αυτή.

3.3.1.1. Αναζήτηση “χώρου” και βελτιστοποίηση, για κυρτά πτερύγια

Αρχικά πραγματοποιείται μια διερεύνηση του χώρου λύσεων, εξετάζοντας τις τιμές του ακροπτερυγίου S_{tip} , στο διάστημα $[0 - 8m]$ με βάση την εξίσωση:

$$sweep = S_{tip} \left(\frac{r}{R_{tip}} \right)^2 \quad (3.1)$$

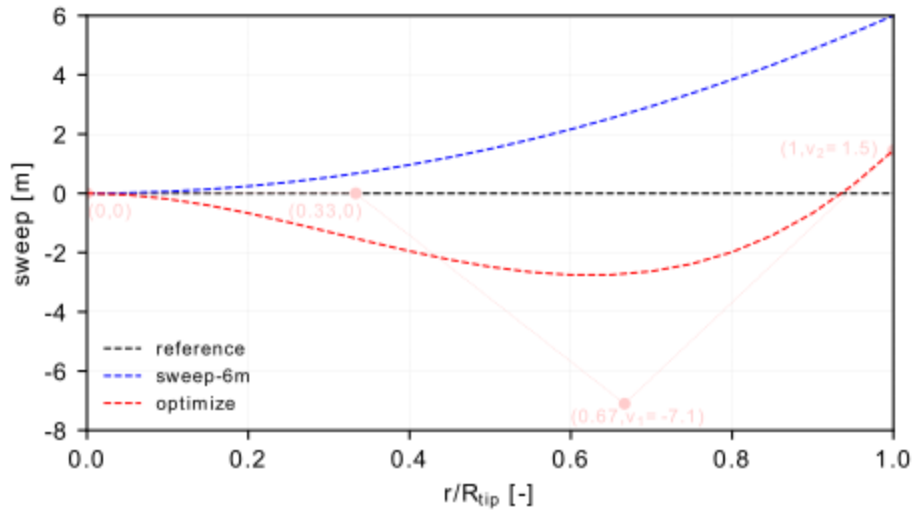
Σύμφωνα με τον Πίνακα 3.1, η μεγαλύτερη μείωση μάζας επιτυγχάνεται για $S_{tip} = 6m$ (στο εξής θα καλείται ‘sweep-6m’). Παρατηρείται ότι καθώς αυξάνεται η τιμή του S_{tip} , η κάμψη πτερυγίωσης (flap-wise moment) φαίνεται να μειώνεται - ενώ η ροπή στρέψης (torsion moment) παρουσιάζει αύξηση. Αντίθετα η κάμψη στην κατεύθυνση περιστροφής (edge-wise moment), δεν παρουσιάζει σαφή τάση. Το γεγονός αυτό, οφείλεται σε δυο παράγοντες: (i) στο συνολικό μήκος του πτερυγίου και (ii) στην εκκεντρότητα των τμημάτων του πτερυγίου σε σχέση με τον άξονα βήματος. Η ροπή στην κατεύθυνση περιστροφής (edge-wise moment) μειώνεται για μέτριες τιμές S_{tip} (έως και 6m) ως αποτέλεσμα του μειωμένου πάχους τοιχωμάτων, ενώ αυξάνεται για μεγαλύτερες τιμές. Σύμφωνα με τον Pavesi [56], διάφορες διαμορφώσεις πτερυγίου έχουν αξιολογηθεί, λαμβάνοντας τρεις παραμέτρους σχεδιασμού: (i), το σημείο εκκίνησης της κύρτωσης, (ii) η μέγιστη απόκλιση της κύρτωσης και (iii) η προς τα εμπρός κύρτωση του πτερυγίου. Στην παρούσα εφαρμογή, εξετάστηκε μια αντίστοιχη προσέγγιση χρησιμοποιώντας καμπύλες Bezier τεσσάρων σημείων ελέγχου (ισαπέχοντων ως προς την ακτινική

θήση). Φυσικά, στη ρίζα του πτερυγίου θεωρείται μηδενική κυρτότητα και για αυτό τα πρώτα δυο σημεία έχουν τοποθετηθεί στον άξονα βήματος. Κύριες μεταβλητές σχεδιασμού του προβλήματος, έχουν θεωρηθεί οι συντεταγμένες των δυο τελευταίων σημείων (v_1 και v_2 στο Σχ. 3.4), ενώ το πάχος των τοιχωμάτων του πτερυγίου καθορίζεται από τον εσωτερικό βρόχο (δευτερεύουσες μεταβλητές) του διαγράμματος στο Σχ. 3.3. Αντικειμενική συνάρτηση θεωρείται η συνολική μάζα του πτερυγίου, ενώ η βελτιστοποίηση βασίζεται στην προσέγγιση BFGS.

Πίνακας 3.1: Επίδραση κυρτότητας στη μάζα και τα φορτία πτερυγίου.

$S_{tip}[m]$	Blade mass [kg]	Flap-wise [kNm]	Edge-wise [kNm]	Torsion [kNm]
0	40089	69256	23237	384
1	-0.67%	-0.26%	-2.12%	+34.83%
2	-1.34%	-0.73%	-3.37%	+137.03%
3	-1.99%	-1.39%	-4.00%	+271.58%
4	-2.72%	-2.17%	-4.16%	+405.12%
5	-3.62%	-3.06%	-4.19%	+530.87%
6	-3.74%	-3.93%	+1.38%	+662.68%
7	-2.18%	-3.92%	+0.39%	+805.72%
8	+0.11%	-4.04%	+12.26%	+961.98%

Η τεχνική βελτιστοποίησης BFGS, απαιτεί τον υπολογισμό του αρχικού μητρώου της Εσσιανής. Πολλές φορές το μητρώο αυτό υπολογίζεται χρησιμοποιώντας πεπερασμένες διαφορές, ενώ μια πιο απλή προσέγγιση είναι η χρήση του μοναδιαίου πίνακα. Στο παράδειγμα αυτό, έχει υιοθετηθεί η πρώτη προσέγγιση, χωρίς όμως τον υπολογισμό των εκτός-διαγωνίου όρων. Στο Σχ. 3.4, παρουσιάζεται το βέλτιστο σχήμα (εφεξής 'sweep-opt'), το οποίο είναι κατά 8.6% ελαφρύτερο σε σχέση με το πτερύγιο αναφοράς.



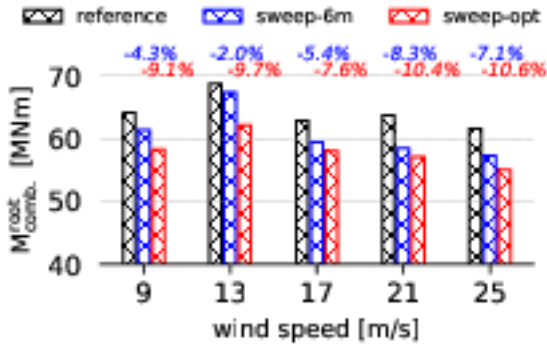
Σχήμα 3.4: Διαμόρφωση κυρτότητας για: (i) πτερύγιο αναφοράς, (ii) sweep-6m και (iii) sweep-opt.

3.3.1.2. Πιστοποίηση των διαμορφώσεων sweep-6m και sweep-opt

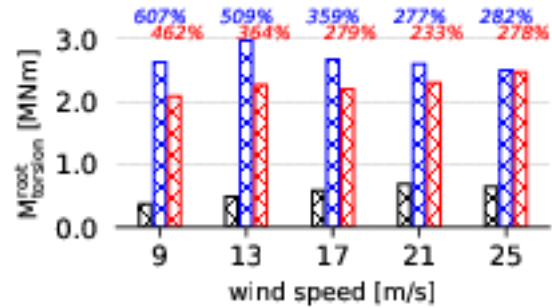
Η επαλήθευση πραγματοποιείται μέσω ενός αντιπροσωπευτικού και εκτεταμένου υπο-συνόλου αεροελαστικών προσομοιώσεων, με βάση το IEC 61400-1. Η αξιολόγηση, περιλαμβάνει ένα εύρος ταχυτήτων ανέμου όπου συγκρίνονται οι δύο διαμορφώσεις (sweep-6m και sweep-opt) σε σχέση με τα αποτελέσματα του πτερυγίου αναφοράς. Στο Σχ. 3.5 παρουσιάζεται η συνισταμένη ροπή κάμψης στη ρίζα του πτερυγίου, ενώ στο Σχ. 3.6 φαίνεται η ροπή στρέψης. Τα αποτελέσματα έχουν προκύψει μέσω τριών 10min προσομοιώσεων ανέμου, με ακραία τύρβη (DLC-1.3). Και οι δυο διαμορφώσεις παρουσιάζουν μικρότερη συνισταμένη ροπή, με τη μεγαλύτερη μείωση να παρατηρείται στο σχέδιο πτερυγίου που προέκυψε από τη διαδικασία βελτιστοποίησης. Παρατηρείται ανακούφιση στη ροπή κάμψης σε κάθε ταχύτητα ανέμου, με τη μεγαλύτερη μείωση να επιτυγχάνεται στα 25 m/s για τη σχεδιαστική διαμόρφωση 'sweep-opt'. Όπως αναμένεται, οποιαδήποτε κυρτότητα οδηγεί σε αύξηση της ροπής στρέψης. Ωστόσο, το βελτιστοποιημένο σχήμα παρουσιάζει μια πιο ήπια αύξηση, εξαιτίας της 'προς-τα-εμπρός' κύρτωσης του εσωτερικού τμήματος. Για παράδειγμα, για ταχύτητα ανέμου 13 m/s, το sweep-6m παρουσιάζει μια αύξηση 509% στη ροπή στρέψης - ενώ η sweep-opt 364%.

Η κυρτότητα δεν έχει αποτελέσει μέρος της έρευνας του κεφαλαίου 4, για τους εξής λόγους:

- η κυρτότητα μπορεί να επηρεάσει τη συμπεριφορά του πτερυγίου ως προς τον λυγισμό, ο οποίος δεν εξετάζεται στην παρούσα εργασία.
- το μοντέλο κόστους δεν περιλαμβάνει το κόστος: (i) του κυρτού καλουπιού, (ii) κατασκευής και (iii) μεταφοράς κυρτών πτερυγίων.



Σχήμα 3.5: Συνισταμένη ροπή στη ρίζα πτερυγίου, για διάφορες ταχύτητες ανέμου: (i) πτερύγιο αναφοράς, (ii) sweep-6m και (iii) sweep-opt.



Σχήμα 3.6: Ροπή στρέψης στη ρίζα πτερυγίου, για διάφορες ταχύτητες ανέμου: (i) πτερύγιο αναφοράς, (ii) sweep-6m και (iii) sweep-opt.

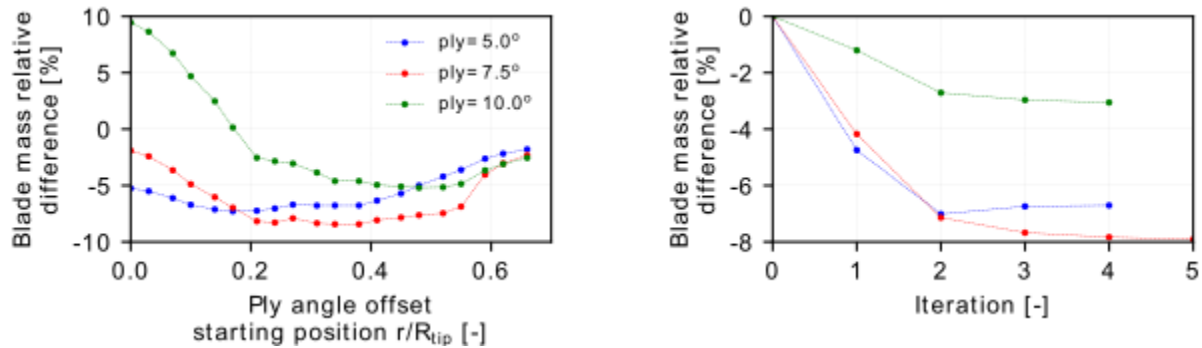
3.3.2. Μείωση μάζας δρομέα, με χρήση τεχνικών BTC

Αξιολογούνται η γωνία στροφής του μονο-κατευθυντήριου υλικού (BTC) και το σημείο εκκίνησης της, με στόχο τη “χαρτογράφηση” του πεδίου των πιθανών λύσεων του προβλήματος ελαχιστοποίησης της μάζας πτερυγίου ανεμογεννήτριας. Στη συνέχεια, με βάση τη διαδικασία βελτιστοποίησης που περιγράφηκε στην ενότητα 3.2 και στο Σχ. 3.3, διερευνάται η τμηματική εισαγωγή γωνίας στο μονο-κατευθυντήριο υλικό, αξιοποιώντας τον βελτιστοποιητή COBYLA. Η μελέτη ολοκληρώνεται με την πλήρη αξιολόγηση των βέλτιστων σχεδίων που έχουν προκύψει, τόσο ως προς τα ακραία φορτία όσο και ως προς τα φορτία κόπωσης.

3.3.2.1. Αναζήτηση “χώρου” και βελτιστοποίηση, για πτερύγια με BTC

Μια πρώτη εκτίμηση της δυνατότητας μείωσης της μάζας των πτερυγίων BTC φαίνεται στο αριστερό διάγραμμα του Σχ. 3.7, όπου αξιολογούνται τρεις γωνίες (5° , 7.5° και 10°) του μονο-κατευθυντήριου υλικού. Εκτός από την επίδραση της γωνίας, στο ίδιο διάγραμμα αξιολογείται το σημείο εκκίνησης, αφού παρουσιάζονται όλοι οι δυνατοί συνδυασμοί (3 γωνίες \times 20 σημεία εκκίνησης) της εισαγωγής γωνίας από τη ρίζα του πτερυγίου, μέχρι τα $2/3$ του μήκους του. Η μάζα του πτερυγίου κάθε περίπτωσης που έχει αξιολογηθεί, στην πραγματικότητα υπολογίζεται από τον εσωτερικό βρόχο της διαδικασίας που έχει περιγραφεί στο Σχ. 3.3, για σταθερές τιμές μεταβλητών σχεδιασμού (σταθερές τιμές γωνίας BTC). Η μέγιστη μείωση είναι περίπου 8% και λαμβάνεται για γωνία 7.5° ξεκινώντας από το 25 – 40% του πτερυγίου. Σημειώνεται ότι οι θετικές σχετικές διαφορές, αντιστοιχούν σε αύξηση της μάζας του πτερυγίου (σε σχέση με το πτερύγιο αναφοράς), όπως συμβαίνει για παράδειγμα στην περίπτωση της γωνίας 10° η οποία καταλαμβάνει όλο το μήκος του πτερυγίου. Η παραπάνω αύξηση, μπορεί να αιτιολογηθεί απ’το γεγονός ότι η στροφή του μονο-κατευθυντήριου υλικού συνεπάγεται μια εξασθένιση στην ικανότητα της πτέρυγας να παραλαμβάνει φορτία, με αποτέλεσμα να απαιτείται η

χρήση μεγαλύτερης ποσότητας υλικού για να διατηρηθούν οι τιμές του κριτηρίου Tsai-Hill στα ίδια επίπεδα με το πτερύγιο αναφοράς. Το δεξί διάγραμμα του Σχ. 3.7, δείχνει τη σύγκλιση της διαδικασίας μείωσης της μάζας. Διαπιστώνεται ότι απαιτούνται 4 – 5 επαναλήψεις του εσωτερικού βρόχου βελτιστοποίησης (περιλαμβάνει αερο-ελαστικές προσομοιώσεις), έως ότου επιτευχθεί η σύγκλιση.

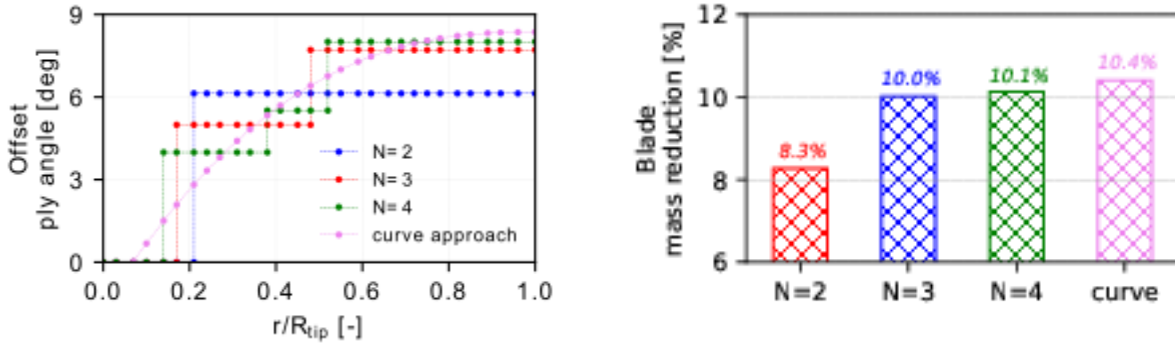


Σχήμα 3.7: Μείωση μάζας πτερυγίων BTC, για τρεις γωνίες μονο-κατευθυντήριου υλικού: 5° , 7.5° και 10° . Εκτός από τη γωνία, αξιολογείται και το σημείο εκκίνησης (κάθε σημείο στις καμπύλες αντιστοιχεί σε διαφορετικό σημείο εκκίνησης) – *αριστερό σχήμα*. Πορεία σύγκλισης του εσωτερικού βρόχου βελτιστοποίησης, για σημείο εκκίνησης=0.3 – *δεξί σχήμα*. Η μείωση της μάζας, πραγματοποιείται για δεδομένες σχεδιαστικές παραμέτρους BTC (γωνία & θέση εκκίνησης) ώστε να διατηρηθεί η κατανομή των μέγιστων τιμών Tsai-Hill, σε σχέση με το πτερύγιο αναφοράς.

Η βέλτιστη σχεδιαστική διαμόρφωση BTC, προκύπτει ενεργοποιώντας και τον εξωτερικό βρόχο της μεθοδολογίας που έχει περιγραφεί στην ενότητα 3.2. Στη συνέχεια εξετάζονται τέσσερις περιπτώσεις κατανομής γωνίας του μονο-κατευθυντήριου υλικού. Στις τρεις πρώτες περιπτώσεις το πτερύγιο χωρίζεται σε 2, 3 ή 4 τμήματα αντίστοιχα (το σύμβολο N δηλώνει το πλήθος των τμημάτων) σταθερής γωνίας. Η τέταρτη περίπτωση, περιγράφει μια θεωρητική συνεχή κατανομή γωνίας, η οποία περιγράφεται από την ακόλουθη μαθηματική έκφραση τριών παραμέτρων:

$$ply(r; ply_{tip}; r_s; \gamma) = ply_{tip} \left[1 - \left(1 - \frac{r - r_s}{1 - r_s} \right)^\gamma \right] \quad (3.2)$$

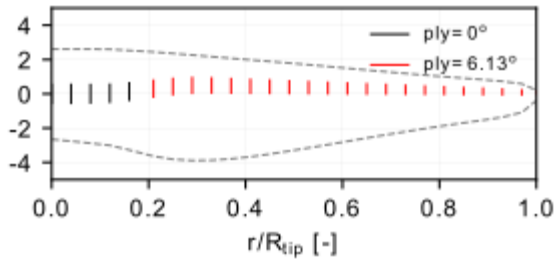
όπου r εκφράζει την αδιάστατη ακτίνα και οι τρεις παράμετροι ply_{tip} , r_s , γ δηλώνουν τη γωνία του μονο-κατευθυντήριου υλικού στο ακροπτερύγιο, την αδιάστατη θέση εκκίνησης της στροφής του υλικού και τον εκθέτη της συνάρτησης αντίστοιχα. Στις τρεις πρώτες περιπτώσεις, ως μεταβλητές βελτιστοποίησης θεωρήθηκαν οι γωνίες καθώς και το μήκος των τελευταίων $N - 1$ τμημάτων - ενώ στην τελευταία περίπτωση, οι μεταβλητές βελτιστοποίησης περιλαμβάνουν τις τρεις παραμέτρους της εξίσωσης Εξ. 3.2.



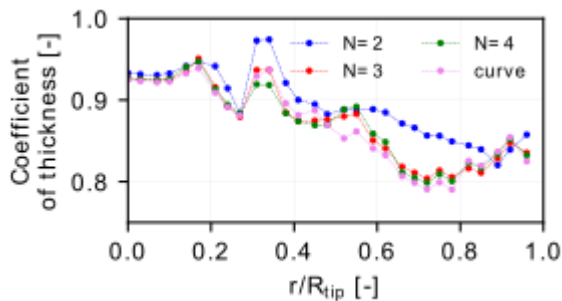
Σχήμα 3.8: Βέλτιστη (ως προς τη μείωση μάζας) κατανομή γωνίας μονο-κατευθυντήριου υλικού – αριστερό διάγραμμα και μέγιστη μείωση μάζας πτερυγίων – δεξί διάγραμμα των διαμορφώσεων BTC που έχουν εξεταστεί.

Στο Σχ. 3.8, παρουσιάζονται οι βέλτιστες τιμές των μεταβλητών σχεδιασμού και η αντίστοιχη τιμή της συνάρτησης κόστους (η σχετική μείωση της μάζας πτερυγίου). Για $N = 2$, η μέγιστη μείωση μάζας είναι 8.3% για γωνία μονο-κατευθυντήριου υλικού 6° και σημείο εκκίνησης της περιστροφής του υλικού στο 22% του μήκους του πτερυγίου. Για $N = 3$, η μέγιστη μείωση μάζας αυξάνεται στο 10% για γωνίες 5° και 7.8° , ξεκινώντας από 20% και 50% αντίστοιχα. Για $N = 4$, δεν επιτυγχάνεται ουσιαστικά καμία περαιτέρω βελτίωση. Η συνεχής κατανομή στην πραγματικότητα ορίζει το ανώτερο όριο μείωσης της μάζας (περίπου 10.5%,) ενός πτερυγίου με διαμόρφωση BTC, με τις τιμές των παραμέτρων: $ply_{tip} = 8.36^\circ$, $r_s = 6.9\%$ και $\gamma = 2.5$. Είναι σαφές, ότι η περίπτωση $N = 3$ πλησιάζει το μέγιστο θεωρητικό όριο, χωρίς να περιπλέκεται η κατασκευή του πτερυγίου. Είναι επίσης αξιοσημείωτο ότι οι τιμές των τριών πρώτων περιπτώσεων είναι σχεδόν τμηματικά σταθερές προσεγγίσεις της συνεχούς κατανομής, όπως φαίνεται στο αριστερό διάγραμμα του Σχ. 3.8. Η διάταξη της βελτιστοποιημένης διαμόρφωσης πτερυγίου για $N = 2$, φαίνεται στο Σχ. 3.9.

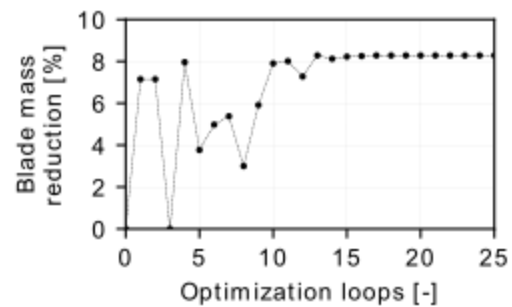
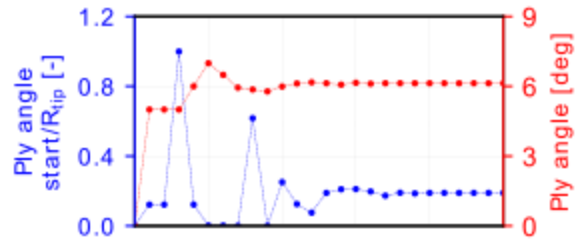
Στο Σχ. 3.10, παρουσιάζεται η βέλτιστη κατανομή του σχετικού πάχους των τοιχωμάτων κατά μήκος του πτερυγίου. Η αναλογία αυτή, υποδεικνύει τη μέγιστη επιτρεπόμενη μείωση του πάχους των τοιχωμάτων του πτερυγίου BTC που επιτρέπει τη διατήρηση των μέγιστων τιμών του κριτηρίου Tsai-Hill στο επίπεδο του πτερυγίου αναφοράς. Στο Σχ. 3.11, παρουσιάζεται η σύγκλιση του εξωτερικού βρόχου για την περίπτωση $N = 2$. Στο ίδιο σχήμα, παρουσιάζονται οι τιμές των μεταβλητών σχεδιασμού καθώς και της συνάρτησης κόστους, σε κάθε επανάληψη που πραγματοποιήθηκε. Είναι προφανές ότι αυξάνοντας το πλήθος των μεταβλητών σχεδιασμού, η βελτιστοποίηση καθίσταται πιο δύσκολη (απαιτούνται περισσότερες επαναλήψεις). Έτσι, για την περίπτωση $N = 3$, απαιτούνται τριαντα-πέντε επαναλήψεις - ενώ για την απλούστερη περίπτωση $N = 2$ μόνο εικοσι-πέντε.



Σχήμα 3.9: Διάταξη βελτιστοποιημένου πτερυγίου, για την περίπτωση $N = 2$. Το σχήμα παρουσιάζει την κατανομή της γωνίας του μονο-κατευθυντήριου υλικού στα ‘καπάκια’.



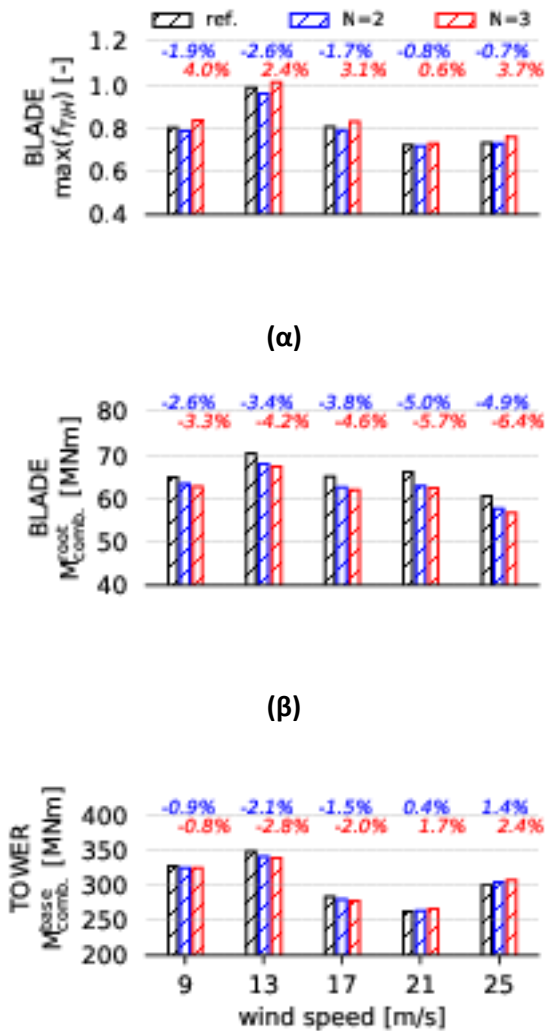
Σχήμα 3.10: Βέλτιστη κατανομή του συντελεστή μεταβολής πάχους τοιχωμάτων κατά μήκος του πτερυγίου. Ο συντελεστής αυτός, εγγυάται την ελαχιστοποίηση του πάχους των τοιχωμάτων κάθε διατομής, διατηρώντας τη μέγιστη τιμή του κριτηρίου Tsai-Hill στα ίδια επίπεδα με το πτερύγιο αναφοράς.



Σχήμα 3.11: Σύγκλιση των μεταβλητών σχεδιασμού – άνω διαγράμματα και συνάρτησης κόστους – κάτω διάγραμμα του εξωτερικού βρόχου βελτιστοποίησης, για την περίπτωση $N = 2$.

3.3.2.2. Πιστοποίηση των διαμορφώσεων $N = 2$ και $N = 3$

Στην ενότητα αυτή, πιστοποιούνται οι δυο απλούστερες ($N = 2$ και $N = 3$) σχεδιαστικές διαμορφώσεις BTC που έχουν προταθεί πιο πάνω. Η πρώτη διαμόρφωση ($N = 2$), αποτελεί την τυπική επιλογή BTC που συνήθως περιγράφεται στη βιβλιογραφία, με μια ομοιόμορφη στροφή στο μονο-κατευθυντήριο υλικό από το 22% του πτερυγίου. Η δεύτερη διαμόρφωση ($N = 3$), αποτελεί ένα ελαφρώς πιο περίπλοκο σχέδιο, με μικρότερη γωνία στο πρώτο τμήμα του πτερυγίου και μεγαλύτερη γωνία στο τελευταίο. Ωστόσο, το μοντέλο αυτό, επιτρέπει σχεδόν 2% επιπλέον μείωση στη μάζα του πτερυγίου. Η κατασκευή και των δυο σχεδίων, θεωρείται εφικτή. Όπως και στην προηγούμενη εφαρμογή, η πιστοποίηση των προτεινόμενων σχεδίων μέσω τριών 10min αερο-ελαστικών προσομοιώσεων σε διάφορες συνθήκες λειτουργίας, θεωρείται επιβεβλημένη. Οι δυο αυτές διαμορφώσεις, αξιολογούνται τόσο σε σχέση με τα ακραία φορτία όσο και ως προς την κόπωση.

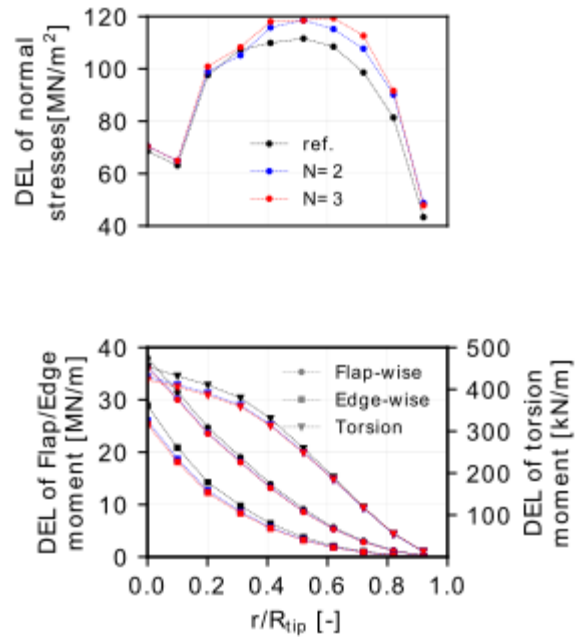


(α)

(β)

(γ)

Σχήμα 3.12: Υπολογισμός ακραίων φορτίων για DTU-10MW RWT και σχεδιαστικών διαμορφώσεων $N = 2$ και $N = 3$, θεωρώντας έντονη τύρβη ανέμου DLC-1.3: (α) μέγιστη τιμή κριτηρίου Tsai-Hill, (β) μέγιστη συνισταμένη ροπή κάμψης στη ρίζα του πτερυγίου και (γ) μέγιστη συνισταμένη ροπή κάμψης στη βάση του πύργου.



Σχήμα 3.13: Υπολογισμός φορτίου κόπωσης ανεμογεννήτριας DTU-10MW RWT και των σχεδιαστικών διαμορφώσεων $N = 2$ και $N = 3$ υιοθετώντας κανονική τύρβη ανέμου DLC-1.2: (α) κατανομή DELs της μέσης ορθής τάσης στα 'καπάκια' και (β) των ροπών του πτερυγίου.

Στο Σχ. 3.12, παρουσιάζονται τα ακραία φορτία για διάφορες ταχύτητες ανέμου, συγκρίνοντας τις σχεδιαστικές διαμορφώσεις $N = 2$ and $N = 3$ σε σχέση με την DTU-10MW RWT. Οι μέγιστες τιμές Tsai-Hill (η αστοχία συμβαίνει όταν λάβει τιμή > 1) φαίνονται στο άνω διάγραμμα, η μέγιστη συνισταμένη ροπή κάμψης στη ρίζα του πτερυγίου παρουσιάζεται στο μεσαίο διάγραμμα και η μέγιστη ροπή

κάμψης στη βάση του πύργου στο κάτω διάγραμμα. Όπως αναμένεται, οι μέγιστες τιμές των Tsai-Hill παρατηρούνται για DLC-1.3, στα 13 m/s για κάθε σχεδιαστική διαμόρφωση.

Πίνακας 3.2: Κοπωτικά φορτία (DEls) ροπών στη βάση του πύργου, για την ανεμογεννήτρια αναφοράς DTU-10MW RWT καθώς και σχετική ποσοστιαία διαφορά των διαμορφώσεων $N = 2$ και $N = 3$, υιοθετώντας κανονική τύρβη DLC-1.2.

	reference	$N = 2$	$N = 3$
Fore-aft moment	123449	-0.77%	-0.74%
Side-side moment	53748	-4.04%	-4.53%
Ροπή συστροφής	32037	-4.49%	-5.38%

Η κόπωση του πτερυγίου εκτιμάται με βάση τα ισοδύναμα φορτία κόπωσης (Damage Equivalent Loads – DELs), που υπολογίζονται υιοθετώντας τις παραμέτρους Weibull $C = 11 \text{ m/s}$ και $k = 2$, $N_{ref} = 10^7$ καθώς και τους συντελεστές Wöhler $m = 10$ για την περίπτωση των πτερυγίων και $m = 4$ για τον πύργο. Στο Σχ. 3.13, παρουσιάζονται τα αποτελέσματα των κοπωτικών φορτίων για την ανεμογεννήτρια αναφοράς DTU-10MW RWT, καθώς και για τις δυο απλούστερες σχεδιαστικές διαμορφώσεις που έχουν προκύψει. Στο πάνω διάγραμμα, φαίνονται τα κοπωτικά φορτία της μέσης ορθής τάσης στην περιοχή των ‘καπακιών’ - ενώ στο κάτω διάγραμμα παρουσιάζονται τα κοπωτικά φορτία των τριών ροπών κατά μήκος του πτερυγίου. Τέλος, στον Πίνακα 3.2 παρουσιάζονται τα κοπωτικά φορτία των ροπών που σχετίζονται με τη βάση του πύργου για κάθε περίπτωση. Τα προτεινόμενα σχέδια BTC, παρουσιάζουν μειωμένα φορτία κατά 0.8% στις ροπές του πύργου και έως 10% στην ροπή του πτερυγίου. Αντίθετα, τα κοπωτικά φορτία της μέσης ορθής τάσης αυξάνεται έως 14% στο 75% του μήκους του πτερυγίου, εξαιτίας του μειωμένου πάχους τοιχωμάτων - ενώ κοντά στη ρίζα αυξάνεται μόνο κατά 2.7%.

3.3.3. Μείωση μάζας δρομέα, με συνδυαστική εφαρμογή BTC και FEC

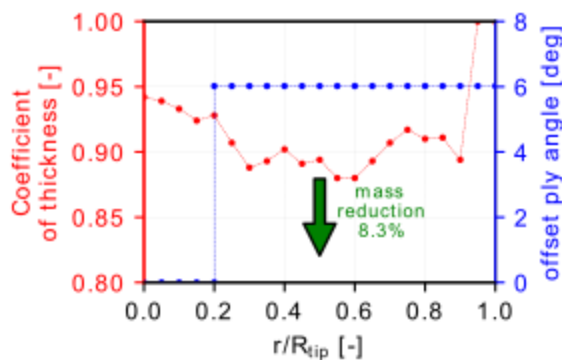
Στην εφαρμογή που ακολουθεί, διερευνάται η δυνατότητα συνδυασμένης χρήσης παθητικών τεχνικών BTC και FEC, με στόχο τόσο τη μείωση της μάζας των πτερυγίων ανεμογεννήτριας όσο και την ελαχιστοποίηση των ταλαντώσεων που προκαλούνται κατά τη στάθμευση της ανεμογεννήτριας (λειτουργία “ρελαντί”). Ο σχεδιασμός του τροποποιημένου (στο εξής “modified”) πτερυγίου, πραγματοποιείται με βάση τη διαδικασία που έχει περιγραφεί στην ενότητα 3.2. Η διαφορά με την προηγούμενη εφαρμογή, έγκειται στο γεγονός ότι το πτερύγιο θεωρείται πως έχει μια σταθερή σύζευξη των κάμψεων πτερύγισης και περιστροφής FEC 3% - ενώ η μοναδική μεταβλητή σχεδιασμού, θεωρείται η γωνία στροφής του μονο-κατευθυντήριου υλικού (ξεκινώντας απ’το $r/R_{tip} = 20\%$).

3.3.3.1. Μείωση μάζας με χρήση διάφορων μεθόδων βελτιστοποίησης

Χρησιμοποιούνται ανεξάρτητα τρεις μέθοδοι βελτιστοποίησης, με στόχο την αποτύπωση της επίδρασης της μεθόδου βελτιστοποίησης στην εκτίμηση της βέλτιστης λύσης: (i) COBYLA, (ii) SLSQP και (iii) η παραδοσιακή μέθοδος Newton. Στον Πίνακα 3.3, παρουσιάζεται ο αριθμός των κλήσεων της διαδικασίας ελαχιστοποίησης που απαιτεί κάθε μέθοδος. Το υπολογιστικό κόστος, είναι ανάλογο του αριθμού των κλήσεων που απαιτούνται για την αξιολόγηση των υποψήφιων λύσεων και τον υπολογισμό του μητρώου της Ιακωβιανής/Εσσιανής (Jacobian/Hessian). Όπως αναμένεται, η μέθοδος του Νεύτωνα είναι η πιο οικονομική επιλογή εξαιτίας του πολύ μικρού αριθμού μεταβλητών (μόλις 1) - ενώ μπορεί να γίνει εξαιρετικά γρήγορη μέθοδος στην περίπτωση που παραλληλοποιηθεί η διαδικασία του υπολογισμού της Εσσιανής.

Πίνακας 3.3: Αριθμός κλήσεων αντικειμενικής συνάρτησης, που απαιτεί κάθε μέθοδος.

Number of objective function calls	COBYLA	SLSQP	Newton
For assessing the candidate solution	23	14	0
For estimating the Jacobian/Hessian matrix	0	12	15
Total number of calls without parallelization	24	26	15
Total number of calls with parallelization	23	20	5



Σχήμα 3.14: Κατανομή του συντελεστή μεταβολής πάχους τοιχωμάτων (εσωτερικός βρόχος) και γωνίας μονο-κατευθυντήριου υλικού (εξωτερικός βρόχος).

Όλες οι μέθοδοι, φαίνεται να συγκλίνουν στο ίδιο αποτέλεσμα. Το τελικό σχήμα, είναι ένα τροποποιημένο περύγιο “modified” με 8.3% λιγότερη μάζα σε σχέση με το περύγιο της ανεμογεννήτριας αναφοράς. Η μείωση αυτή, επιτυγχάνεται με την εισαγωγή γωνίας 5.8° στο μονο-

κατευθυντήριο υλικό. Στο Σχ. 3.14, παρουσιάζεται η κατανομή του συντελεστή μείωσης του πάχους των τοιχωμάτων του πτερυγίου (μια μέση τιμή του είναι 92%).

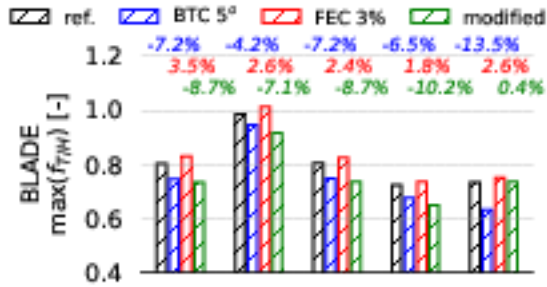
3.3.3.2. Πιστοποίηση σχεδιαστικών διαμορφώσεων BTC 5°, FEC 3% και “modified”

Στην ενότητα αυτή, η τροποποιημένη “modified” πτέρυγα μαζί με τις περιπτώσεις του BTC 5° (εκκινώντας από το 20%) και το FEC 3%, επαληθεύονται μέσω τριών αερο-ελαστικών προσομοιώσεων ενός υπο-συνόλου του φακέλου του κανονισμού IEC. Στον Πίνακα 3.4, παρουσιάζονται οι λεπτομέρειες κάθε διαμόρφωσης που εξετάζεται, όπως η μάζα του πτερυγίου και η μέση παραγόμενη ισχύς. Για παράδειγμα, στην περίπτωση του FEC 3% το πτερύγιο παρουσιάζει 0.3% μεγαλύτερη μάζα - ενώ στη διαμόρφωση BTC 5° η ετήσια απώλεια ισχύος είναι μόλις 0.3%, εξαιτίας του επανα-σχεδιασμού της καμπύλης συστροφής.

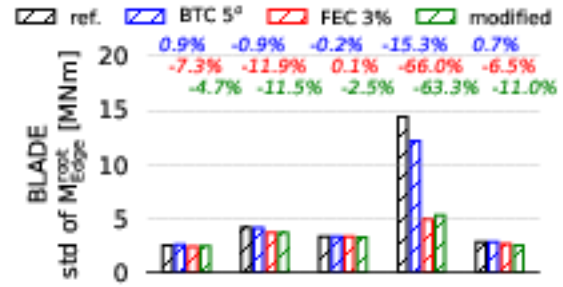
Πίνακας 3.4: Πίνακας εξεταζόμενων διαμορφώσεων και σύγκριση με την DTU-10MW RWT. Οι παράμετροι Weibull για τον υπολογισμό της ετήσιας ισχύος, είναι: $C = 11 \text{ m/s}$ και $k = 2$.

design	Ply angle [°]	Caps displacement [% of the chord]	Blade mass [tn]	Mean power [MW]	Reduce loads of
reference	0	0	39.97	6.13	-
BTC 5°	5	0	39.97	6.11	DLC-1.3
FEC 3%	0	3	40.10	6.13	DLC-6.x
modified	5.8	3	36.69	6.11	DLC-1.3 & 6.x

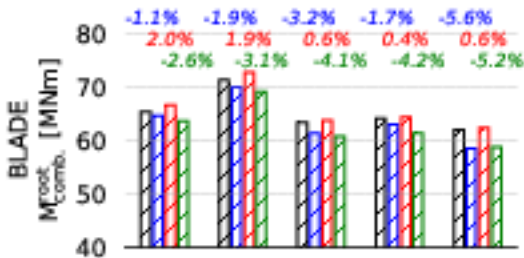
Στα Σχ. 3.15 και 3.16, συγκρίνονται τα αποτελέσματα των ακραίων φορτίων για κάθε μια απ’τις τέσσερις σχεδιαστικές διαμορφώσεις. Συγκεκριμένα, στο Σχ. 3.15 παρουσιάζονται οι μέγιστες τιμές του κριτηρίου αστοχίας Tsai-Hill, καλύπτοντας τις ταχύτητες ανέμου [9 – 25 m/s]. Απ’τα αποτελέσματα, επιβεβαιώνεται ότι η δυσμενέστερη κατάσταση παρουσιάζεται στα 13 m/s για όλες τις διαμορφώσεις. Το βελτιστοποιημένο πτερύγιο, παρουσιάζει χαμηλότερες μέγιστες τάσεις σε κάθε ταχύτητα ανέμου (με τη μεγαλύτερη μείωση να παρουσιάζεται στα 21 m/s). Σημειώνεται ότι η μέγιστη τιμή Tsai-Hill του BTC 5°, είναι πράγματι χαμηλότερη σε σχέση με το πτερύγιο αναφοράς – όχι μόνο στα 13 m/s (μείωση 4.2%), αλλά και σε όλες τις άλλες ταχύτητες ανέμου. Τέλος, το FEC 3% εμφανίζει ελαφρώς μεγαλύτερες τιμές Tsai-Hill σε όλες τις ταχύτητες και υπερβαίνει την τιμή 1 στα 13 m/s. Αυτό οφείλεται στο γεγονός ότι το FEC προορίζεται για την αντιμετώπιση των ακραίων ταλαντώσεων όταν η μηχανή βρίσκεται σε κατάσταση “ρελαντί” και όχι για τη μείωση των ακραίων φορτίων λειτουργίας.



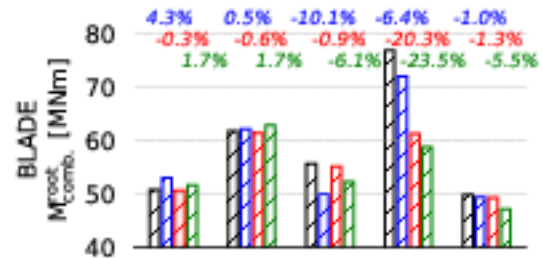
(α)



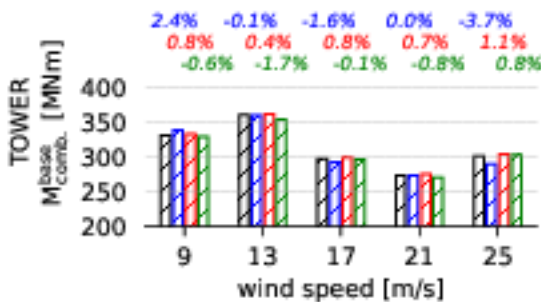
(α)



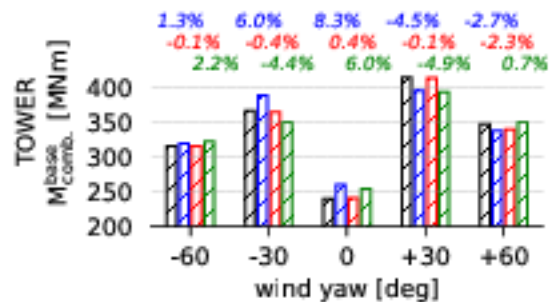
(β)



(β)



(γ)



(γ)

Σχήμα 3.15: Ακραία φορτία DLC-1.3 σε σχέση με τις ταχύτητες ανέμου, για κάθε σχεδιαστική διαμόρφωση (με συντελεστές ασφαλείας): (α) μέγιστη τιμή κριτηρίου Tsai-Hill failure στο πτερύγιο, (β) μέγιστη συνισταμένη ροπή στη ρίζα πτερυγίου και (γ) μέγιστη συνισταμένη ροπή στη βάση του πύργου. Οι ποσοστιαίες διαφορές, καταγράφονται πάνω απ'τις μπάρες.

Σχήμα 3.16: Ακραία φορτία DLC-6.x σε σχέση με τις γωνίες ανέμου, για κάθε σχεδιαστική διαμόρφωση (με συντελεστές ασφαλείας) (α) τυπική απόκλιση (std) της κάμψης περιστροφής στη ρίζα πτερυγίου, (β) μέγιστη συνισταμένη ροπή στη ρίζα πτερυγίου και (γ) μέγιστη συνισταμένη ροπή στη βάση του πύργου. Οι ποσοστιαίες διαφορές, καταγράφονται πάνω απ'τις μπάρες.

Στο Σχ. 3.16, συγκρίνονται τα φορτία του DLC-6.x για τις τέσσερις διαμορφώσεις. Όπως αναμενόταν, η μέγιστη φόρτιση παρουσιάζεται για γωνία ανέμου +30° τόσο για το πτερύγιο όσο και για τον πύργο. Φαίνεται ότι ο παθητικός έλεγχος BTC, δεν επηρεάζει σημαντικά τη συμπεριφορά της ανεμογεννήτριας σε κατάσταση “ρελαντί”, σε αντίθεση με την τεχνική FEC η οποία για μια μετατόπιση 3% των

‘καπακιών’, πετυχαίνει μείωση της τυπικής απόκλισης των ροπών περιστροφής (edge-wise moment) μέχρι και 66%. Τέλος, η συνδυαστική εφαρμογή BTC και FEC έχει ένα παρόμοιο αποτέλεσμα τόσο στην τυπική απόκλιση των φορτίων της ρίζας του πτερυγίου (μείωση 63.3%), όσο και στη συνισταμένη ροπή (μείωση 23.5%). Ως εκ τούτου, η συνολική επίδραση του FEC στα σχεδιαστικά φορτία είναι ευεργετική παρά την ελαφρώς δυσμενή επίδραση που παρατηρείται στα λειτουργικά φορτία της πτέρυγας.

Πίνακας 3.5: Σύγκριση φορτίων κόπωσης DLC-1.2 μεταξύ του DTU-10MW RWT και των διαμορφώσεων παθητικού ελέγχου που εξετάζονται. Τα DELs υπολογίζονται για διάστημα είκοσι ετών με συντελεστή Wöhler $m = 10$ για τα πτερύγια και $m = 4$ για τον πύργο, $N_{ref} = 10^7$ κύκλοι και παράμετροι Weibull: $C = 11 m/s$ και $k = 2$. Τα απόλυτα φορτία (σε kNm) καταγράφονται για την ανεμογεννήτρια αναφοράς καθώς και η σχετική ποσοστιαία διαφορά των διαμορφώσεων.

designs	Blade Root			Tower Base		
	M_{flap}	M_{pitch}	M_{edge}	$M_{fore-aft}$	M_{yaw}	$M_{side-side}$
reference	25045	420	27791	111751	24460	33549
BTC 5°	-5.1%	-3.6%	-0.3%	-3.3%	-3.9%	-2.0%
FEC 3%	+0.7%	+10.7%	+0.4%	+0.7%	+0.6%	+1.8%
modified	-5.5%	+1.9%	-8.9%	-1.3%	-5.2%	-0.5%

Η αξιολόγηση των τεσσάρων σχεδίων, πραγματοποιείται με βάση το DLC-1.2. Τα ισοδύναμα φορτία κόπωσης (Damage Equivalent Loads - DELs), υπολογίζονται για τις ταχύτητες ανέμου στο διάστημα 5 – 25 m/s , υποθέτοντας ότι η ανεμογεννήτρια έχει διάρκεια ζωής είκοσι ετών. Για τον πιο πάνω υπολογισμό, έχουν υποθεθεί οι παράμετροι Weibull: $C = 11 m/s$, $k = 2$ και $N_{ref} = 10^7$ κύκλοι αναφοράς. Τέλος, για τα πτερύγια έχει ληφθεί ο συντελεστής Wöhler ίσος με $m = 10$ και για τον πύργο $m = 4$. Στον Πίνακα 3.5, παρουσιάζονται τα DELs της ανεμογεννήτριας αναφοράς μαζί με τις ποσοστιαίες διαφορές των άλλων τριών διαμορφώσεων που εξετάζονται στην παρούσα ενότητα. Σύμφωνα λοιπόν με τα αποτελέσματα, η καθαρή εφαρμογή BTC έχει μειώσει τα κοπωτικά φορτία τόσο του πύργου όσο και του πτερυγίου, με τη μεγαλύτερη μείωση να αφορά τη ροπή πτερύγησης (flap-wise), 5.1%. Αντίθετα, το FEC 3% προκαλεί μια μικρή αύξηση σε όλα τα κοπωτικά φορτία τόσο του πύργου όσο και του πτερυγίου. Όπως αναμενόταν, η συνδυαστική εφαρμογή BTC και FEC, συνδυάζει τα πλεονεκτήματα και τα μειονεκτήματα και των δύο τεχνικών, οδηγώντας σε 5.5% μείωση των κοπωτικών φορτίων πτερύγησης (flap-wise moment) και 8.9% στα φορτία περιστοφής (edge-wise moment).

Αυτή η σελίδα μένει κενή

Κεφάλαιο 4

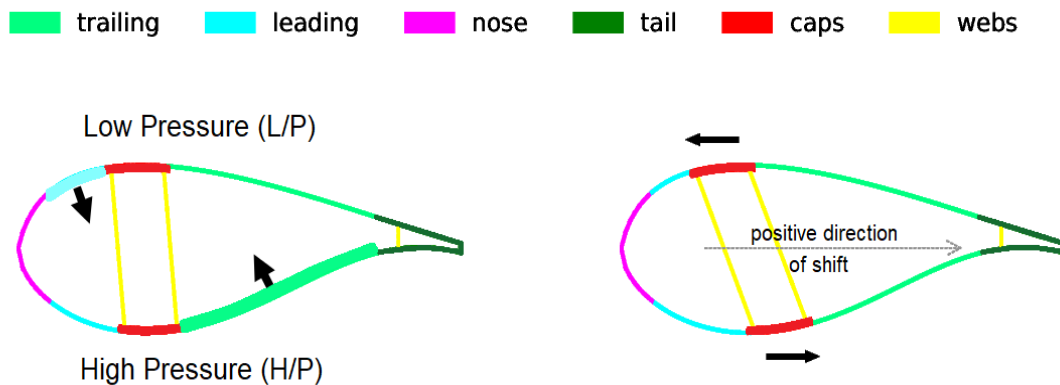
4. Πολυ-πεδιακή αερο-ελαστική βελτιστοποίηση DTU-10MW RWT

Η πρόσφατη τάση στο σχεδιασμό ανεμογεννητριών, είναι η πολυ-πεδιακή αερο-ελαστική βελτιστοποίηση [21], κατά την οποία αντιμετωπίζονται σε κοινό βρόχο τόσο οι αεροδυναμικές παράμετροι του προβλήματος σχεδιασμού όσο και οι κατασκευαστικές. Στο κεφάλαιο αυτό, υιοθετείται το περιβάλλον σχεδιασμού που έχει αναπτυχθεί στην ενότητα 3.2, συνδέοντας το μοντέλο κόστους της ενότητας 2.3 για την κοστολόγηση της παραγόμενης ενέργειας. Σε αντίθεση με το προηγούμενο κεφάλαιο, εδώ ως αντικειμενική συνάρτηση θεωρείται το σταθμισμένο κόστος ενέργειας (Levelized Cost of Electricity - LCoE), ενώ ορισμένες απ'τις μεταβλητές σχεδιασμού συνδέονται με τα τη γεωμετρία του δρομέα (π.χ. κατανομή χορδής και συστροφής καθώς και το μήκος του πτερυγίου). Εκτός από εφαρμογές BTC (Bend-Twist-Coupling), στο κεφάλαιο αυτό παρουσιάζεται μια διαφορετική προσέγγιση του FEC (Flap-Edge-Coupling) καθώς και η δυνατότητα συνδυαστικής εφαρμογής τους.

4.1. Βέλτιστος συνδυασμός BTC και FEC – και μια εναλλακτική προσέγγιση του FEC

Συχνά οι κατασκευαστές αντιμετωπίζουν το πρόβλημα της “απόκλισης ευθυγράμμισης”, δηλαδή όταν η ανεμογεννήτρια βρίσκεται εκτός λειτουργίας (κατάσταση “ρελαντί”) και πνέει άνεμος υπό μεγάλη γωνία απόκλισης, παρουσιάζονται έντονες ταλαντώσεις που μπορεί να υπερβούν τα σχεδιαστικά όρια. Μια ad hoc λύση είναι η ενίσχυση των πτερυγίων με επιπλέον υλικό. Τέτοιες λύσεις μπορεί να

θεραπεύουν το πρόβλημα, ωστόσο απέχουν από το να είναι βέλτιστες, αυξάνοντας το βάρος/κόστος του πτερυγίου και επηρεάζοντας τα λειτουργικά φορτία της μηχανής. Στο κεφάλαιο αυτό, επιδιώκεται ο βέλτιστος συνδυασμός των παθητικών συστημάτων (BTC – για τα λειτουργικά φορτία και FEC – για τα φορτία σε συνθήκες “ρελαντί”), τα οποία σχεδιάζονται ταυτόχρονα με τα κατασκευαστικά/γεωμετρικά χαρακτηριστικά της μηχανής (π.χ. κατανομή χορδής και συστροφής ή/και μήκος πτερυγίου). Για τον μετριασμό των φορτίων που προκαλούνται στην ανεμογεννήτρια όταν βρίσκεται σε κατάσταση εκτός λειτουργίας, αξιοποιούνται δυο προσεγγίσεις. Η πρώτη έχει ήδη μελετηθεί στο κεφάλαιο 3 και σχετίζεται με τη μετατόπιση των ‘καπακιών’, ενώ η δεύτερη παρουσιάζεται για πρώτη φορά στο κεφάλαιο αυτό. Σύμφωνα με την τελευταία προσέγγιση, η σύζευξη των κατευθύνσεων πτερύγισης (flap-wise) και περιστροφής (edge-wise), μπορεί να υλοποιηθεί αποτελεσματικότερα μέσω της αντισυμμετρικής ενίσχυσης των υλικών TRIAX και UNIAX που βρίσκονται στις περιοχές: (i) του χείλους προσβολής (leading) της πλευράς υπο-πίεσης και (ii) της ακμής εκφυγής (trailing) της πλευράς υπερπίεσης (βλέπε Σχ. 4.1, αριστερά). Μια ακόμα διαφορά του κεφαλαίου αυτού σε σχέση με το προηγούμενο, είναι ότι οι εφαρμογές FEC (είτε πρόκειται για μετατόπιση ‘καπακιών’ – γεωμετρικό FEC, είτε πρόκειται για την ασύμμετρη μεταβολή του πάχους – υλικό FEC), αντιμετωπίζεται μέσω της βέλτιστης κατανομής τους κατά μήκος του πτερυγίου.



Σχήμα 4.1: Διατομή πτερυγίου ανεμογεννήτριας, με εφαρμογή υλικού FEC (αριστερά) και γεωμετρικού FEC (δεξιά), μέσω ασύμμετρης μεταβολής στο πάχος των τοιχωμάτων και μετατόπισης ‘καπακιών’.

4.2. Εφαρμογές

Στις εφαρμογές του προηγούμενου κεφαλαίου, αξιολογήθηκε η δυνατότητα ελαχιστοποίησης του LCoE με τη συμπίεση της μάζας των υλικών κατασκευής (ελαχιστοποίηση CAPital EXpenditure – CAPEX). Παρά τ’αυτά, μελέτες [7] έχουν αποδείξει ότι μια πιο αποτελεσματική προσέγγιση για τη συμπίεση του LCoE είναι η αύξηση της διαμέτρου του δρομέα (μείωση ειδικής ισχύος). Το πρώτο παράδειγμα της

ενότητας αυτής, πραγματεύεται τη δυνατότητα εφαρμογής πτερυγίων με BTC, αξιολογώντας τόσο τα περιθώρια μείωσης των υλικών κατασκευής (σε κάποια σημεία του πτερυγίου ίσως αυξηθούν και λίγο) του πτερυγίου όσο και τη δυνατότητα επιμήκυνσης του. Στη δεύτερη εφαρμογή, αξιολογείται η δυνατότητα συνδυαστικής εφαρμογής BTC και FEC (γεωμετρικό και υλικό), αξιολογώντας παράλληλα και τα λειτουργικά φορτία (DLC-1.3) και τα φορτία που προκύπτουν όταν η μηχανή είναι εκτός λειτουργίας (DLC-6.x). Έχει ακολουθηθεί μια όμοια πρακτική με το κεφάλαιο 3, όπου τα λειτουργικά φορτία εντοπίζονται κατόπιν 150sec προσομοίωσης - ενώ η πράξη έχει δείξει ότι τα φορτία της σταθμισμένης μηχανής απαιτούν μεγαλύτερο χρονικό διάστημα (τουλάχιστον 300sec).

4.2.1. Ελαχιστοποίηση LCoE, με τεχνικές BTC

Το βελτιστοποιημένο σχέδιο του πτερυγίου (εφεξής “*modified*”), προκύπτει απ’τη διαδικασία MDAO (Multi-Disciplinary Aero-elastic Optimization) που έχει περιγραφεί στην ενότητα 2.5 και 3.2), με αντικειμενική συνάρτηση το LCoE. Οι μεταβλητές σχεδιασμού είναι:

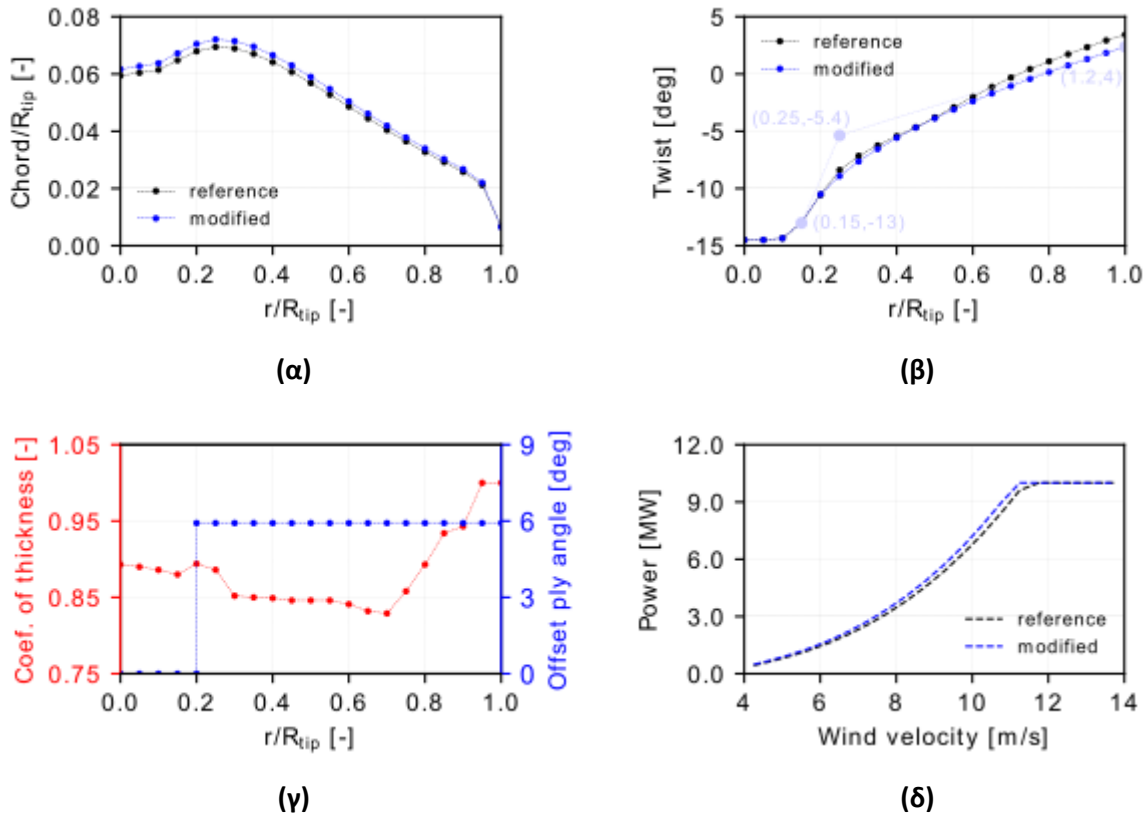
- Το πάχος των τοιχωμάτων του πτερυγίου: καθορίζεται από τις δευτερεύουσες μεταβλητές που αξιολογούνται απ’τον εσωτερικό βρόχο της διαδικασίας του Σχ. 3.3.
- Η γωνία του μονο-κατευθυντήριου υλικού – εκκινώντας απ’το 20% (κύρια μεταβλητή) την οποία χειρίζεται ο εξωτερικός βρόχος.
- Το μήκος του πτερυγίου και η κατανομή χορδής και συστροφής (κύριες μεταβλητές), οι τιμές των οποίων αξιολογούνται επίσης απ’τον βελτιστοποιητή – εξωτερικός βρόχος.

4.2.1.1. Περιγραφή διαδικασίας και αποτελέσματα

Κατά τη διαδικασία βελτιστοποίησης, όλες οι συνιστώσες της ανεμογεννήτριας αναφοράς DTU-10MW (π.χ. πύργος, γεννήτρια και κιβώτιο ταχυτήτων) εκτός απ’τα πτερύγια, παραμένουν αμετάβλητα. Αμετάβλητες επίσης, παραμένουν οι αεροτομές που χρησιμοποιούνται και οι σχετικές τους θέσεις. Η ελαχιστοποίηση του LCoE, υλοποιείται υπό την προϋπόθεση ότι η ονομαστική ισχύς της μηχανής παραμένει στα 10MW και η κατανομή των μέγιστων τιμών του κριτηρίου Tsai-Hill δεν υπερβαίνει τις αντίστοιχες τιμές του πτερυγίου αναφοράς. Η βελτιστοποιημένη πτέρυγα είναι κατά 3.7% μακρύτερη και κατά μόλις 1% βαρύτερη, με 5.9° στο μονο-κατευθυντήριο υλικό. Σε ετήσια βάση, ο νέος δρομέας παράγει 2.4% περισσότερη ενέργεια και έχει μειωμένο LCoE κατά 0.71%. Στον Πίνακα 4.1, συγκρίνονται τα κύρια χαρακτηριστικά του τροποποιημένου “*modified*” πτερυγίου, σε σχέση με την ανεμογεννήτρια αναφοράς καθώς και τον ελαφρύτερο δρομέα που προέκυψε απ’την εφαρμογή 3.3.2. (απλούστερη περίπτωση $N = 2$) – όπου συμβολίζεται με το ακρώνυμο L/R (Lightweight Rotor).

Πίνακας 4.1: Σύγκριση κύριων χαρακτηριστικών ανεμογεννήτριας DTU-10MW RWT, δρομέα L/R απ' την ενότητα 3.3.2. και τροποποιημένης διαμόρφωσης “modified”.

parameter	reference	L/R “modified”
Rated power [MW]	10.0	10.0
Rated omega [rpm]	9.6	9.3
Radius [m]	89.2	92.5
Blade mas [tn]	40.0	36.8
Combined moment at blade root [MNm]	64.0	59.9
AEP [GWh]	45.1	50.2
W/T cost [\$]	14.67	14.59
LCoE [\$/MWh]	44.96	44.64

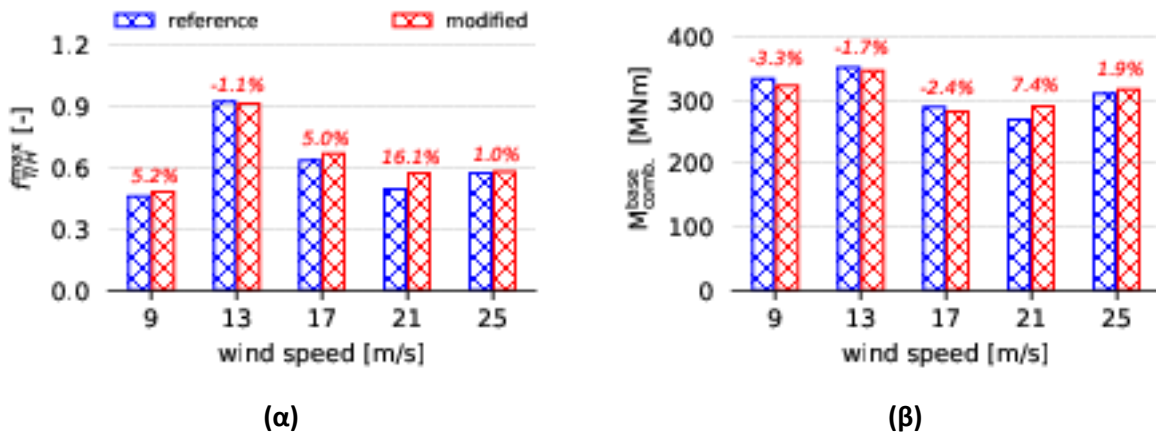


Σχήμα 4.2: Σύγκριση των μεταβλητών σχεδίασης μεταξύ πτερυγίου αναφοράς και τροποποιημένης διαμόρφωσης με ακτίνα $R_{tip} = 92.49m$: (α) κατανομή χορδής, (β) κατανομή συστροφής, (γ) κατανομή πάχους τοιχωμάτων και γωνίας μονο-κατευθυντήριου υλικού και (δ) καμπύλη ισχύος.

Στο Σχ. 4.2, συγκρίνονται οι μεταβλητές σχεδιασμού μεταξύ του πτερυγίου αναφοράς και του βέλτιστου “modified” σχεδιασμού. Συγκεκριμένα, στο Σχ. 4.2α και στο Σχ. 4.2β παρουσιάζονται οι κατανομές χορδής και συστροφής αντίστοιχα – ενώ στο Σχ. 4.2γ φαίνεται η κατανομή του συντελεστή μεταβολής του πάχους των τοιχωμάτων και η γωνία στο μονο-κατευθυντήριο υλικό που βρίσκεται στα ‘καπάκια’. Παρατηρείται ότι είναι εφικτή μια μεσοσταθμική μείωση του πάχους γύρω στο 11 – 12%, ενώ ο βέλτιστος σχεδιασμός έχει “μετατοπίσει” ελαφρώς προς τα αριστερά το μεταβλητό μέρος της καμπύλης ισχύος, μειώνοντας με τον τρόπο αυτό την ειδική ισχύ (βλέπε Σχ. 4.2δ).

4.2.1.2. Αξιολόγηση τροποποιημένου σχεδίου

Στην ενότητα αυτή, πραγματοποιείται η πιστοποίηση του βελτιστοποιημένου σχεδίου μέσω ενός υπο-συνόλου τριών 10min προσομοιώσεων, απ’τον φάκελο του κανονισμού IEC 61400-1. Στο Σχ. 4.3α, παρουσιάζονται οι μέγιστες τιμές του κριτηρίου Tsai-Hill που εμφανίζονται στο πτερύγιο για διάφορες ταχύτητες ανέμου, ακραίας τύρβης (DLC-1.3). Είναι σαφές, ότι οι μέγιστες τιμές του κριτηρίου παρουσιάζονται για ταχύτητα ανέμου 13 m/s, σε κάθε διαμόρφωση πτερυγίου – χωρίς να υπερβαίνουν σε καμία περίπτωση την μέγιστη τιμή Tsai-Hill του πτερυγίου αναφοράς. Στο Σχ. 4.3β, φαίνεται η συνισταμένη ροπή στη βάση του πύργου για κάθε ταχύτητα ανέμου. Η μέγιστη καταπόνηση, παρουσιάζεται επίσης στα 13 m/s - με τη βέλτιστη διαμόρφωση να εμφανίζει 1.7% χαμηλότερη μέγιστη τιμή, σε σχέση με το πτερύγιο αναφοράς.



Σχήμα 4.3: Ανάλυση ακραίων φορτίων, κατόπιν αερο-ελαστικών προσομοιώσεων DLC-1.3 για διάφορες ταχύτητες ανέμου: (α) μέγιστη τιμή κριτηρίου Tsai-Hill ($f_{T/H}^{max}$) και (β) μέγιστη τιμή συνισταμένης ροπής στη βάση του πύργου. Οι ποσοστιαίες διαφορές σε σχέση με την ανεμογεννήτρια αναφοράς, καταγράφονται πάνω απ’τις μπάρες.

4.2.2. Ελαχιστοποίηση LCoE, εστιάζοντας σε συνθήκες “ρελαντί”

Στην παρούσα ενότητα, περιγράφονται αναλυτικά οι διάφορες σχεδιαστικές διαμορφώσεις που εξετάζονται στη συνέχεια.

4.2.2.1. Περιγραφή σχεδίων

Στον Πίνακα 4.2, παρατίθενται οι πέντε σχεδιαστικές διαμορφώσεις (CASE A, B, C, D και E) που εξετάζονται, μαζί με τις τεχνικές παθητικού ελέγχου που εφαρμόζονται σε κάθε περίπτωση.

Πίνακας 4.2: Παθητικός έλεγχος ανεμογεννήτριας, με στόχο την ελαχιστοποίηση του LCoE.

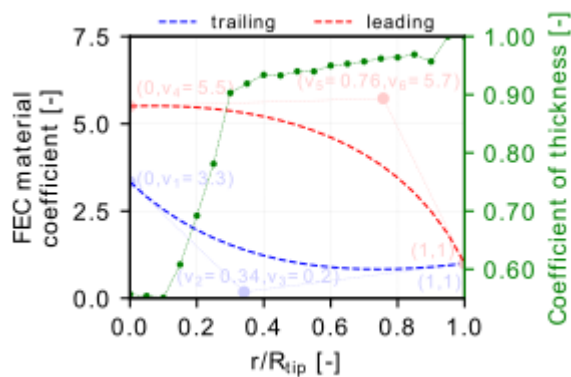
design	material FEC	geometrical FEC	re-twist	material BTC	Comments
reference					DTU-10MW RWT
CASE A	✓				FEC control
CASE B	✓	✓			FEC control
CASE C	✓	✓			FEC control
CASE D	✓	✓	✓		FEC with re-twist
CASE E	✓	✓	✓	✓	FEC&BTC with re-twist

- **CASE A:** προσεγγίζεται το υλικό FEC, με βάση την αύξηση του πάχους των περιοχών: “leading” υποπίεσης και “trailing” υπερπίεσης (βλέπε Σχ. 4.1, αριστερά). Εισάγεται ένας συντελεστής μεταβολής του πάχους των πιο πάνω περιοχών σε κάθε διατομή του πτερυγίου, υιοθετώντας καμπύλες Bezier. Εξετάζονται τρεις μεταβλητές σχεδιασμού/βελτιστοποίησης σε κάθε πλευρά (συνολικά έξι): (i) η τιμή της τεταγμένης του πρώτου σημείου (στη ρίζα του πτερυγίου) και (ii) οι τιμές (τεμημένη και τεταγμένη) του μεσαίου σημείου. Το τελευταίο σημείο ελέγχου, θεωρείται «παγωμένο». Εκτός από τους πιο πάνω συντελεστές, λαμβάνεται υπόψη ένας επιπλέον συντελεστής που αφορά το πάχος των τοιχωμάτων ολόκληρης της διατομής.
- **CASE B:** προσεγγίζεται το γεωμετρικό FEC, με βάση τη μετατόπιση των δύο ‘καπακιών’ (βλέπε Σχ. 4.1 δεξιά). Η μετατόπιση αυτή (σε κάθε πλευρά του πτερυγίου), υλοποιείται μέσω μιας καμπύλης Bezier τριών σημείων που εκφράζει την ποσοστιαία μετατόπιση κατά μήκος του πτερυγίου. Όπως και στην προηγούμενη προσέγγιση (CASE A), το τελευταίο σημείο ελέγχου είναι παγωμένο - ενώ μεταβλητές σχεδιασμού αποτελούν η τεταγμένη του πρώτου, καθώς και οι συντεταγμένες του μεσαίου σημείου. Επιπλέον, η εισαγωγή ενός ολικού συντελεστή επιτρέπει την συνολική μεταβολή των τοιχωμάτων κάθε διατομής.

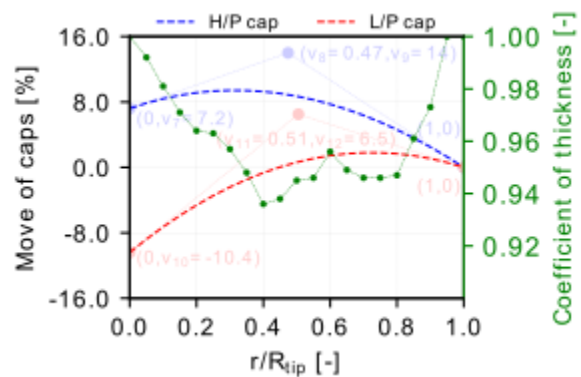
- **CASE C:** πρόκειται για τη συνδυαστική εφαρμογή των δυο πιο πάνω τεχνικών (υλικό και γεωμετρικό FEC). Προκειμένου να μειωθεί το πλήθος των μεταβλητών σχεδιασμού/βελτιστοποίησης, κρατήθηκε σταθερή η τιμή της τετμημένης του μεσαίου σημείου ελέγχου κάθε καμπύλης.
- **CASE D:** στην πραγματικότητα πρόκειται για την περίπτωση CASE C, επιτρέποντας αυτή τη φορά δύο επιπλέον μεταβλητές να καθορίσουν την κατανομή συστροφής του πτερυγίου. Συγκεκριμένα, και η συστροφή παραμετροποιείται με τρία σημεία Bezier, όπου οι τεταγμένες του σημείου στο $r/R_{tip} = 0.25$ καθώς και του τελευταίου (στο ακροπτερύγιο) αποτελούν τις επιπλέον μεταβλητές βελτιστοποίησης.
- **CASE E:** στην τελευταία περίπτωση, απλά εισάγεται μια ακόμα μεταβλητή σχεδιασμού η οποία καθορίζει τη γωνία στο μονο-κατευθυντήριο υλικό των ‘καπακιών’, ξεκινώντας από $r/R_{tip} = 0.20$. Στόχος του BTC αυτή τη φορά είναι να μετριάσει την τυχόν αρνητική επίδραση του FEC στα λειτουργικά ακραία φορτία.

4.2.2.2. Υλικό και γεωμετρικό FEC (CASE A και B)

Σε αυτή την ενότητα, παρουσιάζονται τα αποτελέσματα των πρώτων δυο σχεδιαστικών διαμορφώσεων (CASE A και B). Κάθε μια απ’αυτές, εξετάζει μεμονωμένα τις δυο προσεγγίσεις FEC που έχουν περιγραφεί πιο πάνω.

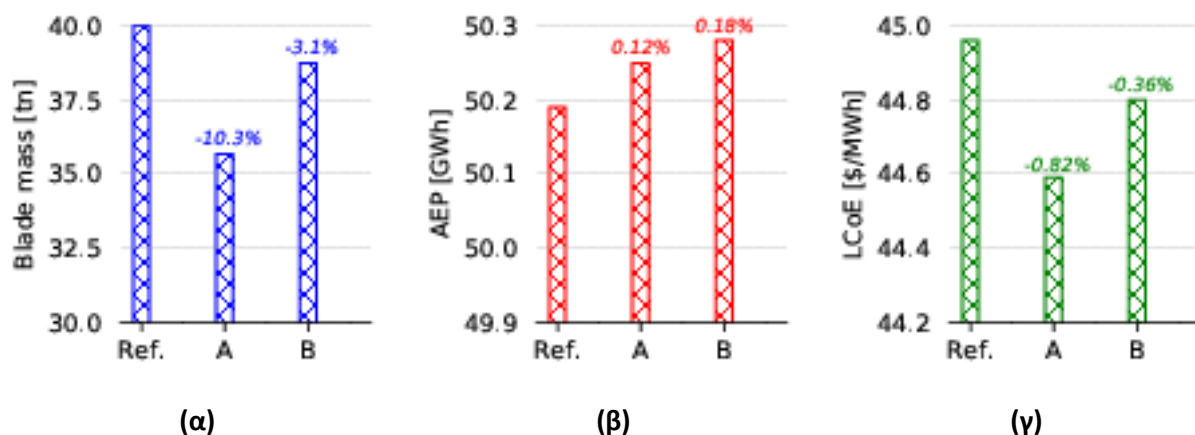


Σχήμα 4.4: Υλικό FEC (CASE A): συντελεστές μεταβολής πάχους των υλικών “TRIAx” και “UNIAX”, για τις περιοχές “trailing” (υπερπίεσης) και “leading” (υπο-πίεσης), καθώς και ο συνολικός συντελεστής πάχους που αφορά όλη τη διατομή (πράσινο χρώμα).



Σχήμα 4.5: Γεωμετρικό FEC (CASE B): κατανομές ποσοστιαίας μετατόπισης των ‘καπακιών’ του πτερυγίου σε σχέση με τη χορδή, καθώς και ο συνολικός συντελεστής πάχους που αφορά όλη τη διατομή (πράσινο χρώμα).

Οι βέλτιστες καμπύλες Bezier (μαζί με τις τιμές των μεταβλητών σχεδιασμού) για τη σχεδιαστική διαμόρφωση CASE A, παρουσιάζεται στο Σχ. 4.4. Επιπλέον, στο σχήμα αυτό παρουσιάζεται η κατανομή του συνολικού συντελεστή μεταβολής των τοιχωμάτων του πτερυγίου (πράσινο χρώμα). Είναι γεγονός, ότι για την περιοχή “leading” απαιτείται μεγαλύτερη αύξηση του πάχους της σε σχέση με την περιοχή “trailing”. Συγκεκριμένα, στη ρίζα οι αντίστοιχες τιμές του συντελεστή μεταβολής πάχους είναι 5.5 και 3.3. Φυσικά, αυτή η σχετικά μεγάλη αύξηση του πάχους συνοδεύεται και από ένα επιπλέον συντελεστή (0.5 για τη ρίζα), που εφαρμόζεται σε όλες τις περιοχές της διατομής. Το πιο πάνω σχήμα, επιτρέπει τη μείωση της μάζας του πτερυγίου κατά 10.3% και του LCoE κατά 0.82%. Παράλληλα, στο Σχ. 4.5 παρουσιάζονται οι βέλτιστες καμπύλες για το CASE B (γεωμετρικό FEC). Όπως φαίνεται, το ‘καπάκι’ στην πλευρά υπο-πίεσης μετατοπίζεται προς το πρόσθιο άκρο κατά 10.4% στη ρίζα του πτερυγίου - ενώ η αντίστοιχη μετατόπιση του ‘καπακιού’ υπερ-πίεσης είναι περίπου 7.2% προς την αντίθετη κατεύθυνση. Ωστόσο, η επίδραση αυτής της προσέγγισης, φαίνεται να είναι πολύ πιο περιορισμένη (μείωση μάζας πτερυγίου μόλις 3.1%) σε σχέση με την προηγούμενη (βλέπε Σχ. 4.6).

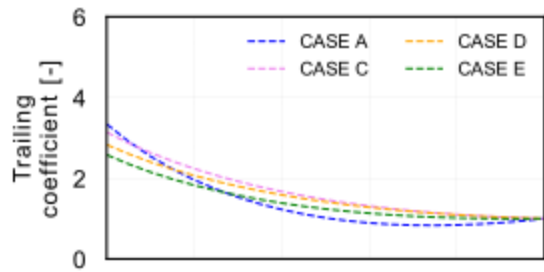


Σχήμα 4.6: (α) μάζα πτερυγίου, (β) ετήσια παραγωγή ενέργειας και (γ) κόστος ενέργειας LCoE για τις περιπτώσεις υλικού FEC (CASE A) και γεωμετρικού FEC (CASE B), καθώς και οι ποσοστιαίες τους διαφορές.

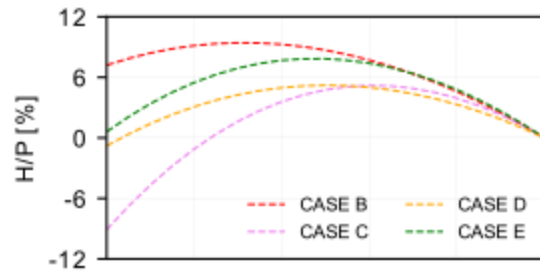
4.2.2.3. Συνδυαστική εφαρμογή τεχνικών παθητικού ελέγχου (CASE C, D και E)

Στην ενότητα αυτή, εξετάζονται τα συνδυαστικά σχέδια CASE C, D και E. Στα Σχ. 4.7 και 4.8, παρουσιάζονται οι ακτινικές κατανομές των συντελεστών πάχους των υλικών και μετατόπισης αντίστοιχα. Φαίνεται ότι η συνδυασμένη εφαρμογή των δυο τεχνικών FEC δεν μεταβάλλει σημαντικά τις παραμέτρους σχεδιασμού του υλικού FEC, σε αντίθεση με τις παραμέτρους του γεωμετρικού FEC (βλέπε Σχ. 4.8). Επίσης, είναι ενδιαφέρον να σημειωθεί ότι στο CASE C, η βέλτιστη μετατόπιση των ‘καπακιών’ της επιφάνειας υπερ-πίεσης είναι προς την ακμή πρόσπτωσης (L/E), ενώ το ‘καπάκι’ της επιφάνειας υπο-πίεσης παραμένει σχεδόν αμετακίνητο. Αυτό, μπορεί να αιτιολογηθεί απ’το γεγονός

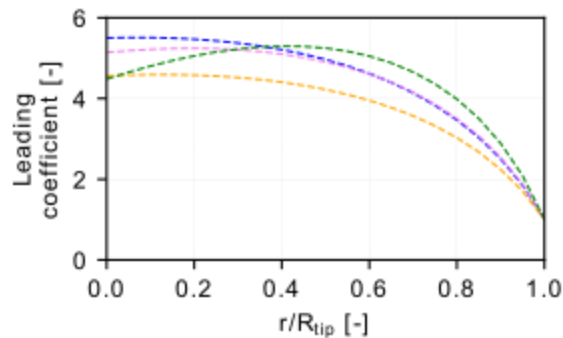
ότι με τον τρόπο αυτό μένει περισσότερος “χώρος” της περιοχής “trailing” της πλευράς υπερ-πίεσης, επιτρέποντας έτσι την καλύτερη αξιοποίηση του υλικού FEC. Η μείωση της μάζας που επιτυγχάνεται στο CASE C είναι 13.3%, το οποίο αποτελεί το άθροισμα των μειώσεων που προκαλούνται απ’τις διαμορφώσεις CASES A και B.



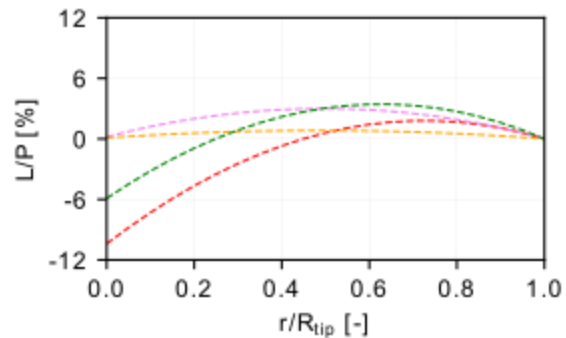
(α)



(α)



(β)



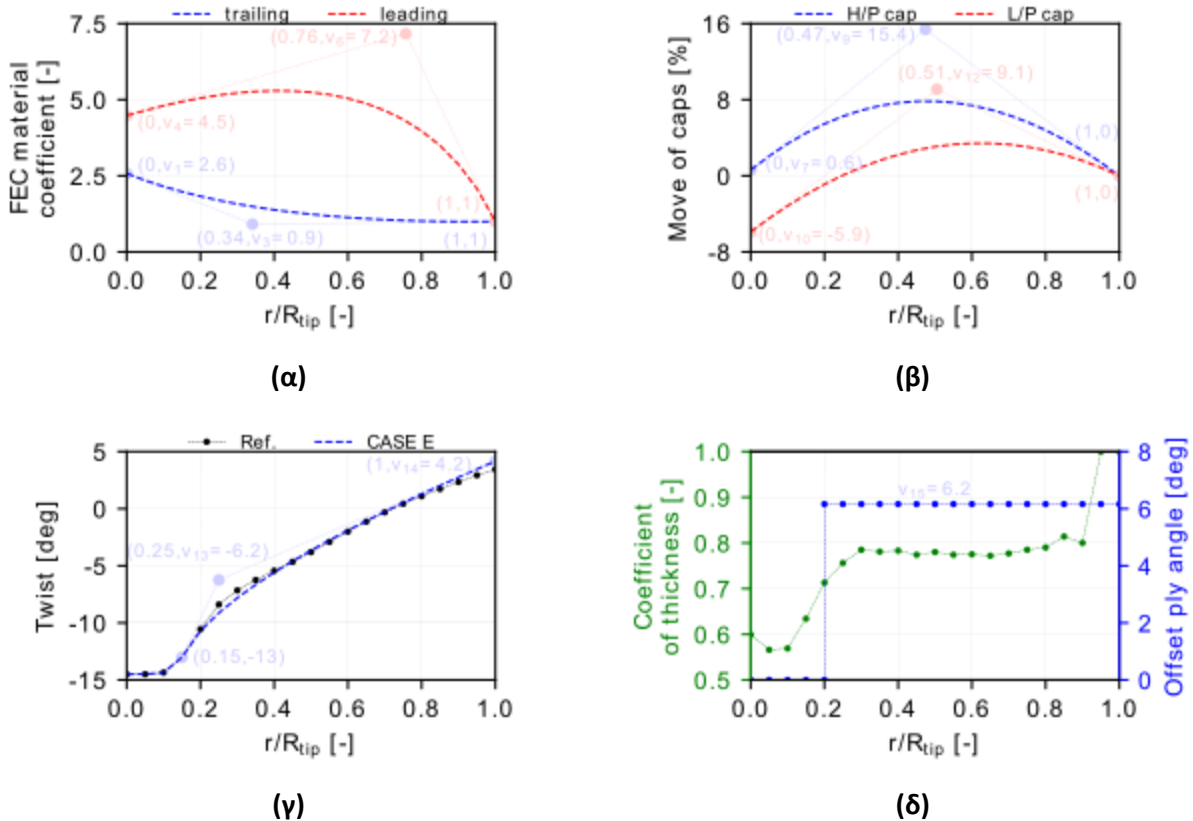
(β)

Σχήμα 4.7: Κατανομή συντελεστών υλικού FEC για τις περιοχές: (α) “leading” και (β) “trailing” των διαμορφώσεων: A, C, D και E.

Σχήμα 4.8: Κατανομή συντελεστών γεωμετρικού FEC για τις επιφάνειες: (α) υπερ-πίεσης και (β) υπο-πίεσης των διαμορφώσεων: B, C, D και E.

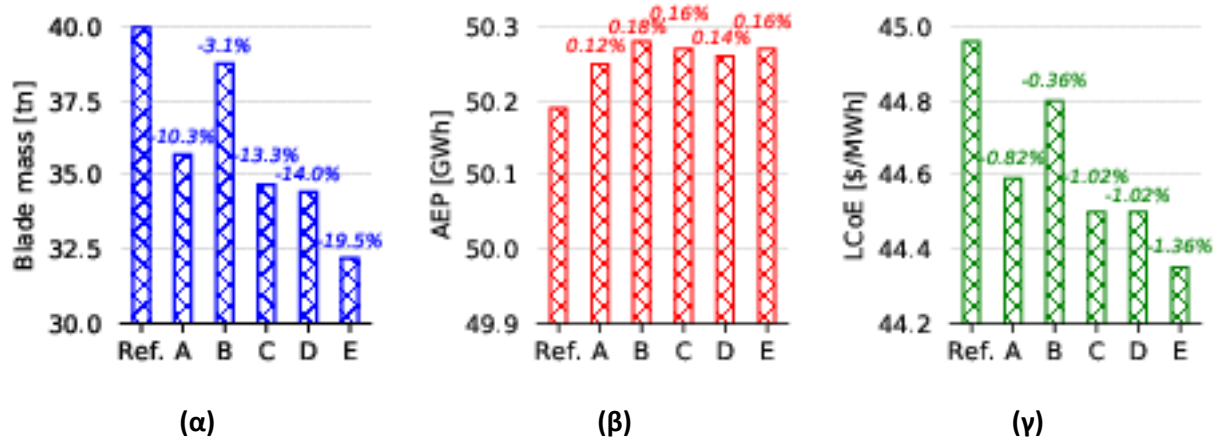
Στην περίπτωση CASE D, ο επανα-σχεδιασμός της συστροφής λειτουργεί ως επιπλέον μηχανισμός ρύθμισης της δομικής συστροφής. Το γεγονός αυτό, οδηγεί σε περαιτέρω μείωση της μάζας του πτερυγίου (περίπου 14%), σε σχέση με την προηγούμενη σχεδιαστική διαμόρφωση. Τέλος, η διαμόρφωση CASE E συνδυάζει όλους τους μηχανισμούς και τα αποτελέσματα των βέλτιστων τιμών των παραμέτρων της, παρουσιάζονται συνοπτικά στο Σχ. 4.9. Συγκεκριμένα, η βέλτιστη γωνία μονοκατευθυντήριου υλικού (βλέπε Σχ. 4.9δ) είναι 6.2° – ενώ μια μέση μείωση (συνολικός συντελεστής πάχους διατομών) είναι ~ 0.75 . Η κατανομή της συστροφής διαμορφώνεται με τρόπο ώστε να αυξηθεί η δομική συστροφή του πτερυγίου, χωρίς να προκύπτουν μεγάλες απώλειες ενέργειας λόγω της

εφαρμογής BTC. Όπως έχει ήδη παρατηρηθεί (βλέπε CASE C και D), το υλικό FEC κυριαρχεί μεταξύ των τεχνικών παθητικής σύζευξης των κατευθύνσεων πτερύγισης και περιστροφής. Σε αντίθεση με τις περιπτώσεις CASE C και D, επιτυγχάνεται μια σημαντική μετατόπιση του ‘καπακιού’ της πλευράς υποπίεσης προς το L/E (βλέπε Σχ. 4.9β).



Σχήμα 4.9: CASE E: κατανομή (α) υλικού FEC, (β) γεωμετρικού FEC, (γ) συστροφής και (δ) γωνίας μονο-κατευθυντήριου υλικού καθώς και συνολικού συντελεστή μεταβολής πάχους τοιχωμάτων.

Η σχεδιαστική διαμόρφωση του CASE E, έχει ένα σημαντικό αποτύπωμα στη μείωση της μάζας του πτερυγίου (περίπου 19.5%) καθώς και 1.36% στο σταθμισμένο κόστος ενέργειας (LCoE). Τα συγκεντρωτικά αποτελέσματα κάθε σχεδίου, παρουσιάζονται στο Σχ. 4.10. Τέλος, στον Πίνακα 4.3 παρουσιάζονται λεπτομερώς οι τιμές των μεταβλητών σχεδιασμού που προέκυψαν για κάθε σχέδιο βελτιστοποίησης.



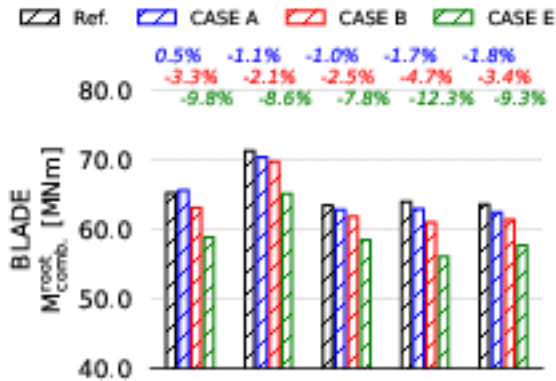
Σχήμα 4.10: (α) μάζα πτερυγίου, (β) ετήσια παραγωγή ενέργειας και (γ) κόστος ενέργειας (LCoE), καθώς και οι ποσοστιαίες τους διαφορές.

Πίνακας 4.3: Αποτελέσματα των μεταβλητών σχεδιασμού των σχεδιαστικών διαμορφώσεων που εξετάστηκαν. Οι τιμές με κόκκινο χρώμα, αντιστοιχούν στις μεταβλητές σχεδιασμού με σταθερή τιμή.

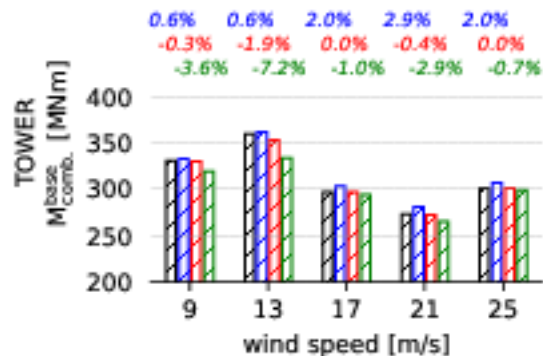
	CASE A	CASE B	CASE C	CASE D	CASE E
V1 (trailing/root C/P in y-axis)	3.34	-	3.14	2.83	2.58
V2 (trailing/interm. C/P in x-axis)	0.34	-	0.34	0.34	0.34
V3 (trailing/interm. C/P in y-axis)	0.18	-	1.18	1.18	0.91
V4 (leading/root C/P in y-axis)	5.50	-	5.14	4.56	4.48
V5 (leading/interm. C/P in x-axis)	0.76	-	0.76	0.76	0.76
V6 (leading/interm. C/P in y-axis)	5.73	-	5.90	4.92	7.17
V7 (H/P cap/root C/P in y-axis)	-	7.20	-9.10	-0.80	0.60
V8 (H/P cap/interm. C/P in x-axis)	-	0.47	0.47	0.47	0.47
V9 (H/P cap/interm. C/P in y-axis)	-	14.00	13.80	10.80	15.40
V10 (L/P cap/root C/P in y-axis)	-	-10.40	0.20	0.10	-5.90
V11 (L/P cap/interm. C/P in x-axis)	-	0.51	0.51	0.51	0.51
V12 (L/P cap/interm. C/P in y-axis)	-	6.50	5.90	1.60	9.10
V13 (twist/interm. C/P in y-axis)	-	-	-	-5.54	-6.24
V14 (twist/tip C/P)	-	-	-	2.47	4.16
V15 (BTC angle)	-	-	-	-	6.16
Number of design variables	6	6	8	10	11

4.2.2.4. Πιστοποίηση βέλτιστων σχεδίων

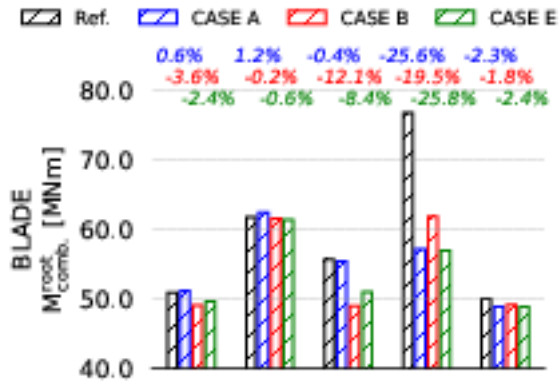
Στην ενότητα αυτή, πραγματοποιείται η πιστοποίηση των σχεδίων CASE A, B και E μέσω 10min αερο-ελαστικών προσομοιώσεων. Κάθε διαμόρφωση, εξετάζεται για διάφορες ταχύτητες ανέμου σε έντονη τύρβη (DLC-1.3) και σε διάφορες γωνίες ανέμου σε κατάσταση “ρελαντί” (DLC-6.x), βλέπε Σχ. 4.11 και Σχ. 4.12.



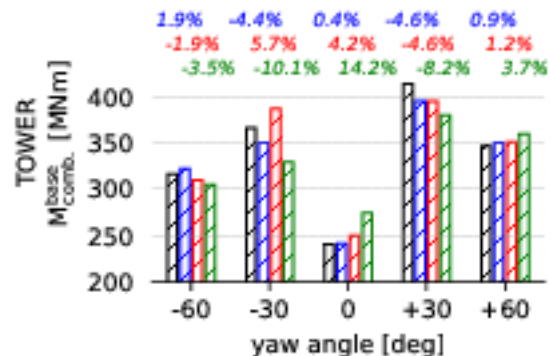
(α)



(β)



(α)



(β)

Σχήμα 4.11: Ακραία φορτία DLC-1.3 για διάφορες ταχύτητες ανέμου (περιλαμβάνονται οι συντελεστές ασφαλείας), για τη μέγιστη συνισταμένη ροπή: (α) στη ρίζα του πτερυγίου και (β) στη βάση του πύργου.

Σχήμα 4.12: Ακραία φορτία DLC-6.x για διάφορες γωνίες ανέμου (περιλαμβάνονται οι συντελεστές ασφαλείας), για τη μέγιστη συνισταμένη ροπή: (α) στη ρίζα του πτερυγίου και (β) στη βάση του πύργου.

Όλες οι διαμορφώσεις που εξετάστηκαν, περιορίζουν σημαντικά το μέγιστο φορτίο της DTU-10MW RWT (βλέπε Σχ. 4.12α), που παρατηρείται στο DLC-6.x για γωνία +30°. Μάλιστα, η μέγιστη μείωση επιτυγχάνεται για το CASE E, 25.8%. Παρόμοιο ποσοστό μείωσης, φαίνεται να παρουσιάζει και το CASE

A - όχι όμως το CASE B (μόλις 19.5%). Προφανώς, ο περιορισμός των ταλαντώσεων του πτερυγίου κατά τη διάρκεια της μη-λειτουργίας της μηχανής, έχει ευεργετικό αποτέλεσμα και στα φορτία του πύργου (βλέπε Σχ. 4.12β). Όπως φαίνεται στο Σχ. 4.11α, τα ακραία λειτουργικά φορτία του πτερυγίου παρουσιάζουν χαμηλότερες τιμές για όλα τα σχέδια. Όπως αναμενόταν, η χρήση BTC (CASE E) έχει ευεργετικά αποτελέσματα στα λειτουργικά φορτία τόσο στη ρίζα του πτερυγίου όσο και στη βάση του πύργου.

Αυτή η σελίδα μένει κενή

Κεφάλαιο 5

5. Συμπεράσματα

Στο κεφάλαιο αυτό, συνοψίζονται τα σημαντικότερα συμπεράσματα και οι παρατηρήσεις της εργασίας. Εκτός των άλλων, παρατίθεται μια σειρά από αναπάντητα ερωτήματα που μπορούν να τροφοδοτήσουν τη μελλοντική έρευνα.

5.1. Γενικές παρατηρήσεις και συμπεράσματα

Στόχος της εργασίας, ήταν η ανάπτυξη ενός πολυ-πεδιακού περιβάλλοντος σχεδιασμού και βελτιστοποίησης (Multi-Disciplinary Aero-elastic Optimization – MDAO) πτερυγίων ανεμογεννήτριας. Στο περιβάλλον αυτό, οι αεροδυναμικές παράμετροι (π.χ. κατανομή χορδής και συστροφής) καθώς και οι κατασκευαστικές (π.χ. κατανομή του πάχους των υλικών και εφαρμογή παθητικού ελέγχου φορτίων BTC ή/και FEC), βελτιστοποιούνται στον ίδιο βρόχο. Στόχος του σχεδιασμού, είναι η ελαχιστοποίηση του σταθμισμένου κόστους ενέργειας (Levelized Cost of Electricity – LcoE). Ο χειρισμός των μεταβλητών σχεδιασμού, πραγματοποιείται με μια απ'τις μεθόδους βελτιστοποίησης: COBYLA, SLSQP και Newton, η οποία αποτελεί τον πυρήνα του πιο πάνω MDAO περιβάλλοντος σχεδιασμού - ενώ διάφορα υπολογιστικά εργαλεία αξιοποιούνται για την εκτίμηση των μηχανικών ιδιοτήτων της κατασκευής, των φορτίων και του κόστους ενέργειας:

- σέρβο-αέρο-ελαστικός επιλύτης hGAST
- εργαλείο ανάλυσης διατομών
- μοντέλο κόστους ανεμογεννητριών

Σε πρώτη φάση, στόχος της διαδικασίας MDAO είναι η ελαχιστοποίηση της αναγκαίας μάζας υλικών κατασκευής πτερυγίων (CAPital EXpenditure – CAPEX), κατόπιν εφαρμογής τεχνικών παθητικού ελέγχου φορτίων. Εξετάστηκαν τρεις εφαρμογές/παραδείγματα:

- Στην πρώτη εφαρμογή, αξιολογείται η δυνατότητα κατασκευής πτερυγίων με κύρτωση (sweep). Η καμπυλότητα του πτερυγίου, προσεγγίζεται με μια καμπύλη Bezier – τα σημεία ελέγχου της οποίας αποτελούν τις μεταβλητές σχεδιασμού/βελτιστοποίησης. Το αποτέλεσμα που προέκυψε ήταν ένα πτερύγιο με 8.6% λιγότερη μάζα υλικών.
- Στη δεύτερη εφαρμογή, αξιολογείται η δυνατότητα τμηματικής στροφής του μονο-κατευθυντήριου υλικού που βρίσκεται στα ‘καπάκια’ του πτερυγίου. Διαπιστώθηκε ότι για την ανεμογεννήτρια αναφοράς DTU-10MW RWT, μια μέτρια γωνία $5^\circ - 7.5^\circ$ απ’το 15 – 30% του πτερυγίου, μπορεί να οδηγήσει σε μείωση της μάζας του κατά 8%. Μια πιο περίπλοκη διάταξη, με σταδιακή αύξηση της γωνίας (καθώς προσεγγίζεται το ακροπτερύγιο), μπορεί να οδηγήσει μέχρι και σε 10% μείωση στη μάζας του πτερυγίου.
- Στο τελευταίο παράδειγμα, αξιολογήθηκε η απλούστερη διάταξη της προηγούμενης εφαρμογής σε ένα τροποποιημένο πτερύγιο (με FEC 3%), το οποίο παρουσιάζει περιορισμένες ταλαντώσεις κατά την στάθμευση του. Το πρόβλημα αντιμετωπίστηκε με διάφορες τεχνικές βελτιστοποίησης, οι οποίες εξετάστηκαν ως προς την ταχύτητα σύγκλισης και την ευστάθεια τους. Όλες οι μέθοδοι έδωσαν παρόμοιες τελικές βέλτιστες λύσεις (δηλαδή πτερύγιο με μειωμένη μάζα κατά περίπου 8%).

Στη συνέχεια, πραγματοποιήθηκε πολυ-πεδιακός σχεδιασμός του δρομέα ανεμογεννήτριας 10MW. Στόχος, ήταν η ελαχιστοποίηση του LCoE, συνδυάζοντας με βέλτιστο τρόπο τις διάφορες τεχνικές παθητικού ελέγχου (BTC και FEC), μαζί με τα κατασκευαστικά/γεωμετρικά χαρακτηριστικά της μηχανής (κατανομή χορδής και συστροφής). Δυο εφαρμογές, έχουν παρουσιαστεί:

- Στην πρώτη εφαρμογή, ως μεταβλητές σχεδιασμού θεωρήθηκαν το μήκος του πτερυγίου, η κατανομή χορδής και συστροφής, η κατανομή του πάχους των τοιχωμάτων του πτερυγίου, καθώς και η γωνία του μονο-κατευθυντήριου υλικού. Το αποτέλεσμα που προέκυψε από την παραπάνω ανάλυση, ήταν ένα πτερύγιο με 3.7% μεγαλύτερο μήκος και μόλις 1% βαρύτερο, με εισαγωγή μιας μέτριας γωνία 5.9° στο UD υλικό που βρίσκεται στα ‘καπάκια’.
- Στη δεύτερη εφαρμογή, αξιολογήθηκαν πέντε σχεδιαστικές διαμορφώσεις (CASE A-E) οι οποίες σταδιακά ενσωματώνουν διάφορες τεχνικές σύζευξης των κατευθύνσεων πτερύγισης και περιστροφής (υλικό και γεωμετρικό FEC), καθώς και την τεχνική σύζευξης κάμψης/στρέψης (BTC). Το αποτέλεσμα που προέκυψε, ήταν μια σειρά προτεινόμενων πτερυγίων που περιορίζουν σημαντικά τόσο τα λειτουργικά φορτία της μηχανής (DLC-1.3), όσο και τα φορτία κατά τη μη-λειτουργία (DLC-6.x) – κατάσταση “ρελαντί”. Φυσικά, το αποτέλεσμα στη μείωση της μάζας και του LCoE ποικίλει από σχέδιο – σε σχέδιο και φτάνει το 19.5% και 1.36% αντίστοιχα, για την περίπτωση του συνδυασμού όλων των τεχνικών ελέγχου.

5.2. Μελλοντική έρευνα

Φιλοδοξία της εργασίας αυτής ήταν να συμβάλει στην ανάπτυξη και κατανόηση νέων τεχνικών σχεδιασμού και διαμόρφωσης πτερυγίων ανεμογεννητριών. Στην κατεύθυνση αυτή, η εργασία έδωσε απαντήσεις σε πλήθος ερωτημάτων που άπτονται της βέλτιστης χρήσης καινοτόμων μεθόδων

παθητικού ελέγχου. Παρά τ'αυτά, παραμένει μια σειρά από αναπάντητα ερωτήματα, τα οποία μπορούν να αποτελέσουν το εφαλτήριο για μελλοντική έρευνα. Αυτα συνοψίζονται:

- στην επέκταση του βέλτιστου σχεδιασμού και σε άλλες επιμέρους συνιστώσες της ανεμογεννήτριας (π.χ. πύργος, κιβώτιο ταχυτήτων κ.λπ.) ή ακόμη και στο σύνολο της. Μια τέτοια έρευνα, στην πραγματικότητα θα αποτελούσε τη φυσική συνέχεια της παρούσας εργασίας,
- στη 3D ανάλυση, με χρήση τρισδιάστατων εμπορικών πακέτων (π.χ. ANSYS ή ABAQUS), ιδιαίτερα για την αποτίμηση της πιθανότητας αστοχίας σε λυγισμό,
- στο σχεδιασμό νέων πολυ-μεγάλων υπεράκτιων ανεμογεννητριών $> 20MW$.
- στην ανάπτυξη νέων μοντέλων κόστους που θα προβλέπουν την επιπλέον οικονομική επιβάρυνση απ'τη χρήση τεχνικών παθητικού ελέγχου.

5.3. Χρηματοδότηση

Η διατριβή, έχει στηριχθεί οικονομικά από τις ακόλουθες πηγές:

- Η έρευνα έχει υποστηριχθεί απ'το Ελληνικό Ίδρυμα Έρευνας & Καινοτομίας (ΕΛ.ΙΔ.Ε.Κ.) στο πλαίσιο της 2^{ης} Προκήρυξης Υποτροφιών ΕΛ.ΙΔ.Ε.Κ. για Υποψήφιους Διδάκτορες (Αριθμός Αίτησης: 867).
- Η υλοποίηση της διδακτορικής διατριβής συγχρηματοδοτήθηκε απ'την Ελλάδα και την Ευρωπαϊκή Ένωση (Ευρωπαϊκό Κοινωνικό Ταμείο) μέσω του Επιχειρησιακού Προγράμματος «Ανάπτυξη Ανθρώπινου Δυναμικού, Εκπαίδευση και Διά Βίου Μάθηση», 2014-2020, στο πλαίσιο της Πράξης «Ενίσχυση του ανθρώπινου δυναμικού μέσω της υλοποίησης διδακτορικής έρευνας Υπόδραση 2: Πρόγραμμα χορήγησης υποτροφιών ΙΚΥ σε υποψήφιους διδάκτορες των ΑΕΙ της Ελλάδας». (Αριθμός Σύμβασης: 2022-050-0502-52636).
- Ιδιωτική εταιρεία έρευνας ανανεώσιμων πηγών ενέργειας "iWind" (για περισσότερες λεπτομέρειες, επισκεφτείτε τη σελίδα <https://www.iwind.gr> ή e-mail: info@iwind.gr).



Αυτή η σελίδα μένει κενή

Βιβλιογραφία

- [1] 'Our World In Data', <https://ourworldindata.org/>
- [2] Blair N., Bolinger M., Elliott D., George R., Goldberg M., Hand M., Heimiller D., Hem T., Miller B., O' Connell R., Schwartz M., Tegen S. and Wisler R. **(2008)** '20% Wind Energy By 2030: Executive Summary', DOE/GO-102008-2578, <http://www.nrel.gov/docs/fy08osti/41869.pdf>
- [3] REPowerEU Plan **(2022)** 'Communication From The Commission To The European Parliament, The European Council, The Council, The European Economic And Social Committee And The Committee Of The Regions', COM(2022) 230 final
- [4] Chaviaropoulos P., Politis E., Lekou D., Sørensen N., Hansen M., Bulder B., Winkelaar D., Lindenburg C., Saravanos D., Philippidis T., Galiotis C., Hansen M. and Kossivas T. **(2006)** 'Enhancing The Damping Of Wind Turbine Rotor Blades, The Dampblade Project', Wind Energ. 2006; 9:163-177, doi: 10.1002/we.183
- [5] 'STABCON', <https://cordis.europa.eu/project/id/ENK5-CT-2002-00627>
- [6] 'UpWind', <https://cordis.europa.eu/project/id/19945>
- [7] 'INNWIND.EU', <https://cordis.europa.eu/project/id/308974>
- [8] 'AVATAR', <https://cordis.europa.eu/project/id/608396>
- [9] Sieros G., Chaviaropoulos P., Sørensen D., Bilder H. and Jamieson P. **(2012)** 'Upscaling Wind Turbines Theoretical And Practical Aspects And Their Impact On The Cost Of Energy', Wind Energy, 15(1),3-17, doi: 10.1002/we.527
- [10] Bossanyi E. **(2003)** 'Individual Blade Pitch Control For Load Reduction', Wind Energy, 6(2), 119-128, doi: 10.1002/we.76
- [11] Lackner M. and Kuik G. **(2010)** 'A Comparison Of Smart Rotor Control Approaches Using Trailing Edge Flaps And Individual Pitch Control', Wind Energy, 13(2-3), 117-134, doi: 10.1002/we.353
- [12] Ashwill T., Kanaby G., Jackson K. and Zuteck M. **(2010)** 'Development Of The Swept Twist Adaptive Rotor (STAR) Blade', 48th AIAA Aerospace Sciences Meeting Including the New Horizons Forum and Aerospace Exposition, doi: 10.2514/6.2010-1582

-
- [13] Knight & Carve Wind Group **(2009)** *'Sweep-Twist Adaptive Rotor Blade'*, Final Project Report, SAND2009-8037, Sandia National Laboratories, Albuquerque, NM, December 2009, <https://www.osti.gov/servlets/purl/973353>
- [14] Brøndsted P., Lilholt H. and Lystrup A. **(2005)** *'Composite Materials For Wind Power Turbine Blades'*, Annual Review of Materials Research, 35(1), 505-538, doi: 10.1146/annurev.matsci.35.100303.110641
- [15] Jones R. **(1999)** *'Mechanics Of Composite Materials'*, 2nd edition, ISBN: 978131527296, <https://doi.org/10.1201/9781498711067>
- [16] Chordis D. **(2012)** *'Structural Analysis Of Composite Wind Turbine Blades'*, PhD thesis, ISBN: 978-3-319-00863-9, doi: 10.1007/978-3-319-00864-6, <http://www.springer.com/series/11859>
- [17] Mansfield E. and Sobey A. **(1979)** *'The Fibre Composite Helicopter Blade, Part 1: Stiffness Properties And Part 2: Prospects For Aeroelastic Tailoring'*, <https://doi.org/10.1017/S0001925900008623>
- [18] Chopra I. and Hong C. **(1985)** *'Aero-Elastic Stability Analysis Of A Composite Rotor Blade'*, J. of the American Helicopter Society, 30(2), 57-67, doi: 10.4050/jahs.30.57
- [19] Sundar D., Narasimalu S. and Yaiwen Y. **(2018)** *'Study Of Bend To Twist Coupling Of Composite Laminates For Passive Load Alleviation Of A Wind Turbine Blade'*, 2018 Asian Conference on Energy, Power and Transportation Electrification (ACEPR), doi: 10.1109/accept.2018.8610671
- [20] Meng H., Lien F., Glinka G. and Geiger P. **(2018)** *'Study On Fatigue Life Of Bend-Twist Coupling Wind Turbine Blade Based On Anisotropic Beam Model And Stress-Based Fatigue Analysis Method'*, Composite Structures, 208, 678-701, doi: 10.1016/j.compstruct.2018.10.032
- [21] Croce A., Sartori L., Lunghini M., Clozza L., Bortolotti P. and Bottasso C. **(2016)** *'Lightweight Rotor Design By Optimal Spar Cap Offset'*, J. of Phys.: Conf. Ser., 753, 062003, doi: 10.1088/1742-6596/753/6/062003
- [22] Lobitz D., Veers P. and Migliore P. **(1996)** *'Enhanced Performance Of HAWTS Using Adaptive Blades'*, Proceedings of the Wind 1996 ASME Wind Energy Symposium, January 29-February 2 1996
- [23] Fedorov V. **(2012)** *'Bend-Twist Coupling Effects In Wind Turbine Blades'*, PhD thesis, https://backend.orbit.dtu.dk/ws/portalfiles/portal/54637711/PhD_Thesis_Vladimir_Fedorov.pdf
- [24] Ståblein R. and Hansen H. **(2016)** *'Effect Of Turbulence On Power For Bend-Twist Coupled Blades'*, J. of Phys.: Conf. Ser., 753, 042018, doi: 10.1088/1742-6596/753/4/042018
- [25] Wang K., Riziotis V. and Voutsinas S. **(2016)** *'Aero-Elastic Stability Of Idling Wind Turbines'*, J. of Phys.: Con. Ser., 753, 042008, doi: 10.1088/1742-6596/753/4/042008
- [26] Bak C., Zahle F., Bitsche R., Kim T., Yde A., Henriksen L., Natarajan A. and Hansen M. **(2013)** *'Description Of The DTU 10MW Reference Wind Turbine'*, DTU Wind Energy Report-I-0092, https://backend.orbit.dtu.dk/ws/portalfiles/portal/55645274/The_DTU_10MW_Reference_Turbine_Christian_Bak.pdf

- [27] Ashuri T., Zaaijer M., Martins J. and Zhang J. (2016) *'Multi-disciplinary Design Optimization Of Large Wind Turbines – Technical, Economic And Design Challenges'*, Energy Conversion and Management, 123, 56-70, doi: 10.1016/j.enconman.2016.06.004
- [28] Manolas D., Riziotis V., Papadakis G. and Voutsinas S. (2020) *'Hydro-servo-aero-elastic Analysis of Floating Offshore Wind Turbines'*, J. of Fluids, 5(4), 200, special issue on Wind and Wave Renewable Energy Systems, doi: 10.3390/fluids5040200
- [29] IEC 61400-1, IEC, 2003. 188184CDV, Edited by TC88-MT1 25-26, May 2004, 3rd edition, pp. 26-29
- [30] Madsen H., Riziotis V., Zahle F., Larsen J., Politis E., Hanses L., Snel H. and Grasso F. (2012) *'BEMT Modeling Of Inflow With Shear In Comparison With Advanced Model Results'*, Wind Energy 2012, 15, 63-81, doi: 10.1002/we.493
- [31] Bottasso C., Croce A., Savini B., Sirchi W. and Trainelli L. (2006) *'Aero-servo-elastic Modeling And Control Of Wind Turbines Using Finite-element Multibody Procedures'*, Multibody Syst Dyn (2006) 16:291-308, doi: 10.1007/s11044-006-9027-1
- [32] Hodges D. (2006) *'Non-linear Composite Beam Theory'*, ISBN: 978-1-56347-697-6, <https://doi.org/10.2514/4.866821>
- [33] Sravanos D., Varelis D., Plagianakos T. and Chrisochoidis N. (2006) *'A Shear Beam Finite Element For The Damping Analysis Of Tubular Laminated Composite Beams'*, J. of Sound and Vibration 291 (3-5), 802-823, doi: 10.1016/j.jsv.2005.06.045
- [34] Chordis D., Varelis D. and Saravanos D. (2012) *'Prediction Of Material Coupling Effect On Structural Damping Of Composite Beams And Blades'*, J. of Composite Structures, 94(5), 1646-1655, doi: 10.1016/j.compstruct.2011.12.004
- [35] Wu W., Cheng H. and Kang C. (2000) *'Random Field Formulation Of Composite Laminates'*, J. of Composite Structures, 49(1), 87-93, doi: 10.1016/s0263-8223(99)00128-2
- [36] Burton T., Jenkins N., Sharpe D. and Bossanyi E. (2011) *'Wind Energy Handbook'*, Second Edition, ISBN: 9780470699751, doi: 10.1002/9781119992714
- [37] Fingersh L., Hand M. and Laxson A. (2006) *'Wind Turbine Design Cost And Scaling Model'*, Technical Report, NREL/TP-500-40566
- [38] Bortolotti P., Berry D., Murray R., Gearthner E., Jenne D., Damiani R., Barter G. and Dykes K. (2019) *'A Detailed Wind Turbine Blade Cost Model'*, Golden, CO: National Renewable Energy Laboratory, NREL/TP-5000-73585, <https://www.nrel.gov/docs/fy19osti/73585.pdf>
- [39] Bergeles G. (2005) *'Wind Turbine'* 1st edition, ISBN: 960-7888-57-x
- [40] Virtanen P., Gommers R., Oliphant T. et al. (2020) *'SciPy 1.0: Fundamental Algorithms For Scientific Computing In Python'*, Nature Methods 17, 261-272 (2020), <https://doi.org/10.1038/s41592-019-0686-2>
- [41] Powell (1994) *'A Direct Search Optimization Method That Models The Objective And Constraint Functions By Linear Interpolation'*, Advances in Optimization and Numerical Analysis, 51-67, doi: 10.1007/978-94-0158330-5_4

- [42] Powell M. (2007) *'A View of Algorithms For Optimization Without Derivatives'*, Department of Applied Mathematics and Theoretical Physics, Center for Mathematical Sciences, 2007/NA03, http://www.damtp.cam.ac.uk/user/na/NA_papers/NA2007_03.pdf
- [43] Kraft D. (1988) *'A Software Package For Sequential Quadratic Programming'*, Technical Report. DFVLR-FB 88-28, DLR German Aerospace Center – Institute for Flight Mechanics, Koln - Germany
- [44] Broyden C. (1970) *'The Convergence Of A Class of Double-rank Minimization Algorithms'*, IMA Journal of Applied Mathematics, 6(3), 222-231, doi: 10.1093/imamat/6.3.222
- [45] Fletcher R. (1970) *'A New Approach To Variable Metric Algorithms'*, The Computer Journal, 13(3), 317-322, doi: 10.1093/comjnl/13.3.317
- [46] Goldfarb D. (1970) *'A Family Of Variable-metric Methods Derived By Variational Means'*, Mathematics of computation, 24(109), 23, doi: 10.2307/2004873
- [47] Shanno D. (1970) *'Conditioning Of Quasi-newton Methods For Function Minimization'*, Mathematics of Computation, 24(111), 647-647, doi: 10.1090/s0025-5718-1970-0274029-x
- [48] Serafeim G., Manolas D., Riziotis V. and Chaviaropoulos P. (2020) *'Lightweight Optimal Rotor Design Of A 10W-scale Wind Turbine Using Passive Load Control Methods'*, J. of Phys.: Con. Ser. 1618, 022061, doi: 10.1088/1742-6596/1618/2/011061
- [49] Serafeim G., Manolas D., Riziotis V., Chaviaropoulos P. and Saravanos D. (2022) *'Optimized Blade Mass Reduction Of A 10MW-scale Wind Turbine Via Combined Application Of Passive Control Techniques Based Of Flap-Edge And Bend-Twist Coupling Effects'*, J. of Wind Engineering & Industrial Aerodynamics 225 (2022) 105002, <https://doi.org/10.1016/j.jweia.2022.105002>
- [50] Bergami L. and Poulsen N. (2015) *'A Smart Rotor Configuration With Linear Quadratic Control Of Adaptive Trailing Edge Flaps For Active Load Alleviation'*, Wind Energ. 2015; 18:625-641, doi: 10.1002/we.1716
- [51] Gonzalez A., Enevoldsen P., Barlas A. and Madsen H. (2021) *'Field Test Of An Active Flap System On A Full-scale Wind Turbine'*, WES 6, 33-43, <https://doi.org/10.5194/wes-6-33-2021>
- [52] Lobitz D. and Veers P. (2003) *'Load Mitigation With Bending/Twist-Coupled Blades On Rotors Using Modern Control Strategies'*, Wind Energ. 2003; 6:105-117, doi: 10.1002/we.74
- [53] Bagherpour T., Li X., Manolas D. and Riziotis V. (2018) *'Modeling Of Material Bend-Twist Coupling On Wind Turbine Blades'*, J. of Composite Structures 193 (2018) 237-246, <https://doi.org/10.1016/j.compstruct.2018.03.071>
- [54] Manolas D., Serafeim G., Chaviaropoulos P., Riziotis V. and Voutsinas S. (2018) *'Assessment Of Load Reduction Capabilities Using Passive And Active Control Methods On A 10MW-scale Wind Turbine'*, J. of Phys.: Con. Ser. 1037 (2018) 032042, doi: 10.1088/1742-6596/1037/3/032042
- [55] Hansen H. (2007) *'Aero-elastic Instability Problems For Wind Turbines'*, Wind Energy, 10(6), 551-577, doi: 10.1002/we.242
- [56] Pavese C., Kim T. and Murcia J. (2017) *'Design Of A Wind Turbine Swept Blade Through Extensive Load Analysis'*, Renewable Energy, 102, 21-34, doi: 10.1016/j.renene.2016.10.039